

INFORMATION TO USERS

This manuscript has been reproduced from the microfilm master. UMI films the text directly from the original or copy submitted. Thus, some thesis and dissertation copies are in typewriter face, while others may be from any type of computer printer.

The quality of this reproduction is dependent upon the quality of the copy submitted. Broken or indistinct print, colored or poor quality illustrations and photographs, print bleedthrough, substandard margins, and improper alignment can adversely affect reproduction.

In the unlikely event that the author did not send UMI a complete manuscript and there are missing pages, these will be noted. Also, if unauthorized copyright material had to be removed, a note will indicate the deletion.

Oversize materials (e.g., maps, drawings, charts) are reproduced by sectioning the original, beginning at the upper left-hand corner and continuing from left to right in equal sections with small overlaps.

Photographs included in the original manuscript have been reproduced xerographically in this copy. Higher quality 6" x 9" black and white photographic prints are available for any photographs or illustrations appearing in this copy for an additional charge. Contact UMI directly to order.

**Bell & Howell Information and Learning
300 North Zeeb Road, Ann Arbor, MI 48106-1346 USA
800-521-0600**

UMI[®]

.

STUDY OF THE ${}^9\text{Li}(d,p){}^{10}\text{Li}$ REACTION

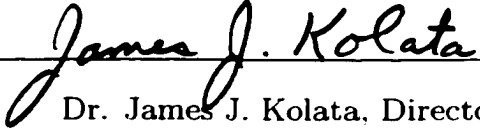
A Dissertation

Submitted to the Graduate School
of the University of Notre Dame
in Partial Fulfillment of the Requirements
for the Degree of

Doctor of Philosophy

by

Peter Angelo Santi, B.S., M.S.


Dr. James J. Kolata, Director

Department of Physics

Notre Dame, Indiana

December 2000

UMI Number: 9991258

UMI[®]

UMI Microform 9991258

Copyright 2001 by Bell & Howell Information and Learning Company.

**All rights reserved. This microform edition is protected against
unauthorized copying under Title 17, United States Code.**

**Bell & Howell Information and Learning Company
300 North Zeeb Road
P.O. Box 1346
Ann Arbor, MI 48106-1346**

STUDY OF THE ${}^9\text{Li}(d,p){}^{10}\text{Li}$ REACTION

Abstract

by

Peter Angelo Santi

The structure of the particle unbound nucleus, ${}^{10}\text{Li}$, was investigated in a kinematically complete experiment using the ${}^9\text{Li}(d,p){}^{10}\text{Li}$ reaction in inverse kinematics at an incident ${}^9\text{Li}$ energy of 20 MeV/A. The experiment utilized the S800 Spectrograph at the National Superconducting Cyclotron Laboratory to measure the outgoing ${}^9\text{Li}$ from the breakup of ${}^{10}\text{Li}$ in coincidence with the recoiling protons from the (d,p) reaction which were measured using a series of silicon detectors. Based on the measured kinematics of the recoiling protons from the ${}^9\text{Li}(d,p)$ reaction, a lower limit to the mass of ${}^{10}\text{Li}$ was measured at $\Delta = 33.098 \pm 0.08$ MeV which is consistent with previous measurements.

A complete reconstruction of the breakup of ${}^{10}\text{Li}$ was performed based on the measured properties of the outgoing ${}^9\text{Li}$ nucleus, the recoiling proton, and the incident ${}^9\text{Li}$ beam. This reconstruction made it possible to isolate the structure of ${}^{10}\text{Li}$ associated with a ground state ${}^9\text{Li}$ core from structure associated with a ${}^9\text{Li}$ core in its first excited state. The observed ratio of ${}^9\text{Li}^*$ core events to the total number of ${}^{10}\text{Li}$ events that were detected in the experiment was 0.098 ± 0.04 at forward center of mass angles (2.7° to 9.5°), and 0.244 ± 0.04 at more backward center of mass angles (11° to 26°). This ability to identify ${}^{10}\text{Li}$ events associated with a ${}^9\text{Li}$ ground state core allowed for a relatively background free measurement of the low-lying structure of ${}^{10}\text{Li}$. The best fit to the Q-value spectra for ${}^{10}\text{Li}$ events

with a ${}^9\text{Li}$ ground state core yielded a state located at $Q = -2.58(11)$ MeV which corresponds to a neutron separation energy $S_n = -0.35(11)$ MeV. Due to the poor Q -value resolution that was observed in this experiment, however, the existence of an additional low-lying state at $Q > -2.43$ MeV ($S_n > -0.2$ MeV) could not be ruled out. The angular distribution of this structure was measured and compared with coupled reaction channel (CRC) calculations for an s-wave and a p-wave state. The comparison between the data and theory was inconclusive, however, in determining the nature of the observed structure in ${}^{10}\text{Li}$.

Dedicated to my parents. Joe and Marie Santi.

CONTENTS

TABLES	v
FIGURES	vi
ACKNOWLEDGEMENTS	xv
CHAPTER 1: INTRODUCTION	1
CHAPTER 2: THEORETICAL BACKGROUND	6
2.1 Binding Energy	6
2.2 Shell Model	12
2.3 Scattering Theory	15
2.4 Optical Model	21
2.5 Coupled Channels Calculation	24
CHAPTER 3: EXPERIMENTAL METHOD	28
3.1 Overview	28
3.1.1 The (d,p) reaction	29
3.1.2 Kinematics of the ${}^9\text{Li}(d,p){}^{10}\text{Li}$ Reaction	30
3.2 Beam Production	35
3.3 S800 Analysis Line	37
3.4 Target Chamber	47
3.4.1 CD detectors	52
3.4.2 Silicon Strip Array	53
3.4.3 Calibrating the silicon detectors	58
3.5 S800 spectrograph	61
CHAPTER 4: ANALYSIS	71
4.1 Overview	71
4.2 Analysis of Experimental Systematics	74
4.2.1 S800 spectrograph	74
4.2.2 Incident ${}^9\text{Li}$ Energy Measurement	82

4.2.3	Analysis line	90
4.2.4	Testing the transfer maps	99
4.2.5	$^{13}\text{C}(\text{d,p})^{14}\text{C}$ Reaction	102
4.3	Analysis of $^9\text{Li}(\text{d,p})^{10}\text{Li}$ Data	121
4.3.1	Mass measurement	129
4.3.2	Q-value measurement	131
CHAPTER 5: INTERPRETATION AND CONCLUSIONS		137
5.1	Full Reconstruction	137
5.2	Monte Carlo Simulation	150
5.2.1	Overview	150
5.2.2	Event Generation	151
5.2.3	Detection of simulated events	159
5.2.4	Monte Carlo results	163
5.2.5	Fitting procedure	175
5.3	Angular Distribution	184
5.4	Conclusions	187
APPENDIX A: SILICON DETECTOR INFORMATION		190
BIBLIOGRAPHY		192

TABLES

1.1	Summation of the previous studies of the structure of ^{10}Li	5
3.1	Optical model parameters used in the FRESCO calculation shown in Fig. 3.12.	50
4.1	Results of weighted fits to δ_E vs a_{803} for various direct beam runs with 1% momentum spread (Runs 8 and 62) and 1/4% momentum spread (Run 61).	86
4.2	Altered first order transfer map elements for the analysis line.	96
4.3	Estimated background in the coincidence spectra for the strip detectors due to the ^{241}Am source.	128
5.1	Size of limiting apertures within S800 spectrograph.	160
5.2	Fitting parameters for the CD Q-value spectra.	184
A.1	Energy resolution for individual sectors of CD1 and CD2 as determined by measuring the width of the 3.18 MeV α -line in ^{148}Gd	190
A.2	Energy resolution for the individual strip detectors based on the measured width of the 3.18 MeV α -line in ^{148}Gd	191
A.3	Average position resolution of the different strips on the strip detectors based on the measured width of the slits on the calibration mask. All resolutions given are FWHM in mm.	191

FIGURES

1.1	Chart of the nuclides in the region of proton numbers from $Z = 1$ (Hydrogen) to $Z = 6$ (Carbon) showing the location of the various types of neutron halo nuclei.	3
1.2	Schematic diagram of the Borromean nucleus ^{11}Li	4
2.1	Neutron density distribution for a neutron bound by 0.2 MeV (dashed curve) and 8.0 MeV (solid curve) based on the square well potential model.	11
2.2	Level structure in ^{10}Li based on naive shell model.	13
2.3	Plot of the calculated difference between the excitation energy of the $1/2^+$ and $1/2^-$ states and the neutron separation energy for $N=7$ isotones.	15
2.4	(a) Typical radial wave function for a bound state showing a positive scattering length a. (b) Radial wave function for an unbound state showing a negative scattering length.	21
2.5	Plot of two sample (a) volume and (b) surface Woods Saxon potentials. The solid curves in (a) and (b) are the real and imaginary potentials used to describe the $^9\text{Li} + \text{deuteron}$ system, respectively, while the dashed curves are the potentials used to describe the $^{10}\text{Li} + \text{proton}$ system. The parameters for both sets of potentials are given in Table 3.1.	23
3.1	Schematic diagram of the $^9\text{Li}(d,p)^{10}\text{Li}^* \Rightarrow ^9\text{Li} + n$ reaction performed in the (a) lab frame and (b) center of mass reference frame for the (d,p) reaction. The solid lines indicate the quantities measured in this experiment whereas the dashed lines are those quantities which were reconstructed from the data.	32
3.2	Plot of the calculated (a) ^{10}Li lab angle and (b) proton lab angle as a function of the ^{10}Li center of mass scattering angle in the $^9\text{Li}(d,p)^{10}\text{Li}$ reaction based on an incident ^9Li energy of 177 MeV. The calculations were performed using the relativistic kinematic code, PKIN.	33
3.3	Diagram of the A1200 fragment separator.	36

3.4	Diagram of the S800 analysis line and spectrograph.	38
3.5	Plot of pad signal vs pad number in S803 for a single direct beam event.	43
3.6	Plot of pad signal vs pad number in S803 for a pulser run (a) before and (b) after the pads were gain matched. In this particular run, the pulser was set to half scale.	44
3.7	Diagram of the intermediate image chamber showing S803, S804 and the two masks for a calibration run. The imaging of the masks is carried out with E1 as the trigger in the focal plane. For the actual data runs, the masks were lowered completely out of the beam.	45
3.8	Diagram of the masks used for calibrating (a) S803 and (b) S804.	46
3.9	Reconstructed mask pattern for (a) S803 mask and (b) S804 mask without correcting for the non-linear response of S803 and S804 in the drift direction. The arrows indicate where the non-linear response of the detectors is most evident in the mask patterns. The corrected mask patterns are shown in (c) and (d) for S803 mask and S804 mask, respectively.	48
3.10	Diagram of the S800 target chamber	49
3.11	Plot of the energy of the proton as a function of its scattering angle in the lab for the ${}^9\text{Li}(d,p)$ reaction (solid curve) in comparison with the kinematics of the lighter recoiling nuclei from potential background reactions between the ${}^9\text{Li}$ beam and the CD_2 target. The arrows indicate the range of angles covered by the silicon detectors in the target chamber. All of the kinematics were calculated using the code PKIN assuming a ${}^9\text{Li}$ incident energy of 19.7 MeV/A.	51
3.12	Calculated angular distributions for populating an s-state (dark curve) or a p-state (red curve) in ${}^{10}\text{Li}$ for the ${}^9\text{Li}(d,p)$ reaction. The dashed lines indicate the range of angles covered by each of the silicon detectors.	52
3.13	Block diagram of the electronics for a CD detector. The large arrows indicate multiple signals being processed through separate channels in the same module.	54
3.14	Schematic diagram of the Silicon Strip Array as seen by the target. In the diagram, the incident beam is coming out of the page. Note that Strip Detector #5 was not used in the experiment.	56
3.15	Block diagram of the electronics for a Strip detector. The large arrows indicate multiple signals being processed through separate channels in the same module.	57

3.16	(a) Schematic diagram of the masks used to calibrate the strip position. The first three strips were located at the edge of the detector closest to the target. (b) Measured mask pattern along strip #11 on Strip Detector #3, using the method described in equation 3.21. (c) Mask pattern for strip #11 on Strip Detector #1 using method described in equation 3.22.	60
3.17	Diagram of S800 focal plane.	64
3.18	Plot of (a) S801 TAC and (b) S802 TAC as a function of time as measured by the number of buffers written to tape starting with Run #12 in comparison to the pad response in (c) S803 and (d) S804 over that same time period. The plots correspond to the behavior of the CRDC's over a period of approximately 75 hours in time. The arrows indicate when Run #18 and Run #34 occurred relative to Run #12.	67
3.19	Plot of the initially measured y-position in (a) S801 and (b) S802 as a function of the number of buffers from Run # 18. The solid line represents the 5th order polynomial weighted fit used to described the drift as a function of buffer number. The effects of the correction are shown in (c) and (d) for S801 and S802, respectively.	68
3.20	Plot of the Ion Chamber signal as a function of the (a) signal in E1 and (b) BLT TAC for the direct ${}^9\text{Li}$ beam as measured in the focal plane of the S800.	70
4.1	Diagram of the coordinate system used to measure the motion of a beam particle with momentum \vec{p} through the beam line.	74
4.2	Plots of the magnetic field as a function of the distance traveled inside a given element for the four elements of the spectrograph. The red solid curve is the interpolated field while the black dashed curve is the fit using a 4th-order Enge function. The residuals for each fit are plotted directly above each magnetic field plot. The field settings shown were used within the spectrograph to measure the recoiling ${}^9\text{Li}$ from the breakup of ${}^{10}\text{Li}$	78
4.3	Distribution of the reconstructed energy at the target for the direct beam run with 1/4% momentum slits in place.	81
4.4	Distribution of the reconstructed y position at the target for the hole target run from the measured focal plane information.	82
4.5	Ray trace diagram of the S800 Analysis line from the BLT to S804 for ray with three different momenta, + 1/2% δ_p (black), - 1/2% δ_p (red), and the central momentum (green) of the beam line. The diagram was generated using COSY and assumes that the ray originated from a single point at the center of the beam line.	84

4.6	Plot of δ_E vs a_{803} for the direct ${}^9\text{Li}$ beam for Run #8. The solid curve represents the linear weighted fit used to determine the slope of δ_E in terms of a_{803}	85
4.7	Distribution of (a) δ_{a803} and (b) $\delta_{a803} - \delta_E$ for the 1/4% momentum run.	87
4.8	Ray trace diagram of the S800 Analysis line from the PPAC to S804 for a series of rays spaced 3 mm apart about the center of the PPAC, at different momenta.	88
4.9	Plot of a_{803} as a function of PPAC x for Run #8.	89
4.10	(a) Distribution of the initially reconstructed x position at the target for the hole target run using the COSY transfer map for the 'hole target' run. (b) Distribution of the reconstructed y position at the target using the COSY transfer map for the 'hole target' run. The black histogram is the forward reconstruction using information from S803 and S804 while the purple histogram is inverse reconstruction from Figure 4.4.	92
4.11	Plot of the difference between reconstructed y positions at the target (Δy_{target}) as a function of (a) y_{803} and (b) b_{803}	94
4.12	Plot of the difference between reconstructed y positions at the target (Δy_{target}) as a function of b_{803} (top row) and y_{803} (bottom row) for the (a) initial transfer map elements, (b) final (y b) element but initial (y y) element, and (c) final (y b) and (y y) elements included in the transfer map. The horizontal line indicates no correlation between the two parameters.	95
4.13	(a) Reconstructed x_{target} distribution using the corrected forward map for the 'hole target' run. (b) Reconstructed y_{target} distribution for the 'hole target' run.	97
4.14	(a) Reconstructed y_{target} distribution using the corrected forward map (black histogram) and the inverse transfer map (purple histogram) for the 'hole target' run. (b) Δy_{target} distribution for the hole target run. (c) Δa_{target} distribution and (d) Δb_{target} distribution for the 'hole target' run.	98
4.15	(a) Plot of b_{focal} vs a_{focal} as measured in the focal plane for Run # 51. (b) Plot of x_{focal} vs y_{focal} as measured in the focal plane for Run # 51. (c) Plot of the reconstructed b_{focal} vs a_{focal} . (d) Plot of the reconstructed x_{focal} vs y_{focal}	101
4.16	Difference distributions between reconstructed and measured parameters in the focal plane.	102
4.17	Level diagram for ${}^{14}\text{C}$	104

4.18	(a) Plot of ΔE vs E from the focal plane for the direct ^{13}C beam. (b) Plot of ΔE vs E for the reaction products from the $^{13}\text{C}(\text{d,p})^{14}\text{C}$ reaction. (c) Plot of ΔE vs E for reaction events in coincidence with the silicon detector array. The cross in (b) and (c) indicates the location of the direct ^{13}C beam for reference.	106
4.19	(a) Plot of energy vs angle for the ^{14}C events in coincidence with the silicon detectors. (b) Plot of energy vs angle for all of the proton events in coincidence with the focal plane. The solid curves are the calculated kinematics from PKIN for the ground state and 1st excited state ($E_x = 6.093$ MeV) of ^{14}C	108
4.20	Plot of ^{14}C energy vs proton angle for the coincidence events. The solid curves are the calculated kinematics from PKIN for the ground state and 1st excited state in ^{14}C	109
4.21	(a) Plot of the ^{14}C energy vs angle in the focal plane showing the gate used to identify the ground state band in the silicon detectors. (b) Plot of the proton energy as a function of angle for the gated ground state events in the focal plane. The solid curve represents the ideal kinematics of the proton while the dashed and dotted curve correspond to the expected kinematics for the punch through events assuming the protons passed through the center of the detector or the edge of the detector, respectively.	111
4.22	(a) Proton kinematic plots for the various strip detectors corresponding to the excited states in ^{14}C . The solid curve in each plot is the expected kinematic curve for the population of the 1st excited state in ^{14}C while the dashed curve corresponds to the threshold for the breakup of ^{14}C . (b) Corresponding Q-value histograms for the various strip detectors.	113
4.23	(a) Proton kinematic plots for the various strip detectors corresponding to the excited states in ^{14}C with array offset in the x direction by 1.1 cm. (b) Corresponding Q-value histograms for the strip detectors with the offset.	114
4.24	Plot of the proton energy vs angle for the ground state events in the strip detectors with the 1.1 cm x offset in place.	115
4.25	(a) Plot of the measured Q-value in CD2 as a function of the sector number. The dashed line indicates the calculated Q-value for the ground state in ^{14}C . (b) Q-value spectra from CD2.	116
4.26	(a) Plot of the measured Q-value in CD2 as a function of the sector number with CD2 offset from the optical axis. (b) Corrected Q-value spectra as measured by CD2.	117

4.27	(a) Comparison of the measured Q-value spectra in CD1 (solid histogram) with the measured Q-value spectra in CD2 (dashed histogram). (b) Plot of the measured proton energy vs angle for CD1 (circle) and CD2 (square). The solid curves represent constant Q-value. (c) Corrected Q-value spectra for the energy-shifted CD1 (solid histogram) compared with the measured Q-value spectra in CD2 (dashed histogram). (d) Measured proton energy vs angle for energy shifted CD1 (circle) and CD2 (square).	120
4.28	(a) Plot of the ΔE vs E spectra of the reaction products from the ${}^9\text{Li}(d,p){}^{10}\text{Li}$ reaction. (b) Plot of the ΔE vs E spectra for reaction events in coincidence with a silicon detector.	122
4.29	(a) Plot of the silicon energy as a function of angle for all of the events detected by the silicon detectors. (b) Plot of the silicon energy as a function of angle for events in coincidence with ${}^9\text{Li}$ in the focal plane. The solid line indicates the calculated kinematic edge for the ${}^9\text{Li}(d,p){}^{10}\text{Li}$ reaction.	123
4.30	(a) Plot of the proton energy as a function of buffer number for (a) Strip #2 (b) Strip #3 and (c) Strip #6 for the ${}^9\text{Li}(d,p){}^{10}\text{Li}$ reaction runs. The arrow indicates the start of Run # 25.	125
4.31	Energy spectrum of the ${}^{241}\text{Am}$ source as measured by (a) Strip #2, (b) Strip #4, and (c) Strip #6 in singles mode. The solid line indicates the lower edge of the alpha peak used to separate the alpha peak from the flat background.	127
4.32	Plot of calculated uncertainty in the Q-value as a function of the proton scattering angle with the measurement of the incident included (solid curve) and without a measured incident energy (dashed curve). Both calculations were performed for a Q-value of -2.25 MeV assuming an uncertainty in the measured proton energy of $\pm 1.5\%$ (σ) for all of the scattering angles.	130
4.33	Plot of proton energy vs proton angle for data in coincidence with ${}^9\text{Li}$ in focal plane, S803, and S804. The solid curve is the best kinematic fit to the data varying only the mass of ${}^{10}\text{Li}$ while the gold points indicate the events which were considered in fitting the kinematic edge. In the inset, the reduced χ^2 for the kinematic fit as a function of the mass excess of ${}^{10}\text{Li}$	132
4.34	(a)-(b) Q-value spectra for the CD detectors and Strip detectors, respectively, for all coincident proton events. (c)-(d) Q value spectra for CD detectors and Strip detectors, respectively, for proton data in coincidence with S803 and S804 as well as the focal plane. In all of the figures, the dotted line is Q-value corresponding to the ${}^9\text{Li}+n$ threshold while the dashed line is the Q-value corresponding to the measured mass of ${}^{10}\text{Li}$	133

4.35	Relative angular distribution of the (d,p) events with $Q \geq -4.0$ MeV as a function of (a) the proton laboratory scattering angle and (b) the ^{10}Li center of mass angle.	136
5.1	Plot of β as a function of the mass of ^{10}Li . The β value was calculated assuming an incident ^9Li energy of 177.09 MeV and a detected proton energy of 2.4 MeV. The dashed curve represents a 2σ error in the determined ^{10}Li total energy assuming that the energy of the incident ^9Li was detected. The dotted curve is the error without an incident energy measurement.	140
5.2	Summed reconstructed breakup Q-value spectra for the (a) CD detectors and the (b) Strip detectors. In both (a) and (b), the dashed histogram is the distribution of events in which the Q-value for the (d,p) reaction was measured larger than -2.20 MeV.	142
5.3	Reconstructed Q-value spectra for the breakup of ^{10}Li as a function of the Q-value for the (d,p) reaction as measured by (a) the CD detectors and the (b) strip detectors. In both figures, the dashed line indicates the reaction Q-value corresponding to the measured ^{10}Li mass while the dotted line indicates the reaction Q-value corresponding to the $^9\text{Li} + n$ threshold.	144
5.4	(a) Q_{break} vs Q-value for the Strip detector data from Fig. 5.3(b). (b) Proton Energy vs Proton Angle for the Strip data. In both cases, the solid dots indicate the events which do not have the proper correlation between Q_{break} and the reaction Q-value.	145
5.5	a_{target} vs b_{target} as reconstructed from the spectrograph information for the outgoing ^9Li measured in coincidence with the proton detected in (a) Strip #1, (b) Strip #2, and (c) Strip #4. In each figure, the black filled circles are events with the (d,p) Q-value > -4.1 MeV, the gold filled circles are events with Q-values ranging from -4.1 MeV down to -6.3 MeV, and the open black circles are events with $Q < -6.3$ MeV.	148
5.6	Q-value of the (d,p) reaction as a function of ^{10}Li laboratory breakup angle θ_{br} for (a) the CD and (b) the Strip detectors. The solid dots in (b) are the uncorrelated events which were selected in Fig. 5.4 . . .	149
5.7	(a) Illustration of the rejection method in producing the a_{inc} distribution. (b) Resultant a_{inc} distribution from the Monte Carlo calculation (solid line) compared with the measured a_{inc} distribution from a direct beam run (red circles).	153

5.8	(a) Measured b_{inc} as a function of y_{inc} for the direct beam Run #62. (b) Rotated b_{inc} as a function of the rotated y_{inc} used to determine the projections of the two variables onto the rotated axes. (c) b_{inc} vs y_{inc} for 2500 events generated in the Monte Carlo simulation. The line in Figures (a) and (c) represents the slope used to determine the angle for rotating the spectrum.	155
5.9	Comparison between data (black curve) and the Monte Carlo results (gold curve) for (a) x_{801} (b) y_{801} (c) a_{focal} and (d) b_{focal} for a run with no target in place and the spectrograph set to measure the direct ${}^9\text{Li}$ beam. In all of the figures, the data have been scaled down by a factor of 15 to match the Monte Carlo results.	161
5.10	Comparison between data (blue histogram) and Monte Carlo results (gold histogram) for (a) x_{801} (b) y_{801} (c) a_{focal} and (d) b_{focal} with the CD_2 target in place. In all of the figures, the simulated results have been scaled to match the measured data.	164
5.11	Simulated excitation energy of ${}^{10}\text{Li}$ E_x as a function of the kinetic energy of the outgoing ${}^9\text{Li}$ for events in which the corresponding proton was detected by (a) the CD detectors and (b) Strip detectors. The solid gold circles indicate events which were detected by S801 and S802, the open black circles indicate events which were not detected in the focal plane, and the open green squares are the events which hit the beam block in front of S801.	167
5.12	(a)-(b) Reaction Q-value as a function of θ_{br} for the CD and Strip detectors, respectively. In the figures, the red circles are the data gated based on the results of the Monte Carlo simulation which assumed the ${}^9\text{Li}$ core in its ground state (light blue circles), while the blue open circles indicate the data that were not included in the gate. (c)-(d) Q_{break} as a function of the reaction Q-value for the CD and Strip detectors, respectively.	169
5.13	(a)-(b) Gated reaction Q-value distributions for the CD and Strip detectors, respectively, (black circles) along with the normalized results of the Monte Carlo simulation. (c)-(d) Gated Q_{break} distributions for the CD and Strip detectors, respectively, with the corresponding normalized Monte Carlo results.	171
5.14	(a)-(b) Reaction Q-value as a function of θ_{br} for the CD and Strip detectors, respectively. The brown circles are the result of the simulation where a ${}^9\text{Li}^*$ was produced in the breakup, while the yellow circles indicate the simulated results producing ${}^9\text{Li}$ in its ground state shown in Fig. 5.12. (c)-(d) Q_{break} as a function of the reaction Q-value for the CD and Strip detectors, respectively.	173

5.15	(a)-(b) ${}^9\text{Li}^*$ gated reaction Q-value distributions for the CD and Strip detectors, respectively, (black circles) along with the normalized results of the Monte Carlo simulation. (c)-(d) ${}^9\text{Li}^*$ gated Q_{break} distributions for the CD and Strip detectors, respectively, with the corresponding normalized Monte Carlo results.	175
5.16	(a)-(b) Simulated Q-value spectra for the CD and Strip detectors, respectively. (c)-(d) Simulated Q_{break} spectra for the CD and Strip detectors, respectively. In both cases, a delta function was assumed for the excitation of ${}^{10}\text{Li}$ centered at $E_x = 0.5$ MeV. The solid lines in the figures are the results of fits to the simulation using Gaussian distributions.	178
5.17	Ground state Q-value spectrum of the ${}^{13}\text{C}(\text{d,p}){}^{14}\text{C}$ as measured by the CD2 detector compared with the results from the Monte Carlo simulation normalized by the number of events in each spectrum.	179
5.18	(a)-(b) Simulated Q_{break} spectra for the CD and Strip detectors, respectively, assuming a delta function excitation curve located at $E_x = 0.2$ MeV (solid histogram) and $E_x = 1.2$ MeV (dashed histogram). (c)-(d) Simulated Q-value spectra for the CD and Strip detectors, respectively, for $E_x = 0.2$ MeV (solid histogram) and $E_x = 1.2$ MeV (dashed histogram).	182
5.19	Fits to the CD Q-value spectrum assuming a single resonance (solid curve) and 2 resonances (dashed curve) along with an uncorrelated background (dotted curve). The parameter for the fits are presented in Table 5.2.	183
5.20	Efficiency corrected relative angular distribution of the (d,p) events with $Q \geq -4.0$ MeV as a function of (a) the proton laboratory scattering angle and (b) the ${}^{10}\text{Li}$ center of mass angle. The black and red curves in (b) are the FRESCO calculations for the s-wave and p-wave, respectively. The calculations have been normalized to match the data based on the first data point.	186

ACKNOWLEDGEMENTS

First and foremost, I must thank my advisor, Dr. James J. Kolata, whose wisdom, support, patience, and confidence in me made this thesis possible.

As with all projects in Nuclear physics, my thesis experiment was the result of a collaborative effort. I must thank the people at Michigan State University, specifically Brad Sherrill, whose work on the A1200 fragment separator and the S800 Spectrograph was crucial for this experiment, Daniel Bazin who designed the detector array used in this experiment and whose knowledge of the S800 Spectrograph was quite helpful in understanding the data, and John Yurkon, who designed and maintained the detectors used in the S800 Spectrograph as well as the tracking detectors.

I would be remiss if I didn't thank my fellow group-mates here at Notre Dame, who I feel are more like friends than colleagues. Specifically, Don Peterson, with whom I have had many conversations about the difficulties with our data, Valdir Guimarães, and Ryan White-Stevens, who assisted in the initial analysis of this data.

I would like to thank Paul DeYoung, Graham Peaslee, and Pete Jolivette from Hope College who provided their time and talents during the running of the experiment and helped keep me on track. I appreciate the time we have spent together working on experiments and hope to do so again in the future.

I would also like to acknowledge the staff at Notre Dame's Nuclear Structure Laboratory: Jim Kaiser, whose support of the lab's computer cluster was crucial for

this work as well as many others at Notre Dame; Larry Lamm, with whom I have had many productive and entertaining conversations. and Charles Guy.

Of course life is not worth living without people to love. and so I must thank my wife, Naomi, whose unconditional love and support helped get through all of the rocky times in my life in the last few years. I also must thank my son, Joseph Mordecai, for giving me the burst of energy that was needed to complete this thesis and focus on the tasks at hand.

Finally, I must thank my parents, Joe and Marie Santi, who gave me the perfect example of how to live in this world, and who taught me everything that is important in life. I am afraid my gratitude to them can never be expressed in this lifetime. I dedicate this thesis to them and to their memory. May they rest in peace.

CHAPTER 1

INTRODUCTION

Since its discovery by Rutherford in 1911 [1], the study of the atomic nucleus has advanced considerably over the past century. A vast number of stable and radioactive nuclides have been studied and cataloged, allowing for a general understanding of the basic properties of the nucleus as well as how these properties vary as a function of the neutron and proton number. While much is known about the nucleus, many questions still remain in terms of the behavior of the nucleus as it is pushed to the extreme limits of stability. It is not clear, for example, if the properties that are observed in stable nuclei remain the same for those nuclei which are barely bound against particle decay. It is also unclear how much the current models of the nucleus that were developed to describe the properties of stable nuclei will need to be adjusted for nuclei which are weakly bound. It is these questions, among many others, which need to be addressed in order to enhance our understanding of the atomic nucleus.

Until recently, the study of the nucleus was limited to those nuclei near the valley of stability due in part to the fact that the majority of the beams and targets available for use in experiments consisted of nuclei which were either stable or had extremely long lifetimes. This restriction in the incident beam limited the ability of earlier experiments to produce nuclei which were far from stability. With the development of radioactive ion beams (RIB), nuclei which exist far from stability

could now be produced by various experimental techniques and studied systematically. The subsequent expansion in the range of nuclei which are accessible as a result of the development and usage of RIBs has led to the discovery of new and exotic properties of the nucleus. One of the more interesting discoveries that has occurred through the use of RIBs is the existence of a “neutron halo” in weakly bound nuclei near the neutron drip line, where neutron rich nuclei reach the limit of particle stability. This neutron halo consists of one or more neutrons that exist at rather large distances away from the center of the nucleus, which is evident as an extended tail in the neutron density distribution [2]. As a result of this tail in the neutron density distribution, halo nuclei have a more diffuse surface region as well as a larger radius than is observed for most nuclei. The increased size of the halo nucleus relative to other nuclei generally increases the probability of the halo nucleus interacting with other nuclei as is evident by large interaction cross sections [3].

Figure 1.1 shows the location of the various neutron halo nuclei that have been discovered relative to the valley of stability in the chart of the nuclides. The most common type of halo nucleus that has been discovered to date is the two neutron halo nucleus such as ${}^{11}\text{Li}$, ${}^6\text{He}$ and ${}^{14}\text{Be}$. The two neutron halo nuclei that have been discovered to date, with the exception of ${}^{12}\text{Be}$, exhibit the unique property of being stable against particle decay while the nucleus with one less neutron is particle unstable. This implies that removing one neutron from a two neutron halo nucleus produces a particle unstable nucleus, which results in the halo nucleus breaking apart into a core nucleus plus two neutrons. Since neither of the two body subsystems in these two neutron halo nuclei are bound against particle decay, the forces which keep these nuclei bound must be due to the three body interaction of the core nucleus plus the two individual neutrons. Hence the structure of these nuclei is best described by a three body system and they are often referred to as “Borromean” nuclei, due

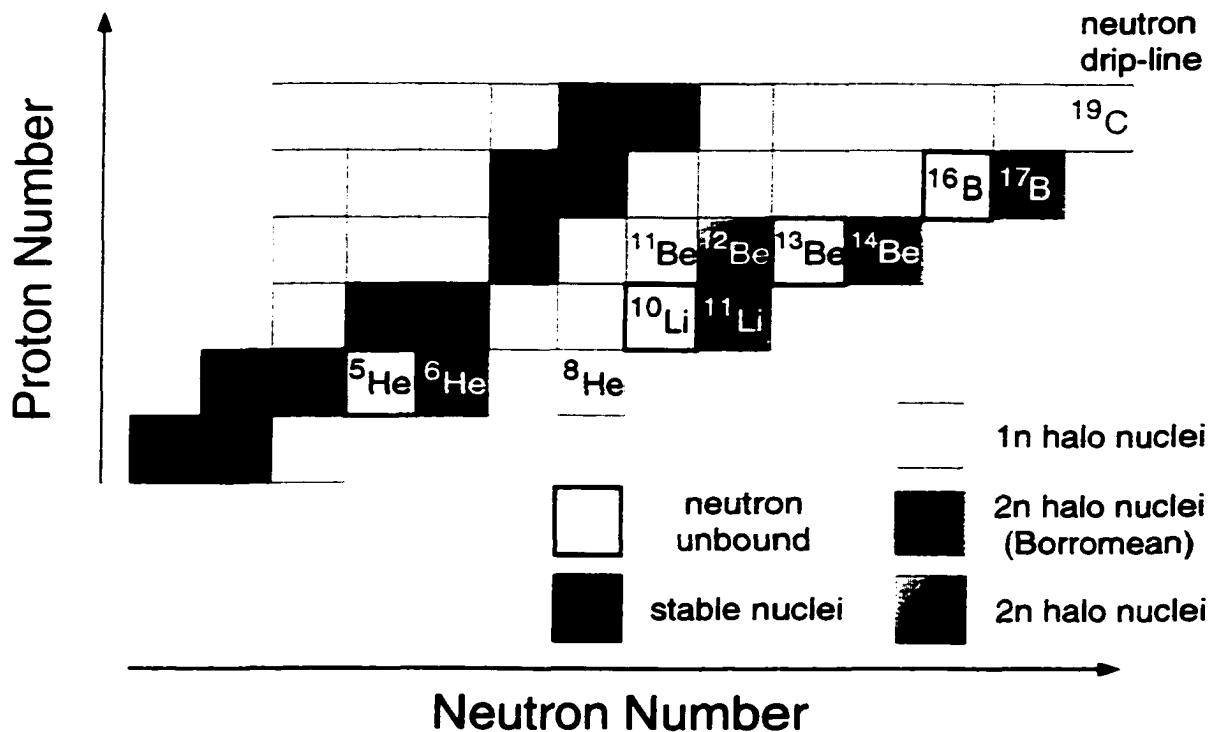


Figure 1.1. Chart of the nuclides in the region of proton numbers from $Z = 1$ (Hydrogen) to $Z = 6$ (Carbon) showing the location of the various types of neutron halo nuclei.

to the similarity of their structure with the Borromean rings which consist of three interlocking circles [4]. (An example of such a comparison can be seen in Figure 1.2 where the Borromean rings are superimposed onto a schematic diagram of the three body structure of the Borromean nucleus ^{11}Li .) Because of this unique structure, Borromean nuclei exhibit properties which have not been observed before in the nucleus.

In order to properly model and understand Borromean nuclei, it is necessary to determine what the structure of the two body subsystems is within the nucleus. While the structure of the neutron + neutron system is relatively well understood, the structure of the core + neutron subsystem is quite uncertain for most of these

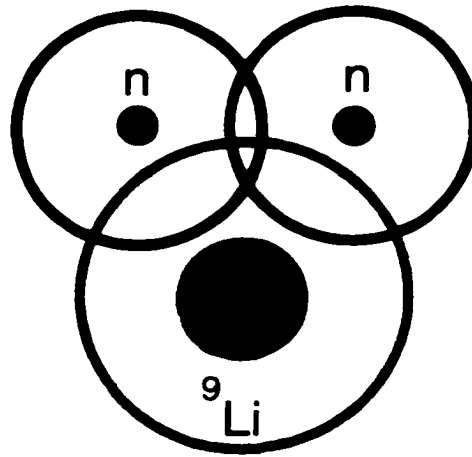


Figure 1.2. Schematic diagram of the Borromean nucleus ^{11}Li .

Borromean nuclei. In the case of ^{11}Li , which has been the most studied halo nucleus to date, the study of the core + neutron subsystem involves a determination of the structure of the unbound nucleus, ^{10}Li [4]. One major question which exists concerning the structure of ^{10}Li is the location, spin and parity of the ground state configuration. Previous studies on the structure of ^{10}Li have produced varying results and do not provide a clear picture of the structure of ^{10}Li . This is illustrated in Table 1.1 in which the results of the previous studies of ^{10}Li are listed in terms of the reaction used in the experiment, the energies and widths of the states that were observed as well as the assignment of the state in the structure of ^{10}Li . Of particular interest is the possible presence of a low-lying s-wave state that was first observed by Kryger, et al. [5] who investigated the neutron decay of ^{10}Li from the fragmentation of ^{18}O and observed a state which decays by very low energy neutron emission. Other groups have also observed a similar state which decays with low energy neutron emission [6, 7, 8, 9]. The presence of a low-lying s-wave state in ^{10}Li

Table 1.1. Summation of the previous studies of the structure of ^{10}Li

Reaction	$-S_n$ (MeV)	Γ (MeV)	State	Ref.
$^9\text{Be}(^9\text{Be}, ^8\text{B})^{10}\text{Li}$	0.80(25)	1.2(3)	ground state	[11]
$^{11}\text{B}(\pi^-, \text{p})^{10}\text{Li}$	0.15(15)	<0.4	ground state	[12]
$^{18}\text{O} + \text{natC}$ fragmentation	<0.15		ground state	[5]
$^{11}\text{B}(^7\text{Li}, ^8\text{B})^{10}\text{Li}$	<0.10	<0.23	ground state ($s_{1/2}$)	[7]
	0.54(6)	0.36(2)	excited state ($p_{1/2}$)	
$^{11}\text{Li} + \text{C}$ stripping	<0.05		ground state ($s_{1/2}$)	[8]
$^{10}\text{Be}(^{12}\text{C}, ^{12}\text{N})^{10}\text{Li}$	0.24(6)		($p_{i/2}$)	[13]
$^9\text{Be}(^{13}\text{C}, ^{12}\text{N})^{10}\text{Li}$	0.53(6)	0.30(8)		[13]
Breakup of ^{11}Li	0.21(5)	$0.12^{+0.10}_{-0.05}$		[9]
	0.62(10)	0.6(1)		
$^{18}\text{O} + ^9\text{Be}$ fragmentation	<0.05		ground state	[6]
$^9\text{Be}(^9\text{Be}, ^8\text{B})^{10}\text{Li}$	0.50(6)	0.40(6)	($p_{1/2}$)	[14]

has important theoretical consequences in the modeling and understanding of ^{11}Li as has been demonstrated in the work of Thompson, et al. [10] among others.

In order to clarify the ambiguity surrounding the structure of ^{10}Li in terms of the states that are present in ^{10}Li , as well as to identify the spins and parities of the states, a study of the structure of ^{10}Li was performed via the $^9\text{Li}(d, p)^{10}\text{Li}$ reaction. It is the results of this study which are presented in this work. This thesis is organized into the following chapters. In Chapter 2, the principles of nuclear physics which are relevant to this work will be discussed together with various aspects of halo nuclei, specifically the two neutron halo nucleus, ^{11}Li , and how it is related to the study of the unbound nucleus ^{10}Li . In Chapter 3, the experimental method will be presented, and a discussion of the experimental technique used to produce and study the unbound nucleus ^{10}Li will be given. In Chapter 4, a systematic analysis of the experimental technique will be presented, along with the analysis of the ^{10}Li data. In Chapter 5, the results of the data will be interpreted and compared with other recent experiments.

CHAPTER 2

THEORETICAL BACKGROUND

2.1 Binding Energy

The binding energy of a nucleus is defined as the mass difference between a nucleus ${}^A X$, and the mass of the protons Z , and neutrons N , which make up the nucleus:

$$B = [Zm_p + Nm_n - (m({}^A X) - Zm_e)]c^2 \quad (2.1)$$

where m_p , m_n , and m_e are the masses of the proton, neutron and electron, respectively, and c is the speed of light [15]. As is evident from this definition, the binding energy of the nucleus results from a conversion of a portion of the mass of the constituent nucleons into energy. This conversion of mass into energy is a result of the interaction between the individual nucleons within the nucleus. This interaction is governed by the strong force which is an attractive force between two nucleons when they are separated by approximately 2 - 3 fm, but turns repulsive if the two nucleons come within 0.8 fm of one another [15]. Because the nucleon-nucleon force is attractive for only a short range of distances, any particular nucleon within a given nucleus is only bound to those nucleons which are nearest to it. Hence, nucleons which exist on the surface of a nucleus are in general less bound to the nucleus than those nucleons in the interior of the nucleus since the surface nucleons have fewer neighbors with which to interact. A related quantity to the binding energy of the nucleus is the separation energy for the removal of a neutron or proton from the

nucleus in question. The neutron separation energy S_n for the nucleus ${}^A X$ is defined as:

$$S_n = [m({}^{A-1}X) + m_n - m({}^A X)]c^2 \quad (2.2)$$

A small neutron separation energy indicates that the last neutron is weakly bound to the nucleus whereas a large neutron separation energy indicates that the last neutron is more tightly bound to the nucleus.

In addition to its influence on the binding of the nucleus, the nucleon-nucleon interaction also strongly affects the density of nuclear matter within the nucleus. Because the nucleon-nucleon interaction turns repulsive when two nucleons are separated by less than 1 fm or so, an average separation is maintained between the nucleons within the nucleus. This implies that the density of nuclear matter remains relatively constant within the interior of the nucleus regardless of the number of nucleons that are in the system. Since adding nucleons to the surface of a nucleus subsequently decreases the binding energy of the nucleus, the most tightly bound nuclei would be those which have a minimal amount of surface area relative to their volume. Hence, the most tightly bound nuclei are spherically symmetric since the ratio of the surface area to volume for these nuclei are minimized [16].

Stable nuclei are found in a narrow region of proton and neutron numbers known as the valley of stability where, for light nuclei ($A < 40$), the number of neutrons is roughly equal to the number of protons within the nucleus. Nuclei which deviate from this ratio of neutrons to protons that is seen in the valley of stability have decay lifetimes due to the fact that β decay now becomes energetically favorable in order to increase the stability of the nucleus. If the ratio of neutrons to protons deviates further from the ratios seen in the stable nuclei of that mass region, then particle emission becomes possible for the nucleus to decay towards a more bound configuration [16]. In the case of the Li isotopes, for instance, the addition of two

neutrons to the stable nucleus ${}^7\text{Li}$ leads to the formation of the particle stable nucleus ${}^9\text{Li}$. Adding one more neutron to ${}^9\text{Li}$ leads to the unbound nucleus ${}^{10}\text{Li}$ which immediately decays upon formation via neutron emission back to ${}^9\text{Li}$. Since an additional neutron cannot be added to ${}^9\text{Li}$ to form a particle stable nucleus, ${}^9\text{Li}$ is considered to exist at the neutron drip line, since a neutron added to ${}^9\text{Li}$ would just drip off and not form a bound system. This would seem to indicate that ${}^9\text{Li}$ is near the limit of stability for the neutron rich Li isotopes.

While the addition of one neutron to ${}^9\text{Li}$ does not produce a particle stable nucleus, the addition of two neutrons to ${}^9\text{Li}$ does yield the particle stable nucleus ${}^{11}\text{Li}$. The fact that ${}^{11}\text{Li}$ exists as a particle stable nucleus indicates the presence of certain properties and characteristics within ${}^{11}\text{Li}$ that are unique relative to those properties seen in nuclei near the valley of stability. One obvious characteristic that is different from stable nuclei is the presence of the neutron halo in ${}^{11}\text{Li}$. The basic principle behind the existence of a halo can be understood through the use of a potential model to describe the interaction between the core nucleus and the neutrons in the halo [3]. If the separation energy for the outer one or two neutrons in a nucleus is less than 1 MeV, the probability of their existence at large distances relative to the center of the nucleus increases dramatically. Assuming the potential between the core nucleus and a loosely bound neutron to be spherically symmetric, given by $W(r)$, the radial wave function is determined by the eigenvalue equation:

$$\frac{-\hbar^2}{2\mu} \frac{1}{r^2} \frac{\partial}{\partial r} r^2 \frac{\partial}{\partial r} \psi + \left(\frac{\hbar^2 l(l+1)}{2\mu(r^2)} + W(r) \right) \psi = E\psi \quad (2.3)$$

where \hbar is Planck's constant divided by 2π , μ is the reduced mass of the system, l is the angular momentum of the state, and E is the energy of the state. Setting $\psi(r) = u(r)/r$ so as to eliminate first-order derivatives, we get the modified radial

wave equation:

$$\frac{-\hbar^2}{2\mu} \frac{d^2 u(r)}{dr^2} + \left[\frac{\hbar^2 l(l+1)}{2\mu(r^2)} + W(r) \right] u(r) = E u(r) \quad (2.4)$$

The simplest interaction between the neutron and the core nucleus can be represented by a square well potential of the form:

$$W(r) = \begin{cases} -V_0 & r < R \\ = 0 & r > R \end{cases}$$

where R is the width of the potential from the center of the nucleus. If we consider R to correspond to the radius of the core nucleus, then the behavior of the wave function of the neutron at large distances away from the center of the nucleus will be determined in the region where $r > R$. In the simplest case of an $l = 0$ bound neutron ($E < 0$), the wave function outside the potential is given by [3]:

$$\psi(r) = \frac{2\pi}{\kappa} \frac{e^{-\kappa r}}{r} \frac{e^{kR}}{(1+kR)^{1/2}} \quad (2.5)$$

where κ is the wave number outside the potential:

$$\kappa = \sqrt{\frac{2\mu|E|}{\hbar^2}} \quad (2.6)$$

and k is the wave number inside the potential:

$$k = \sqrt{\frac{2\mu(V_0 + |E|)}{\hbar^2}} \quad (2.7)$$

The density distribution of the neutron outside the nucleus is given by:

$$\begin{aligned} \rho(r) &= |\psi(r)|^2 \\ &= \frac{4\pi^2}{\kappa^2} \frac{e^{-2\kappa r}}{r^2} \frac{e^{2kR}}{(1+kR)} \end{aligned} \quad (2.8)$$

As the energy of the state approaches zero, which indicates that the neutron is becoming more and more weakly bound, the parameter κ becomes smaller which

in turn increases the range of the neutron density distribution [3]. This increase in the range of the density distribution can be seen as a tail in the distribution which is referred to as the halo. Such an increase in the density distribution is illustrated in Figure 2.1 where the form of the density distribution for a neutron that is bound by 0.2 MeV (dashed curve) is shown relative to the density distribution for a neutron which bound by 8 MeV (solid curve). In each of the two cases, the density distribution was determined assuming a potential with a 2.6 fm width. The development of the neutron halo is thus understood, in part, as a result of the weak binding of the last one or two neutrons in the nucleus. In the case of ^{11}Li where the two neutron separation energy is 0.247 MeV [3], the range of the last two neutrons in the nucleus extends out quite far forming the two neutron halo in ^{11}Li . The effect that the neutron halo has on the density distribution of ^{11}Li is quite remarkable considering the fact that the root-mean-square radius R_{rms} of the neutron halo is 4.8 ± 0.8 fm [3] which is nearly the same size as the R_{rms} of ^{208}Pb of 5.5 fm [17] and twice the size of ^7Li with $R_{rms} = 2.33 \pm 0.02$ fm [18].

While the nature of the neutron halo can be understood in terms of a simple potential model, many other unique facets of ^{11}Li cannot be described in such a simple manner. One such feature which requires a more complete description of the structure of ^{11}Li is the three body interaction between the two valence neutrons in the halo and the ^9Li core nucleus which causes ^{11}Li to remain bound against particle decay. To construct a complete description of ^{11}Li , all of the possible interactions between the ^9Li core and the two valence neutrons must be accounted for within the calculation of the wave function for the system. The wave function for the two neutron halo nucleus can be determined using the eigenvalue equation:

$$H\psi = E\psi \quad (2.9)$$

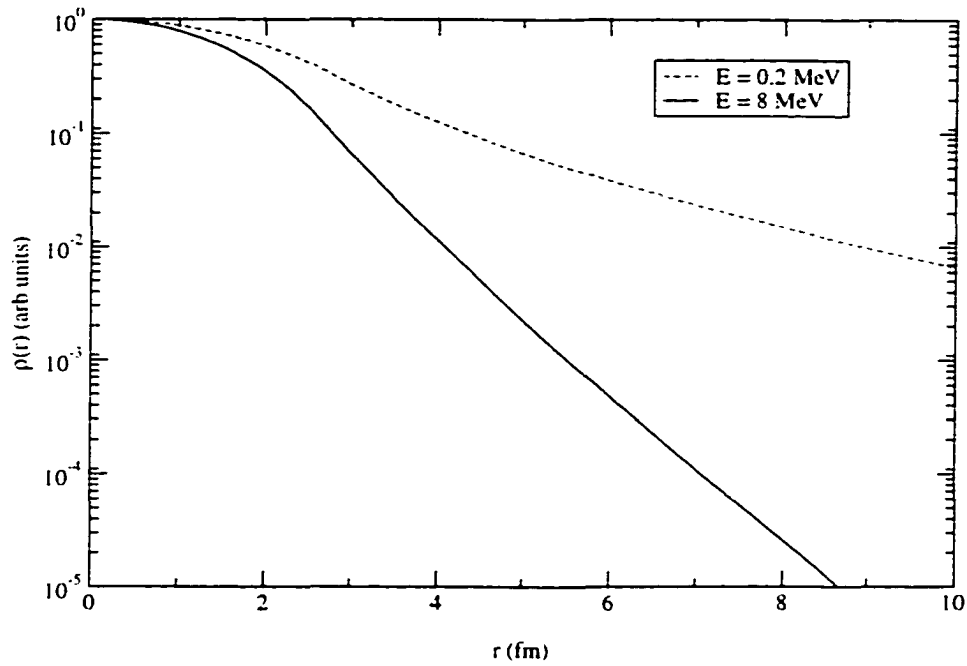


Figure 2.1. Neutron density distribution for a neutron bound by 0.2 MeV (dashed curve) and 8.0 MeV (solid curve) based on the square well potential model.

where H is the Hamiltonian for the three body system which has the form [19]:

$$H = \frac{p_{(1)}^2}{2m_n} + \frac{p_{(2)}^2}{2m_n} + V_{nc}(1) + V_{nc}(2) + V_{nn} + \frac{(\vec{p}_{(1)} + \vec{p}_{(2)})^2}{2A_c m_n} \quad (2.10)$$

The first two terms in the Hamiltonian are the kinetic energies for the two valence neutrons, labeled (1) and (2), V_{nc} is the interaction of a specific neutron with the core, V_{nn} is the neutron-neutron interaction, and the last term is the kinetic energy of the recoiling core nucleus which has the mass number A_c . As seen from the form of the three body Hamiltonian, an important term in developing a complete understanding of ^{11}Li is the interaction between the core nucleus and a valence neutron, which is determined by the structure of the unbound nucleus, ^{10}Li . Hence, an understanding of the structure of ^{10}Li is essential in developing a better understanding of ^{11}Li . One can deduce some properties of ^{10}Li based on an understanding of the shell structure for the nucleus.

2.2 Shell Model

The basic principle behind the nuclear shell model is to describe the various energy states within the nucleus based on the nucleon degrees of freedom [16]. Each nucleon occupies a specific single particle level within the nucleus which can be calculated using a potential model to describe the binding of the individual nucleon within the nucleus. Choosing a realistic potential to represent the interaction between the valence nucleons and the core nucleus is crucial in order to produce an accurate model of the nucleus. Two simple forms that can be used for this potential would be the square well potential as described in the previous section, and the three dimensional harmonic oscillator. However, neither potential reproduces the properties of the nuclear potential accurately due to discrepancies between the edge of these potentials and the edge of the surface of the nuclear matter distribution, which closely resembles the edge of the nuclear potential [15]. One form that resembles the nuclear potential more closely is the Woods-Saxon potential:

$$V(r) = \frac{-V_0}{1 + e^{\frac{(r-R)}{a}}} \quad (2.11)$$

where R is the mean radius of the nucleus, and a is the skin thickness which is defined as the distance over which the potential changes from $0.9V_0$ to $0.1V_0$ [15].

To increase the accuracy of this shell model in predicting the appropriate behavior of the nucleus, an additional potential is added to account for the spin-orbit interaction which couples the intrinsic spin of the nucleon, s , with its angular momentum, l , and takes the general form:

$$V_{so} = V(r)\vec{l} \cdot \vec{s} \quad (2.12)$$

where $V(r)$ is the radially dependent strength of the spin-orbit term which is often determined by fitting the observed single particle levels in the given nucleus [16].

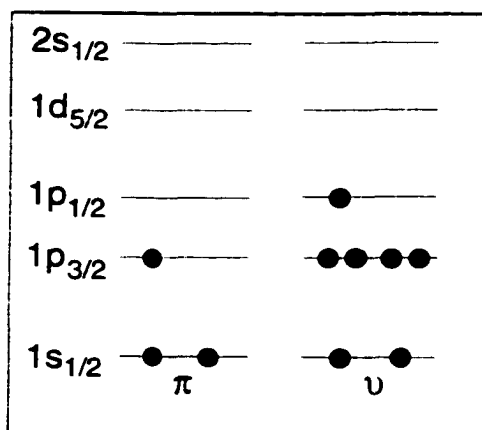


Figure 2.2. Level structure in ^{10}Li based on naive shell model.

Although simple in construction, this naive shell model can be useful in developing a starting point for attempts to understand the basic properties of specific nuclei. Figure 2.2 shows the filled energy levels for the proton and neutron shells for ^{10}Li based on this naive shell model. As seen in Fig. 2.2, ^{10}Li has one proton (π) in the $1p_{3/2}$ shell and one neutron (ν) in the $1p_{1/2}$ shell. The ground state configuration for ^{10}Li in this naive shell model is thus determined by the interaction between these two valence nucleons since the rest of the nucleons completely fill the lower energy levels and are thus assumed to form an inert core with 0^+ spin and parity. In this configuration then, there are two possibilities for the ground state spin and parity of ^{10}Li depending on how the total angular momentum of the valence proton and neutron couple together:

$$\begin{aligned}
 [\pi 1p_{3/2} \otimes \nu 1p_{1/2}] &\Rightarrow 1^+ (j_1 - j_2) \\
 &\Rightarrow 2^+ (j_1 + j_2)
 \end{aligned}$$

To check if this type of assignment for the ground state of ^{10}Li is accurate, one can apply this same model to other nuclei having the same number of neutrons as ^{10}Li . In the case of ^{11}Be , which has one more proton than ^{10}Li and has an experimentally

determined ground state spin and parity of $1/2^+$ [20], the application of the naive shell model to ^{11}Be would yield a $1/2^-$ assignment for the ground state due to the presence of the lone valence neutron in the $1p_{1/2}$ shell. This discrepancy in the parity of the ground state of ^{11}Be between the naive shell model and the experiment indicates that the level structure of ^{11}Be does not follow the predictions of the naive shell model, but rather has a configuration where the $2s_{1/2}$ shell is lower in energy than the $1p_{1/2}$ shell. This discrepancy between the measured shell structure of ^{11}Be has implications for the structure of ^{10}Li . In calculations which were first performed by Sagawa, et al. [21], the inversion of the $2s_{1/2}$ shell with the $1p_{1/2}$ shell was reproduced by considering the coupling of an excited core nucleus in ^{11}Be to neutrons in the sd shell. These same calculations also predicted a possible inversion of the $1p_{1/2}$ and $2s_{1/2}$ states in ^9He , as shown in Figure 2.3[22]. Since both ^{11}Be and ^9He are $N=7$ isotones, this implies that ^{10}Li may also have an inversion between the $1p_{1/2}$ and $2s_{1/2}$ levels. Such an inversion would have strong implications for the ground state configuration of ^{10}Li , with the valence proton in ^{10}Li now coupling with a $2s_{1/2}$ neutron yielding a ground state configuration of:

$$\begin{aligned} [\pi 1p_{3/2} \otimes \nu 2s_{1/2}] &\Rightarrow 1^- \quad (j_1 - j_2) \\ &\Rightarrow 2^- \quad (j_1 + j_2) \end{aligned}$$

In addition to this possible change in the parity of the ground state configuration for ^{10}Li from the naive shell model, the calculation also suggests that the $2s_{1/2}$ state would lie just above the threshold energy for particle decay in ^{10}Li . Because this is an s-wave neutron state, it would be possible for the state to overlap the threshold due to the fact that it is not affected by the presence of the Coulomb barrier or the centrifugal barrier of the ^9Li nucleus. If the position and width for such a state were such as to overlap the threshold, then the state would be ‘virtual’ since it is neither

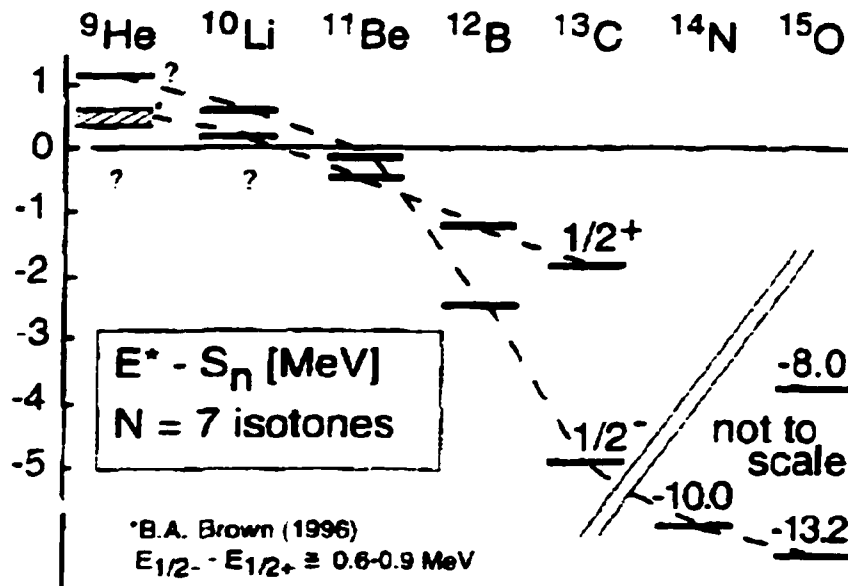


Figure 2.3. Plot of the calculated difference between the excitation energy of the $1/2^+$ and $1/2^-$ states and the neutron separation energy for $N=7$ isotones (from Ref. [22]).

completely a bound state nor is it a resonant state. The concept of a virtual state will be further discussed in the next section

2.3 Scattering Theory

The most common technique for determining the properties and structure of various nuclei is to perform experiments where an incident nucleus is scattered from a target nucleus in order to form specific final states. To understand the results of such scattering experiments, it is first necessary to understand the scattering process by which the desired state is formed.

In a typical nuclear scattering experiment, a beam of particles with mass M_1 and with an energy, E_0 , is incident on a target nucleus with mass M_2 which is usually at rest in the lab. The wave function of the composite scattered system, $\psi(\vec{r})$, is

determined by:

$$\frac{-\hbar^2}{2\mu}\nabla^2\psi(\vec{r}) + V(r)\psi(\vec{r}) = E\psi(\vec{r}) \quad (2.13)$$

where E is the energy of the relative motion of the two particles which is related to the incident energy E_0 by [23]:

$$E = \frac{M_2}{M_1 + M_2}E_0 \quad (2.14)$$

and the vector \vec{r} is the relative position between the two nuclei. The incident wave can be represented by a plane wave of the form:

$$\psi_i(\vec{r}) = Ae^{i\vec{k}\cdot\vec{r}} \quad (2.15)$$

where \vec{k} is related to the initial momentum of the incident nucleus by:

$$\vec{k} = \frac{\vec{p}}{\hbar} \quad (2.16)$$

and A is a normalization constant for the wave function. Upon scattering, the wave function moves radially outward and takes the form:

$$\psi_f(\vec{r}) = f(\theta, \phi)\frac{e^{ikr}}{r} \quad (2.17)$$

where $f(\theta, \phi)$ is an angular function which describes the dependence of the scattering on the angle of the outgoing nucleus.

If the scattering potential is of finite range, then at large separations the wave equation reduces to one for a free particle which implies that the wave function must satisfy the asymptotic boundary condition [24]:

$$\psi(\vec{r}) \sim A(e^{i\vec{k}\cdot\vec{r}} + f(\theta, \phi)\frac{e^{ikr}}{r}) \quad (2.18)$$

The differential cross section would be given by [24]:

$$\frac{d\sigma}{d\Omega} = |f(\theta, \phi)|^2 \quad (2.19)$$

If the potential is spherically symmetric and thus dependent only on the absolute distance between the two nuclei, then the angular function can be expanded in terms of spherical harmonics $Y_l^m(\theta, \phi)$ which leads directly into the partial wave expansion of the wave function:

$$\psi(\vec{r}) = \sum_{l=0}^{\infty} a_{lm} \frac{u_l(r)}{r} Y_l^m(\theta, \phi) \quad (2.20)$$

where $u_l(r)$ satisfies the modified radial wave equation (Eqn. 2.4) [16]. The fact that the scattering potential chosen in this case is spherical implies that a separate radial wave equation exists for each partial wave. At the asymptotic boundary, u_l must take the form:

$$u_l(r) = C_l (e^{-i(kr - \frac{1}{2}l\pi)} - e^{2i\delta_l} e^{i(kr - \frac{1}{2}l\pi)}) \quad (2.21)$$

where C_l is a constant which is determined by the boundary conditions, and δ_l is the phase shift of the wave with angular momentum l [16].

In the case of elastic scattering, the outgoing waves can only change in phase relative to the incoming wave, and this is represented by the phase shift δ_l . In this case, the angular factor $f(\theta, \phi)$ and subsequently the differential cross section, is given in terms of the phase shifts of the partial waves:

$$\frac{d\sigma}{d\Omega} = \frac{4\pi}{k^2} \left| \sum_{l=0}^{\infty} \sqrt{2l+1} e^{i\delta_l} \sin(\delta_l) Y_l^0(\theta) \right|^2 \quad (2.22)$$

where it has been assumed that the incident wave is traveling along the z axis subsequently removing the dependency of the scattering on the azimuthal angle. The elastic cross section is then given by:

$$\sigma = \frac{\pi}{k^2} \sum_{l=0}^{\infty} (2l+1) |1 - S_{\alpha,\alpha}^l|^2 \quad (2.23)$$

where $S_{\alpha,\alpha}^l$ is the elastic scattering S-matrix element for the partial wave with angular momentum l [25]. The elements of the S-matrix $S_{\alpha\alpha}$ describe the amount of

the incident wave function that is in the elastic channel relative to the amount that was scattered into other open reaction channels. In this case, $S_{\alpha\alpha}$ is given by:

$$S_{\alpha,\alpha}^l = e^{2i\delta_l} \quad (2.24)$$

The elastic scattering S-matrix is useful in developing an understanding in the presence of virtual states in the scattering process as well as differentiating between a virtual state and a resonance. Consider an s-wave neutron incident on a nucleus with energy E . A resonance will occur if the phases of the wave functions in the regions outside and inside the nucleus matches smoothly at the boundary $r = a$. The S matrix element in this case can be expressed in terms of the wave number of the incident neutron by [25, 26]:

$$S_{\alpha,\alpha}(k) = e^{-2ika} \frac{f + ika}{f - ika} \quad (2.25)$$

where $u(r)$ is the reduced radial wave function given in 2.21 and f is the derivative of the radial wave function at the boundary given by:

$$f = \left(\frac{a}{u(r)} \frac{du(r)}{dr} \right)_{r=a} \quad (2.26)$$

A similar relation can be made between the S-matrix element and the energy of the incident neutron from Equation 2.25:

$$S_{\alpha,\alpha}(E) = e^{-2ika} \frac{E - E_r - \frac{1}{2}i\Gamma_0}{E - E_r + \frac{1}{2}i\Gamma_0} \quad (2.27)$$

where Γ_0 is defined as the width of the resonance. The S-matrix will possess poles in the complex energy plane corresponding to the resonances in the reaction. For a single isolated resonance that is far from threshold, the location of the pole in terms of energy is determined by the equation [27]:

$$E_{pole} = E_r - \frac{i\Gamma_0}{2} \quad (2.28)$$

While this equation works for s-wave resonances which are well away from threshold, for those resonances which exist near threshold, such as the possible unbound s-wave state in ^{10}Li , the energy dependence of the width due to presence of the potential barrier has an influence on the location of the pole in the complex k-plane for s-wave neutrons.

A generalized condition for the energy of the pole which takes into account the probability of a neutron with angular momentum l to penetrate the barrier of the nucleus is given in terms of the energy-dependent width $\Gamma(E)$ [27]:

$$\Gamma(E) = \Gamma_{l_0} \left[\frac{P_l(E)}{P_l(E_r)} \right] \quad (2.29)$$

$$E_{pote} = E_r - \frac{i}{2}\Gamma(E) \quad (2.30)$$

where $P_l(E)$ is the penetrability factor which is determined, in general, by using the coulomb wave functions F_l and G_l evaluated at the channel radius R [28]:

$$P_l(E) = \frac{kR}{(F_l(kR))^2 + (G_l(kR))^2} \quad (2.31)$$

For a neutron with $l = 0$ or $l = 1$ [27]:

$$P_0(E) = kR \quad (2.32)$$

$$P_1(E) = \frac{(kR)^3}{(1 + (kR)^2)} \quad (2.33)$$

Because of the difference between the penetrability factors for s-waves and p-waves, the two states behave differently near threshold. In the case of the p-wave, the presence of the centrifugal barrier forces the cross section to go to zero as E approaches threshold. The cross section for a single resonance is given by the Breit-Wigner one-level formula:

$$\sigma_{res} = \frac{\pi}{k^2} \frac{(\Gamma(E))^2}{(E - E_r)^2 + \frac{(\Gamma(E))^2}{4}} \quad (2.34)$$

Since the cross section goes to zero at the threshold, a p-wave resonance can never overlap threshold. However, in the case of the s-wave neutron, there is no such restriction in the cross section since there is no centrifugal barrier. Hence, an overlap with threshold can occur causing an ambiguity to develop in terms of whether or not the state is bound or unbound. This ambiguity in the structure of the state is reflected in the location of the pole in the S-matrix, which for a virtual state lies on the imaginary k axis such that that the real part of the wave number vanishes [27]. Because the pole for the virtual state lies on the imaginary k axis with $k_\nu = -i\gamma$ ($\gamma > 0$), a virtual state corresponds to negative energy even though it is an unbound state [29]:

$$E_\nu = \frac{k^2 \hbar^2}{2\mu} = \frac{-\gamma^2 \hbar^2}{2\mu} \quad (2.35)$$

While the “resonance energy” for a virtual state is not a good measure of the location of the state, and is in fact not well defined, one can specify its characteristics in terms of a scattering length a .

At low bombarding energies, the scattering cross section is often expressed in terms of the scattering length a :

$$\lim_{k \rightarrow 0} \sigma = 4\pi a^2 \quad (2.36)$$

This expression for the cross section results from the fact that the scattering cross section must be finite at $E = 0$. Hence the cross section reduces to the scattering of the incident wave function from a hard sphere with radius a . This scattering length can be expressed in terms of the s-wave phase shift δ_0 for elastic scattering [16]:

$$a = \lim_{k \rightarrow 0} \text{Re} \left(-\frac{1}{k} e^{i\delta_0} \sin \delta_0 \right) \quad (2.37)$$

In this convention, a positive scattering length indicates a bound state whereas a negative scattering length indicates that no bound state is present as indicated in

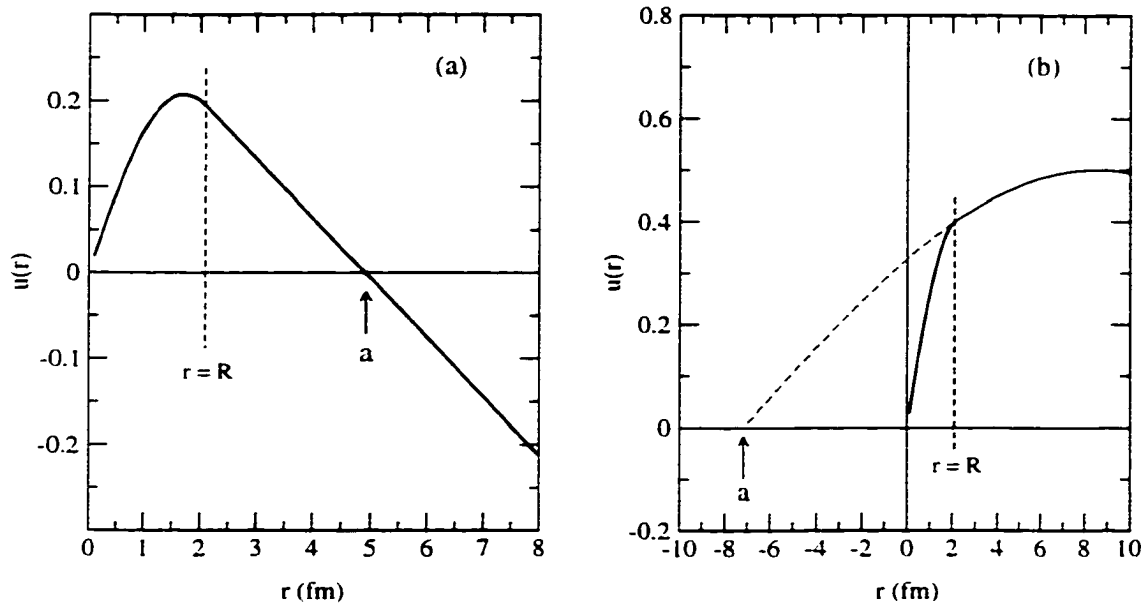


Figure 2.4. (a) Typical radial wave function for a bound state showing a positive scattering length a . (b) Radial wave function for an unbound state showing a negative scattering length.

Figure 2.4. [15] Because the scattering length is defined in terms of k , which is dependent on momentum, the scattering length will depend on the energy level of the state as well as its phase shift. This definition of scattering length becomes useful in describing the low energy properties of the possible unbound s-wave neutron state near threshold in ^{10}Li due to the fact that such a state does not necessarily have a central energy associated with it. Assuming that the initial state is known for ^{10}Li , the scattering length for the s-wave neutron is calculated by solving Eqn. 2.13 for the neutron wave function in the $^9\text{Li} + \text{neutron}$ system with a suitably chosen potential and determining the phase shift for the scattered neutron within the nucleus.

2.4 Optical Model

If during the scattering process the nature of the incident wave is altered through the transfer of energy or particles between the target and the projectile, then flux is

removed from the elastic channel to other possible reaction channels. To account for this loss of flux from the elastic channel to the various other reaction channels, an imaginary scattering potential is added to the real scattering potential to alter the characteristics of the incoming wave and thus remove it from the elastic channel. The scattering potential now takes the form:

$$U(r) = V_R(r) + iV_I(r) \quad (2.38)$$

where V_R (V_I) is the real (imaginary) part of the potential. Due to the similarities between the form of the complex scattering potential and the real and imaginary indices of refraction used in optics, the description of the nuclear interaction using this type of potential is known as the optical model. A typical form that is used for the real part of the optical model potential is the Woods-Saxon form (Eqn. 2.11) due to its similarities with the shape of the nucleus. The form of the imaginary potential that is used depends in part on the type of reaction that is occurring to remove flux from the elastic channel. If the change in the incoming nucleus involves the transfer of nucleons from the surface of the nucleus, then the derivative of a Woods Saxon potential is often used, due to the fact that the strength of such a potential is peaked near the surface of the nucleus and hence absorbs most of the flux from the elastic channel in this region of the nucleus. This potential, known as the surface Woods-Saxon potential, has the form:

$$V_I(r) = \frac{V_I e^{\frac{r-R_I}{a_I}}}{a_I (1 + e^{\frac{r-R_I}{a_I}})^2} \quad (2.39)$$

For both the Woods-Saxon and surface Woods-Saxon potentials, the radius R is determined by:

$$R = r_o (A_T)^{1/3} \quad (2.40)$$

where A_T is the mass number for the target nucleus and r_o is the reduced radius.

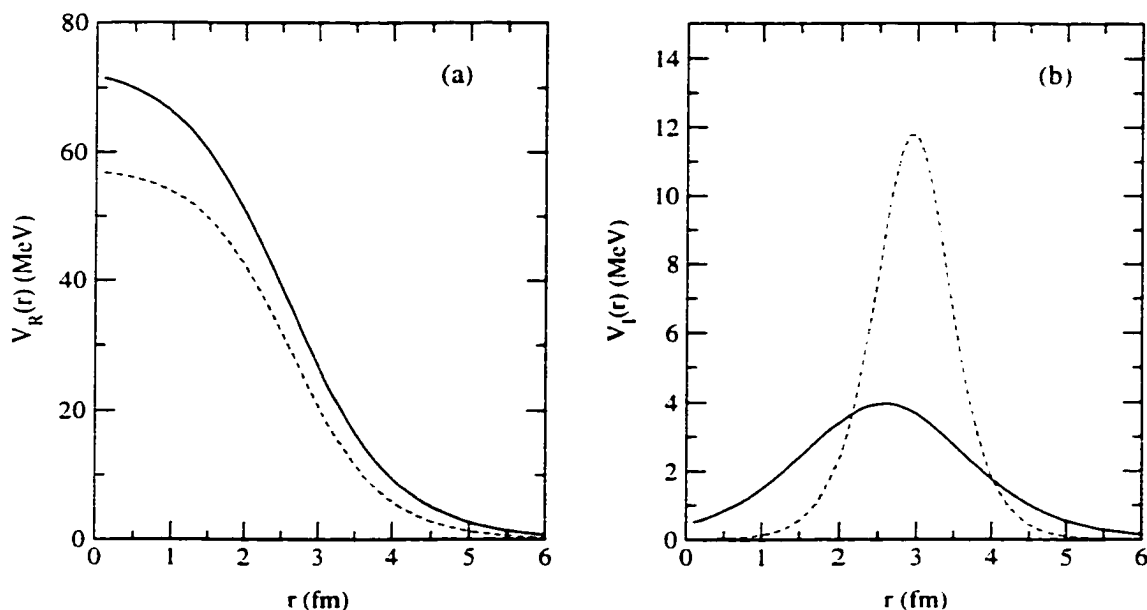


Figure 2.5. Plot of two sample (a) volume and (b) surface Woods Saxon potentials. The solid curves in (a) and (b) are the real and imaginary potentials used to describe the ${}^9\text{Li} + \text{deuteron}$ system, respectively, while the dashed curves are the potentials used to describe the ${}^{10}\text{Li} + \text{proton}$ system. The parameters for both sets of potentials are given in Table 3.1.

Examples of the volume and surface Woods-Saxon potentials are shown in Figures 2.5(a) and (b) respectively. In both figure (a) and (b), the solid curves represent the potentials used to describe the ${}^9\text{Li} + \text{deuteron}$ system while the dashed curves represent the potentials used to describe the ${}^{10}\text{Li} + \text{proton}$ system in the coupled channels calculation described in the next section. The parameters for these two sets of potentials are given in Table 3.1.

By using a complex scattering potential instead of a completely real potential, the phase shifts themselves become complex quantities. A complex phase shift in turn means that the flux is removed from the elastic channel and into other reaction channels. The partial reaction cross section from one particular channel α to another

channel β is given as [25]:

$$\sigma_{\alpha\beta} = \frac{\pi}{k^2} (2l_\alpha + 1) |\delta_{\alpha\beta} - S_{\alpha\beta}^l|^2 \quad (2.41)$$

The total absorption cross section is given by [25]:

$$\sigma_{abs} = \frac{\pi}{k^2} \sum_{l=0}^{\infty} (2l_\alpha + 1) [1 - |S_{\alpha\alpha}^l|^2] \quad (2.42)$$

2.5 Coupled Channels Calculation

In the previous sections, the incident and scattered nuclei have been treated as if they were single particles without any internal structure. Such a treatment in essence couples the incident wave to specific reaction channels and ignores the possible coupling of the reaction channels to each other, which in the end will affect the net result of the scattering process. If there is strong coupling between the various reaction channels, then additional flux may be added or removed from the elastic channel relative to what is calculated in a one-step process that only couples the incident channel to the final reaction channel [30]. Coupling among the various reaction channels will occur if the scattering potential affects the internal structure of either of the two nuclei that are involved in the scattering process. To account for these changes in the internal structure of the nuclei, the wave equation is separated into parts which describe the internal states of the nuclei as well as the relative motion. The complete set of internal wave functions for the projectile nucleus ψ_a and target nucleus ψ_A are determined by the Schrödinger equations:

$$H_a \psi_a = \epsilon_a \psi_a \quad (2.43)$$

$$H_A \psi_A = \epsilon_A \psi_A \quad (2.44)$$

where the internal Hamiltonians H_a and H_A possess terms for both the kinetic and potential energies of the projectile and target in their respective rest frames, and

the eigenvalues ϵ_a and ϵ_A are the energy levels within the separated nuclei. Because the two internal Hamiltonians operate on the nuclei separately, the internal wave functions ψ_a and ψ_A are representative of the specific nuclear states within the nuclei and are functions of the internal coordinates τ_a and τ_A respectively. Each of the two internal wave functions represent a specific reaction channel [25].

The Hamiltonian for the system is now given by:

$$H = H_A + H_a - \frac{\hbar^2}{2\mu_\alpha} \nabla_\alpha^2 + V_\alpha \quad (2.45)$$

where ∇^2 operates on the radial vector, \vec{r}_α , between the two centers of mass for the two nuclei, and V_α is the potential between the two nuclei. The total wave-function is thus expanded in terms of the internal wave functions:

$$\psi = \sum_{a'A'} \chi_{aA}(\tau_\alpha) \psi_a \psi_A \quad (2.46)$$

where the function χ_{aA} describes the relative motion of the centers-of-mass for the two nuclei in states a and A . This expansion of the total wave function allows for the reduction of the total Schrödinger wave equation into a set of coupled equations which give the relative motion of a given internal state in terms of the off-diagonal potential terms of the matrix $U_{aA,a'A'}$ corresponding to the interaction potential V_α [25]:

$$[\nabla_\alpha^2 - U_{aA,aA}(\vec{r}_\alpha)] \chi_{aA}(\tau_\alpha) = \sum_{\substack{a' \neq a \\ A' \neq A}} \chi_{aA}(\vec{r}_\alpha) U_{aA,a'A'}(\vec{r}_\alpha) \quad (2.47)$$

where the quantity k_{aA} is given by:

$$k_{aA} = \frac{\sqrt{2\mu_\alpha(E - \epsilon_a - \epsilon_A)}}{\hbar} \quad (2.48)$$

For every pair of possible states in the two nuclei that are energetically allowed in the reaction, a separate $k_{a'A'}$ occurs in Equation 2.47. The off-diagonal matrix

elements of U are given in terms of the internal states of the two nuclei:

$$U_{aA,a'A'}(\vec{r}_\alpha) = \frac{2\mu_\alpha}{\hbar^2} \int \int \psi_a^*(\tau_a) \psi_A^*(\tau_A) V_\alpha \psi_{a'}(\tau_a) \psi_{A'}(\tau_A) d\tau_a d\tau_A \quad (2.49)$$

In Eqn. 2.47, the diagonal elements of the matrix $U_{aA,aA}$ which appear on the left hand side are coupled with the excited states which appear on the right hand side of the equation in order to enable description of the inelastic scattering and its effects on the elastic scattering.

The internal wave functions that are used as the basis states for the coupled reaction channels (CRC) model are not just restricted to bound states, but can also be discrete representations of states that are unbound and in the continuum via the ‘coupled discrete continuum channels’ (CDCC) approximation [31]. The difficulty in calculating the transfer of flux into the continuum is that an unbound eigenstate has a wave function which does not decay to zero in the asymptotic limit. To deal with wave functions which have an infinite range, the CDCC approximation averages the continuum states over a range of energies instead of a single energy as is done with bound states. The result of treating the continuum states over a range of energies is the creation of ‘bin’ states. A bin state $\Phi(\tau)$ that is defined in the range from k_1 to k_2 is given by [31]:

$$\Phi(\tau) = \sqrt{\frac{2}{\pi N}} \int_{k_1}^{k_2} w(k) \Phi_k(\tau) dk \quad (2.50)$$

where $w(k)$ is a weight function and N is:

$$N = \int_{k_1}^{k_2} |w(k)|^2 dk \quad (2.51)$$

By defining a ‘bin’ state in this manner, the normalization of $\Phi(\tau)$ is:

$$\langle \Phi | \Phi \rangle = 1 \quad (2.52)$$

provided that the potential is energy-independent and that the maximum radius is sufficiently large [31]. The weight function $w(k)$ is chosen in such a manner so as to

incorporate some of the effects of varying ϕ_{kr} within the range. The bin states are orthogonal to the bound states or other continuum ‘bin’ states assuming that the ‘bin’ states do not overlap in energy. In performing a coupled channels calculation for the reaction ${}^9\text{Li}(d,p){}^{10}\text{Li}$ using the CRC code FRESCO [31], a continuum bin size of 1 MeV was chosen, centered at 0.5 MeV above the threshold in ${}^{10}\text{Li}$ so as to cover the continuum region where the two possible low-lying “resonances” are located. The results of this calculation will be discussed in the next chapter.

CHAPTER 3

EXPERIMENTAL METHOD

3.1 Overview

In a number of the previous attempts to study the structure of ^{10}Li , complex reactions such as the multiple nucleon transfer reaction $^{11}\text{B}(^7\text{Li}, ^8\text{B})^{10}\text{Li}$ [7], and the fragmentation reactions $^{18}\text{O} + ^{nat}\text{C}$ and $^{18}\text{O} + ^9\text{B}$ [5, 6], have been used to populate the low lying resonances of ^{10}Li . In many of these cases, the effect that the reaction mechanisms had on the production of ^{10}Li in its low lying states remains unclear. A way to avoid the complications which arise from these complex reactions is to perform a single nucleon transfer reaction to study the structure of ^{10}Li . One particular single particle transfer reaction that is ideal for studying low-lying excited states in stable nuclei is the (d,p) reaction, where one neutron is transferred from the deuteron to the nucleus of interest. Since the structure of the deuteron consists only of a ground state and no excited states below the threshold of particle stability [32] the initial states of the target and projectile (in the case of stable nuclei) are well defined. The effect that the (d,p) reaction mechanism has on the states of the outgoing nucleus can be calculated exactly [15]. In addition, the states that are populated in the nucleus of interest during the reaction can be determined by measuring the energy and angle of the outgoing proton. Thus, an experiment involving the (d,p) stripping reaction to study the unbound nucleus ^{10}Li has several

advantages over what has been done previously and has the potential to answer some of the remaining questions concerning the structure of ^{10}Li .

3.1.1 The (d,p) reaction

Consider the reaction $A(d,p)B$ where a deuteron is incident on a target nucleus, A, with an incident kinetic energy T_d and a total relativistic energy given by:

$$E_d = T_d + m_d c^2 \quad (3.1)$$

where m_d is the rest mass of the deuteron and c is the speed of light. The kinetic energy of the proton, T_p , is determined by conservation of energy to be:

$$T_p = T_d + T_A - T_B + Q \quad (3.2)$$

where Q is the Q-value of the reaction, defined as either the difference in kinetic energy between the final and initial states of the reaction, or equivalently as the difference between the initial masses and final masses involved in the reaction [15]. If the recoiling nucleus, B, were produced in an excited state with an energy E_x above the ground state, then the Q-value for the reaction $A(d,p)B^*$ would be:

$$Q = Q_o - E_x \quad (3.3)$$

where Q_o is Q-value of the reaction which produces the recoiling nucleus in its ground state. The kinetic energy of the proton then, depends linearly on the excitation of the recoiling nucleus if the target nucleus was at rest.

In addition to its kinetic energy, the angular momentum of the states populated in the recoil nucleus can be determined by study the angular distribution of the outgoing proton. The momentum of the recoiling nucleus, \vec{p}_B , is determined by applying conservation of momentum:

$$\vec{p}_B = \vec{p}_d - \vec{p}_p \quad (3.4)$$

Furthermore, the law of cosines can be applied to relate the magnitude of the momentum vectors as:

$$p_B^2 = (p_d - p_p)^2 + 2p_d p_p (1 - \cos(\theta)) \quad (3.5)$$

where θ is the scattering angle for the outgoing proton in the laboratory frame. Since the transfer of the neutron is a direct process, it is assumed that the reaction takes place at the surface of the target nucleus. This assumption has been confirmed in many different studies of the (d,p) reaction using stable nuclei. Since the reaction occurs at the surface of the target nucleus, the transferred nucleon must be placed in a state in the target nucleus which has an angular momentum, $l = R \times p_B$ where R is the radius of the target nucleus [15]. Substituting for p_B , a direct relationship can thus be established between the proton scattering angle and the angular momentum of the populated state as:

$$\cos(\theta) = 1 - \frac{(p_d - p_p)^2 - (l/R)^2}{2p_d p_p} \quad (3.6)$$

3.1.2 Kinematics of the ${}^9\text{Li}(\text{d,p}){}^{10}\text{Li}$ Reaction

When the (d,p) reaction is performed with stable nuclei, it is often done in forward kinematics with the lighter deuteron incident on a heavier target. Because ${}^9\text{Li}$ has a half-life of 178.3 ms [33], this reaction must be performed using inverse kinematics with a beam of radioactive ${}^9\text{Li}$ ions incident on a target composed of deuterons. As a result, the recoiling ${}^{10}\text{Li}$ nucleus, and subsequently the ${}^9\text{Li}$ nucleus resulting from the breakup of ${}^{10}\text{Li}$, is now forward focused due to the motion of the center of mass of the system (see Figure 3.1). This implies that the ${}^9\text{Li}$ produced from the breakup of ${}^{10}\text{Li}$ can be detected with relatively high efficiency with a detector located near 0° . Figure 3.2(a) shows the ${}^{10}\text{Li}$ laboratory scattering angle as a function of the center of mass angle for the (d,p) reaction at an incident ${}^9\text{Li}$

energy of 176 MeV calculated using the relativistic kinematics code PKIN, based on the algorithms developed in Ref. [34]. The calculation shows that the motion of ^{10}Li in the center of mass frame translates into a forward cone ranging in angle from 0° to a little over 8° in the lab frame.

In contrast to the motion of ^{10}Li in the reaction, the proton scatters at all angles in the lab as is shown in Figure 3.2(b) in which the calculated proton lab scattering angle is plotted as a function of the ^{10}Li center of mass angle. While this large spread in proton angles makes it difficult to detect the protons efficiently, it does provide a precise way to determine the angle of the outgoing ^{10}Li nucleus prior to its breakup which is important in reconstructing the breakup process. An accurate measurement of the proton angle in the lab, along with knowledge of the incident ^9Li energy, translates into an accurate determination of the lab angle of the ^{10}Li nucleus prior to its breakup.

The fact that the structure of ^{10}Li does not consist of low-lying bound states but rather resonances which exist above the threshold for neutron decay adds a further complication to the experiment. Because ^{10}Li is unbound to neutron decay, it only exists for approximately 10^{-23} seconds before it breaks up into $^9\text{Li} + n$. As a result, the final state of the $^9\text{Li}(d,p)$ reaction involves three nuclei (^9Li , neutron, and proton) and an experiment involving this reaction is no longer kinematically complete if one only measures the outgoing proton. To account for the breakup of ^{10}Li , one can use the kinematic coincidence technique which measures two or more particles produced in the same reaction in coincidence with each other in order to reconstruct the kinematics of the event of interest [35]. In this particular case, if the energy and angle of the outgoing ^9Li from the breakup of ^{10}Li is measured in coincidence with the proton, then a complete reconstruction of the reaction which produced the ^{10}Li nucleus, and its subsequent decay, can be carried out. The total

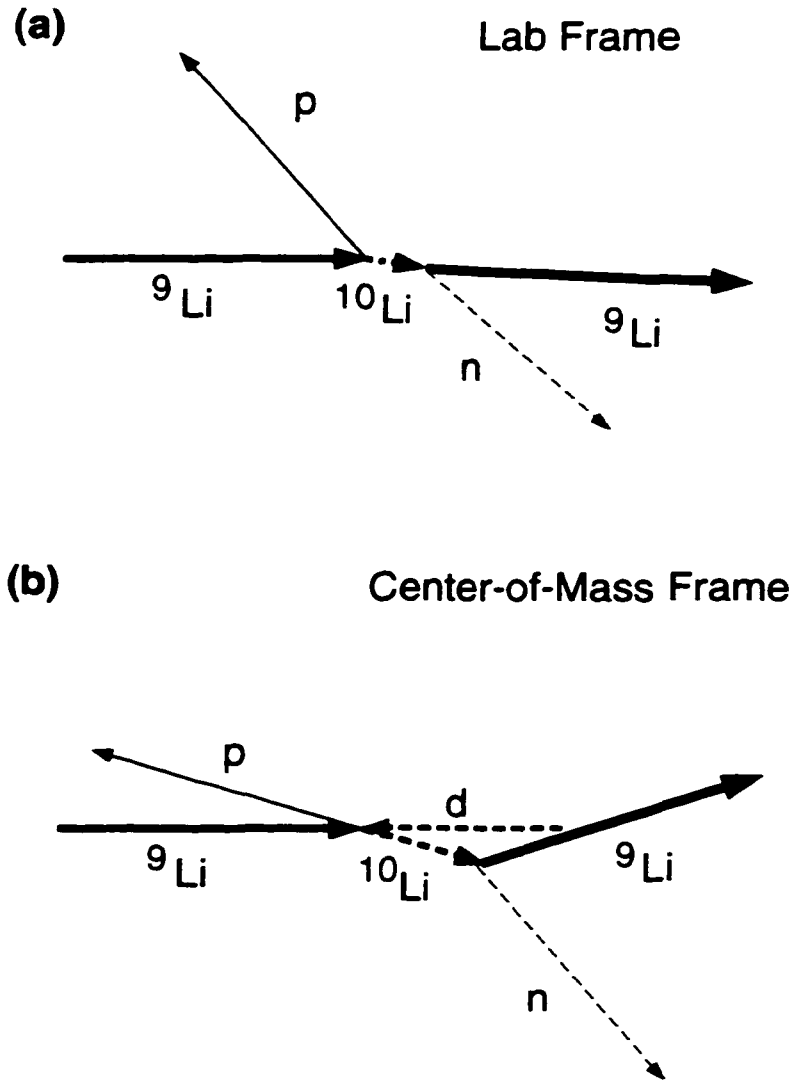


Figure 3.1. Schematic diagram of the ${}^9\text{Li}(d,p){}^{10}\text{Li}^* \Rightarrow {}^9\text{Li} + n$ reaction performed in the (a) lab frame and (b) center of mass reference frame for the (d,p) reaction. The solid lines indicate the quantities measured in this experiment whereas the dashed lines are those quantities which were reconstructed from the data.

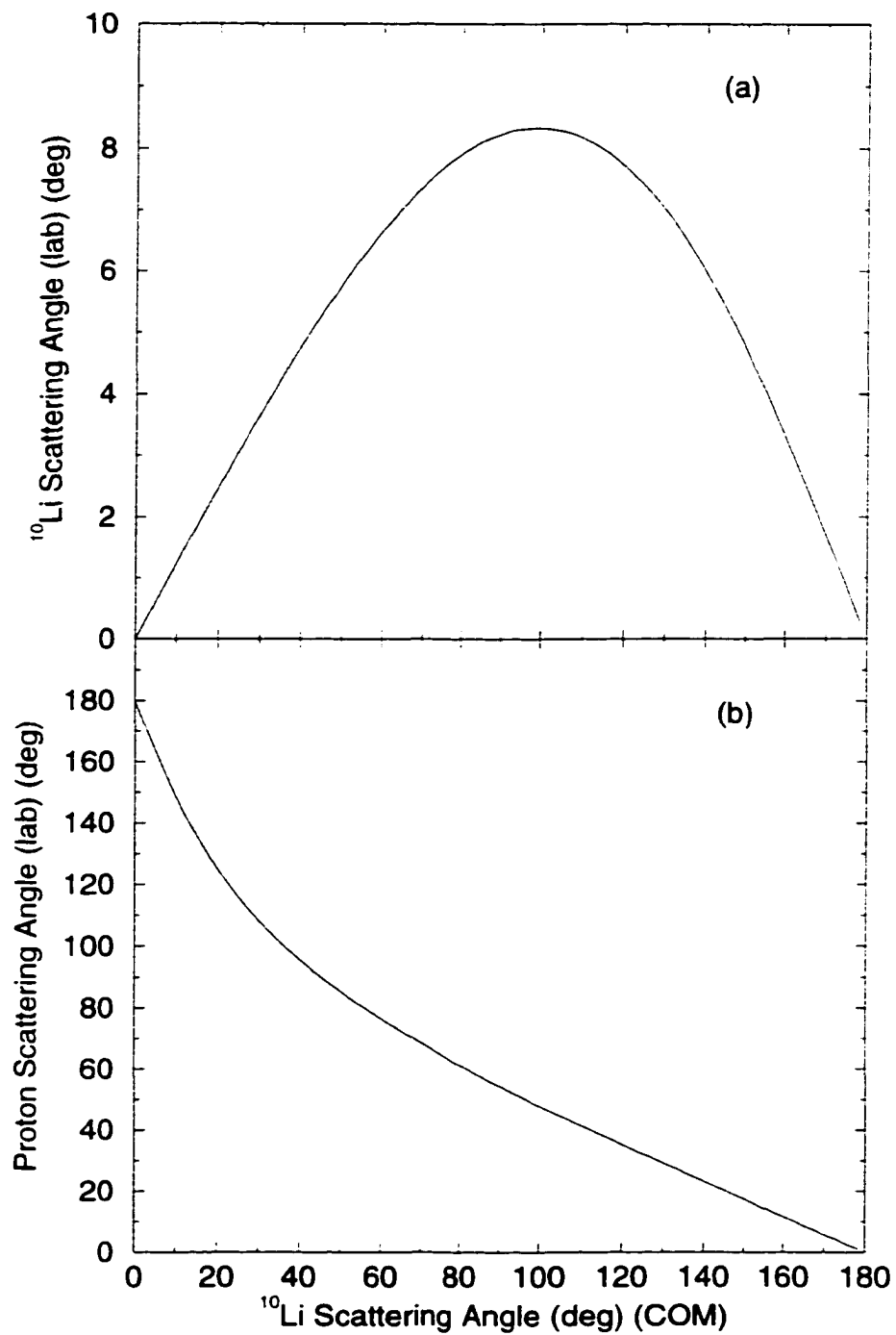


Figure 3.2. Plot of the calculated (a) ^{10}Li lab angle and (b) proton lab angle as a function of the ^{10}Li center of mass scattering angle in the $^9\text{Li}(d,p)^{10}\text{Li}$ reaction based on an incident ^9Li energy of 177 MeV. The calculations were performed using the relativistic kinematic code, PKIN.

lab energy of the recoiling ^{10}Li nucleus from the $^9\text{Li}(d,p)^{10}\text{Li}$ reaction is:

$$E_{10} = E_9 + m_d c^2 - E_p \quad (3.7)$$

where E_9 and E_p are the total energies of the incident ^9Li and proton, respectively. By measuring the proton and the incident particle in coincidence with one another, the energy and angle of ^{10}Li , or subsequently its momentum, can be determined precisely in the laboratory frame. With the momentum of ^{10}Li determined in the lab frame, a Lorentz transformation can be made from the laboratory reference frame to the breakup center of mass where the ^{10}Li nucleus is at rest. If ^{10}Li has a momentum in the lab \vec{p}_{10} , then the velocity of the breakup center of mass reference frame with respect to the laboratory frame is given by:

$$\vec{\beta} = \frac{\vec{p}_{10} c^2}{E_{10}} \quad (3.8)$$

where $\vec{\beta}$ is expressed in units of c . To simplify the notation, the value for c can be set to 1. The Lorentz transformation of the energy and momentum of ^9Li from the breakup of ^{10}Li from the laboratory frame to the breakup center of mass frame is then given by:

$$\begin{pmatrix} E_{9,cm} \\ p_{\parallel,cm} \end{pmatrix} = \begin{pmatrix} \gamma & -\gamma\beta \\ -\gamma\beta & \gamma \end{pmatrix} \begin{pmatrix} E_9 \\ p_{\parallel} \end{pmatrix} \quad (3.9)$$

$$p_{\perp,cm} = p_{\perp} \quad (3.10)$$

where

$$\gamma = \frac{1}{\sqrt{1 - \beta^2}} \quad (3.11)$$

and p_{\parallel} and p_{\perp} are the parallel and perpendicular components of the ^9Li momentum relative to the motion of the center of mass frame $\vec{\beta}$, respectively [36].

In the breakup center of mass frame, the momentum of ${}^9\text{Li}$ and neutron are related by conservation of momentum:

$$\vec{p}_{9,cm} = -\vec{p}_{n,cm} \quad (3.12)$$

The Q-value of the breakup of ${}^{10}\text{Li}$ in the center of mass frame is :

$$Q_{break} = E_{n,cm} + E_{9,cm} - m_n - m_9 \quad (3.13)$$

where

$$E_{n,cm} = \sqrt{(p_{n,cm})^2 + (m_n)^2} \quad (3.14)$$

Substituting for $p_{n,cm}$ from Equation 3.12 to get Q_{break} in terms of known quantities. we find:

$$Q_{break} = \sqrt{p_{9,cm}^2 + m_n^2} - m_n + E_{9,cm} - m_9 \quad (3.15)$$

Hence, the Q-value of the breakup of ${}^{10}\text{Li}$, and subsequently the structure of the ${}^{10}\text{Li}$ nucleus prior to its breakup, can be reconstructed by measuring the energies and angles of the incident and outgoing ${}^9\text{Li}$ nucleus in coincidence with the measured energy and angle of the recoiling proton.

3.2 Beam Production

The experiment was performed at the National Superconducting Cyclotron Laboratory (NSCL) at Michigan State University (MSU). A primary beam of ${}^{13}\text{C}$ was accelerated via the K1200 Cyclotron at the NSCL to an energy of 30 MeV/nucleon and then transported to the A1200 fragment separator [37], shown in Figure 3.3. The ${}^{13}\text{C}$ beam was focused onto a 470 mg/cm² ${}^9\text{Be}$ target placed in a chamber upstream of the entrance to the A1200 separator, causing a fragmentation reaction to occur. The fragments, which are forward focused due to the inverse kinematics of

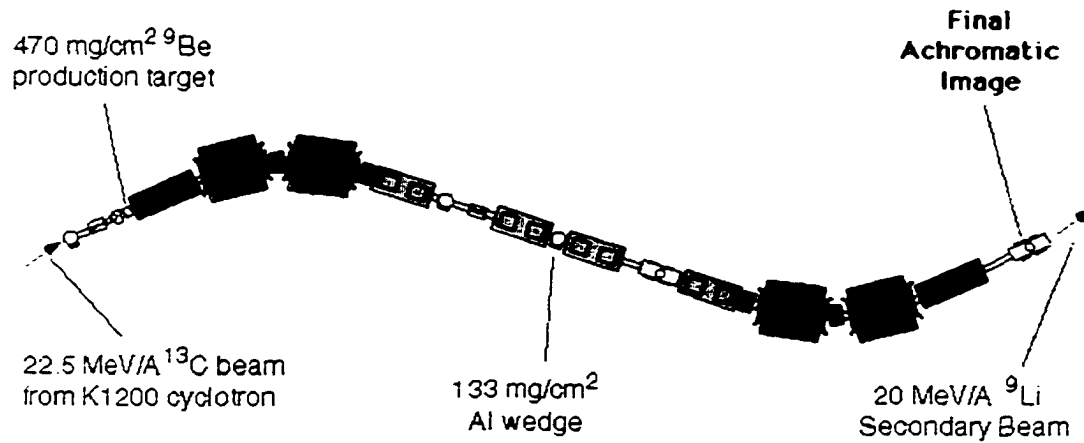


Figure 3.3. Diagram of the A1200 fragment separator.

the reaction, are then selected based on their momentum to charge ratio through the use of the first series of superconducting dipoles and quadrupoles as shown in Fig. 3.3. Passing the beam through the first set of dipoles does not completely clean the beam, however, since any particle which has the appropriate momentum to charge ratio will pass through the dipoles along with the beam of interest.

To further clean the contaminants out of the beam, a 133 mg/cm² Al wedge was put in the middle chamber of the A1200 separator to act as an energy degrader which alters the momentum to charge ratio for the various ions based on their differential energy loss. The differential energy loss of an ion with a velocity, β through a material having an atomic number, Z , an atomic weight, A , and a density, ρ , can be described using the Bethe formula:

$$\frac{dE}{dx} = \left(\frac{e^2}{4\pi\epsilon_0}\right)^2 \frac{4\pi z^2 N_o Z \rho}{m_e c^2 \beta^2 A} \left[\ln\left(\frac{2m_e c^2 \beta^2}{I}\right) - \ln(1 - \beta^2) - \beta^2 \right] \quad (3.16)$$

where ze is the electric charge of the ion, m_e is the mass of the electron, N_o is Avogadro's number, and I is ionization potential of the stopping material [15]. As is seen in Equation 3.16, the differential energy loss is dependent on the nuclear

charge of the ion as well as its velocity. Because the ions which were present in the beam were not monoenergetic the choice of the shape of the degrader is important in order to optimize the ability to select out the desired ion from the beam. If these ions were to pass through a degrader with a flat surface, the energy spread of the beam would be larger since the faster ions would lose less energy in the absorber than the slower ones. To account for this, the aluminum degrader used in the A1200 was a wedge, oriented in the mid-chamber in such a way that those ions with a higher velocity would pass through the thicker end of the wedge. Orienting the wedge in this fashion reduces the effect of the energy spread of the beam on the change in the momentum to charge ratio for the various ions in the beam [38]. This change to the momentum to charge ratio for the different ions in the beam allows for a further reduction in the amount of contaminants in the beam through the use of the second set of dipoles in the A1200. By thus choosing appropriate fields for the two sets of dipoles in the A1200, as well as an appropriate thickness for the Al wedge, a relatively pure ${}^9\text{Li}$ secondary beam was produced with a central energy of 19.7 MeV/nucleon.

3.3 S800 Analysis Line

Once the ${}^9\text{Li}$ secondary beam was produced by the A1200, it was then transported to the secondary target, located in the target chamber of the S800 spectrograph, through the S800 analysis line, as shown in Fig. 3.4. Similar to the setup of the A1200, the S800 analysis line defined the profile and momentum spread of the incident beam on target through the use of a series of quadrupoles, dipoles and momentum defining slits. Through the use of these slits, the spread in momentum of the incident beam on target was limited to 1% full width at half maximum (FWHM). Since the secondary ${}^9\text{Li}$ beam was initially produced using a fragmenta-

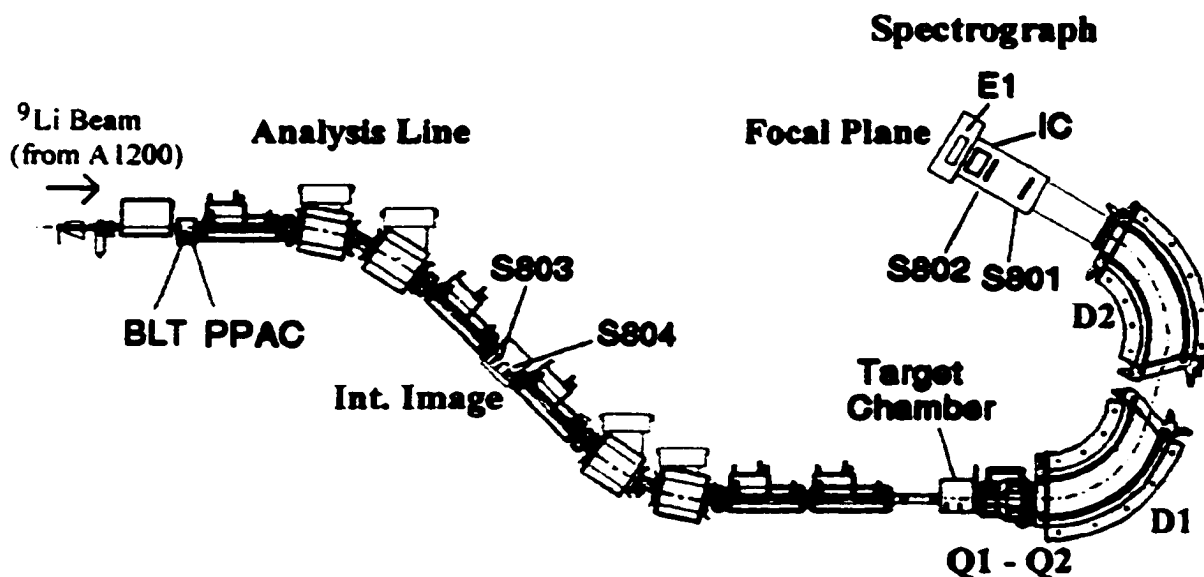


Figure 3.4. Diagram of the S800 analysis line and spectrograph.

tion reaction, the resultant physical size and angular divergence of the secondary beam was quite large, approximately 1 cm in spot size and 7 mr in angular divergence (FWHM). In order then to perform an accurate reconstruction of the (d,p) reaction and subsequent breakup of ${}^{10}\text{Li}$, it was necessary to track the incident secondary beam onto the target as well as to measure its energy on an event by event basis. These measurements were done using a series of detectors located at various places along the analysis line of the S800 which will be described in detail in this section.

The Beam Line Timer (BLT) was a plastic scintillator located in the first chamber of the analysis line which measured the time-of-flight (TOF) of the particles as they traveled the 37.2 meter flight path from the entrance of the analysis line up to the focal plane of the S800 spectrograph. To perform this measurement, a Time to Analog Converter (TAC) was used with the start signal taken from the signal produced by the BLT and the stop signal taken from another scintillator, labeled

E1, located at the end of the focal plane. (See Fig. 3.4.) This TOF measurement was useful in identifying the particles of interest from the small background present in the beam. In addition to measuring the TOF of the beam particles, the BLT was also used to monitor the incident rate of the secondary beam into the analysis line.

Following the BLT, a series of position-sensitive detectors were placed before and after the first set of magnetic dipoles in the analysis line of the S800 in order to track the incident beam as well as to measure its momentum on an event by event basis. Prior to the first set of dipoles, a Parallel-Plate Avalanche Counter (PPAC) [39], 5 cm by 5 cm in active area, was placed on a movable ladder 0.56 meters upstream of the entrance of the first quadrupole in the analysis line. The PPAC is a gas filled proportional counter having electrodes in parallel planes. For this particular experiment, the PPAC was filled with isobutane gas at a pressure of 5 torr. An electric field is produced between the parallel planes which are separated by a small distance within the isobutane atmosphere. A charged particle passing through the gap between the parallel plates produces ion pairs in the gas. The electrons in these ion pairs produce avalanches of electrons in the gas due to the acceleration they receive from the homogeneous electric field between the two parallel plates [39]. These electrons are subsequently detected using a series of approximately 0.1 inch wide strips, which are aligned along both directions of the surface of the PPAC. The strips are connected to resistors and a signal is measured on both ends of the strips. The strength of the signal measured at a given end of the strip will depend on how close the particle was to that end of the detector as it passed through the PPAC. The position of the particle can thus be determined by resistive division, in which the ratio of the difference in the signals measured at both ends of the strip to the sum of the two signals is determined. For instance, the relative position of a

particle in the horizontal plane, x , can be determined by calculating:

$$x = \frac{Left - Right}{Left + Right} \quad (3.17)$$

where *Left* and *Right* are the signals from the two ends of the strip which runs along the horizontal axis of the detector. A similar method is used to calculate the vertical position on the PPAC by using the signals from the top and bottom of the detector.

To calibrate the PPAC, a mask was placed on the upstream side of the detector with a series of holes separated by 1.2 cm in both directions. The detector was then illuminated with the direct beam in an attempt to project the mask pattern onto the PPAC. Unfortunately, the spot size of the beam was too small to illuminate more than one hole in the mask at a time. To compensate for the small beam size, the PPAC was moved vertically in order to illuminate more than one hole in the mask. However, due to the limited range in the motion of the ladder, the beam was only able to pass through two holes in the mask in the vertical direction thus only providing a two point calibration for the vertical direction of the PPAC. No calibration was possible for the horizontal, or non-dispersive direction, of the PPAC since there was no way to move either the detector or the beam horizontally to illuminate a second hole in the mask.

Two other tracking detectors, S803 and S804, were placed inside the intermediate image chamber (labeled as *Int. Image* in Fig. 3.4) located in between the two sets of magnetic dipoles in the analysis line. These detectors were Cathode Readout Drift Chambers (CRDC) placed in the path of the beam 59 cm apart from each other. The specifics of the operations of the CRDC is given in detail in Ref. [40] and will only be briefly discussed here.

The CRDC is a gas filled drift chamber with a single anode wire located at the bottom of the detector. The two CRDC's used in the S800 analysis line had an

active area of 8 cm x 8 cm, an active depth of 1.5 cm and contained isobutane gas at a pressure of 12 Torr. The detectors were placed inside the beam line perpendicular to the path of the incident beam with the anode wire perpendicular to the dispersive direction of the dipoles in the analysis line, that is the direction in which the particle are dispersed in momentum. The anode wire was maintained at +930 V for S803 and +900 V for S804. As the charged beam particles passed through the gas in a CRDC, the molecules in the gas were ionized producing electrons which subsequently drifted toward the anode wire. The motion of the electrons drifting through the gas towards the anode wire further ionized the gas which in turn spreads out the distribution of electrons traveling toward the anode wire. Once the electrons finally encountered the anode wire, they were collected and converted into an electronic signal. The amount of time it took the cascading electrons to reach the anode wire is related to the distance between the anode wire and the position of the charged particle [41]. In the case of S803 and S804, the drift time of the cascading ions in the two detectors was measured using a TAC with the start signal taken from the E1 scintillator and the stop signal taken from the anode wire of the CRDC. The signal from the E1 scintillator can be used as the start signal because of the fact that the flight time of the beam particles from S803 or S804 to the E1 scintillator is much smaller than the drift time of the electrons in the gas. For an incident ${}^9\text{Li}$ with a kinetic energy, E , the time to travel the distance, D , from S803 to the focal plane of the S800 is approximated by:

$$t \cong \frac{D}{\beta} \quad (3.18)$$

where β is the velocity of the incident ${}^9\text{Li}$ particle given by [36]:

$$\begin{aligned} \beta &= \sqrt{1 - \frac{1}{\gamma^2}} \\ \gamma &= 1 + \frac{E}{m_0} \end{aligned} \quad (3.19)$$

In this case, the ${}^9\text{Li}$ beam had an average energy of 177 MeV corresponding to a β of 0.202 times the speed of light (given the mass for ${}^9\text{Li}$, $m_9 = 8408.4001 \text{ MeV}/c^2$ [42]), and the distance between S803 and the E1 scintillator was 28.31 meters, yielding an approximate time of flight for the ${}^9\text{Li}$ particles of 467 ns. On the other hand, the average drift time of the electrons in the isobutane is estimated to be on the order of several μs based on the general properties of electrons drifting in a gas [41].

In addition to measuring the position of the detected particle perpendicular to the anode wire, the CRDC also measured the position parallel to the anode wire through the use of a technique called induced cathode readout [40]. A series of 32 cathode pads, 2.54 mm wide, surround the anode wire on three sides in S803 and S804 and collect an induced charge from the anode wire. The cathode pads were maintained at -240 V in both detectors. The amount of induced charge collected by an individual pad is proportional to the amount of charge collected by the anode wire at the location nearest the pad. To determine the center of the induced charge distribution on the pads, and hence the location of the detected particle along the anode wire, the measured distribution was fitted with a Gaussian function on an event by event basis. An example of this process is shown in Figure 3.5 where the signal from each pad is plotted against its number in S803 for a single direct beam event. For the event shown in Fig. 3.5, pads 11 - 22 were triggered by the incident particle. Using a Gaussian fit to the pad distribution, the centroid of the charge distribution, and hence the position of the detected particle in the direction of the anode wire, can be determined to within one tenth of one pad width, or 0.25 mm. In the example given in Fig. 3.5, the centroid of the distribution was measured at pad 16.8, which corresponds to 2.0 mm away from the center of the detector.

Since each pad in S803 and S804 had a fixed width, the position of the particle on the detector is immediately determined once the central pad is identified. However,

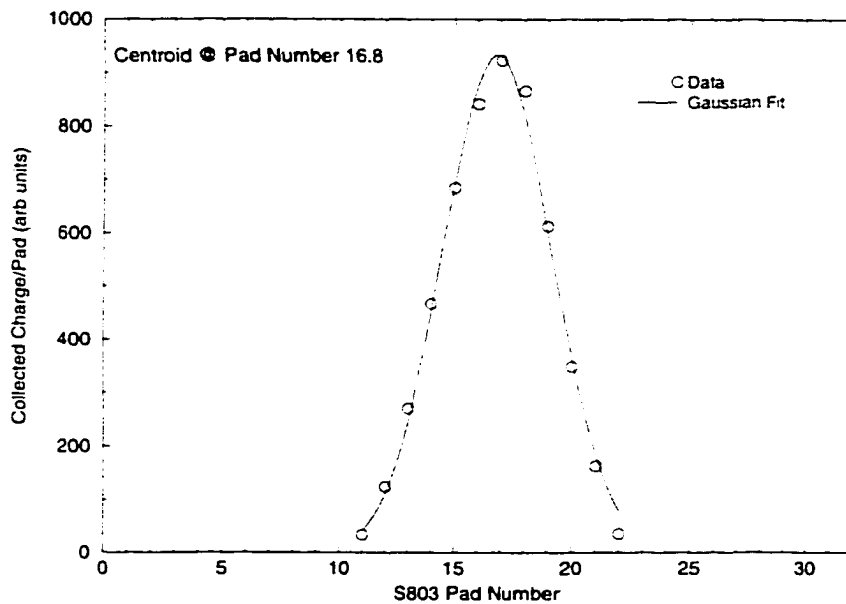


Figure 3.5. Plot of pad signal vs pad number in S803 for a single direct beam event.

this assumes that each pad in a given detector produced the same output for the same amount of collected induced charge from the anode wire. Hence, to ensure that each individual pad was properly gain matched, a pulser signal was applied onto the anode wire which, in turn, induced a fixed charged on each pad. Two different pulser settings, full scale and half scale, were used to correct both the offset and slope for each pad. By observing the pad signals from these pulser runs, corrections were made in software to ensure that the response from each pad was exactly the same for a given amount of induced charge. The effect of these corrections to the pad signals in S803 can be seen in Figure 3.6 which shows the response of the pads in S803 to a pulser setting of 0.5 before and after the pads were gain matched. A similar effect was seen in S804.

The drift direction of the CRDC was calibrated by performing a series of direct beam runs with two masks placed in the path of the direct beam in between S803 and S804 as shown in Figure 3.7. Each of the masks had an asymmetric pattern of

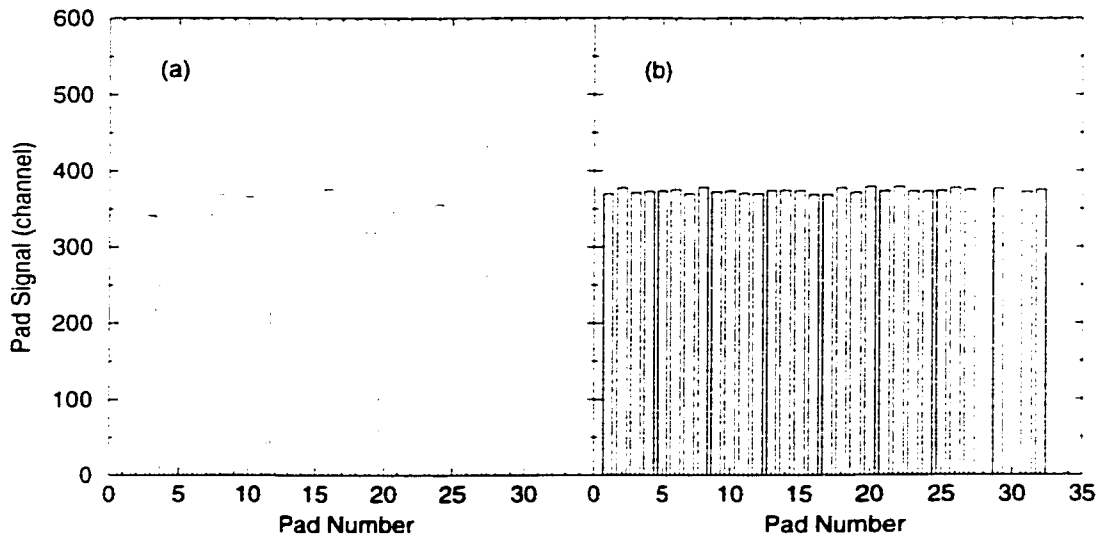


Figure 3.6. Plot of pad signal vs pad number in S803 for a pulser run (a) before and (b) after the pads were gain matched. In this particular run, the pulser was set to half scale.

holes, as shown in Figure 3.8, in order to unambiguously determine the orientation of the two detectors. The masks were thick enough to stop the beam particles which did not go through the holes in the mask. Hence, when the masks were placed in the path of the beam, either simultaneously or individually, the two detectors measured images of the nearest mask, due to the fact that the trigger for the event came from the E1 scintillator in the focal plane of the S800.

Due to the fact that the masks were not located next to the detectors, but rather at a distance from the detectors, the process of determining the calibrations from the direct beam data was done in several iterations. In the first iteration, the calibration for the two detectors was determined based on the pattern that was directly measured by S803 and S804. This is only an approximate calibration, since S803 and S804 measured images of the masks, which were affected by the varying angles of the beam particles as they passed through the masks. To correct for these

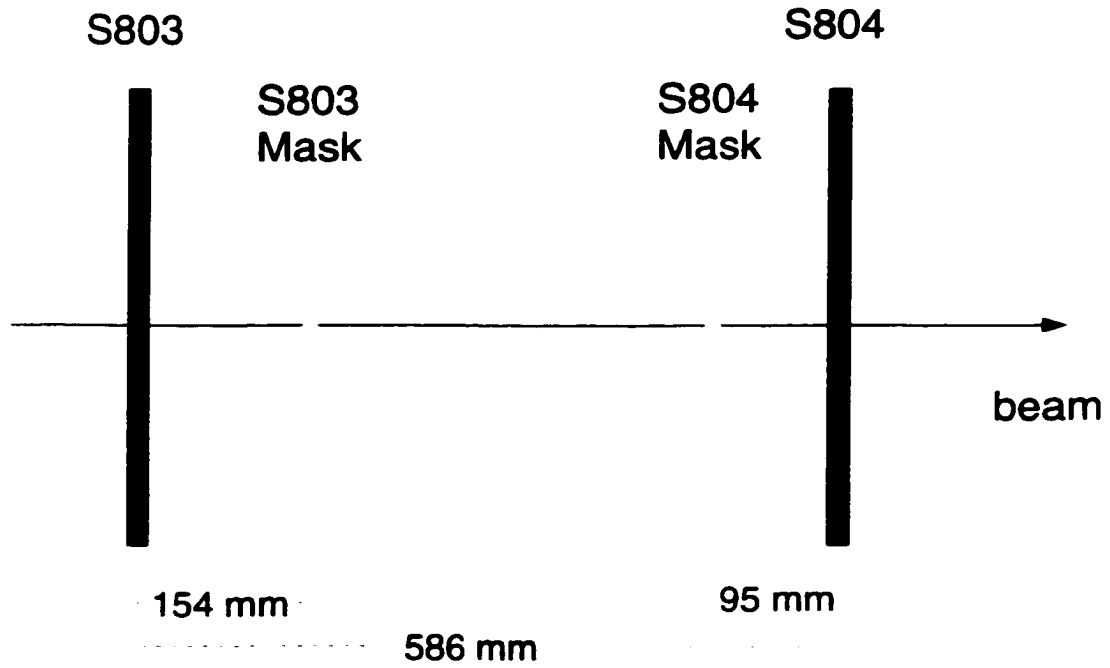


Figure 3.7. Diagram of the intermediate image chamber showing S803, S804 and the two masks for a calibration run. The imaging of the masks is carried out with E1 as the trigger in the focal plane. For the actual data runs, the masks were lowered completely out of the beam.

effects on the calibration of the detectors, the angles measured by S803 and S804, based on these preliminary calibrations, were used to reconstruct the positions of the beam particles at the locations of the masks themselves. For instance, the position of the beam particles in the dispersive (x) direction at the two masks were reconstructed in the following way:

$$\begin{aligned}
 x_{m3} &= \frac{(x_{804} - x_{803})}{D_{34}} * (D_{m3}) + x_{803} \\
 x_{m4} &= -\frac{(x_{804} - x_{803})}{D_{34}} * (D_{m4}) + x_{804}
 \end{aligned} \tag{3.20}$$

where x_{m3} (x_{m4}) is the position at the S803 mask (S804 mask), x_{803} and x_{804} correspond to the positions at S803 and S804, respectively, D_{34} is the distance between

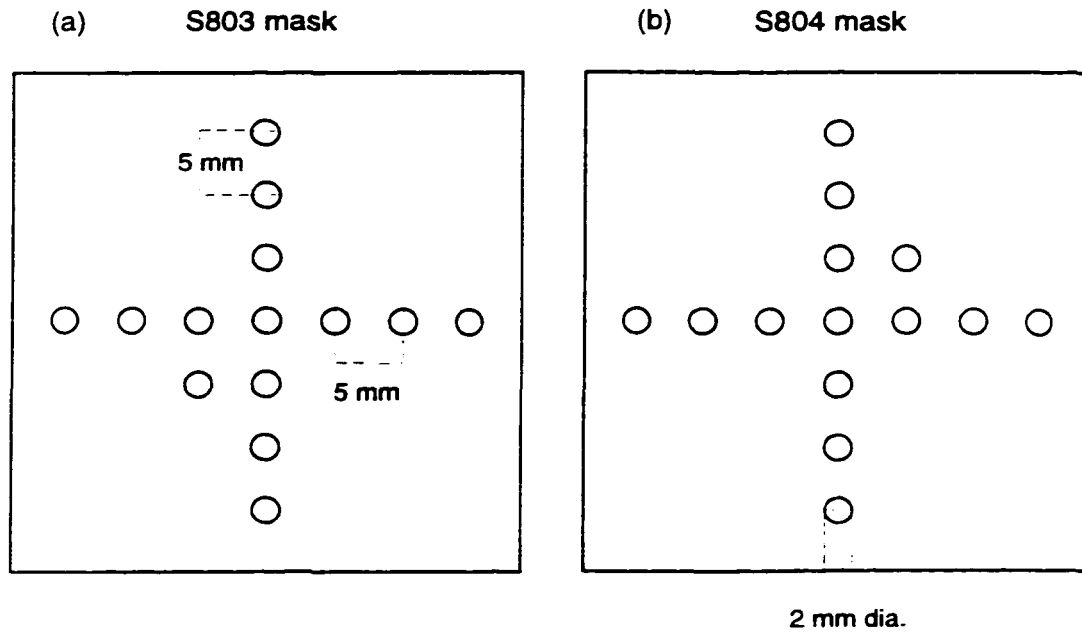


Figure 3.8. Diagram of the masks used for calibrating (a) S803 and (b) S804.

S803 and S804, D_{m3} is the distance between S803 and its mask, and D_{m4} is the distance between S804 and its mask. A similar calculation was made for the non-dispersive (y) direction at the two masks. Once the beam particles had been tracked to the location of the two masks, the calibrations for S803 and S804 were then adjusted so as to recreate the proper spacing between the holes for both masks. These images can be seen in Figures 3.9(a) and (b) for the S803 mask and the S804 mask, respectively. From these images, it became evident that the response of S803 and S804 in the drift direction was non-linear toward the edges of the detectors as indicated by the arrows in Figs. 3.9(a) and (b). Since the measured position in this direction is dependent on the time it takes the electrons produced with the passage of the beam particle to drift down to the anode wire, the non-linear response of the detectors was attributed to non-uniformities in the electric field produced by the anode wire. To correct for this effect in the detectors, the positions for the set of four holes in the mask patterns which were aligned parallel to the y -axis (pad

direction) were measured for both masks. A quadratic correction term was then applied to the measured x-position for both S803 and S804 as a function of the event's location in the y-direction in each detector based on the observed curvature in the mask pattern for this set of four holes. The effect of these corrections on the projected mask patterns can be seen in Figures 3.9(c) and (d) for the S803 mask and S804 mask, respectively.

When in coincidence with each other, the two CRDC's measured the position and angle of the incident beam prior to entering the second set of dipoles in the analysis line. These measurements, along with knowledge of the magnetic fields of the dipoles and quadrupoles in the analysis line, allowed us to perform ray reconstruction using the particle optics code COSY INFINITY [43] in order to determine the position and angle of the incident beam at the target on an event by event basis. This will be discussed further in the next chapter.

3.4 Target Chamber

After passing through the analysis line, the beam was then focused onto a 1.94 mg/cm² CD₂ target, located in the target chamber of the S800 spectrograph. The target was mounted on an aluminum frame with a 3 cm diameter hole which defined the available surface area of the target, and was placed on a movable target ladder mounted at the bottom of the target chamber. The average secondary beam rate on target was about 7,000 particles/second based on measurements provided by the BLT.

A series of silicon surface barrier detectors were placed inside this chamber to detect the outgoing protons from the (d,p) reaction as shown in Figure 3.10. The detectors were placed at backward scattering angles in part because of the use of inverse kinematics to produce ¹⁰Li. Since the motion of the center of mass of

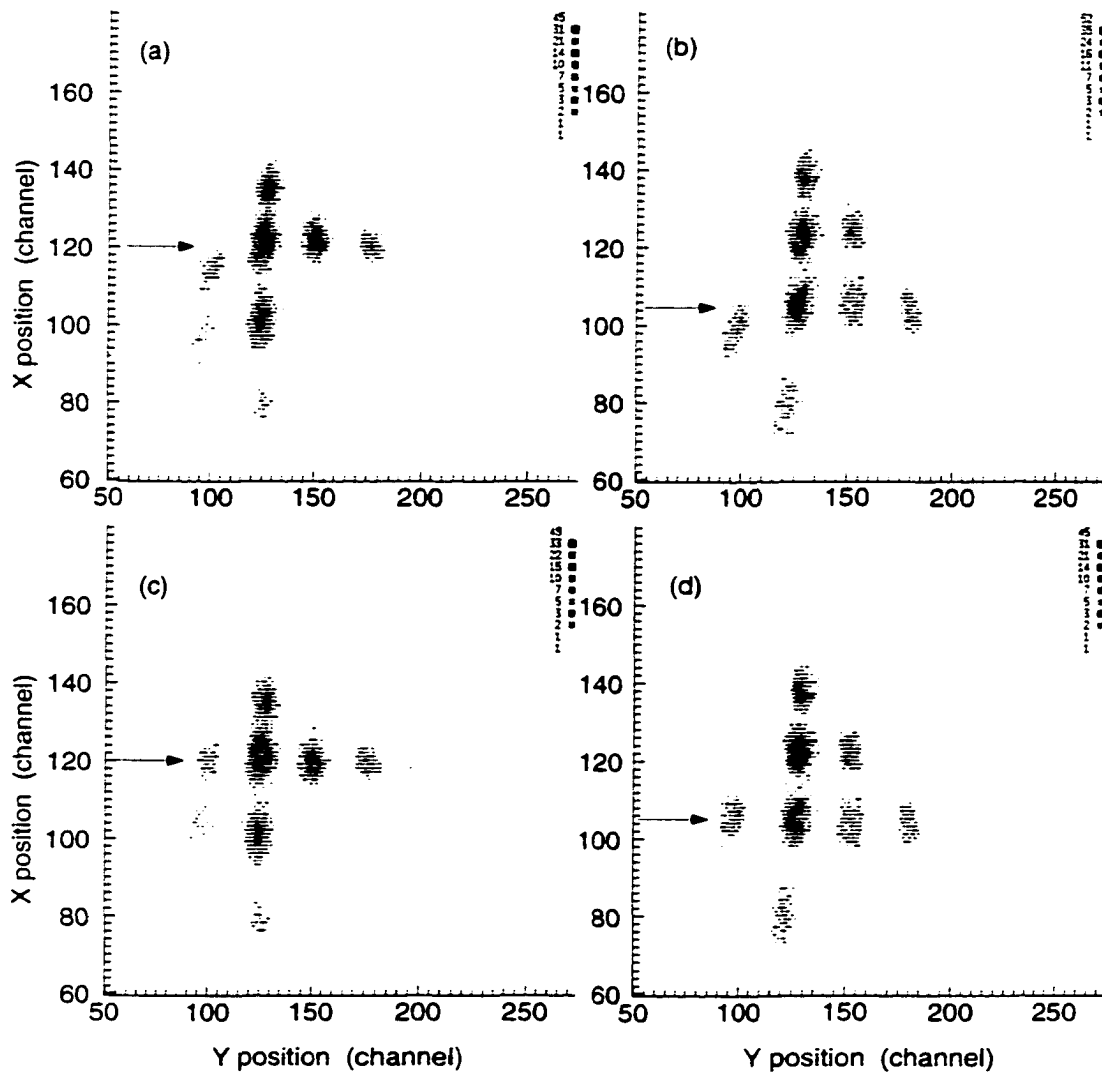


Figure 3.9. Reconstructed mask pattern for (a) S803 mask and (b) S804 mask without correcting for the non-linear response of S803 and S804 in the drift direction. The arrows indicate where the non-linear response of the detectors is most evident in the mask patterns. The corrected mask patterns are shown in (c) and (d) for S803 mask and S804 mask, respectively.

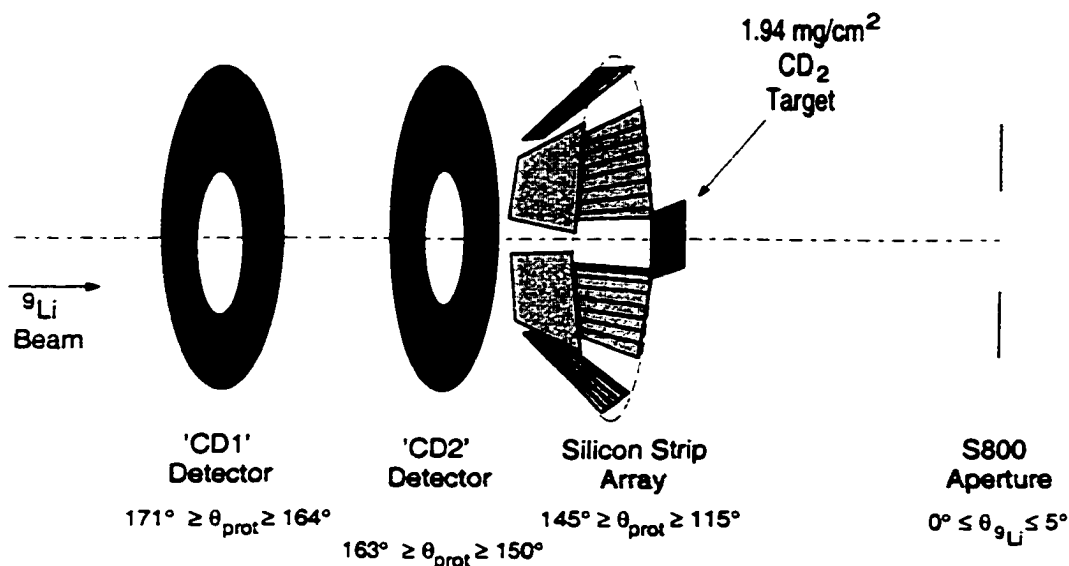


Figure 3.10. Diagram of the S800 target chamber

the reaction is forward, the subsequent proton energies in the lab decrease as a function of increasing angle. With an incident ${}^9\text{Li}$ energy of 19.7 MeV/A, the proton energies were calculated using the kinematic code PKIN to range from 80 MeV at forward angles in the lab to 2.5 MeV at backward angles, shown as the solid curve in Figure 3.11. Hence, the detectors were placed at angles where the proton energy was low so as to completely stop in the detectors.

An additional benefit to placing the proton detectors at backward scattering angles is that very little background was expected from other interactions between the beam and the target. This is evident in Fig. 3.11 which shows the calculated kinematics of the outgoing deuteron for the ${}^9\text{Li} + d$ elastic and inelastic scattering reactions, which are the reactions most likely to produce light nuclei at backward angles. Since there may have also been a small proton contamination in the CD_2 , the ${}^9\text{Li} + \text{proton}$ scattering reactions are also shown in Fig. 3.11. In all these cases,

Table 3.1. Optical model parameters used in the FRESKO calculation shown in Fig. 3.12.

System	V_r^a	R_r^b	a_r	W_i^c	R_i^b	a_i	R_C^b
${}^9\text{Li} + \text{d}$	74.03	2.58	0.736	11.67	2.58	0.736	2.58
${}^{10}\text{Li} + \text{p}$	57.82	2.63	0.625	15.63	2.95	0.33	2.37

^aVolume Woods-Saxon Potential

^bActual Radius (fm)

^cSurface Woods-Saxon Potential

the kinematics of the reaction are insufficient to produce a light nucleus at backward scattering angles.

A final reason for placing the detectors at backward angles was due to the fact that the initial calculations for the angular distribution of the ${}^9\text{Li}(\text{d},\text{p})$ reaction were peaked at forward center of mass angles for the cases where an s-wave virtual state or a p-wave resonance was populated in ${}^{10}\text{Li}$. These calculations were performed using the coupled-channels code FRESKO [31] assuming an incident ${}^9\text{Li}$ energy of 180 MeV. The calculation used two separate optical model potentials to describe the ${}^9\text{Li} + \text{deuteron}$ interaction (entrance channel) and the ${}^{10}\text{Li} + \text{proton}$ interaction (exit channel). Due to the fact that no optical model parameter sets exist for the ${}^9\text{Li} + \text{deuteron}$ or the ${}^{10}\text{Li} + \text{proton}$ systems, optical model parameters from other nuclei having a similar mass to either ${}^9\text{Li}$ or ${}^{10}\text{Li}$ were chosen for use in the calculation. Figure 3.12 shows a sample calculation that was performed using a ${}^9\text{Be} + \text{deuteron}$ parameter set for the entrance channel and a ${}^9\text{Be} + \text{proton}$ parameter set for the exit channel taken from Ref. [44], along with the angles that the various silicon detectors were sensitive to. The optical model parameters used in the calculation shown in Fig. 3.12 are listed in Table 3.1. If the calculation in Fig. 3.12 is correct, then a determination of the angular momentum of the state or states populated in the ${}^9\text{Li}(\text{d},\text{p})$ reaction may be possible based on the angular distributions of the

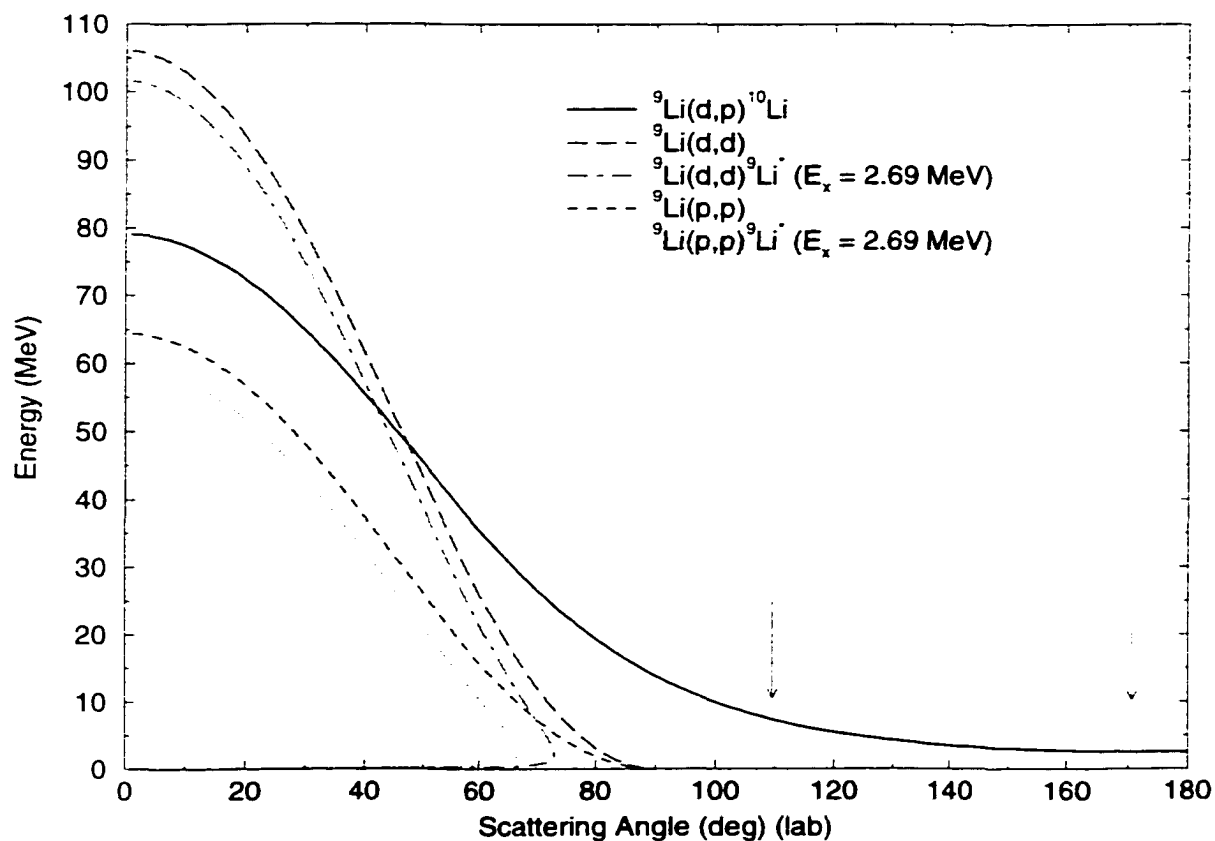


Figure 3.11. Plot of the energy of the proton as a function of its scattering angle in the lab for the ${}^9\text{Li}(d,p)$ reaction (solid curve) in comparison with the kinematics of the lighter recoiling nuclei from potential background reactions between the ${}^9\text{Li}$ beam and the CD_2 target. The arrows indicate the range of angles covered by the silicon detectors in the target chamber. All of the kinematics were calculated using the code PKIN assuming a ${}^9\text{Li}$ incident energy of 19.7 MeV/A.

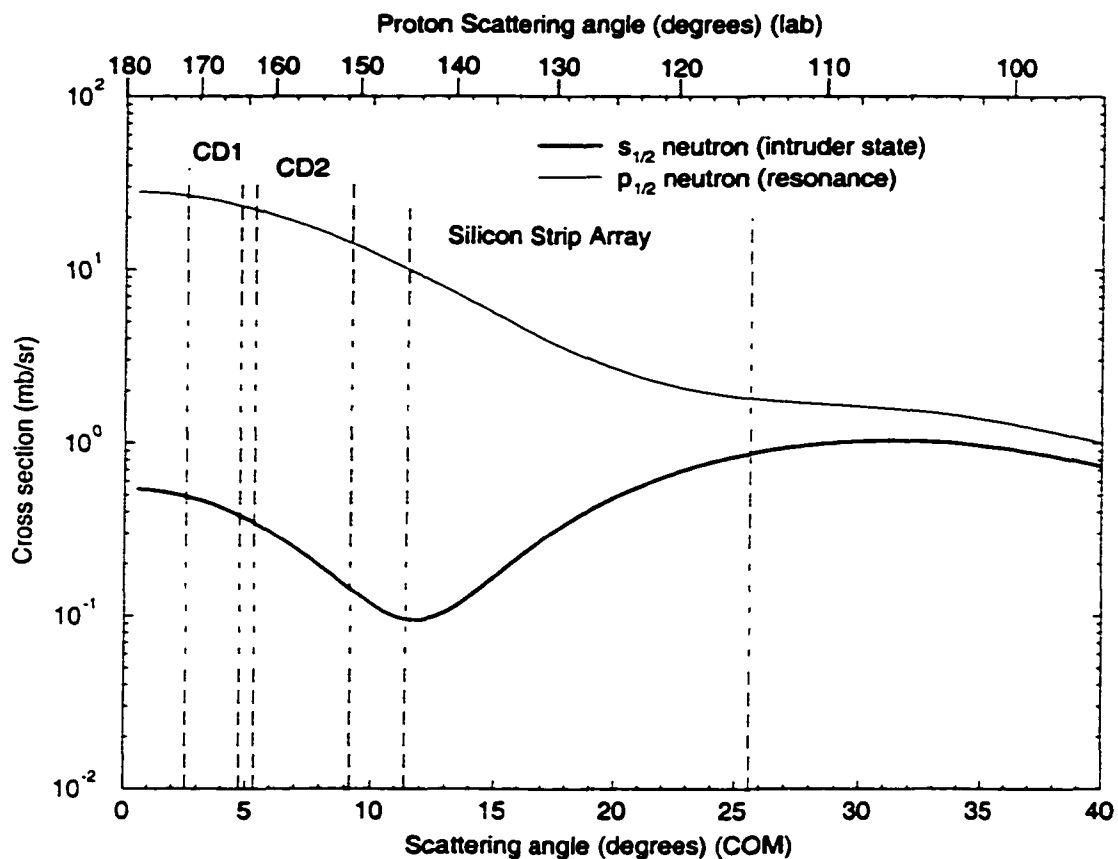


Figure 3.12. Calculated angular distributions for populating an s-state (dark curve) or a p-state (red curve) in ^{10}Li for the $^9\text{Li}(d,p)$ reaction. The dashed lines indicate the range of angles covered by each of the silicon detectors.

protons measured in the various silicon detectors since the behavior of the s-wave virtual state or p-wave resonance are different at angles near 90° in the center of mass.

3.4.1 CD detectors

Two of the silicon detectors, labeled CD1 and CD2, were double sided silicon strip detectors, $300\ \mu\text{m}$ and $500\ \mu\text{m}$ thick, respectively, with a geometry similar to that of a 'compact-disc'. Each detector has an inner diameter of 48 mm, an outer diameter of 96 mm, 16 radial strips (sectors) which measure the azimuthal angle, ϕ ,

and 16 circular strips (rings) which measure the scattering angle, θ . Since every ring and sector produces a signal corresponding to the energy deposited in the detector, each ring and sector was processed individually in the electronics. (See Figure 3.13) The position of the detected particle was determined by which ring and sector were triggered in a given event. On occasion, multiple rings or sectors would fire during a given event due to either the presence of random noise above threshold in the electronics, or due to cross talk between adjacent rings or adjacent sectors. When this occurred, the ring, or sector, closest to the detected particle would have the largest signal relative to the other rings or sectors triggered in the same event. The location of the detected particle was then determined by the intersection of that ring and the sector which produced the strongest signal for that given event. This method of determining the position of the detected event thus limits the angular resolution of the CD detectors to the width of a single ring. In the experimental setup shown in Fig. 3.10, CD1 was 17.1 cm from the target subtending the angles from 164° to 171° in the lab (4.9° to 2.7° , respectively, in the center of mass), and CD2 was 8.1 cm away from the target subtending the angles from 150° to 163° in the lab (9.5° to 5.2° , respectively). At these distances from the target, each ring on CD1 covers 0.5° in the lab ($\sim 0.2^\circ$ in the center of mass) while a ring on CD2 covers 0.9° ($\sim 0.3^\circ$ in the center of mass).

3.4.2 Silicon Strip Array

In addition to the two CD detectors in the target chamber, six silicon strip detectors, 5 cm x 5 cm in active area, were placed in the Silicon Strip Array shown in Fig. 3.10. Each detector in the array was 300 μm thick, having 16 resistive strips on the front of the detector which faced the target as well as a single strip on the back of the detector which was used to measure the total energy deposited in

the detector. When a particle encountered a resistive strip, the resultant signal was measured on both ends of the resistive strip, labeled as 'In' and 'Out' on Figure 3.14. ('In' refers to the side of the detector which measured the angles closest to 90°. 'Out' refers to the side closest to 180°.) The strength of the signal measured on one end of the strip was thus dependent on how far away the particle hit from that side of the detector as well the total amount of energy deposited into the strip. The position along an individual strip, x_{strip} , was determined by taking a ratio of the amount of energy detected on one side of the strip to the total amount of energy deposited in the strip:

$$x_{strip} = \frac{In}{In + Out} \quad (3.21)$$

Unfortunately in this experiment, many of the resistive strips had only one side producing a reasonable signal due to problems in the electronics. However, it was discovered that the position along the strip can still be determined when having only one side of the strip available by using the signal measured on the back of the detector as a measure of the total energy deposited in the strip. The relationship between the position along the strip and the signal from one side of the strip was then related by the equation:

$$x_{strip} = \frac{In}{Back} \quad (3.22)$$

where Back is the measured signal from the back of the detector. The strip position, as calculated by either method, coupled with the knowledge of which strip was hit during the event, provided a measurement of where the incident particle hit the detector.

The downstream edge of the Silicon Strip Array was located 42.4 mm away from the target. At this location, the radial distance from the center of each detector to the beam axis was 9.11 cm. The detectors were mounted in the array at an

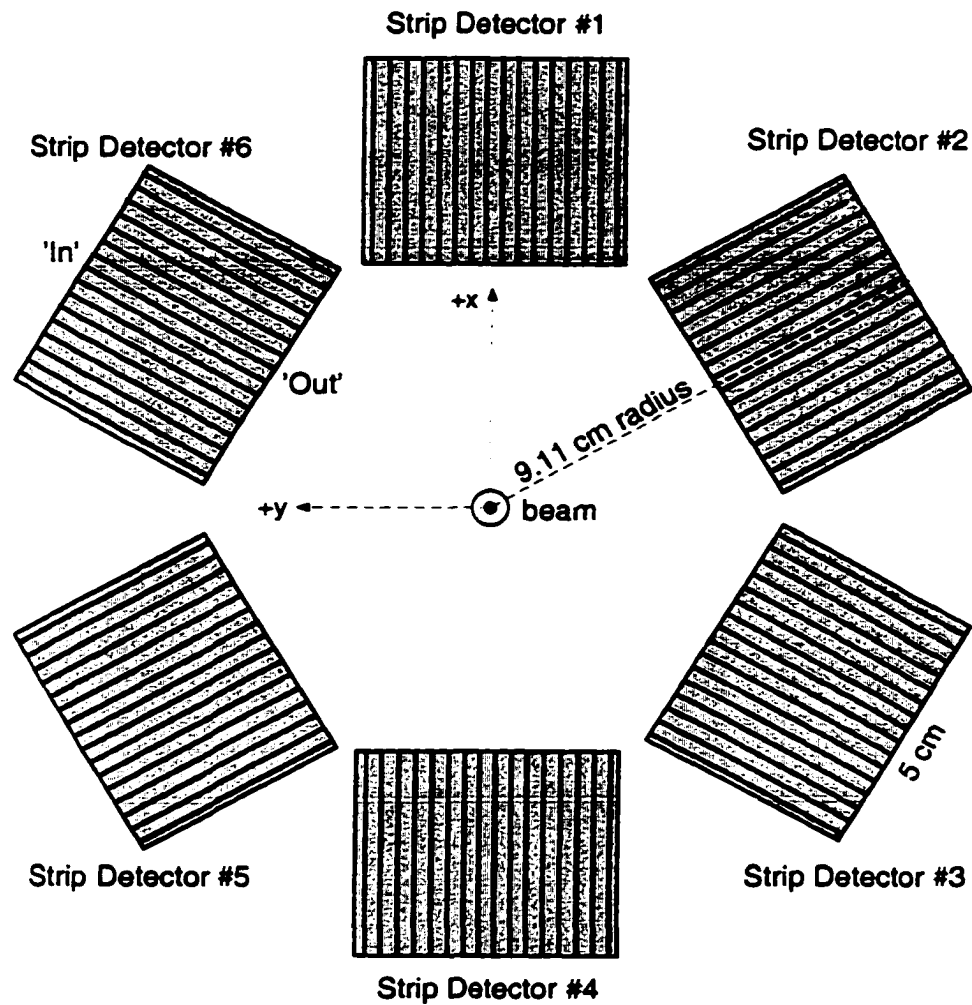


Figure 3.14. Schematic diagram of the Silicon Strip Array as seen by the target. In the diagram, the incident beam is coming out of the page. Note that Strip Detector #5 was not used in the experiment.

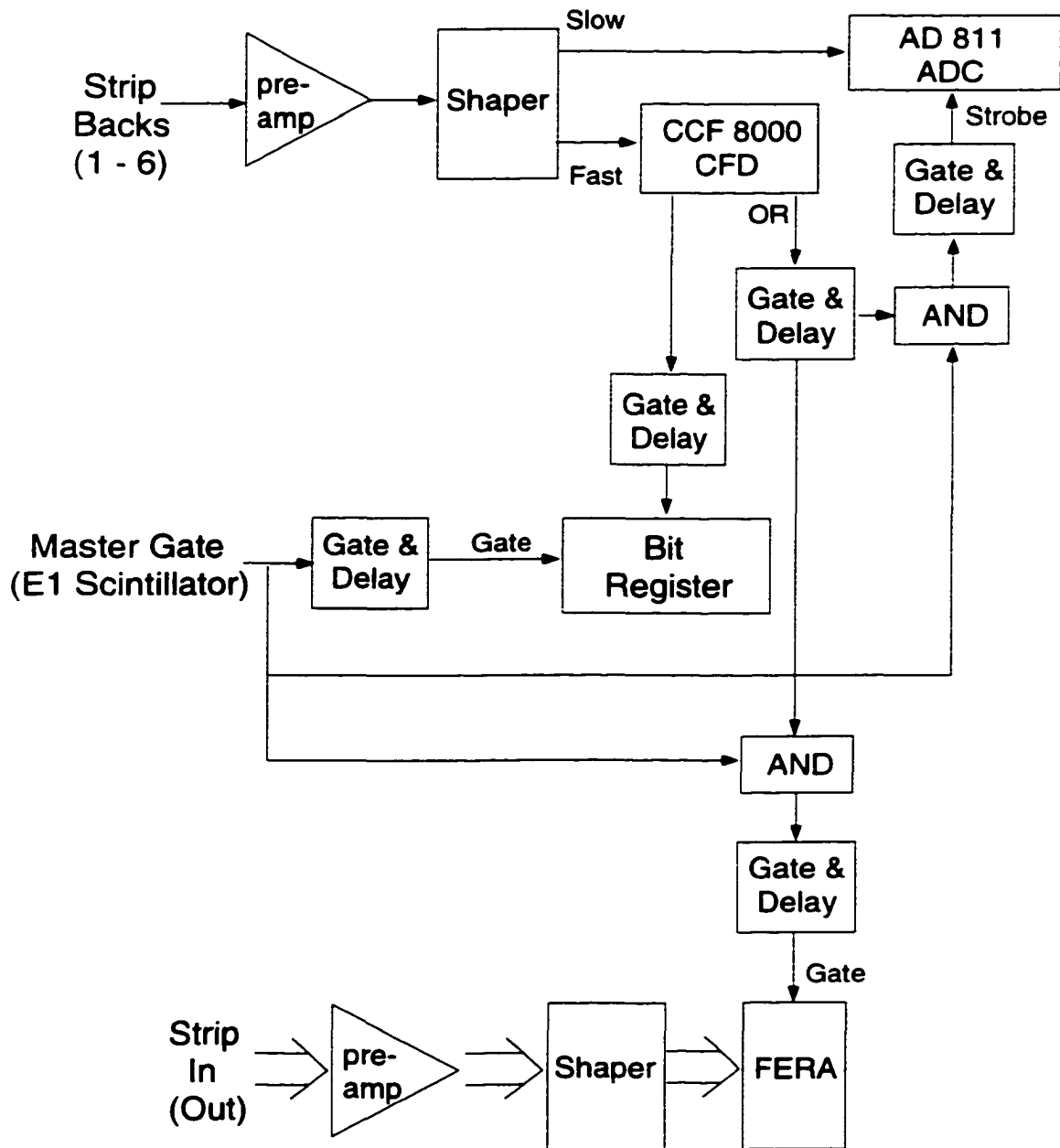


Figure 3.15. Block diagram of the electronics for a Strip detector. The large arrows indicate multiple signals being processed through separate channels in the same module.

angle of 55.3° with respect to the beam axis with the resistive strips pointed along the direction of the beam axis as illustrated in Fig. 3.14. In this arrangement, the measurement of the scattering angle was mostly dependent on the position along the strip rather than on which strip was hit by the particle. This provided an optimal way for measuring the scattering angle assuming that the resolution of the position of the incident proton along the strip was better than the 3 mm separation between adjacent strips. (See Table A.3 for strip position resolution.) With this arrangement, each detector in the array subtended 115° to 145° in the lab (25.6° to 11.3° , respectively, in the center of mass).

3.4.3 Calibrating the silicon detectors

At one point during the experiment, all of the silicon detectors were calibrated using a $0.1 \mu\text{Ci } ^{241}\text{Am}$ α source which was placed on the target ladder and centered on the beam axis for the calibration runs. During most of the data runs when the CD_2 target was in place, the ^{241}Am source was located 6.1 cm below the optical axis. Because the ^{241}Am source only produces α particles ranging from 5.33 MeV to 5.48 MeV, which appeared as one peak in the energy spectra of the silicon detectors, it was only possible to perform a one point calibration on the detectors with this source. To improve this situation, a second set of calibrations was performed at the end of the experiment using a 20 nCi mixed source containing ^{148}Gd as well as ^{241}Am . The presence of ^{148}Gd in the mixed source produced a 3.18 MeV α particle in addition to the α particles produced by the ^{241}Am which thus allowed for a two point calibration to be made for the silicon detectors. In addition, because the 3.18 MeV α is emitted from the ground state of ^{148}Gd [45], and hence has an extremely narrow intrinsic width, the resolution of all of the detectors could now be determined based solely on the measured width of the detected 3.18 MeV α particle.

For reference, the measured widths for the 3.18 MeV α line in the sectors of CD1 and CD2 are given in Table A.1 and for the strip detectors in Table A.2. In general, the resolution of the sectors of the two CD detectors ranged from 58 keV to 197 keV FWHM (for the 3.18 MeV α particle), and from 38 keV to 83 keV FWHM for the strip detectors.

In addition to calibrating the energy spectra of the strip detectors, the strip positions were also calibrated for all of the detectors using the mixed α source. To calibrate the position measurements along the strips, masks were mounted on the array approximately 2 cm in front of each of the 5 working strip detectors. Each mask had a series of slits, 1.6 mm wide, which were oriented perpendicular to the strips on the detector. Figure 3.16(a) shows a schematic diagram of the masks used for calibrating the strip positions. The edge to edge separation between consecutive slits was 3.0 mm, except for one location where the center to center separation between slits was 6.0 mm. This larger gap provided an asymmetry in the mask pattern to ensure that the orientation of the detector as mounted in the array was unambiguous. Furthermore, each mask was arranged so that the first three slits were placed by the edge of the detector closest to the target. (Labeled 'In' in Fig. 3.14)

A typical calibration spectra using the method in Equation 3.21 for determining the position is shown in Figure 3.16(b) which shows the mask pattern as measured by strip #11 in Strip Detector #3, while Figure 3.16(c) shows the spectra for strip #11 in Strip Detector #1 using Equation 3.22 to determine the strip position. Because a number of the individual strips had missing or poor signals on one end, the determination of which method to use was done for every individual strip. When it was possible to use either method to determine the strip position for a given strip, the standard method illustrated in Eqn. 3.21 was chosen.

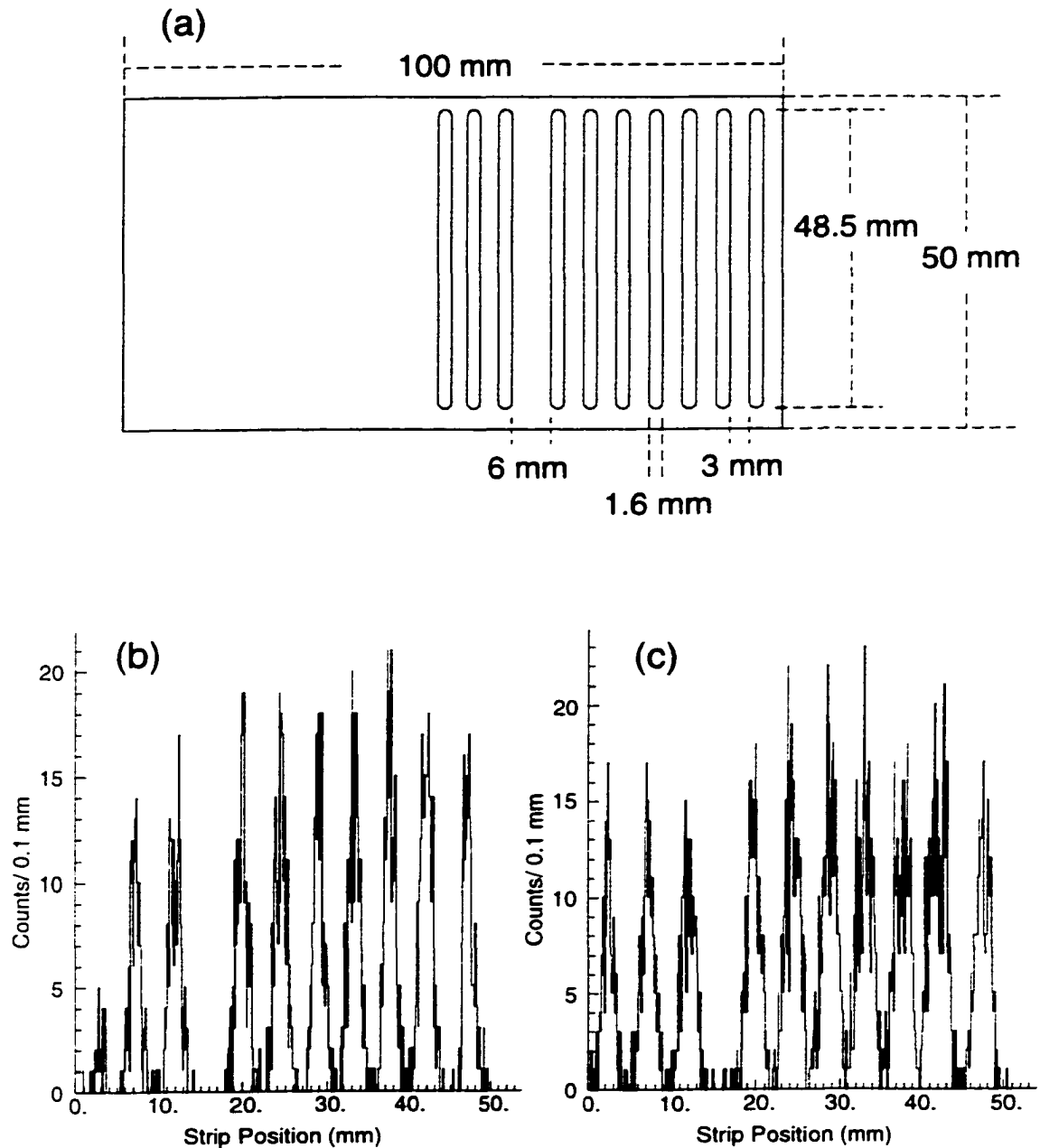


Figure 3.16. (a) Schematic diagram of the masks used to calibrate the strip position. The first three strips were located at the edge of the detector closest to the target. (b) Measured mask pattern along strip #11 on Strip Detector #3, using the method described in equation 3.21. (c) Mask pattern for strip #11 on Strip Detector #1 using method described in equation 3.22.

The resolution of the measured strip position for each individual strip was calculated by subtracting the intrinsic width of the slit, which was taken to be 1.6 mm FWHM, from the average measured width of the slits for a given strip in quadrature, ie:

$$\sigma_{res} = \sqrt{(\sigma_{meas}^2 - \sigma_{int}^2)} \quad (3.23)$$

where σ_{res} is the resolution of the strip. σ_{meas} is the average measured width of the slit. The position resolution for all strips in the strip detectors are presented in Table A.3 along with the method that was used to determine the position for that strip. In general, the resolutions of the strips ranged from 0.5 mm to 2.3 mm (FWHM).

3.5 S800 spectrograph

After the ${}^9\text{Li}$ secondary beam encountered the CD_2 target and subsequently produced the unbound ${}^{10}\text{Li}$ nucleus, the outgoing ${}^9\text{Li}$ nucleus resulting from the breakup of ${}^{10}\text{Li}$ entered the S800 spectrograph and was detected by a series of detectors in the focal plane. Before discussing the details of the detectors used in the focal plane of the S800, a brief overview of the specifics of the S800 spectrograph, and magnetic spectrographs in general, will be given.

The main reason for using magnetic spectrographs to detect charged particles is to perform high-resolution measurements of the momentum and energy of a charged particle by correlating its momentum to a particular position at the focal plane of the spectrograph. This allows for the substitution of a momentum measurement by a position measurement. The basic principle behind the workings of the magnetic spectrograph is the utilization of a strong uniform magnetic field to bend beam particles into a circular path with a radius ρ , based on the particle's momentum. The relationship between the momentum of a charged particle and radius of the

path that the particle is bent by the magnetic field is given by:

$$\rho = \frac{mv}{qB} \quad (3.24)$$

where $m.v$ and q are the mass, velocity and charge of the particle, respectively and B is the strength of the applied magnetic field [15]. By placing a position sensitive detector at the exit of the spectrograph, one can measure how much an individual particle was bent based on its position in the focal plane detector. This measurement of the particle's position in the focal plane along with knowledge of the strength of the magnetic field within the spectrograph provides a precise measurement of the momentum of the beam particle.

This simple picture of a magnetic spectrograph develops complications when dealing with the actual magnetic fields of the magnets used in the spectrographs due to the fact that the fields produced by these magnets are not completely uniform. Any variances in the magnetic fields, due primarily to impurities in the material of the magnet, causes higher order effects, or aberrations, to occur in the motion of the particles within the spectrograph. If these aberrations are strong enough, the position of the particle in the dispersive direction of the focal plane no longer depends solely on its momentum but on other parameters of its motion as well. In the case of the S800, these problems become magnified due to the fact that the S800 has a relatively large angular acceptance. Because the variances in the magnetic field tend to increase toward the edges of the magnets, if a particle is allowed to transverse the spectrograph away from the center of the magnets, the effects of these aberrations on the motion can be quite strong. To correct for the effects of these aberrations on the measurement of a particle's momentum, it is necessary to measure not only the position of the particle in the focal plane, but the angles exiting the spectrograph as well. With knowledge of the specifics of the spectrograph in terms of the physical dimensions of the magnetic elements as well as the magnetic field settings of these

elements, one can then reconstruct the trajectory of the incoming particle as it entered the spectrograph based on measurements made in the focal plane [46].

The S800 spectrograph consists of two superconducting quadrupoles, labeled Q1 and Q2 in Fig. 3.4, and two 75° superconducting dipoles D1 and D2 which have a momentum dispersion of 9.6 cm/% relative to the central momentum of the spectrograph. The total momentum acceptance of the S800 is 5%, which implies that only those particles which had a momentum within $\pm 2.5\%$ of the momentum of the particle which traverses the center of the spectrograph are detected in the focal plane [40]. Because of the large difference in momentum between the ${}^9\text{Li}$ direct beam and the outgoing ${}^9\text{Li}$ nuclei from the breakup of ${}^{10}\text{Li}$, the field settings used in the spectrograph to detect ${}^9\text{Li}$ from the (d,p) reaction were too weak to bend the direct beam up to the focal plane. Hence, during the experiment, it was necessary to use a different spectrograph setting when taking direct beam data than the setting used to take actual data.

The apertures of Q1, Q2 and D1 are relatively large, which translates into a large angular acceptance into the spectrograph. The effective angular acceptance for the spectrograph is approximately $\pm 3.5^\circ$ in the dispersive direction relative to the center of the spectrograph, and $\pm 5^\circ$ in the non-dispersive direction [40]. With the spectrograph centered at 0° for the entire experiment, this translated into complete coverage of the scattering angles from 0° to 3.5° in the lab for the outgoing ${}^9\text{Li}$ particle, and partial coverage from 3.5° to 5° in the lab. The angular range of the spectrograph translates into a complete coverage of the center of mass angles for the outgoing ${}^{10}\text{Li}$ nucleus from 0° to 28° assuming that the breakup angle between the ${}^{10}\text{Li}$ nucleus and the detected ${}^9\text{Li}$ nucleus is small.

Within the focal plane of the spectrograph, two tracking detectors as well as an ion chamber and scintillator (labeled IC and E1 in Fig. 3.4, respectively) were

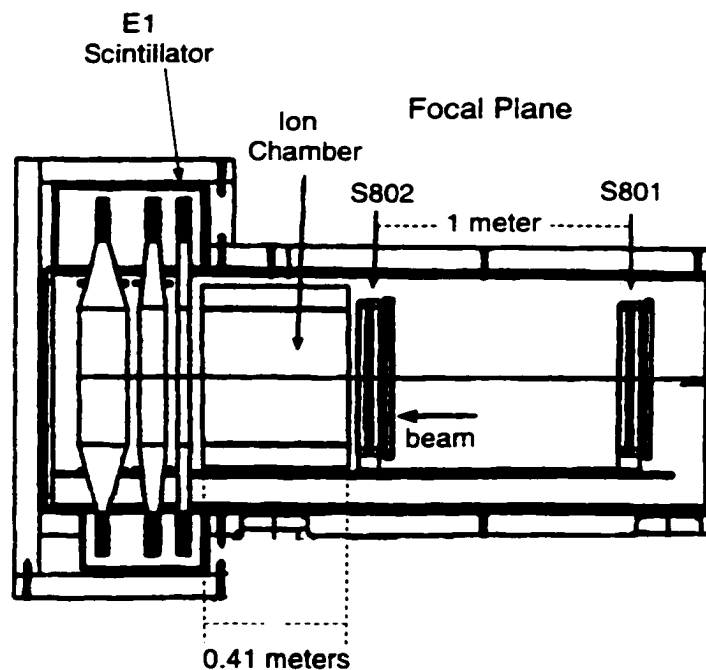


Figure 3.17. Diagram of S800 focal plane.

used to measure the ${}^9\text{Li}$ particles as they exited the spectrograph. The tracking detectors were two large CRDCs, labeled S801 and S802, separated by 1 meter as shown in Figure 3.17. Each CRDC in the focal plane had an active area of 30 cm x 59 cm, an active depth of 1.5 cm, and was filled with a gas mixture of 80% CF_4 and 20% C_4H_{10} at a pressure of 138 Torr. The detectors were arranged in the focal plane with the pad direction, containing 224 cathode pads, parallel to the dispersive direction of the spectrograph. Just as had been done with S803 and S804, pulser runs were performed to gain match the pads. In addition, mask runs were performed to calibrate the detectors by setting the dipoles of the spectrograph to bend the direct ${}^9\text{Li}$ beam up to the focal plane. Unlike the mask calibration runs performed with S803 and S804, the masks in this case were located directly in front of the detectors which made the calibration procedure straightforward to do.

A complication developed during the experiment which affected the performance of S801 and S802 for a portion of the experiment. At the early stages of the experiment, prior to the time when the two detectors were calibrated, it was noticed that the amount of gas flowing through S801 and S802 was lower than the normal operating conditions for these detectors. A low rate of gas flow through the CRDC's can affect the performance of the detector in terms of its resolution and efficiency for detecting charged particles since it allows for the possibility for impurities to develop in the gas as a result of the interaction of the gas with the walls of the chamber. Since any change in the properties of the fill gas can have an immediate impact on the behavior of the CRDC, it was quite possible that the change in the flow of gas through S801 and S802 affected the measurement of the position in the focal plane. In particular, the change in the gas would have had an impact on the measured positions and angles in the non-dispersive direction of the spectrograph since it was measured by the drift time of the electrons through the gas.

The behavior of these detectors around the time when the gas flow was changed is shown in Figures 3.18(a) and (b) in which the raw TAC signals from S801 and S802, respectively, are shown as a function of time as determined by the number of buffers written onto tape starting with the first ${}^9\text{Li}(d,p)$ reaction run taken onto tape, which was Run #12. The gas flow to S801 and S802 was altered before Run #18 which is indicated by the arrow in Figs. 3.18(a) and (b). As shown in these two figures, the behavior of the two detectors is quite non-linear at the time when the change in gas flow occurred. Additionally, the center of the distributions in the two detectors drifted for a period of time after the change in gas flow until eventually reaching a stable point around Run #34. To rule out the possibility that the observed drift was due to an actual drift in the incident beam in this direction, the distribution of the beam in the non-dispersive direction as measured by S803 and S804 is shown

in Figs. 3.18(c) and (d) for that same period of time. While a change in the beam intensity is evident in S803 and S804, the center of the beam distribution remained at essentially the same position on the detectors in comparison to the center of the distribution in S801 and S802. Since the incident beam showed no sign of a drift, and since the apparent drift in S801 and S802 coincided with the recorded change in gas flow, it was concluded that the drift seen in S801 and S802 was due to the focal plane detectors only and not due to changes in the incident beam.

To ensure that the measurements in the focal plane remained consistent throughout the experiment, it was necessary to correct this apparent drift in the two TACs as a function of time so that the absolute positions of the particles could be properly determined for the runs in question. This correction was determined by performing a weighted fit to the measured position distribution as a function of the number of buffers starting with Run #18 as shown in Figures 3.19(a) and (b) for S801 and S802, respectively. Once the behavior of the drift in both detectors was determined, an appropriate correction to the offsets of each detector was then applied as a function of when the event was written to tape. The effect of the corrections to the detectors was to adjust the center of the measured distribution in the y direction for the runs in question to the position it was measured at after Run #34 when the detectors produced a stable output. The results of these corrections are presented in Figures 3.19(c) and (d) showing a relatively flat distribution for both S801 and S802 with the width of the distribution remaining fairly constant as a function of time. A similar method was applied to determine a correction in the offset for the runs prior to Run 18 as well which also showed a drift in the two detectors. (See Figs. 3.18(a) and (b) for the initial drift prior to Run #18)

Once the particles passed through S801 and S802, they passed through the ion chamber and were completely stopped within the E1 scintillator. The ion chamber

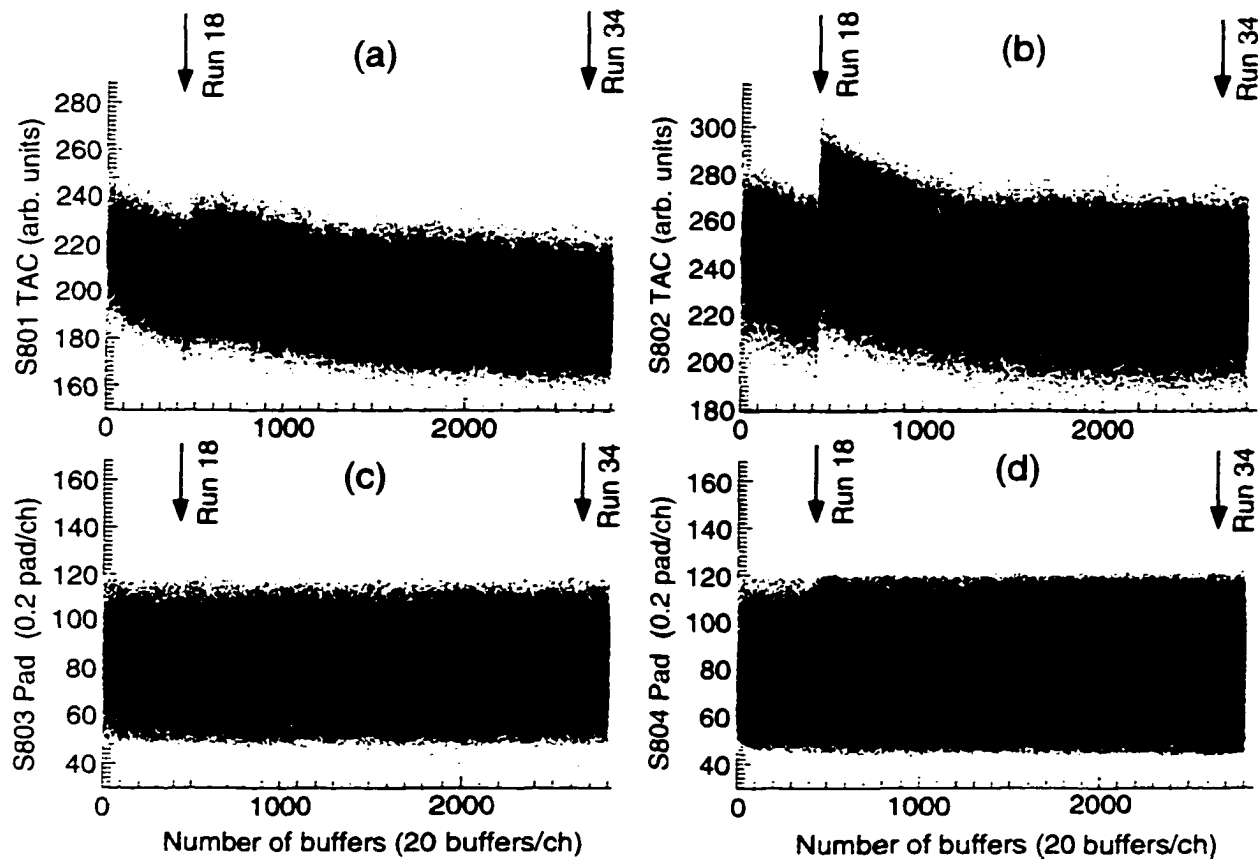


Figure 3.18. Plot of (a) S801 TAC and (b) S802 TAC as a function of time as measured by the number of buffers written to tape starting with Run #12 in comparison to the pad response in (c) S803 and (d) S804 over that same time period. The plots correspond to the behavior of the CRDC's over a period of approximately 75 hours in time. The arrows indicate when Run #18 and Run #34 occurred relative to Run #12.

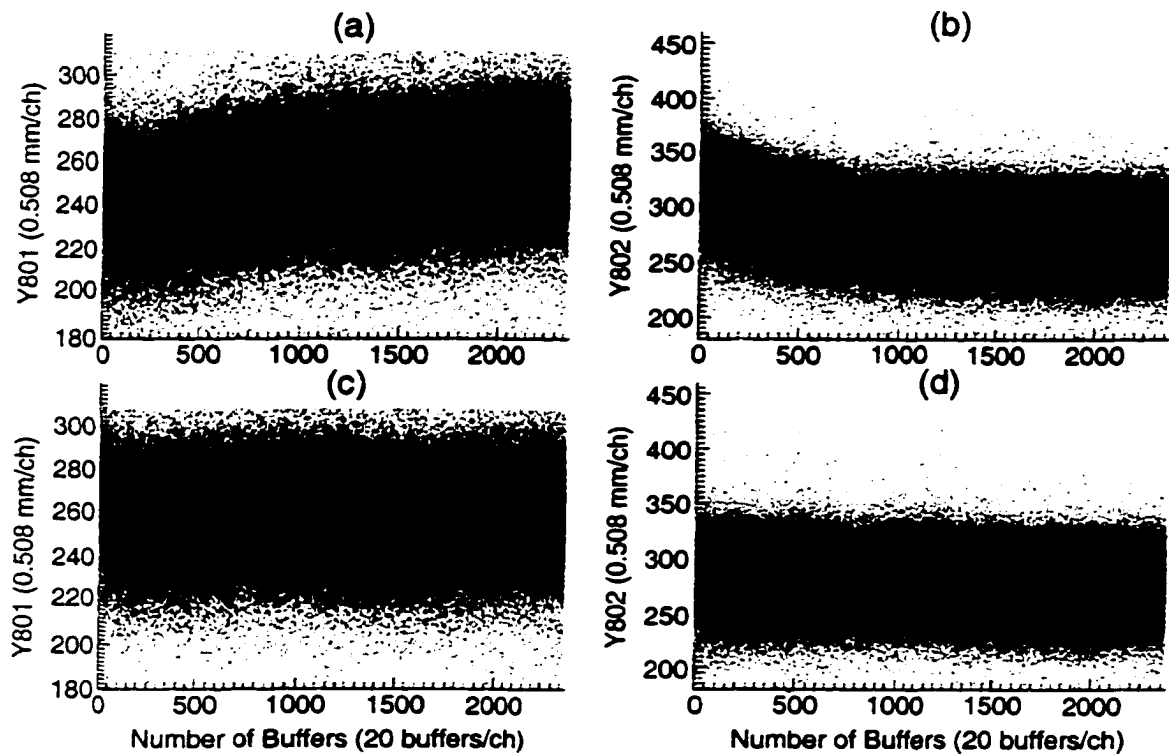


Figure 3.19. Plot of the initially measured y-position in (a) S801 and (b) S802 as a function of the number of buffers from Run # 18. The solid line represents the 5th order polynomial weighted fit used to describe the drift as a function of buffer number. The effects of the correction are shown in (c) and (d) for S801 and S802, respectively.

and E1 scintillator were used as a $\Delta E - E$ telescope to identify the particles by measuring the amount of energy the particles lost in the gas of the ion chamber as a function of the amount of remaining energy the particles deposited in the scintillator. The ion chamber was 41 cm deep and filled with P10 gas at a pressure of 304 Torr, and divided into 16 separate segments. The amount of energy the particles lost within the gas could be measured for each individual segment of the ion chamber. Because of the high energy of the ${}^9\text{Li}$ particles entering the ion chamber, it was sufficient for the purposes of particle identification to just average the signals from the segments to produce an appropriate ΔE signal. In Figure 3.20(a), the ΔE vs E plot for the direct beam is presented, showing a clear identification of ${}^9\text{Li}$, which consisted of 88% of the beam, from the small amount of background that was present. The background group was identified as ${}^9\text{Be}$ in the 3+ charge state which was probably knocked out of the production target. Since ${}^9\text{Be}^{3+}$ has the same charge to mass ratio as ${}^9\text{Li}$, the A1200 was unable to separate it from the beam. However, because of the good separation between the two groups in the ΔE vs E plot as well as the ΔE vs time of flight plot shown in Figure 3.20(b), the background that was present in the beam was easily gated out in the analysis.

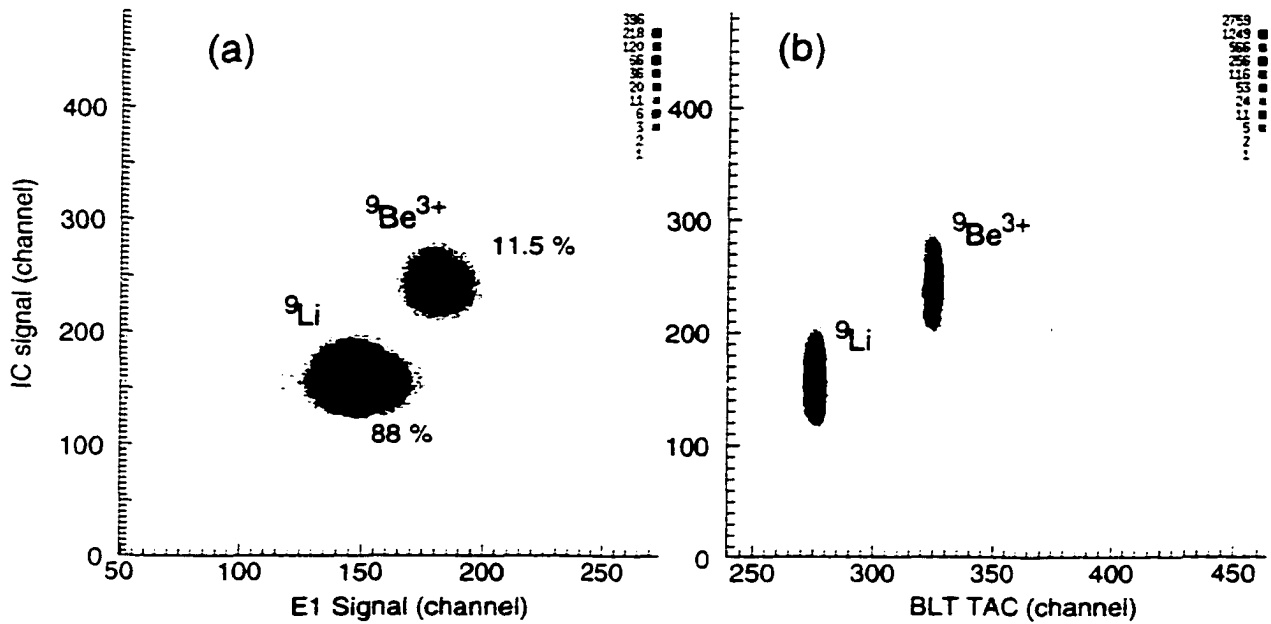


Figure 3.20. Plot of the Ion Chamber signal as a function of the (a) signal in E1 and (b) BLT TAC for the direct ${}^9\text{Li}$ beam as measured in the focal plane of the S800.

CHAPTER 4

ANALYSIS

4.1 Overview

The goal of this experiment was to study the structure of the ^{10}Li nucleus by performing a kinematically complete reconstruction of the $^9\text{Li}(d,p)^{10}\text{Li}$ reaction on an event by event basis. This reconstruction can only be properly performed once the detectors in the analysis line of the S800, the silicon detectors within the target chamber, and the detectors within the S800 focal plane are well understood and properly gated to eliminate any background processes which may have occurred during the experiment. This entailed the coordination of approximately 800 separate channels of information from four different locations for the various detector systems. An additional complication in analyzing the data was the fact that many of the parameters of interest, such as the incident angle of the incoming ^9Li beam as well as the scattering angle of the outgoing ^9Li particle were determined based on the calculated motion of the charged particles through the magnetic elements of the S800 spectrograph and analysis line. Since this information was needed in order to reconstruct the breakup of ^{10}Li , it is necessary to ensure that the calculations were performed accurately and agree with the measured motion of the beam.

To calculate the motion of the beam through the various beam line components, the code COSY INFINITY[43] was used to produce transfer maps which transform an initial set of coordinates to a final set of coordinates located at various points

along the beam line. These transfer maps are multidimensional matrices which characterize the motion of the beam through the elements of the S800 analysis line and spectrograph based on the fact that the motion of a charged particle is determined by the Lorentz force:

$$\vec{F} = Q(\vec{E} + \vec{\beta} \times \vec{B}) \quad (4.1)$$

where Z and $\vec{\beta}$ are the charge and velocity of the charged particle, respectively, and \vec{E} and \vec{B} are the applied electric and magnetic fields, respectively. COSY calculates the effect that each electromagnetic device has on the motion of the beam particle based on the physical dimensions and the field strength within a beam line element, as well as the spacing between the individual elements. The physical dimensions for all of the magnetic elements within the analysis line and spectrograph were provided by the NSCL. In addition, the strengths of the magnetic fields in the various beam line components were measured by NMR probes attached to each element and were periodically recorded in the log book.

In characterizing the motion of the beam particles through the various elements of the beam line, a generalized coordinate system was used which described the relative motion of the particles about a central reference trajectory throughout the beam line. This coordinate system was not fixed in physical space, but rather was defined relative to the central trajectory of the beam line. Furthermore, the motion of the particles was calculated not with respect to time, but rather with respect to the path length, l . By choosing the path length as the independent variable, the coordinates of the particle could be calculated from an initial set of coordinates to any point along the beam line. A diagram of this coordinate system is shown in Figure 4.1 where the x and y positions of a beam particle having a momentum, \vec{p} , are defined as the position of the beam in the dispersive and non-dispersive directions of the beam line, respectively. Because the S800 bends particles in the vertical

direction, the x-axis is defined vertically at the target with +x corresponding to the ceiling and the y axis is defined horizontally with +y corresponding to beam right. In Fig. 4.1. the angles a and b are defined as:

$$\tan (a) = p_x/p_z \quad (4.2)$$

$$\tan (b) = p_y/p_z \quad (4.3)$$

where p_x and p_y are the momentum of the particle in the x and y directions, respectively, and p_z is the momentum of the particle along the reference trajectory of the beam line. The angles a and b are related to the angle θ used in spherical coordinates by:

$$\theta = \tan^{-1} (\sqrt{(\tan a)^2 + (\tan b)^2}) \quad (4.4)$$

This relationship is useful when determining the scattering angle of the particles that entered the spectrograph. A fifth variable used in this coordinate system, δ_E , measures the energy of the beam relative to the energy for the motion along the central trajectory of the beam line. Specifically:

$$\delta_E = \frac{E - E_o}{E_o} \quad (4.5)$$

where E is the energy of the beam particle, and E_o corresponds to the central energy of the beam line.

Once the initial coordinates of the beam have been described in terms of this coordinate system, the final coordinates can then be expressed in the transfer map as a Taylor expansion of the initial coordinates. For instance, the final position in the non-dispersive plane, y_f , can be written as:

$$\begin{aligned} y_f &= f(x_i, a_i, y_i, b_i, \delta_i) \\ &= (y|x)x_i + (y|a)a_i + (y|y)y_i + (y|b)b_i + (y|xx)x_i^2 + (y|xa)x_i a_i + \dots \quad (4.6) \end{aligned}$$

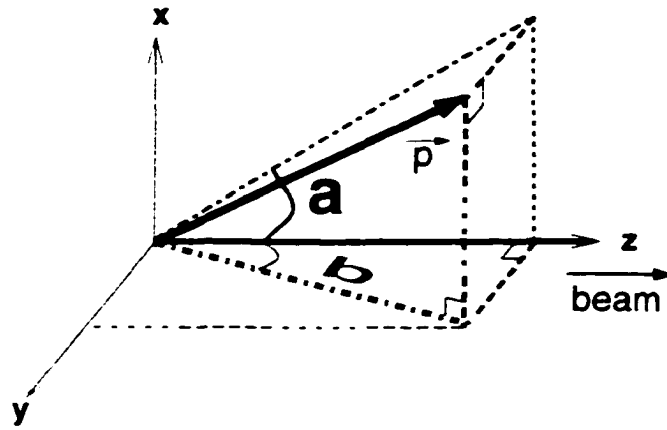


Figure 4.1. Diagram of the coordinate system used to measure the motion of a beam particle with momentum \vec{p} through the beam line.

where

$$(y|xa) = \frac{1}{2!} \frac{\partial^2 f}{\partial x_i \partial a_i} \quad (4.7)$$

is an example of a 2nd order Taylor coefficient [47]. The order of the calculation determines the highest order of the coefficients considered in producing the transfer map. In the analysis of this experiment, 2nd order COSY maps were used to describe the motion of the beam through both the spectrograph and the analysis line.

4.2 Analysis of Experimental Systematics

4.2.1 S800 spectrograph

The purpose of using a COSY generated transfer map when analyzing the data from the S800 spectrograph is to transform the measured positions and angles of the particles in the focal plane into a measurement of the beam at the target location. In calculating the appropriate transfer map for this transformation, COSY first calculates the forward map from the target to the focal plane and then inverts the forward map in order to get the target parameters expressed in terms of the

focal plane coordinates. Since the detectors within the focal plane, S801 and S802, only measure four of the five parameters used to describe the motion of the beam, namely x_{focal} , a_{focal} , y_{focal} and b_{focal} , the target reconstruction is limited to four parameters. Three parameters which were always reconstructed at the target were a_{target} , y_{target} , and b_{target} . The fourth parameter reconstructed was either the energy of the particle, δ_E , or the position of the particle in the dispersive direction, x_{target} . The reconstruction of either of these two target parameters depends strongly on x_{focal} due to the momentum dispersion of the dipoles in the spectrograph. In other words, x_{focal} measures a combination of the particle's initial position and its energy. Because of this, certain assumptions must be made in order to reconstruct either δ_E or x_{target} . When δ_E is reconstructed at the target, it is assumed that the beam spot size at the target is very small in the dispersive direction, thus having a negligible effect on measured x_{focal} position. Conversely, when reconstructing x_{target} , it is assumed that the beam is essentially monoenergetic so that the measured x_{focal} position is only dependent on x_{target} .

In this particular experiment, however, the assumption that the beam was monoenergetic was quite unrealistic since the incident beam for almost all of the data runs had an approximate 2% spread in energy. Because of this fact, the reconstruction of x_{target} using the focal plane parameters is inherently flawed. One can attempt to circumvent the assumption that the beam be monoenergetic in reconstructing x_{target} by using the calculated energy dispersion in the focal plane from the COSY forward map to convert the measured x_{focal} into a measure of the energy of the particle. However, in reconstructing x_{target} in this manner, two parameters used in the reconstruction are determined using only one measurement. This subsequently causes a correlation to exist between x_{target} and δ_E which is arbitrary and not necessarily representative of the data.

While the assumption of a monoenergetic beam is not appropriate in this experiment, the assumption of a small beam spot at the target was relatively accurate due to the fact that the beam was brought to a focus in the dispersive direction at the target. Furthermore, x_{focal} has a stronger dependence on the energy of the particle than on its initial position due to the energy dispersion of the dipoles within the spectrograph. Hence, the ability to reconstruct δ_E at the target using the spectrograph was much more accurate than attempts to reconstruct x_{target} .

To increase the accuracy of the transfer maps in determining the motion of the particles through the spectrograph, the fringe fields for both of the dipoles, D1 and D2, as well as the quadrupoles, Q1 and Q2, within the spectrograph were included in the calculation of the transfer maps. The fringe fields are described in COSY using an Enge function which has the form:

$$F(z) = \frac{1}{1 + \exp a_1 + a_2 \frac{z}{D} + \dots + a_6 \left(\frac{z}{D}\right)^5} \quad (4.8)$$

where z is the distance from the effective boundary of the magnetic field, D is the diameter of the specific element's aperture, and a_1 through a_6 are called the Enge coefficients [46]. For each of the four magnets within the S800 spectrograph, a separate set of coefficients for the Enge function was determined for each aperture. These Enge coefficients were determined by fitting the magnetic field distribution along the central axis of a given magnet starting at the point outside the magnet where the magnetic field strength was negligible and ending at the center of the magnet. For a given spectrograph setting, then, eight sets of Enge coefficients were determined to describe the fringe fields within the spectrograph.

The magnetic field distributions that were used as the basis for this fitting procedure were interpolated from magnetic field data provided by the NSCL for each element within the spectrograph. For a given magnet, seven different sets of magnetic field data were provided with each data set corresponding to measurements

of the magnetic field at various points along the central axis of the magnet, for a specific current setting within the magnet. The seven different current settings that were measured covered the full dynamic range of field strengths possible in the different magnets. Thus, for any current setting within a specific magnet, the profile of the magnetic field as a function of location relative to the upstream edge of the magnetic field could be interpolated from those measurements that were taken at nearby current settings.

A typical set of fits to the fringe fields using the Enge function are shown in Figure 4.2 where the field strength for each element as a function of the distance from the upstream edge of the magnetic field is shown. In this figure, the solid red curve is the interpolated magnetic field for the individual device while the black dashed curve is the fit to the field using a 4th order Enge function. Note that the fits in Fig. 4.2 match the interpolated field strength quite well as indicated by the residuals from each fit plotted directly above each of the magnetic field distributions. The location of the entrance aperture for each device relative to the upstream edge of the magnetic field is indicated by the placement of the vertical axis in the residual plots relative to the horizontal axis in the magnetic field plots. The magnetic field settings shown in Fig. 4.2 were used to measure the recoiling ${}^9\text{Li}$ from the breakup of ${}^{10}\text{Li}$. Similar fits were achieved for the various magnets when the spectrograph was set to measure the direct ${}^9\text{Li}$ beam.

To determine how well the spectrograph could resolve the energy of the beam at the target as well as the position of the beam in the non-dispersive direction, two different direct beam runs were performed. In one of the direct beam runs, the momentum slits were reduced from a setting which allowed a 1% momentum spread in the beam to a 1/4% momentum spread. Since the inverse transfer maps for the spectrograph reconstruct δ_E at the target, and not the relative momentum of the

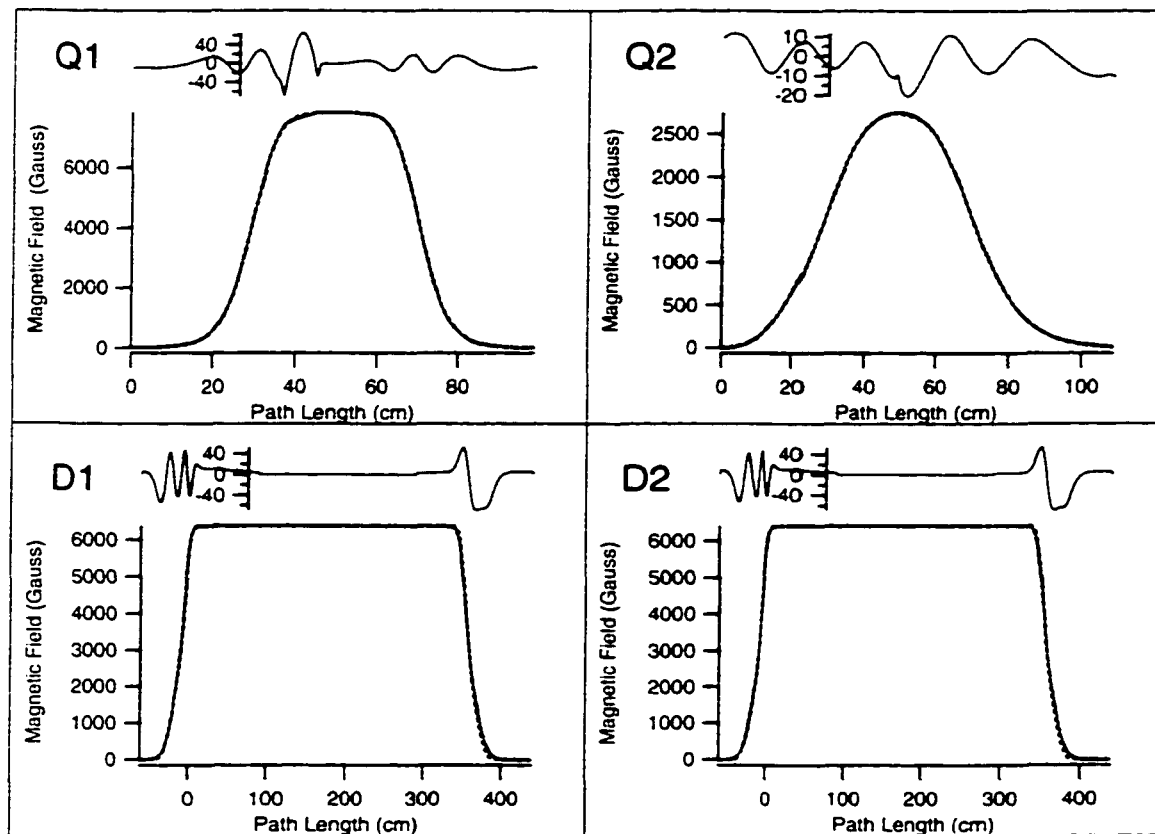


Figure 4.2. Plots of the magnetic field as a function of the distance traveled inside a given element for the four elements of the spectrograph. The red solid curve is the interpolated field while the black dashed curve is the fit using a 4th-order Enge function. The residuals for each fit are plotted directly above each magnetic field plot. The field settings shown were used within the spectrograph to measure the recoiling ${}^9\text{Li}$ from the breakup of ${}^{10}\text{Li}$.

particle, it was necessary to determine what this 1/4% momentum spread in the incident beam corresponded to in terms of the energy spread in the beam. For a fixed spread in momentum, δ_p , the corresponding spread in energies is given by:

$$\delta_E = \frac{(1 + \gamma)}{\gamma} \delta_p \quad (4.9)$$

where γ is defined in Eqn. 3.19. Since γ is dependent on the absolute energy of the particle's motion, an absolute energy determination for the beam needed to be made based on the reconstructed δ_E . This determination is relatively simple with knowledge of the bend radius, ρ and magnetic field, B , of the dipoles within the spectrograph. Rearranging Equation 3.24, we find that for a particle which moves along the center of the spectrograph, the momentum of the particle, p , is given by:

$$\frac{p}{qe} = B\rho \quad (4.10)$$

where q is the charge number of the particle passing through the spectrograph, and e is the electric charge of the electron. If the product $B\rho$ is expressed in units of Tesla-meters, then Equation 4.10 becomes:

$$3.3356\left(\frac{p}{q}\right) = B\rho \quad (4.11)$$

where p is in units of GeV/c [47]. For this particular direct beam run, the magnetic fields of the dipoles were measured by the NMR probes to be 0.6845 T. With a known bend radius for the dipoles in the S800 of 2.8028 ± 0.0056 meters [48], the central momentum for a fully stripped ${}^9\text{Li}$ particle moving through the center of the spectrograph is 1.7264 GeV/c. This translates to a central energy, E_o , of 175.4 MeV for ${}^9\text{Li}$. Solving Equation 4.5 for E , we find

$$E = E_o + E_o\delta_E \quad (4.12)$$

In Figure 4.3 the reconstructed δ_E for the 1/4% momentum run is shown, having a centroid of 0.96% which translates into an incident ${}^9\text{Li}$ beam energy of 177.08 MeV.

This implies that $\gamma = 1.021$ from Equation 3.19. With the value for γ now known, we find from Equation 4.9 that the 1/4% spread in momentum corresponded to a 0.495% spread in energy. The resolution of the incident beam can be deduced based on the measured width of the reconstructed δ_E distribution of 0.500% (FWHM). By subtracting this measured width from the known energy spread of the beam in quadrature, the resolution of the beam energy was determined to be 0.071% (FWHM) which is in relatively good agreement with the energy resolution of 0.054% (FWHM) predicted from the COSY transfer maps. The slight discrepancy between the calculated and the measured resolution of the beam is attributable to the method in which COSY determines the resolution of the spectrograph based on the incident beam profile. COSY calculates the ability of the spectrograph to resolve the energy of the beam by randomly selecting a specific number of rays from an incident beam profile that has been entered as input to the code, and tracing them through the spectrograph [49]. Thus, the resolution that is calculated in COSY is dependent on the beam profile that is selected and is therefore susceptible to systematic error. In addition to the systematic error associated with the calculated resolution from COSY, the method used to determine the resolution of the beam from the data is also susceptible to systematic error since two relatively large numbers were subtracted in quadrature to get a small number.

In the second direct beam run, a collimator with a 1/16" diameter hole, referred to as the 'hole target', was placed at the target position in order to physically restrict the incident beam profile at the target. Since the physical size of the hole in the collimator was well known, the size of the reconstructed image at the target provided a measure of the position resolution in the target reconstruction. Figure 4.4 shows the reconstructed y position at the target for the 'hole target' run using the 2nd order inverse transfer map. The width of the reconstructed position of the beam in

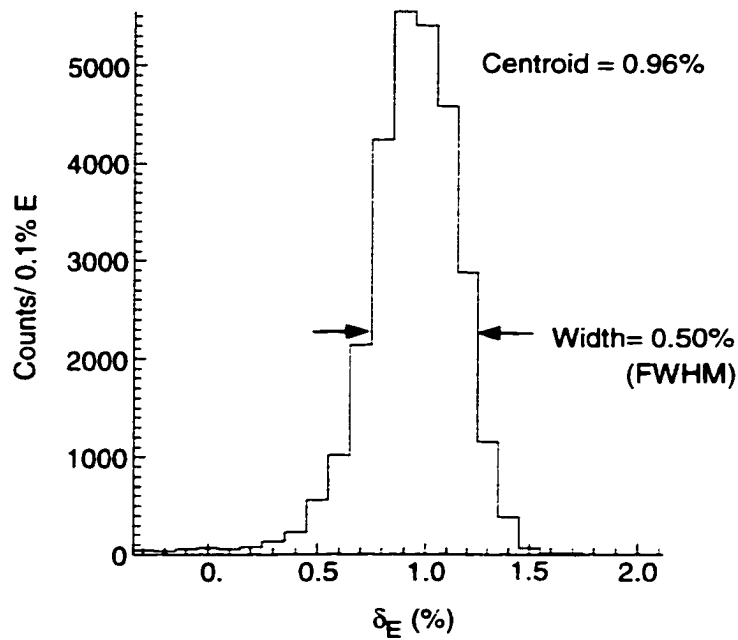


Figure 4.3. Distribution of the reconstructed energy at the target for the direct beam run with 1/4% momentum slits in place.

the y direction was 4.38 mm (FWHM) which is larger than the 1.59 mm diameter of the ‘hole target’. By subtracting the width of the reconstructed y position at the target in quadrature with the known diameter of the hole, the resolution of the position reconstruction using the spectrograph was determined to be 3.9 mm in the non-dispersive direction (FWHM). Due to the fact that in this run, the momentum slits were set for the full 1% momentum spread in the beam, a determination of the resolution in the reconstructed x_{target} position was not possible.

Attempts to improve the position and energy resolution of the reconstructed target image were made using 3rd and 4th order COSY maps to reconstruct the target parameters from the focal plane information. However, the reconstructed position for the ‘hole target’ run as well as the energy reconstruction for the 1/4% momentum run using these higher order transfer maps looked virtually identical to what

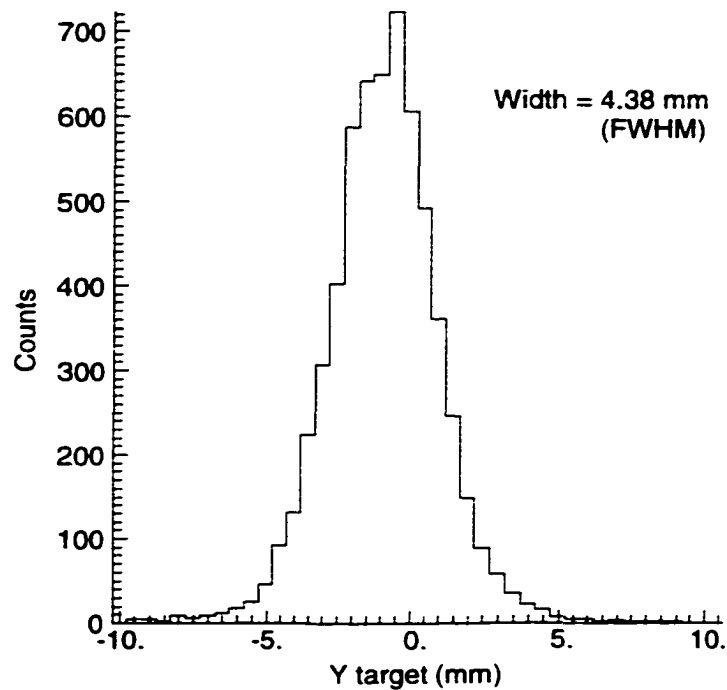


Figure 4.4. Distribution of the reconstructed y position at the target for the hole target run from the measured focal plane information.

had been reconstructed using the 2nd order transfer map. Since using the higher order transfer maps did not improve the resolution of the reconstructed position or energy at the target, only 2nd order transfer maps were used to reconstruct the target parameters from the spectrograph information for both the direct beam runs and the reaction runs.

4.2.2 Incident ${}^9\text{Li}$ Energy Measurement

Since the spectrograph was not able to measure both the direct ${}^9\text{Li}$ beam and the outgoing ${}^9\text{Li}$ particles from the reaction at the same time, it was necessary to measure the energy of the incident beam independently of the spectrograph. For this reason, the motion of the incident beam as it passed through the first set of quadrupoles and dipoles in the analysis line was studied in order to determine the

best way to measure the incident energy of beam based on the measured positions of the beam at the PPAC, S803 and S804.

At the center of the intermediate image box, the beam was brought to a focus in the dispersive direction which caused the motion of the beam in that direction to depend largely on the incident momentum of the beam. The presence of this crossover point within the intermediate image chamber is seen in Figure 4.5 in which the motion in the dispersive direction for three rays with different incident momenta ($+1/2\% \delta_p$ (black), $-1/2\% \delta_p$ (red) and the central momentum of the beam line (green)) were calculated using COSY starting from the center of the BLT through the first half of the analysis line to S804. The calculations were based on the measured magnetic fields within the various magnetic elements in the first half of the analysis line. This crossover point at the intermediate image chamber causes the angle a_{803} to be strongly dependent on the momentum (and consequently the energy) of the incident particle. This relationship is reflected in the data as shown in Figure 4.6 where the reconstructed δ_E from the spectrograph is plotted as a function of a_{803} for Run #8 in which the direct beam with the 1% momentum slit in place was measured in the spectrograph. The figure clearly shows the strong linear correlation between δ_E and a_{803} .

To determine if this correlation between δ_E and a_{803} was consistent throughout the experiment, a linear weighted fit was performed on the δ_E vs a_{803} plots for three different direct beam runs performed at various points during the experiment. In Fig. 4.6, the weighted fit for the data from Run #8 is shown as the solid line. The deduced slopes from these three direct beam runs are shown in Table 4.1. From the three separate runs, an average slope for δ_E as a function of a_{803} was determined to be -0.03615 \%E/mr with a standard deviation of $\pm 1.16 \times 10^{-3} \text{ \%E/mr}$. This is in relatively good agreement with the $(a|\delta_E)$ coefficient from the COSY transfer map

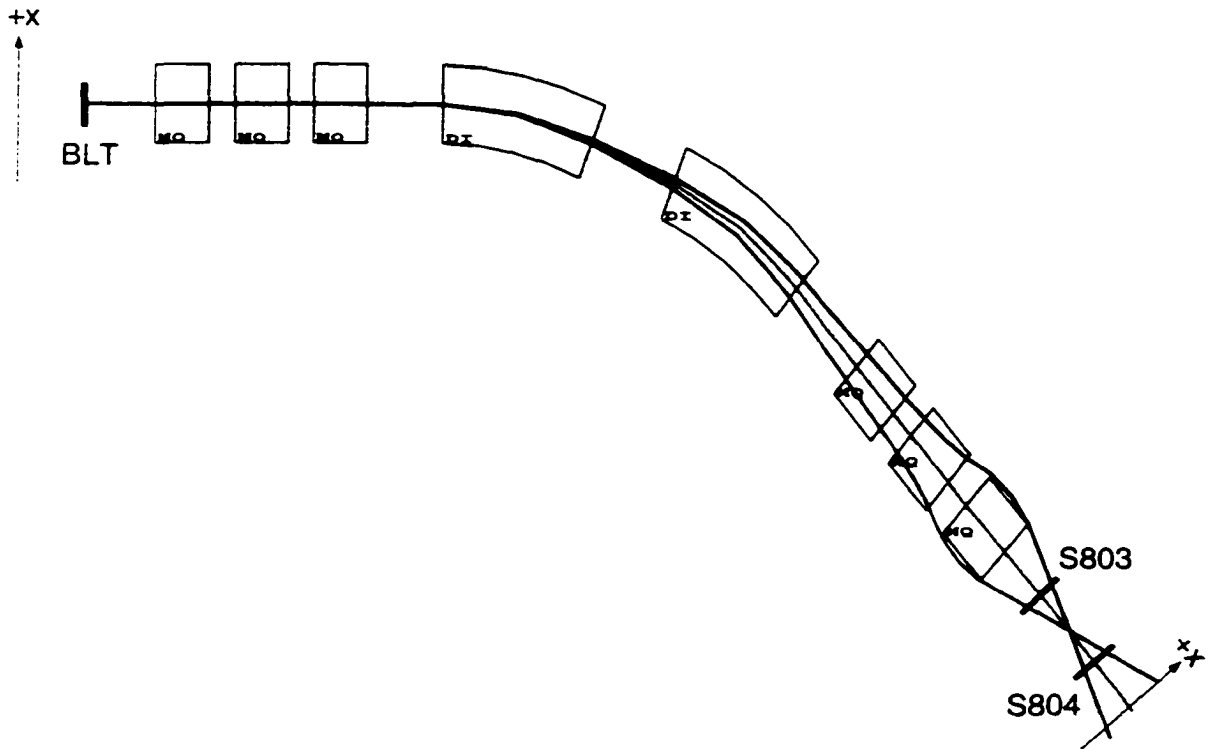


Figure 4.5. Ray trace diagram of the S800 Analysis line from the BLT to S804 for ray with three different momenta, $+ 1/2\% \delta_p$ (black), $- 1/2\% \delta_p$ (red), and the central momentum (green) of the beam line. The diagram was generated using COSY and assumes that the ray originated from a single point at the center of the beam line.

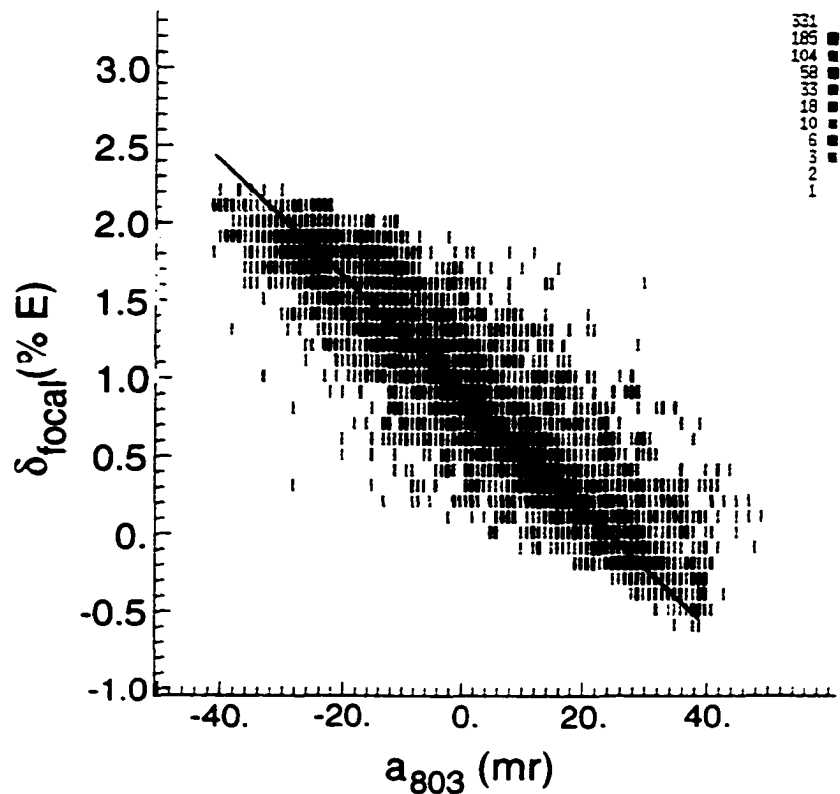


Figure 4.6. Plot of δ_E vs a_{803} for the direct ${}^9\text{Li}$ beam for Run #8. The solid curve represents the linear weighted fit used to determine the slope of δ_E in terms of a_{803} .

Table 4.1. Results of weighted fits to δ_E vs a_{803} for various direct beam runs with 1% momentum spread (Runs 8 and 62) and 1/4% momentum spread (Run 61).

Run #	Date	Slope (%E/mr)
8	1/20/98	-0.0373758
61	1/26/98	-0.0350318
62	1/26/98	-0.0360422

from the BLT to S804 of -0.02809 %E/mr. Since the correlation between δ_E and a_{803} remained quite stable throughout the experiment and was in relatively good agreement with the value predicted by COSY, the average slope was used to convert a_{803} into a measure of the incident energy of the beam relative to the central energy of the spectrograph for the direct beam setting.

Once this relationship between a_{803} and δ_E had been determined, the resolution was deduced based on the data from Run #61 with the same method that was used for determining the resolution for the energy reconstruction of the spectrograph. The measured incident energy, $\delta_{a_{803}}$, for Run #61 is shown in Figure 4.7(a) with a width of 0.61% in energy (FWHM). Subtracting the known 0.495% energy spread in the beam in quadrature, the resolution of the measured incident energy was determined to be 0.36% (FWHM). To confirm this result, the difference between $\delta_{a_{803}}$ and δ_E was determined on an event by event basis for this run as shown in Fig. 4.7(b). The measured width of the difference distribution is 0.40% in energy (FWHM) which is relatively consistent with the deduced resolutions of the incident beam and the reconstructed δ_E resolutions.

Because of the tendency of secondary beams to occupy a relatively large phase space, it was necessary to investigate the possible effects a large beam spot size at the entrance to the S800 analysis line would have on the use of a_{803} as a measure of the incident energy. To this end, another COSY calculation was performed to determine

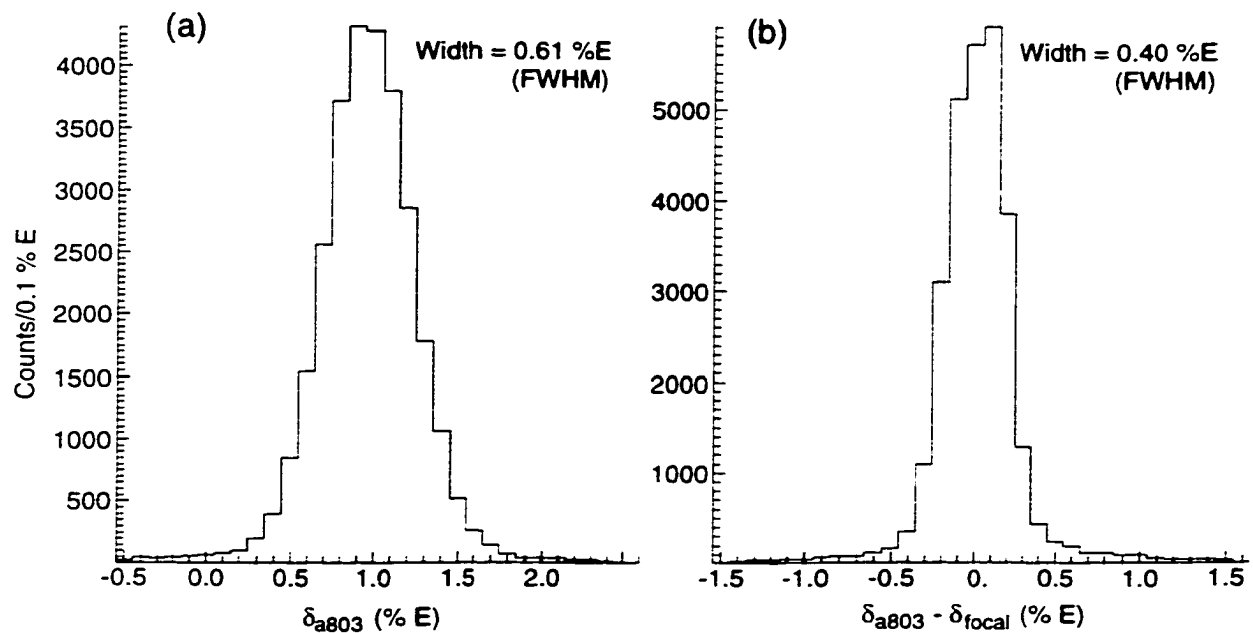


Figure 4.7. Distribution of (a) $\delta_{a_{803}}$ and (b) $\delta_{a_{803}} - \delta_E$ for the 1/4% momentum run.

how different initial positions at the PPAC affected a_{803} . This is illustrated in Figure 4.8 which shows a ray tracing diagram for three sets of rays, spaced at 3 mm intervals about the center of the PPAC. Each set of rays consisted of three rays with different momenta having the same values used in the initial calculation shown in Fig. 4.5. At the intermediate image chamber, those rays which had the same initial momentum are now coming at slightly different angles due to the fact that they came from different initial positions at the PPAC. The $(a|x)$ coefficient in the transfer map gave the relationship between PPAC x and a_{803} as 2.9 mr/mm. Based on the transfer map, it was thought that the measured x position of the beam at the PPAC would provide a way to improve the measurement of the incident energy of the beam by correcting for the effects of the initial position of the particle at the PPAC on a_{803} . However, as shown in Figure 4.9, no correlation was evident between a_{803} PPAC x for the direct beam. A potential reason that no apparent correlation

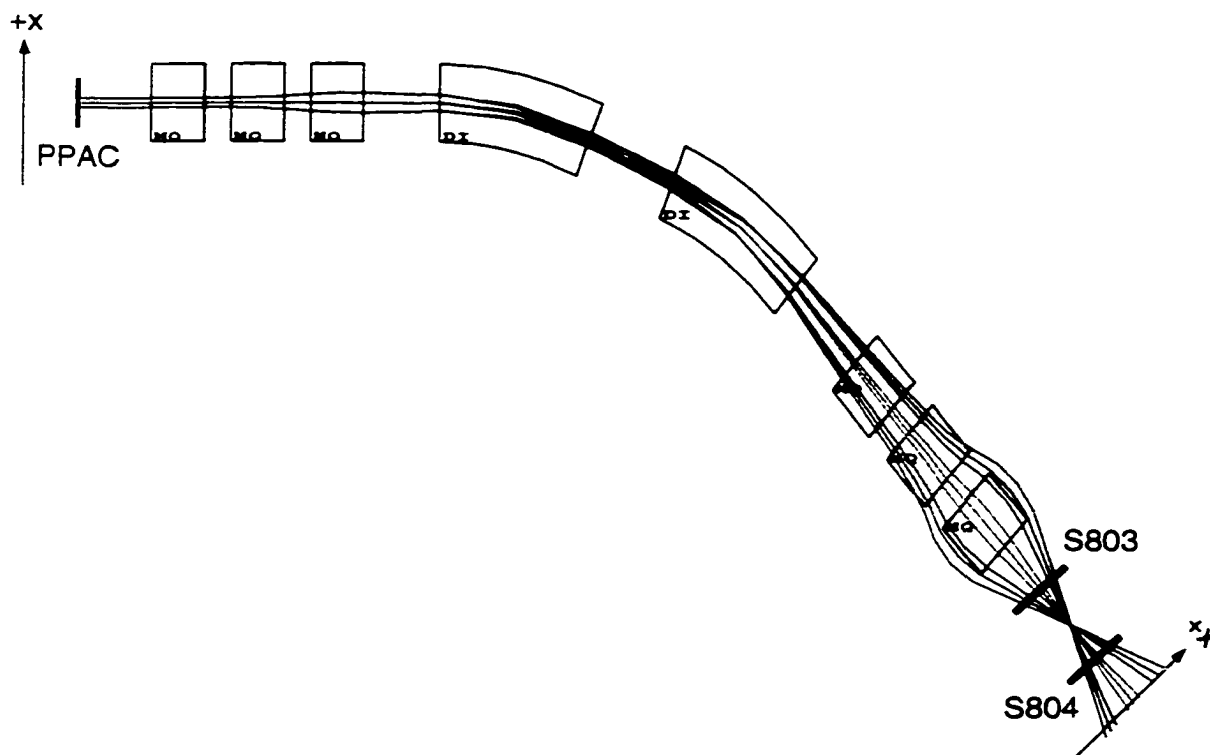


Figure 4.8. Ray trace diagram of the S800 Analysis line from the PPAC to S804 for a series of rays spaced 3 mm apart about the center of the PPAC, at different momenta.

is observed between a_{803} and PPAC x is that the beam spot at the PPAC is quite narrow in the x direction, having a measured width of 2.6 mm (FWHM). This narrow spread in the initial position would correspond to an approximate ± 4 mr spread in a_{803} based on the $(a|x)$ coefficient in the transfer map. This spread in a_{803} could very well be too small for S803 and S804 to resolve. Since a_{803} showed no dependence on the position at the PPAC, the information from the PPAC could not be used to improve the resolution of the initial energy of the beam, and hence was not useful in the analysis of this experiment.

While the magnetic fields within the spectrograph did change between the direct beam runs and the ${}^9\text{Li}(d,p)$ reaction runs (from $B\rho = 1.91953$ T·m for the direct

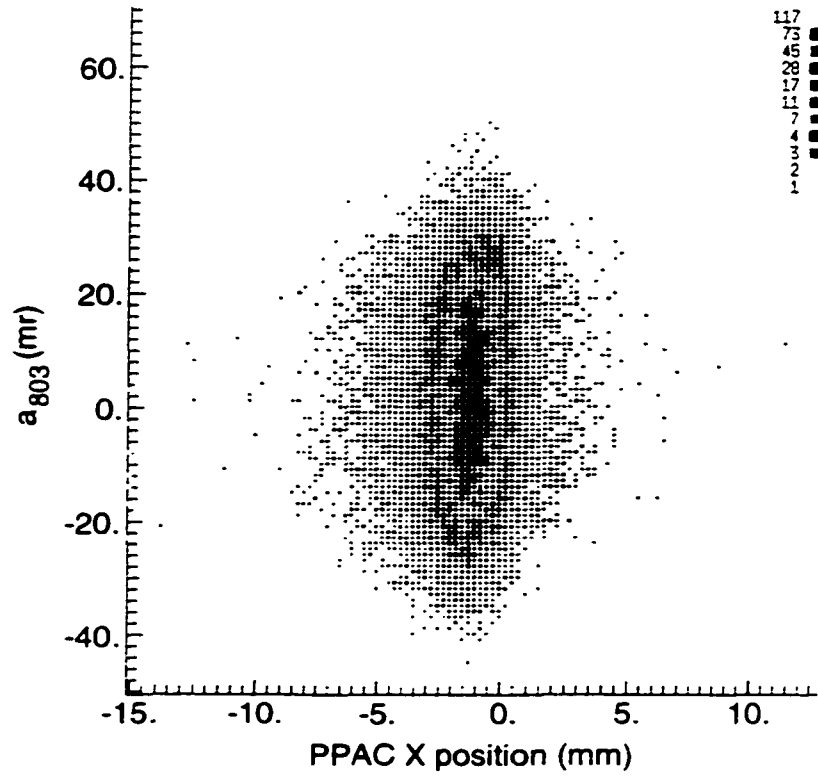


Figure 4.9. Plot of a_{803} as a function of PPAC x for Run #8.

beam runs to $B\rho = 1.78395 \text{ T}\cdot\text{m}$ for the reaction runs), the fields within the analysis line remained the same for the entire experiment. Thus, the relationship between a_{803} and the incident energy of the beam was kept at a constant value throughout the experiment.

4.2.3 Analysis line

The position and angle of the incident beam at the target location were reconstructed based on the measurements from S803 and S804 as well as the specifications of those magnets which were downstream of the Intermediate Image Box in the analysis line. Unlike the magnets used within the spectrograph, however, no fringe field data exist for the elements within the analysis line. Without this knowledge, the transfer maps produced using COSY are quite susceptible to error since the calculation must assume ideal magnetic fields within each element of the analysis line. Hence, the transfer map produced by COSY was only used as a starting point for describing the motion within the analysis line. Since the calculated transfer maps for the analysis line were initially suspect, any differences between the target reconstruction from S803 and S804 for the direct beam runs and the reconstruction from the spectrograph would be attributed to problems in the transfer map for the analysis line. In order to correct for these differences at the target, then, changes were made in the coefficients of the transfer map for the analysis line.

The initial COSY calculation was set up based on calculations performed at the NSCL using the beam transport code TRANSPORT [50] to initialize the fields of the analysis line for transporting the ${}^9\text{Li}$ beam onto the target. Unfortunately, the purpose of the initial TRANSPORT calculations was to predict what fields within the analysis line would optimize the beam spot size at the target position for a 1.6 GeV proton beam. Once these initial fields were established for the 1.6 GeV proton

beam. it was assumed that simply scaling the magnetic fields based on the ratio in magnetic rigidities between the beam of interest and the 1.6 GeV proton beam would suffice in getting the beam on target. Hence. no further calculations have been done to determine what the actual motion for a given beam is as it progresses through the analysis line. While ideally the properties of the beam line should remain the same when scaling the magnetic fields in this manner, this is often not the case in practice. However since no other calculations were available for the analysis line, the NSCL TRANSPORT calculations were used as the template for the initial COSY calculations used in this experiment.

The initially reconstructed incident beam at the target using the 2nd order forward transfer map from COSY (referred to as the forward reconstruction) showed a number of discrepancies with the reconstruction performed using the inverse map with information taken from the spectrograph (referred to as the inverse reconstruction) for the direct beam runs, including the hole target run. A sample of these discrepancies is shown in Figure 4.10(b) in which the forward reconstructed y position for the 'hole target' run (black histogram) has a much larger width than the inverse reconstructed y position (purple histogram). Since it is the same beam that is being reconstructed at the target, the differences between the two reconstructions must be due to problems in the forward reconstruction itself. In addition to the differences in position between the forward and inverse reconstructions, large differences in the reconstructed angles were observed as well. Assuming that the inverse transfer map for the spectrograph was much more accurate in describing the motion of the direct beam than the analysis line map, the discrepancies between the two target reconstructions indicated that a fair number of the coefficients in the forward transfer map needed to be adjusted.

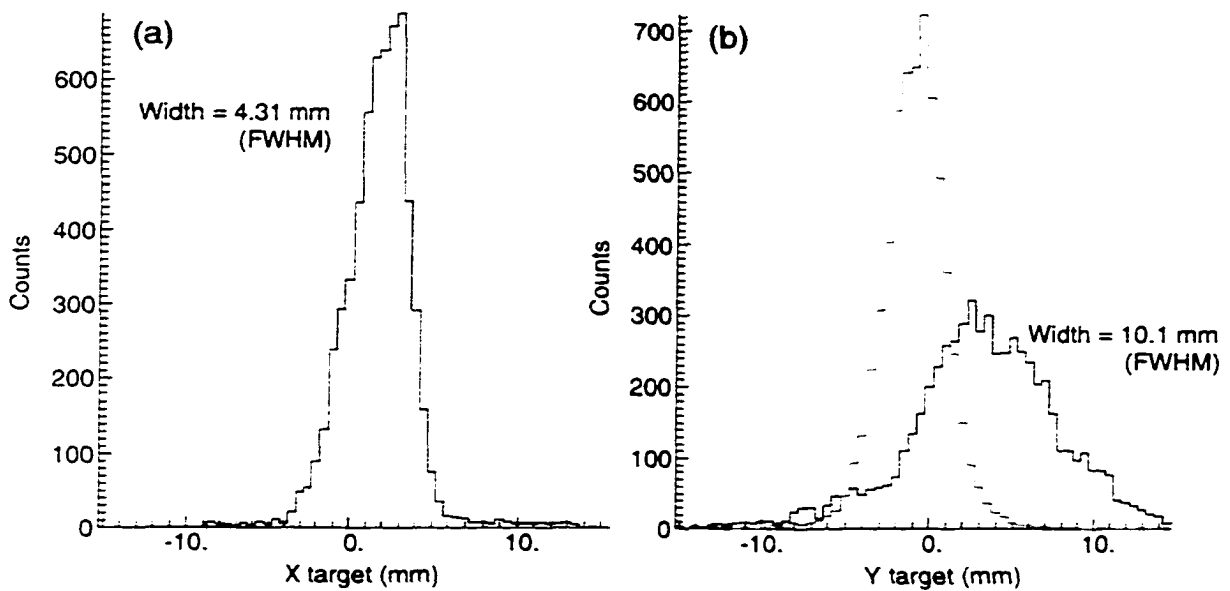


Figure 4.10. (a) Distribution of the initially reconstructed x position at the target for the hole target run using the COSY transfer map for the 'hole target' run. (b) Distribution of the reconstructed y position at the target using the COSY transfer map for the 'hole target' run. The black histogram is the forward reconstruction using information from S803 and S804 while the purple histogram is inverse reconstruction from Figure 4.4.

In order to properly understand how the analysis line transfer map needed to be modified, each of the dependencies of the target parameters on the initial parameters at S803 and S804 were investigated. Any adjustments which needed to be made to the analysis line transfer map were applied to the coefficients themselves based on the discrepancies seen between the forward and inverse reconstructed target parameters. To help make these adjustments, the differences between the forward reconstructed parameters and the inverse reconstructed parameters at the target position were calculated on an event by event basis. These difference functions for the reconstructed parameters were then plotted as a function of all of the initial parameters measured at S803 and S804. The presence of a correlation in a given plot between the difference distribution and the initial parameters indicated that the

coefficient which describes the relationship between that particular initial coordinate and the target coordinate was incorrect.

For example, the difference function for y at the target, Δy_{target} was defined as:

$$\Delta y_{target} = y_{target,f} - y_{target,i} \quad (4.13)$$

where $y_{target,f}$ is the reconstructed y position using the analysis line and $y_{target,i}$ is the reconstructed y position using the spectrograph. To determine which of the coefficients relating $y_{target,f}$ to the initial S803 and S804 parameters were suspect, Δy_{target} was plotted as a function of all of the initially measured parameters at S803 and S804 to look for correlations. In Figures 4.11(a) and (b) Δy_{target} is plotted as a function of y_{803} and b_{803} , respectively, for the ‘hole target’ run. In Fig. 4.11(a), a positive correlation is evident in the plot, indicating that the particles which were further away from the central axis at y_{803} were systematically transformed into having a larger y_{target} than is reconstructed by the spectrograph. The implication of this is that the $(y|y)$ term in the forward transfer map is too large. A similar situation is seen in Fig. 4.11(b) in which a strong negative correlation is present indicating that the $(y|b)$ term did not accurately reflect the data.

To determine how much to adjust a given coefficient in the transfer map, the slopes for the difference functions as a function of the initial S803 and S804 parameters for the various direct beam runs were determined by performing linear weighted fits on the various distributions. Assuming that a consistent correlation between two parameters was seen throughout the experiment, the average slope for a given distribution was then determined and used as the amount to adjust the particular coefficient in question. In the case where more than one initial parameter showed a correlation with a particular difference function, as is the case in Fig. 4.11 with both y_{803} and b_{803} showing a correlation with Δy_{target} , a change in one coefficient could drastically change the correlation between the difference functions and

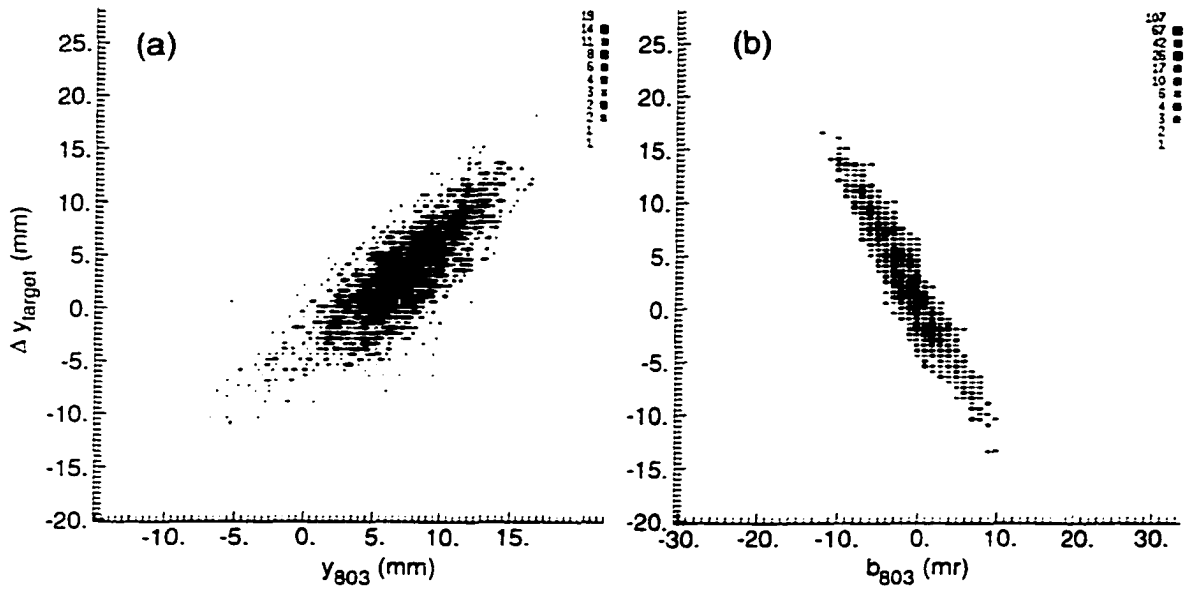


Figure 4.11. Plot of the difference between reconstructed y positions at the target (Δy_{target}) as a function of (a) y_{803} and (b) b_{803} .

the other initial parameters. Hence the coefficients in the forward map were altered one at a time to determine the effects of such a change on the other dependencies. In the case of Δy_{target} shown in Fig. 4.11, the $(y|b)$ coefficient was adjusted first based on the fact that the observed correlation between the difference function and b_{803} appeared to be much stronger than the correlation with y_{803} . The effect of this change in the $(y|b)$ coefficient in the transfer map is shown in Figure 4.12(b) where the resulting Δy_{target} is plotted as a function of b_{803} (top row) and y_{803} (bottom row), respectively. As seen when comparing Fig. 4.12(b) with Fig. 4.12(a), which shows the original data from Fig. 4.11, the slope of Δy_{target} as a function of b_{803} is essentially zero while the dependency of Δy_{target} on y_{803} has been greatly reduced. Taking the correction term for the $(y|y)$ coefficient from this new slope of Δy_{target} as a function y_{803} from Fig. 4.12(b), and applying the resulting $(y|y)$ coefficient along with the corrected $(y|b)$ coefficient in the transfer map resulted in Fig. 4.12(c) which

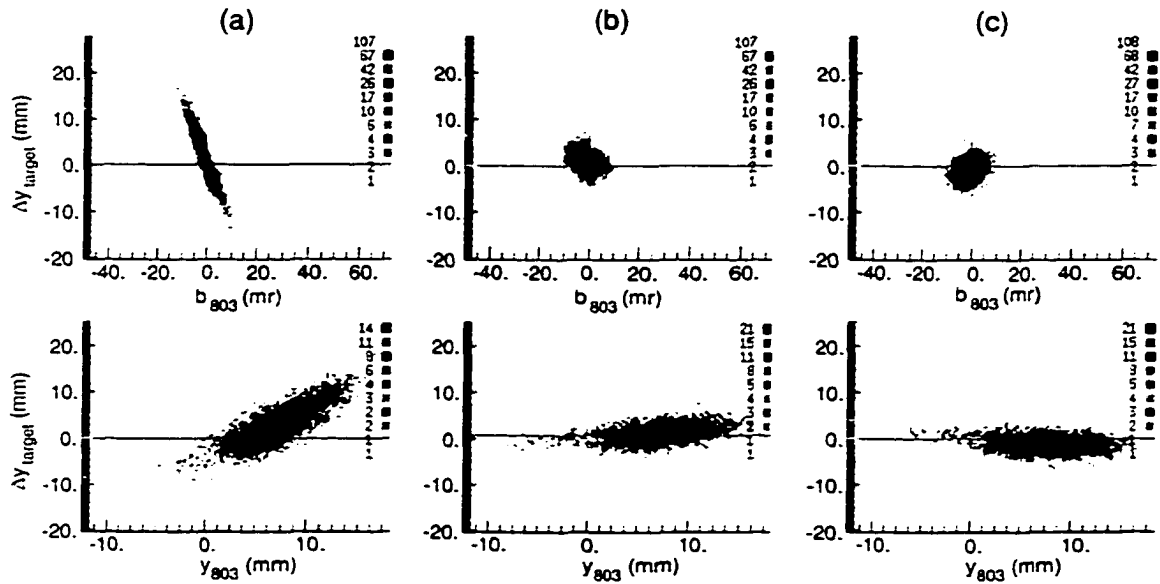


Figure 4.12. Plot of the difference between reconstructed y positions at the target (Δy_{target}) as a function of b_{803} (top row) and y_{803} (bottom row) for the (a) initial transfer map elements, (b) final $(y|b)$ element but initial $(y|y)$ element, and (c) final $(y|b)$ and $(y|y)$ elements included in the transfer map. The horizontal line indicates no correlation between the two parameters.

shows that Δy_{target} is no longer correlated with either y_{803} or b_{803} . This iterative process ended once all of the dependencies had been removed between the difference functions and the initial parameters in the reconstruction, and thus the correct transfer map had presumably been determined.

In Table 4.2 the coefficients which were altered to produce the final transfer map are shown along with the original transfer map coefficients from COSY. The biggest difference between the two sets of coefficients occurred in the y_{target} direction where the $(y|y)$ and the $(y|b)$ coefficients were drastically changed. An additional coefficient was also added to compensate for dependencies of y_{target} on a_{803} seen in the data that were not accounted for in the initial transfer map. This cross term, along with the $(a|y)$ term that was added, indicate that the central motion of the

Table 4.2. Altered first order transfer map elements for the analysis line.

Map Element (final initial)	Calc (COSY)	Data	% Difference
$(x a)^a$	-0.51801	-0.66375	28.14
$(a x)^b$	1.93418	1.87820	2.89
$(a a)^c$	0.59888	0.65673	9.66
$(a y)^b$	-	0.15007	-
$(y a)^a$	-	0.04400	-
$(y y)^d$	-0.00309	-0.31787	10.000.
$(y b)^a$	-1.25468	-0.11982	90.45
$(b y)^b$	0.79706	0.57360	27.70

^a (mm/mr)

^b (mr/mm)

^c (mr/mr)

^d (mm/mm)

beam may not have coincided with the center of the magnets in the analysis line. However, the cross term coefficients are quite small indicating that the possible offset in the beam is small as well. A potential source of concern in the changes made to the transfer map is the huge variation in the amount the initial coefficients were adjusted in order to match the data. As seen in the table, the amount of relative change to the initial coefficients range from just under 3% to 100 times their initial values. This issue will be dealt with in the next section of this chapter.

With the correct transfer map determined for the analysis line, the position resolution of the forward reconstruction was deduced based on the reconstructed target position for the 'hole target' run. Figures 4.13(a) and (b) show the forward reconstructed x_{target} and y_{target} distributions for the 'hole target' runs, respectively. In the case of x_{target} , the width of the reconstructed position was 1.31 mm which is slightly smaller than the known diameter of the 'hole target' of 1.59 mm. In this case, the width of the reconstructed peak for the 'hole target' run was assumed to correspond with the resolution of the reconstruction. In the case of y_{target} , the reso-

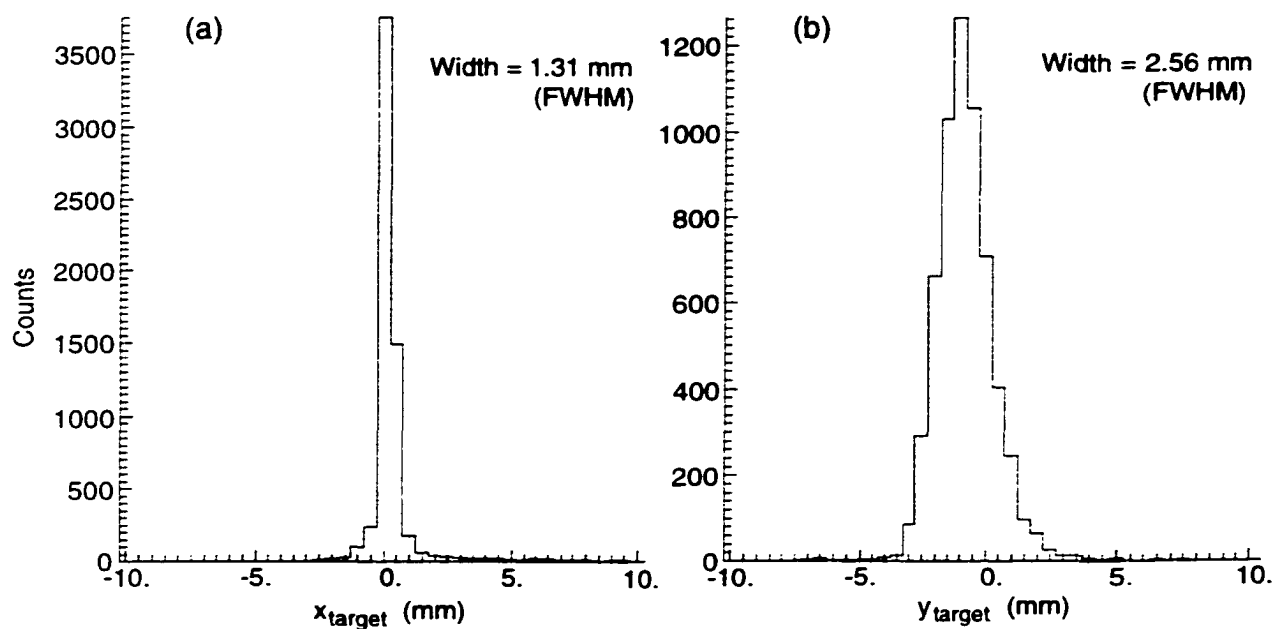


Figure 4.13. (a) Reconstructed x_{target} distribution using the corrected forward map for the ‘hole target’ run. (b) Reconstructed y_{target} distribution for the ‘hole target’ run.

lution of the reconstructed target position was determined to be 2.0 mm (FWHM) based on the measured width of the distribution of 2.56 mm (FWHM).

As a check to see if the reconstruction resolutions of the forward and inverse target positions are accurate, the width of the difference function between the forward and inverse reconstructed y position was measured for the ‘hole target’. In principle, the width of Δy_{target} should be the sum of the resolutions of the two reconstructed target positions added in quadrature, which would be 4.38 mm (FWHM). The final Δy_{target} distributions for the ‘hole target’ is shown in Figure 4.14(b), with a width of 4.48 mm (FWHM), which matches the value attained when adding the two resolutions in quadrature with one another.

While the questions concerning position and energy resolutions at the target were dealt with in a relatively straightforward manner, the question of angular resolution

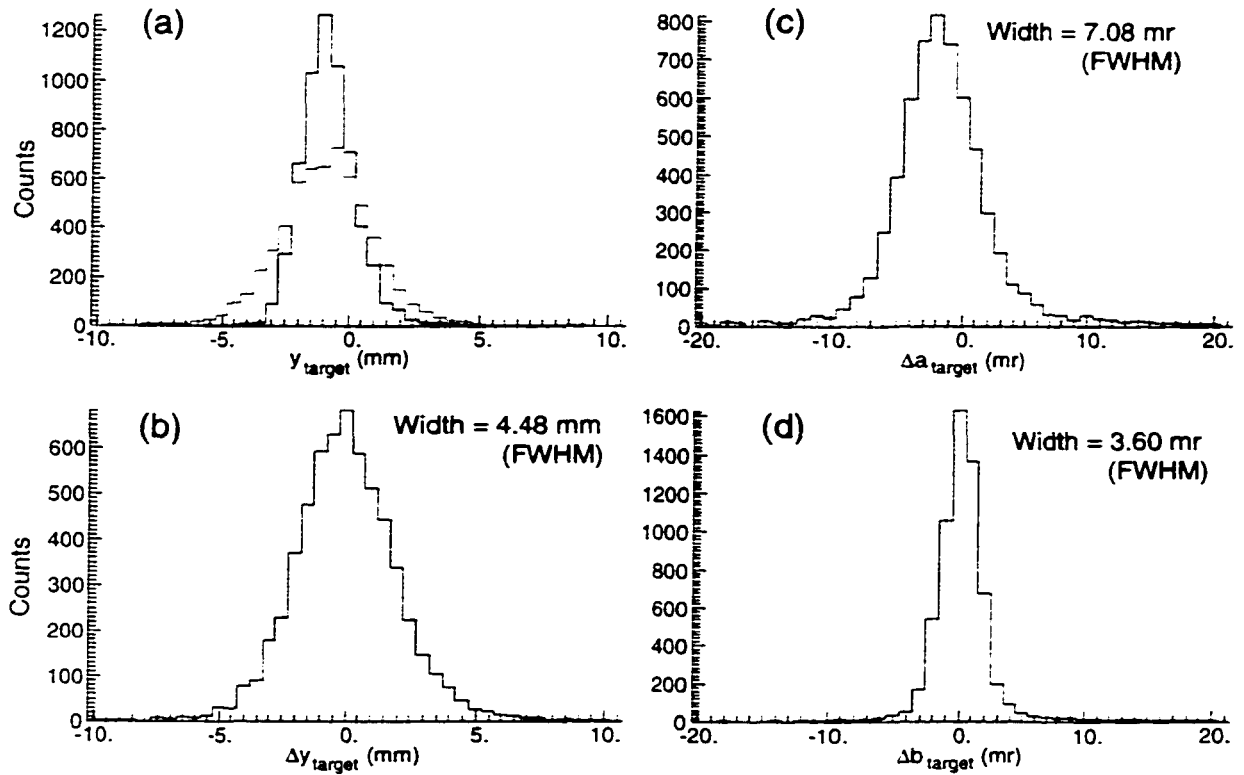


Figure 4.14. (a) Reconstructed y_{target} distribution using the corrected forward map (black histogram) and the inverse transfer map (purple histogram) for the ‘hole target’ run. (b) Δy_{target} distribution for the hole target run. (c) Δa_{target} distribution and (d) Δb_{target} distribution for the ‘hole target’ run.

becomes a bit more difficult due to the fact that no direct beam run was done where the angles entering and exiting the target were well defined. While the ‘hole target’ was able to restrict the physical spot size of the beam at the target, it could not be used to determine the angular resolution since it did not restrict the angular divergence of the beam. Since the width of Δy_{target} matched what was expected from the resolutions of the individual measurements so well, the widths of Δa_{target} and Δb_{target} , which are plotted for the ‘hole target’ run in Figs. 4.14 (c) and (d), respectively, were used to estimate the total uncertainty for the individual angle measurements at the target. The average width for Δa_{target} and Δb_{target} for the direct beam data is 8.31 mr and 3.68 mr, respectively (FWHM). Translating these widths into an uncertainty in θ using Equation 4.4, we find $\delta\theta = 9.1mr$ (0.51°) (FWHM).

4.2.4 Testing the transfer maps

As a final test to confirm that the transfer map used for the analysis line and the COSY generated maps used for the spectrograph were accurate and consistent with one another, a test was performed using data from a direct beam run to see if the information from S803 and S804 could be reconstructed up to the focal plane of the S800. This reconstruction would be performed in two steps. In the first step, the information from S803 and S804 would be reconstructed at the target using the adjusted analysis line transfer map. The forward reconstructed target parameters, along with the measured incident energy, δ_{a803} , would then be reconstructed up to the focal plane using the forward spectrograph transfer map produced by COSY. In this two step reconstruction process, measured information from S803 and S804 for a direct beam run could then be directly compared with what was measured at S801 and S802. The assumption then is that if the reconstructed beam at S801 and

S802 produces the correct position and size of the beam in the focal plane as well as the correct angular divergence. then the reconstructed positions and angles at the target must be accurate.

To put further constraints on this test, the direct beam data that was used in this test had the calibration masks for S803 and S804 in the path of the beam. thus providing an object to image at the focal plane of the spectrograph. By having a distinct image of the beam in the focal plane, the comparison between the reconstructed positions and angles at S801 and S802 with what was measured in those detectors was easier to do. Furthermore, this allowed for the tracking of specific rays from S803 to the focal plane since the two masks physically allow only specific position and angle combinations at S803 and S804. In Figure 4.15, the two dimensional profiles of the beam at the focal plane is shown in terms of the measured (a) angles and (b) positions for this direct beam run, while the reconstructed angular and position profiles are shown in Figs. 4.15(c) and (d), respectively. Both the reconstructed angles and positions of the beam in the focal plane appear to be in good agreement with what was measured in the focal plane. One noticeable difference between what was measured and what was reconstructed is that the data appear to have less of the detailed structure that is evident in the reconstruction. This is most likely due to aberrations in the spectrograph or the analysis line which are not being accounted for in either of the two transfer maps. However, this effect appears to be minor.

To quantify how close the focal plane reconstruction is to the measured data, the differences between the reconstructed and measured parameters in the focal plane were measured for this run, and are shown in Figure 4.16. At first glance, it would appear that the reconstruction does a poor job in reconstructing the x position in the focal plane based on the measured width of 15.6 mm in the difference function.

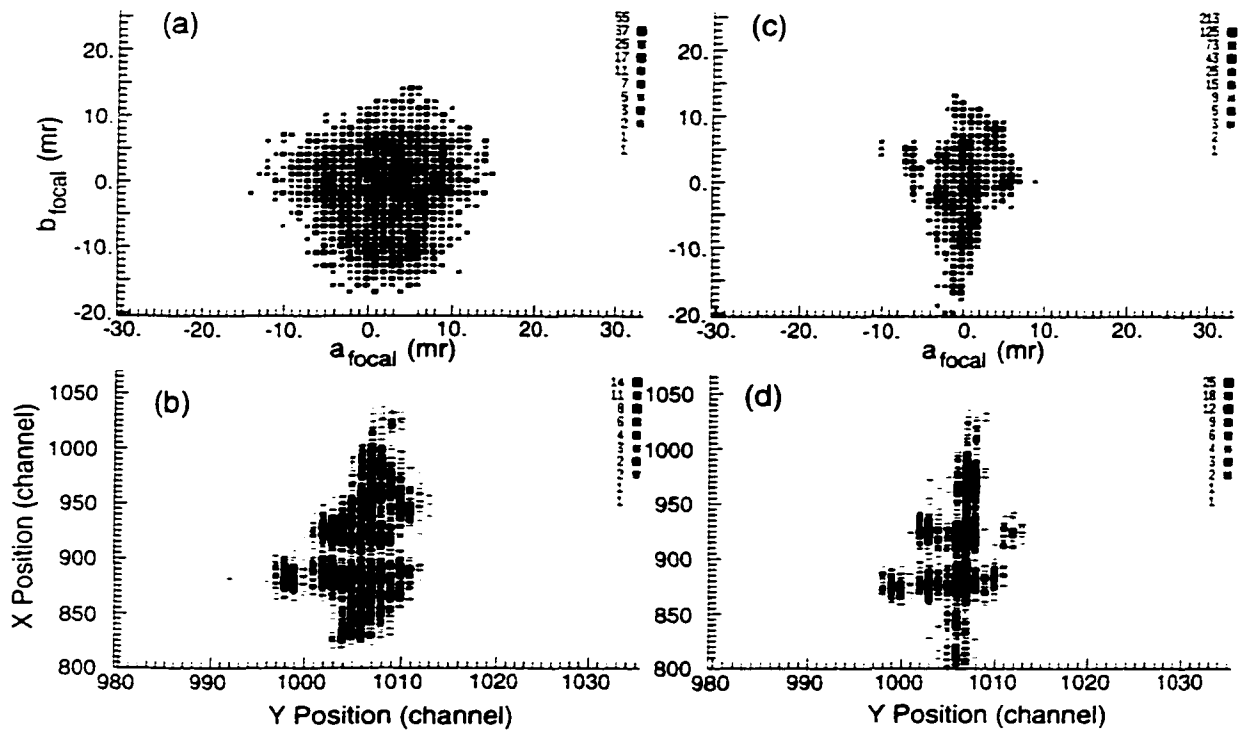


Figure 4.15. (a) Plot of b_{focal} vs a_{focal} as measured in the focal plane for Run # 51. (b) Plot of x_{focal} vs y_{focal} as measured in the focal plane for Run # 51. (c) Plot of the reconstructed b_{focal} vs a_{focal} . (d) Plot of the reconstructed x_{focal} vs y_{focal} .

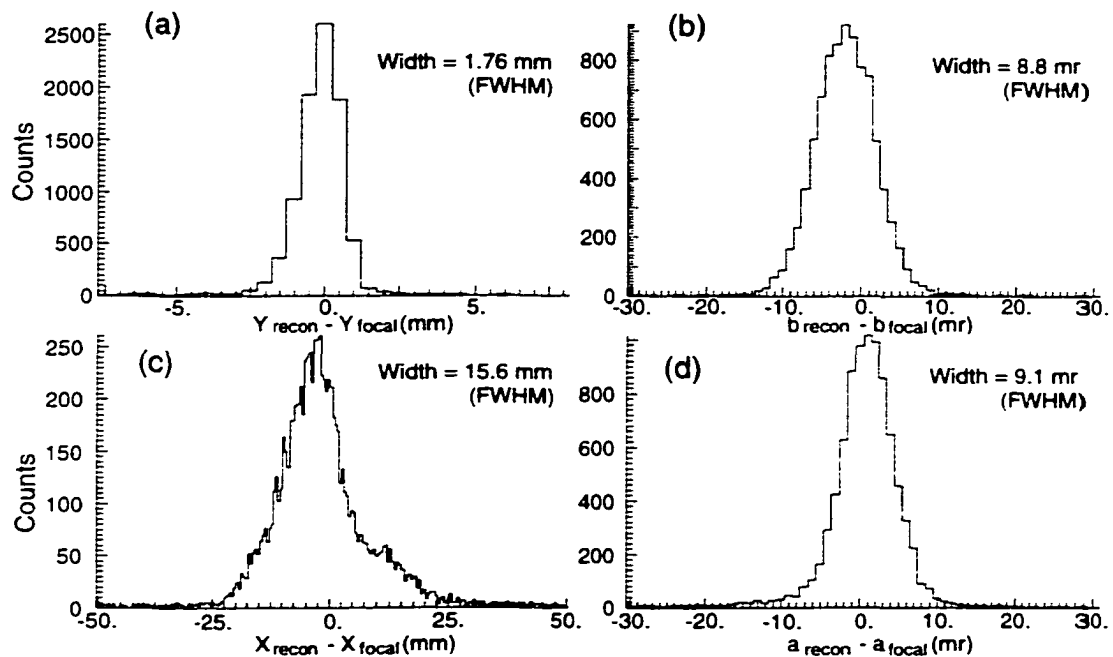


Figure 4.16. Difference distributions between reconstructed and measured parameters in the focal plane.

However, if one translates that width from a position uncertainty into an energy uncertainty based on the predicted energy dispersion from the COSY transfer map for the spectrograph of $(x|\delta_E) = 47.99 \text{ mm}/\%E$, then the 15.8 mm width of the difference function corresponds to a 0.33% uncertainty in energy (FWHM). This of course is primarily due to the (measured) uncertainty in the incident energy which is known to be of that order of magnitude.

4.2.5 $^{13}\text{C}(d,p)^{14}\text{C}$ Reaction

While the various tracking detectors in the analysis line and the spectrograph could be tested using direct beam runs, the coordination of the silicon detectors with the spectrograph could only be tested by performing an experiment using a well known (d,p) reaction in inverse kinematics in order to produce a particle stable

outgoing nucleus in coincidence with a proton at backward angles. The fact that the outgoing nucleus from the (d,p) reaction is detected directly by the spectrograph in this case implies that the measured energies and angles from the spectrograph can be directly related to the measured energies and angles of the protons from the various silicon detectors in the target chamber. Since the results of the reaction are known, discrepancies between the two detector systems can be identified and possibly corrected based on the results of this experiment.

To this end, a measurement of the $^{13}\text{C}(\text{d},\text{p})^{14}\text{C}$ reaction was performed to test the entire experimental method in detecting events from a (d,p) reaction in inverse kinematics. The structure of ^{14}C , shown in Figure 4.17, is well known and has a 6.094 MeV separation between the ground state and 1st excited state [51]. This large separation between the ground state and 1st excited state provides an unambiguous signature in identifying the protons from the $^{13}\text{C}(\text{d},\text{p})$ reaction in the silicon detectors. In addition, this larger separation in energy provides a way to check that the Q-value of the (d,p) reaction is being determined properly using the measured proton angles and energies from the silicon detectors.

In this test experiment, the ^{13}C beam that was used as a primary beam in the $^9\text{Li}(\text{d},\text{p})$ experiment was transported directly to the S800 target chamber via the A1200 fragment separator. While passing through the A1200, the beam was reduced in energy from the initial 30 MeV/nucleon as produced by the K1200 cyclotron down to an energy of 20.5 MeV/nucleon by passing the beam through a 202 mg/cm² ^9Be target at the entrance of the A1200 as well as a 233 mg/cm² Al wedge in the middle chamber of the A1200. The beam energy was reduced in this manner so that the kinematics of the protons in this reaction would closely match the kinematics of the protons in the $^9\text{Li}(\text{d},\text{p})$ reaction. The beam intensity for the ^{13}C beam was much higher than it was for the ^9Li beam. As a result of the higher beam intensities of

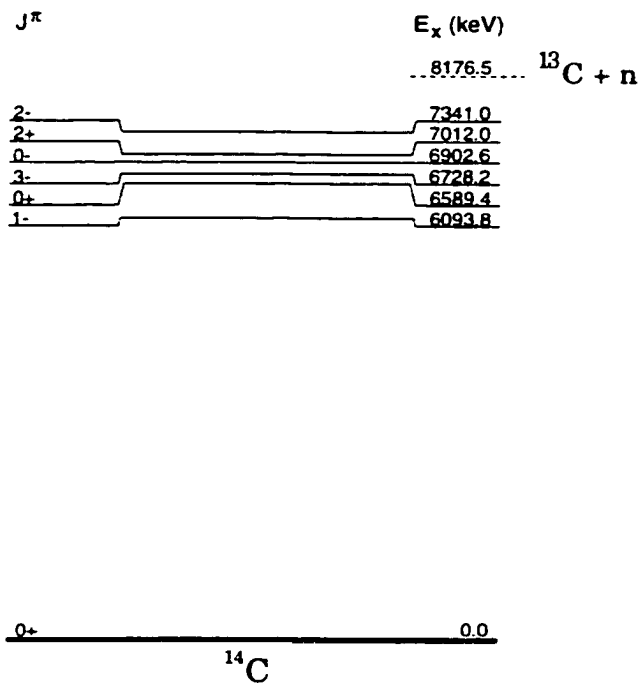


Figure 4.17. Level diagram for ^{14}C .

the ^{13}C beam, a 1/2% momentum spread was chosen instead of the 1% momentum spread that was used for the ^9Li beam. This reduction in the momentum spread of the beam was done in order to improve the resolution of the setup in measuring the various states in the (d,p) reaction. Due to difficulties with S803 and S804 at the time when this test experiment was performed, neither detector was used during the $^{13}\text{C}(d,p)$ experiment. Hence, it was not possible to measure the incident energy of the beam on an event by event basis nor track the beam onto the target.

As was done in the $^9\text{Li}(d,p)$ experiment, two different spectrograph settings were used for the direct ^{13}C beam and the outgoing ^{14}C nucleus. Both of the spectrograph settings used in this case ($B\rho = 1.4219 \text{ T}\cdot\text{m}$ for the direct ^{13}C beam measurement and $B\rho = 1.4769 \text{ T}\cdot\text{m}$ for the outgoing ^{14}C measurement) were lower in field strength than the settings used to study the $^9\text{Li}(d,p)$ reaction. Hence, new inverse COSY maps

were generated in order to reconstruct the outgoing ^{14}C angle and energy. Since the spectrograph setting for the outgoing ^{14}C nucleus did not allow the direct ^{13}C beam up into the focal plane, the direct ^{13}C beam was measured by the spectrograph at a lower field setting and the central incident energy was determined to be 267.32 MeV.

The $^{13}\text{C}(\text{d},\text{p})$ experiment was run for approximately 6 hours with an incident beam rate of approximately 70,000 particles/second on the target. The CD_2 target used in this test experiment was the same as the one used in the $^9\text{Li}(\text{d},\text{p})$ experiment. In Figures 4.18(a) and (b), the ΔE vs E plots for the direct ^{13}C beam and the reaction products are presented, respectively, with the cross in Fig. 4.18(b) indicating the location of the direct beam relative to the various particle groups seen in the focal plane. With the settings of the Ion Chamber and the E1 scintillator remaining constant for both the direct beam runs and the reaction runs, the location of the ^{13}C in the ΔE - E plot was the same for the two different sets of runs. Since ^{14}C is more massive than ^{13}C , it would appear as a group with a slightly larger ΔE signal than ^{13}C due to it losing more energy in the Ion Chamber than the lighter direct beam. While there would be no way of clearly identifying ^{14}C from Fig. 4.18(b), the group does become evident by simply requiring a coincidence between a silicon detector and the spectrograph as shown in Fig. 4.18(c). Specifically, a coincidence event was an event in which the E1 scintillator fired along with both sides of a silicon detector (a ring and a sector for a CD detector or a strip and the back for a strip detector). A total of 754 coincidence events were detected over the duration of this test experiment.

To confirm that the ^{14}C ions detected in the focal plane were produced via the (d,p) reaction, kinematic plots were produced for the events of interest in order to determine if these events had the correct correlations between the various energies

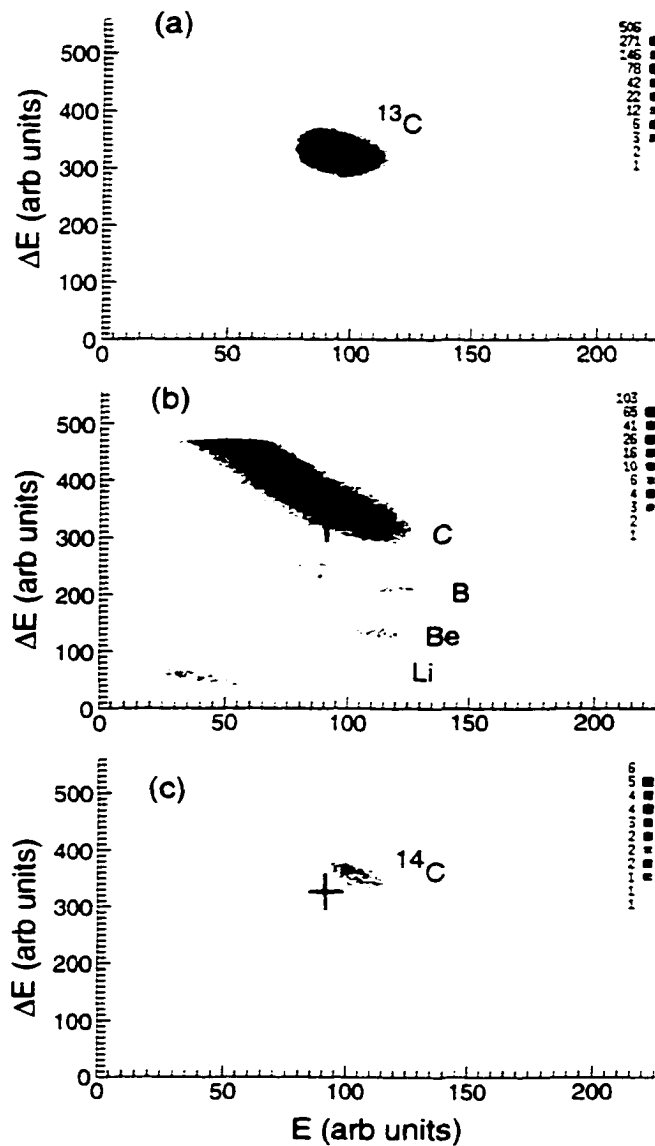


Figure 4.18. (a) Plot of ΔE vs E from the focal plane for the direct ^{13}C beam. (b) Plot of ΔE vs E for the reaction products from the $^{13}\text{C}(d,p)^{14}\text{C}$ reaction. (c) Plot of ΔE vs E for reaction events in coincidence with the silicon detector array. The cross in (b) and (c) indicates the location of the direct ^{13}C beam for reference.

and angles of the particles. Figure 4.19(a) shows a plot of the energy measured in the spectrograph as a function of the entering angle into the spectrograph for ^{14}C , while Fig. 4.19(b) shows the energy vs angle plot for the corresponding protons which were in coincidence with the ^{14}C . As seen in both (a) and (b), two distinct groups are visible. These two groups have the appropriate relationship between their energies and angles to correspond to the population of the ground state and excited states of ^{14}C . To confirm this identification, calculations were performed using PKIN to determine what the expected kinematics would be for ^{14}C and the proton produced in the (d,p) reaction for the various states in ^{14}C . The results of these calculations for the ground state and 1st excited state are shown as the solid curves in Fig. 4.19(a) and (b). In each of these calculations, the reaction was assumed to take place at the center of the target with appropriate energy losses considered for the incident ^{13}C nucleus as well as the outgoing ^{14}C and proton. The energy loss calculations were performed using the code STOPX [52]. In the case of the exiting protons, the thickness of the target was varied in the calculation based on the angle at which the proton was produced in the kinematic calculation of the (d,p) reaction. Although the data do not appear to completely agree with the theoretical kinematic curves, the behavior and relative spacing between the two groups in both detector systems provide evidence that the ^{14}C and the proton were produced via the (d,p) reaction.

With the production and detection of $^{13}\text{C}(\text{d,p})$ events confirmed for both the spectrograph and the silicon detectors, the correlation between the two detector systems was checked by plotting information from the spectrograph as a function of the silicon detector measurements. One such plot is presented in Figure 4.20 where the energy of the ^{14}C is shown as a function of the proton angle along with the expected kinematic curves for the population of the ground state and 1st excited state. As seen in Fig. 4.20 there is a good agreement between the data and the

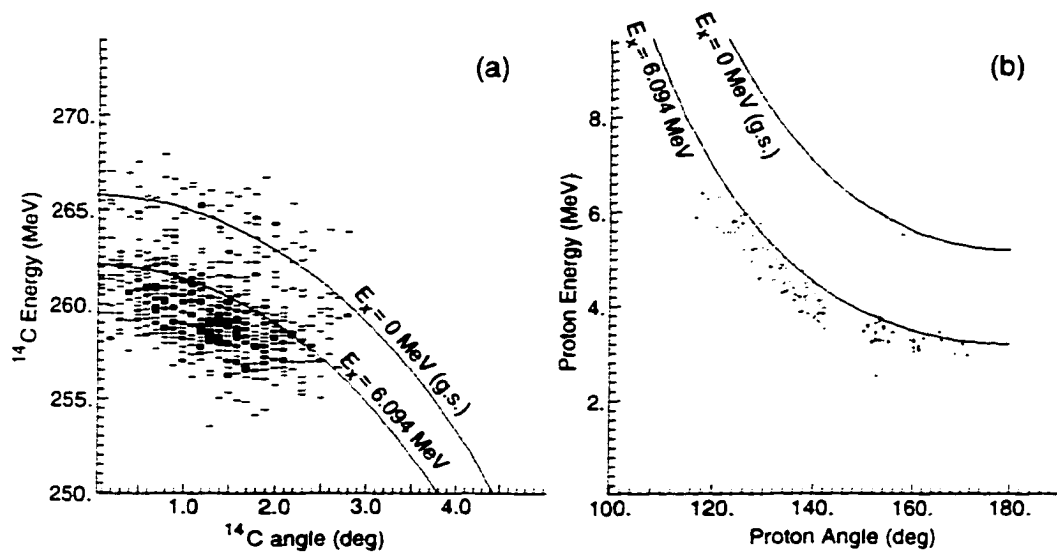


Figure 4.19. (a) Plot of energy vs angle for the ^{14}C events in coincidence with the silicon detectors. (b) Plot of energy vs angle for all of the proton events in coincidence with the focal plane. The solid curves are the calculated kinematics from PKIN for the ground state and 1st excited state ($E_x = 6.093 \text{ MeV}$) of ^{14}C .

predicted kinematics for the (d,p) reaction indicating that the two detector systems were coordinated properly.

However, a discrepancy becomes evident between the focal plane information and the silicon detectors when comparing Fig. 4.19(b) with Fig. 4.20 in that there is evidence for the ground state band in Fig. 4.20 at silicon angles less than 150° in the lab which does not appear in Fig. 4.19(b). Since this angular region was only covered by the silicon strip detectors, the discrepancy between these detectors and the focal plane information indicates that protons with an energy above 6 MeV were not detected properly by the silicon strip detectors. By placing a gate on the ground state band in the two dimensional ^{14}C energy vs angle spectrum (shown in Figure 4.21(a)) and looking at the protons measured in coincidence with the gated focal plane information, it was determined that the protons corresponding to the

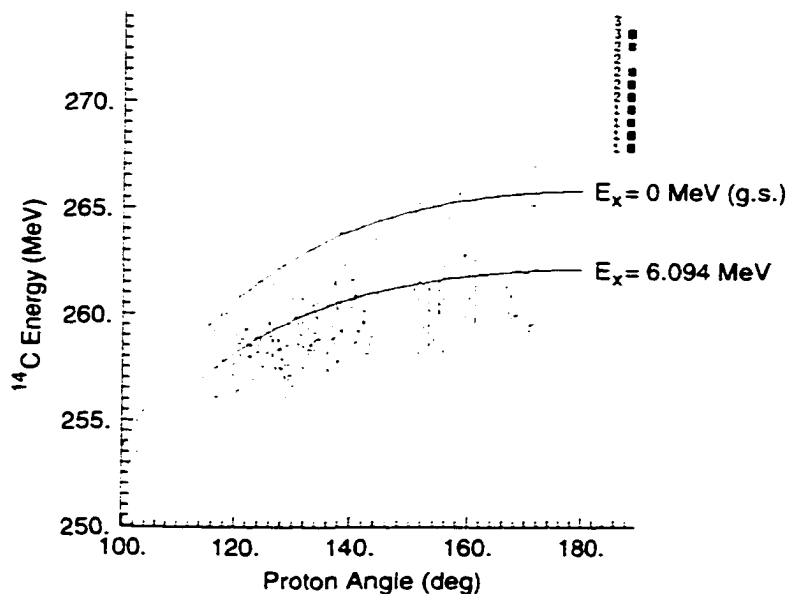


Figure 4.20. Plot of ^{14}C energy vs proton angle for the coincidence events. The solid curves are the calculated kinematics from PKIN for the ground state and 1st excited state in ^{14}C .

ground state of ^{14}C were punching through the silicon strip detectors as is evident in Fig. 4.21(b). Further evidence for this was the fact that the data appeared to agree with the expected punch through curves for the protons from the ground-state (d,p) reaction assuming they were detected either at the center of the strip detector (dashed curve) or at the outer edge of the strip detector (dotted curve). If all of the detectors were at the exact same angle and had the same thickness, all of these events corresponding to the ground state should lie in between the two curves in Fig. 4.21(b). While, in general, the data display the same characteristics as the calculation for the punch through events, the fact that there is some spread in the data indicates possible discrepancies among the strip detectors themselves. This spread in the data indicates that either the energy measurements for at least some of the strip detectors was inaccurate during the experiment, the thickness of

the various detectors was not well known, or that the various strip detectors in the array were covering different angular ranges due to the entire strip array being offset from the beam axis. Due to severe time constraints in performing both this experiment and the real ${}^9\text{Li}(d,p)$ experiment, the strip array as well as the CD detectors were never optically sighted to determine their location relative to the optical axis. Hence, it is quite possible that the detectors were not properly aligned with the optical axis.

To determine if the silicon strip array was offset from the optical axis, separate kinematic plots were made for the protons which corresponded to the excited states of ${}^{14}\text{C}$ for the five strip detectors as shown in Figure 4.22(a). In this figure, the events corresponding to the ground state have been gated out so as to isolate the excited state band and ensure that all of the strip detectors are measuring the same states in ${}^{14}\text{C}$. The solid curve corresponds to the 1st excited state of ${}^{14}\text{C}$ while the dashed curve corresponds to the breakup of ${}^{14}\text{C}$ into ${}^{13}\text{C} + n$. Because of the $B\rho$ setting of the spectrograph, it was not possible to detect the ${}^{13}\text{C}$ from the breakup of ${}^{14}\text{C}$. The dashed curve then is the lower energy limit for the proton events that can be detected in the silicon detectors. A definite discrepancy can be seen in the location of the band of excited states in the plots for the various strip detectors. The only two detectors that appear consistent with one another are Strip #2 and Strip #6, both of which are located at the same relative x-position to the center of the strip array. (Refer to Fig. 3.14 for the location of the various detectors.) It also appears that the location of the excited state band is dependent on the physical location of the strip detectors in the x-direction. This pattern can be more clearly seen in the corresponding Q-value histograms for the various strip detector shown in Fig. 4.22(b). The central Q-value for the excited state band increases as the central x-position of the strip detector decreases. Since the Q-value for the reaction

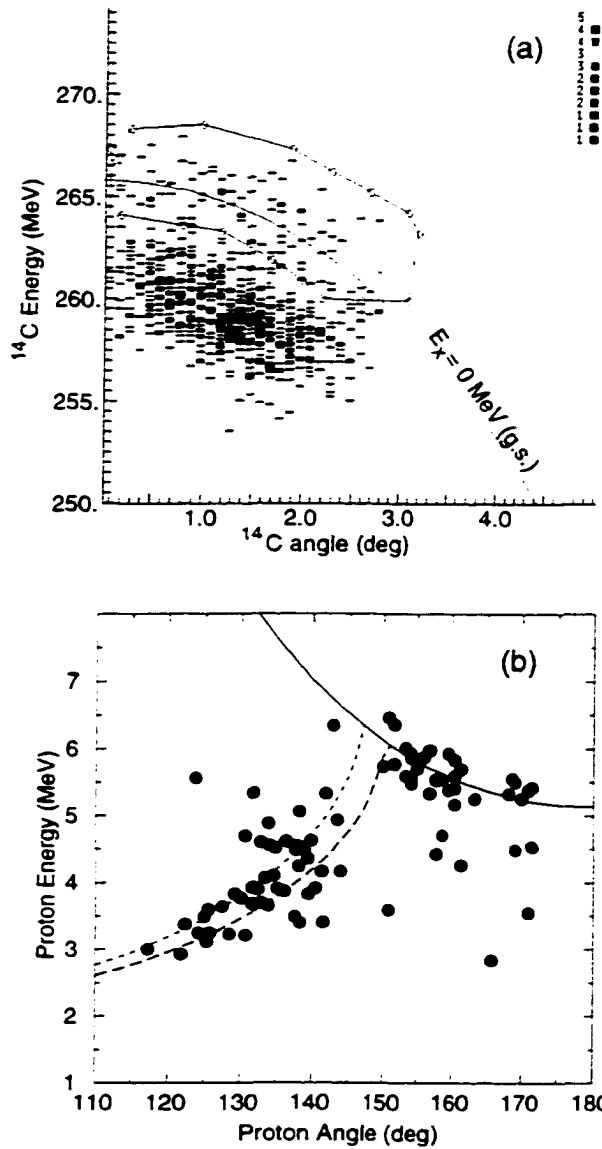


Figure 4.21. (a) Plot of the ^{14}C energy vs angle in the focal plane showing the gate used to identify the ground state band in the silicon detectors. (b) Plot of the proton energy as a function of angle for the gated ground state events in the focal plane. The solid curve represents the ideal kinematics of the proton while the dashed and dotted curve correspond to the expected kinematics for the punch through events assuming the protons passed through the center of the detector or the edge of the detector, respectively.

is independent of the angle at which the reaction occurs, the Q-value as determined by the different strip detectors should be the same since they are detecting the same excited states in ^{14}C . The fact that the Q-value shift is correlated with the physical location of the strip detectors in the array indicates that the array is offset in the x-direction. To correct for this apparent offset, the location of the center of the array was adjusted in the software until the central Q-value for the distribution of excited states was the same for the various strip detectors. The corrected kinematic and Q-value plots are shown in Figures 4.23(a) and (b) respectively. The corresponding x-offset in the array was -11 mm implying that the center of the strip array was below the optical axis. While this offset is a bit large, the fact that such an offset corrects the discrepancies seen in the Q-values from the various strip detectors indicates that it was a real offset.

Since the protons from the ground state punch through the strip detectors, determining the accuracy of Q-value measurements becomes more difficult for these detectors since it is not possible to measure the Q-value for the ground state nor measure the Q-value separation between the ground state and the excited states. However, the data from the protons which punch through the silicon detectors does provide a way to check that the offset in the strip array is necessary by determining if it reduces the spread in the data that was seen in Fig. 4.21(b). Figure 4.24 shows the ground state events for the various strip detectors after the offset was introduced. As seen in the figure, the data are in much better agreement with each other with an offset in place than without it. Since the punch through curve requires the opposite correlation between the energy of the proton and its angle than those protons which were completely stopped in the detector, this implies that the offset is the appropriate correction to make since neither a correction to the energy

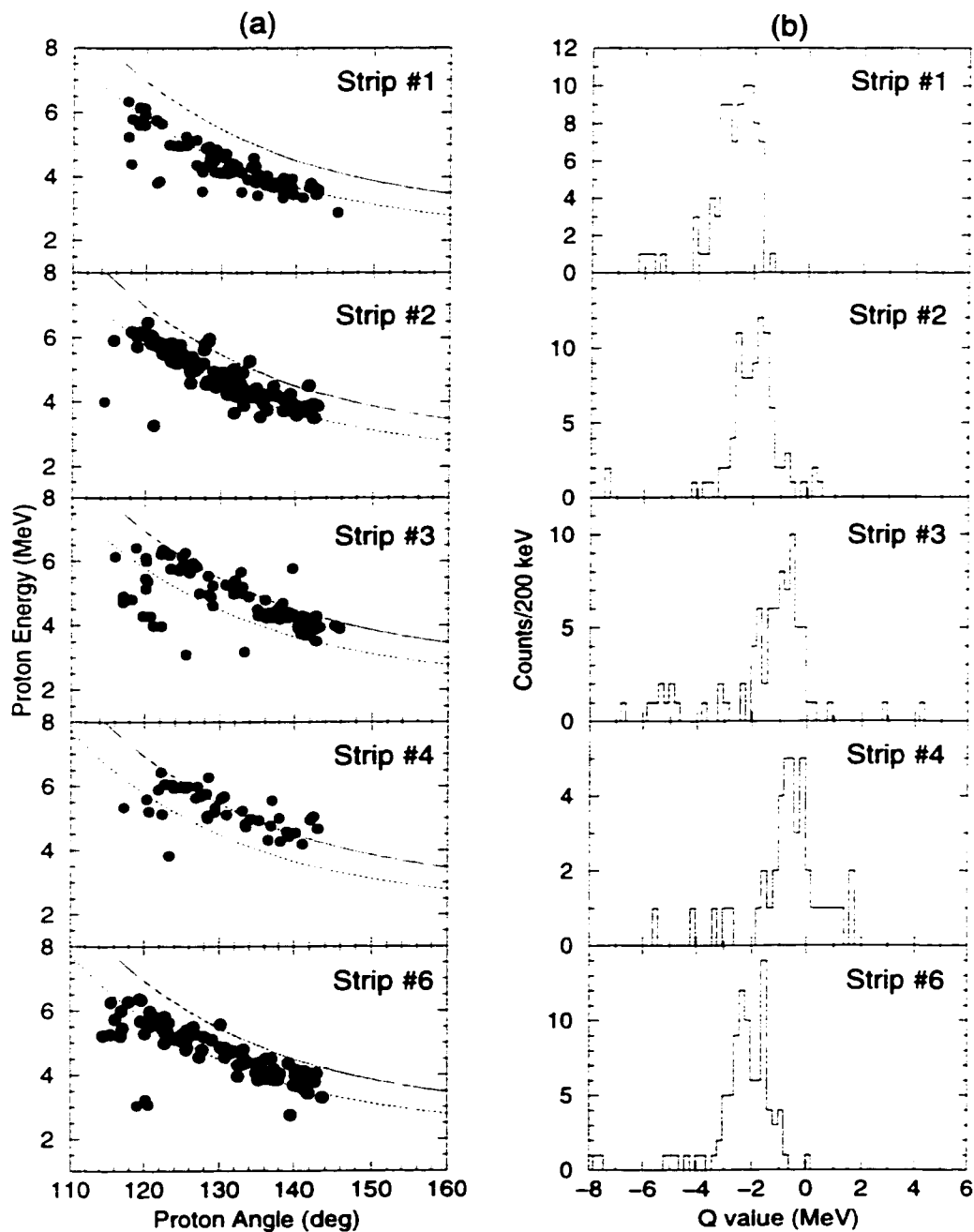


Figure 4.22. (a) Proton kinematic plots for the various strip detectors corresponding to the excited states in ^{14}C . The solid curve in each plot is the expected kinematic curve for the population of the 1st excited state in ^{14}C while the dashed curve corresponds to the threshold for the breakup of ^{14}C . (b) Corresponding Q-value histograms for the various strip detectors.

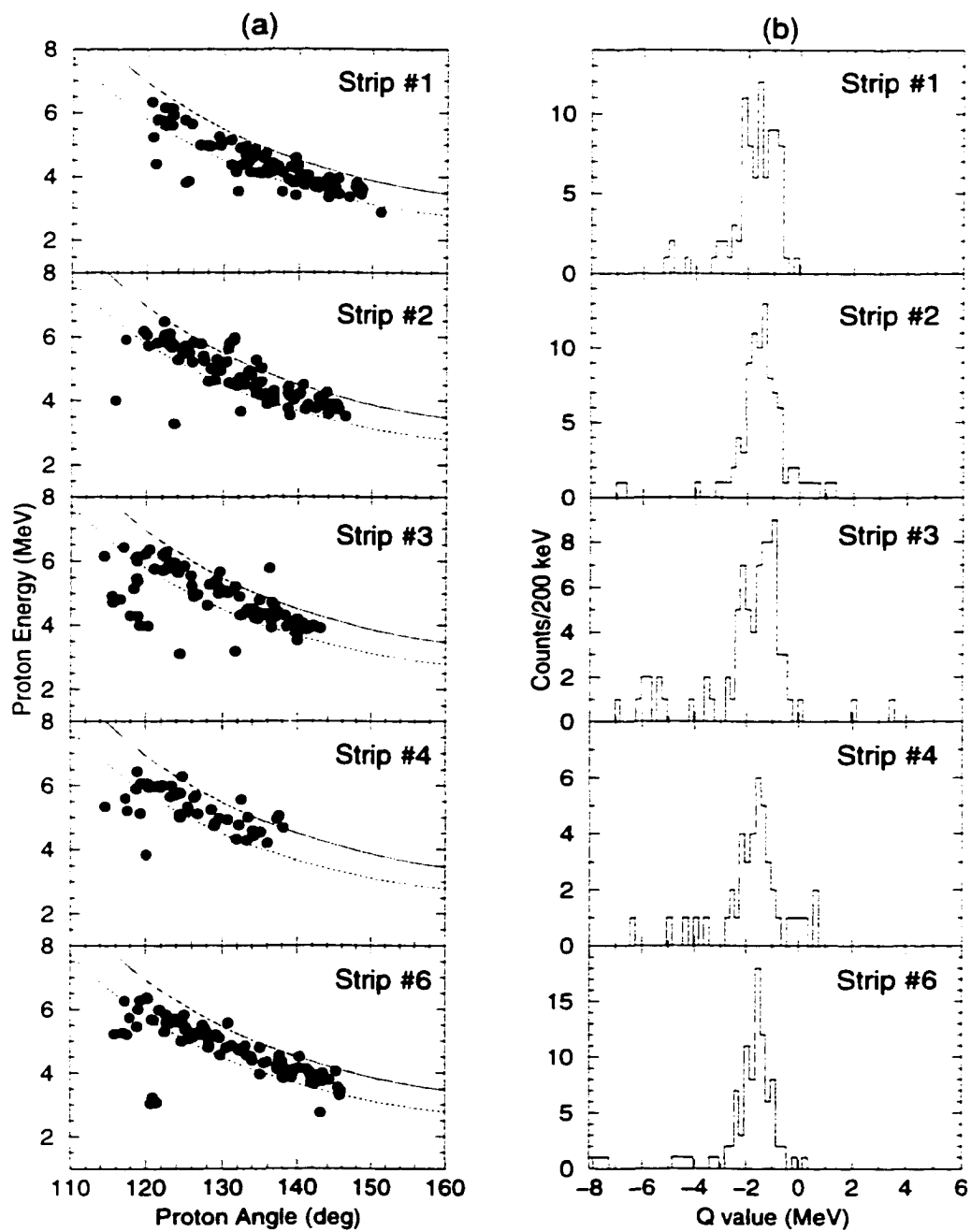


Figure 4.23. (a) Proton kinematic plots for the various strip detectors corresponding to the excited states in ^{14}C with array offset in the x direction by 1.1 cm. (b) Corresponding Q-value histograms for the strip detectors with the offset.

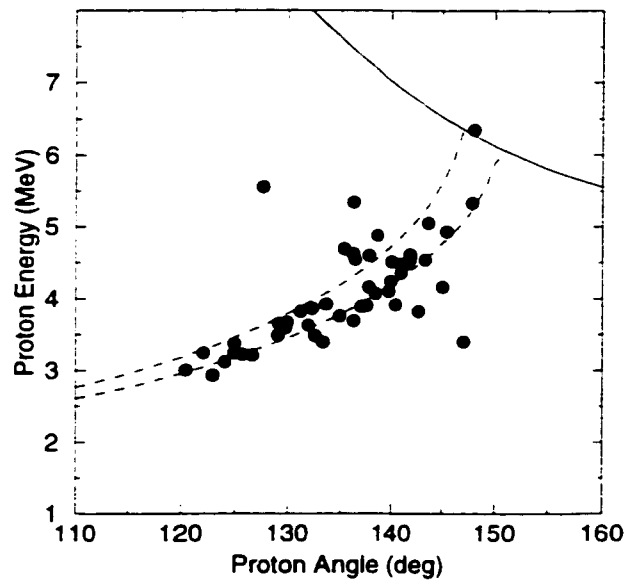


Figure 4.24. Plot of the proton energy vs angle for the ground state events in the strip detectors with the 1.1 cm x offset in place.

calibration nor a correction to the detector thickness could correct both types of events.

In addition to the offset in the silicon strip array, an offset was also discovered for CD2 by plotting the measured Q-value from the measured energies and angles of CD2 as a function of the sector number as shown in Figure 4.25(a) where the Q-value distributions for both the ground state and excited states were discovered to be correlated with the sector that was hit in CD2. Since the sectors vary on the CD detector with the azimuthal angle ϕ when the detector is centered about the beam axis, the measured Q-values for the various states should be independent of the sector number assuming the reaction was isotropic in ϕ . Therefore, a correlation between the Q-value and the sector number indicates that the sectors were measuring slightly different scattering angles due to the detector being offset from the beam axis. This in turn causes the width of the ground state to appear quite

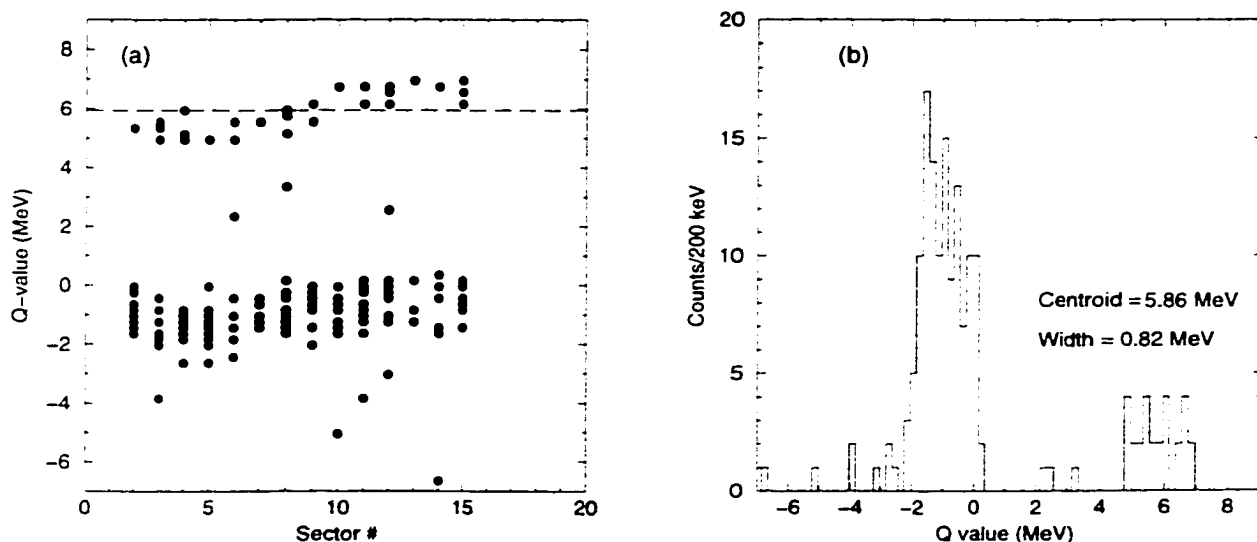


Figure 4.25. (a) Plot of the measured Q-value in CD2 as a function of the sector number. The dashed line indicates the calculated Q-value for the ground state in ^{14}C . (b) Q-value spectra from CD2.

large as shown in Figure 4.25(b). The fact that the centroid of the measured ground state distribution of 5.86 MeV is in agreement with the calculated ground state Q-value of 5.952 MeV indicates that the distance from the detector to the target, and subsequently the central angle of the detector, is correct. The manner in which the Q-value depends on the sector number indicates that the detector was offset primarily in the x-direction. This is due to the fact the largest deviation from the central Q-value of the distribution occurs at sectors 4 and 13 which are on opposite sides of the detector in the x-direction.

To correct for the correlation between the Q-value and the sector number in CD2, the center of CD2 was shifted 0.9 cm in the -x direction relative to the center of the spectrograph. An additional adjustment of 0.4 cm was also made in the +y direction to correct for a slight correlation that was still present between the Q-value and the sector number after the adjustment had been made in the -x direction. The resulting effect on the measured q-value is shown in Figure 4.26(a)

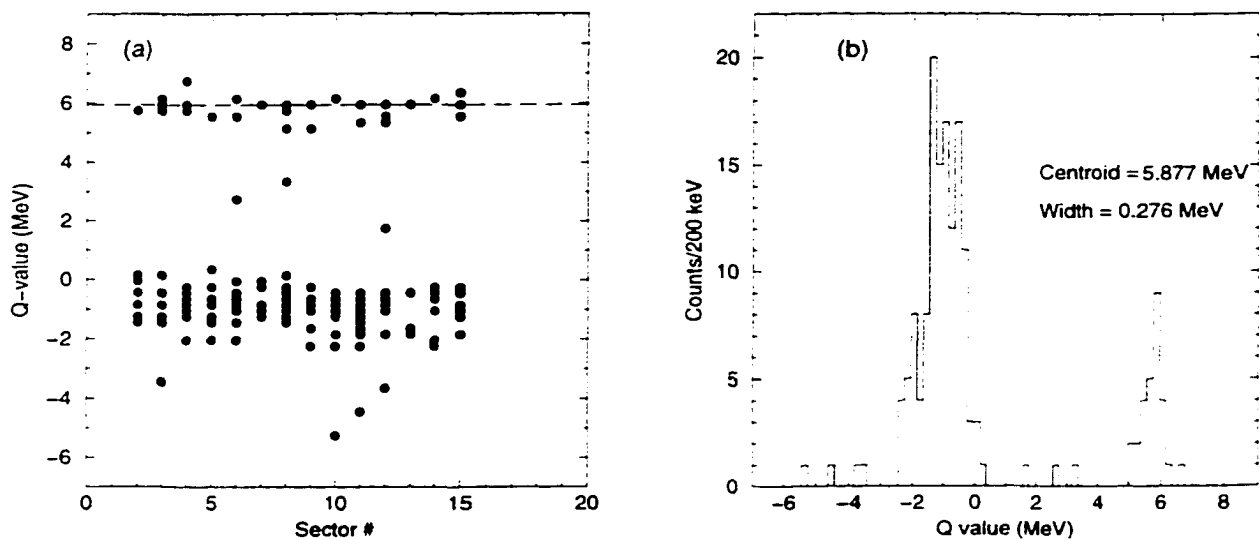


Figure 4.26. (a) Plot of the measured Q-value in CD2 as a function of the sector number with CD2 offset from the optical axis. (b) Corrected Q-value spectra as measured by CD2.

with the correlation eliminated between the Q-value and the sector number. The introduction of these offsets improved the width of the ground state peak from 0.82 MeV (σ) to a width of 0.276 MeV (σ). Since this width was the minimum width that was achievable by offsetting the location of the detector in the x-y plane, the final resolution of CD2 in measuring the Q-value was assumed to be 0.276 MeV (σ) based on the observed width of the ground state in ^{14}C .

Although the resolution of the ground state of 0.276 MeV is not impressive, it should be noted that this resolution was obtained by measuring only the angle and energy of the proton without any measurement of the incident energy of the ^{13}C nor any correction for the incident angle on target. Thus the resolution in measuring the Q-value of the $^9\text{Li}(d,p)$ reaction may improve with the inclusion of the measured incident energy and angle of the beam. Because the incident beam was not tracked onto the target in the $^{13}\text{C}(d,p)$ experiment, and both the Strip detector array and CD2 required offsets in the same general direction, there is a

concern that the observed offsets in the silicon detectors were due to the ^{13}C beam being offset from the optical axis rather than the detectors themselves, which would imply that the detector offsets determined for the $^{13}\text{C}(\text{d,p})$ experiment would not necessarily be applicable for the $^9\text{Li}(\text{d,p})$. However, it is unlikely that the position of either beam at the target could be offset by 1 cm due to the fact that the target itself was only 3 cm in diameter. In addition, similar shifts in the measured Q-value were observed in the strip detectors for the $^9\text{Li}(\text{d,p})$ reaction indicating that the detectors themselves were offset from the optical axis. One plausible explanation for the consistent x-offset that was observed in the Strip array and the CD detectors was the fact that all of the silicon detectors were mounted onto the same movable table in the target chamber. If the table was not set to the correct height in the target chamber, both the Strip array and CD2 would be offset from the optical axis by a similar amount in the x-direction.

Attempts were also made to determine an offset for CD1 in order to improve the width of the measured ground state Q-value. However with only 6 counts in the ground state, it was impossible to make any correction based on the data from CD1. In order to be consistent with CD2 and to a certain degree the Strip array, CD1 was assumed to be offset from the optical axis by the same amount as CD2. It was also assumed that the the ground state Q-value resolution for CD1 was comparable to what was measured in CD2. Although the width of the ground state could not be optimized in CD1 due to the lack of statistics, it was noted that the centroid for both the ground state and excited state band in CD1 was shifted to higher Q-value relative to what was measured in CD2 by 400 keV as shown in Figure 4.27(a). Since both CD1 and CD2 were measuring the same states in ^{14}C , this shift in the central Q-value must be due to either a problem in determining which angles were covered by CD1 or a problem with the proton energy that was measured. This is illustrated

in Fig. 4.27(b) where the measured proton energy from the ground state band is plotted as a function of the proton angle as for CD1 (circle) and CD2 (square). The two curves in the figure represent two different Q-values with the upper curve centered about the distribution of the ground state events in CD1 and the lower curve centered at the actual ground state Q-value of the reaction. As is seen in Fig. 4.27(b), it is highly unlikely that the discrepancy in the ground state Q-value between CD1 and CD2 could be the result of a shift in the angles covered by CD1 since it would require a shift of approximately 8° in the lab. Such a shift in the angles would imply that the measured distance from CD1 to the target would have been off by 7 cm which is quite unrealistic considering that the distance between the target and the detector was measured during the experiment. The more plausible explanation is that the measured energies of the protons were inaccurate due to shifts in the energy response of the detector. The observed shift in the ground state Q-value would require that the proton energy be offset by 170 keV. In order to match the ground state Q-values between CD1 and CD2, the energy of the protons in CD1 were shifted down in energy by 170 keV. The result of this shift in the energy of the protons in CD1 can be seen in Fig. 4.27(c) in which the adjusted CD1 Q-value spectra is shown in comparison with the Q-value spectra from CD2. As Fig. 4.27(c) indicates, the centroids of the ground state band and excited state band are now in agreement between CD1 and CD2. Since shifting the energy of CD1 improved the agreement in the Q-value for the ground state of ^{14}C between CD1 and CD2, the energies of CD1 were subsequently shifted in the analysis of the $^9\text{Li}(d,p)^{10}\text{Li}$ experiment.

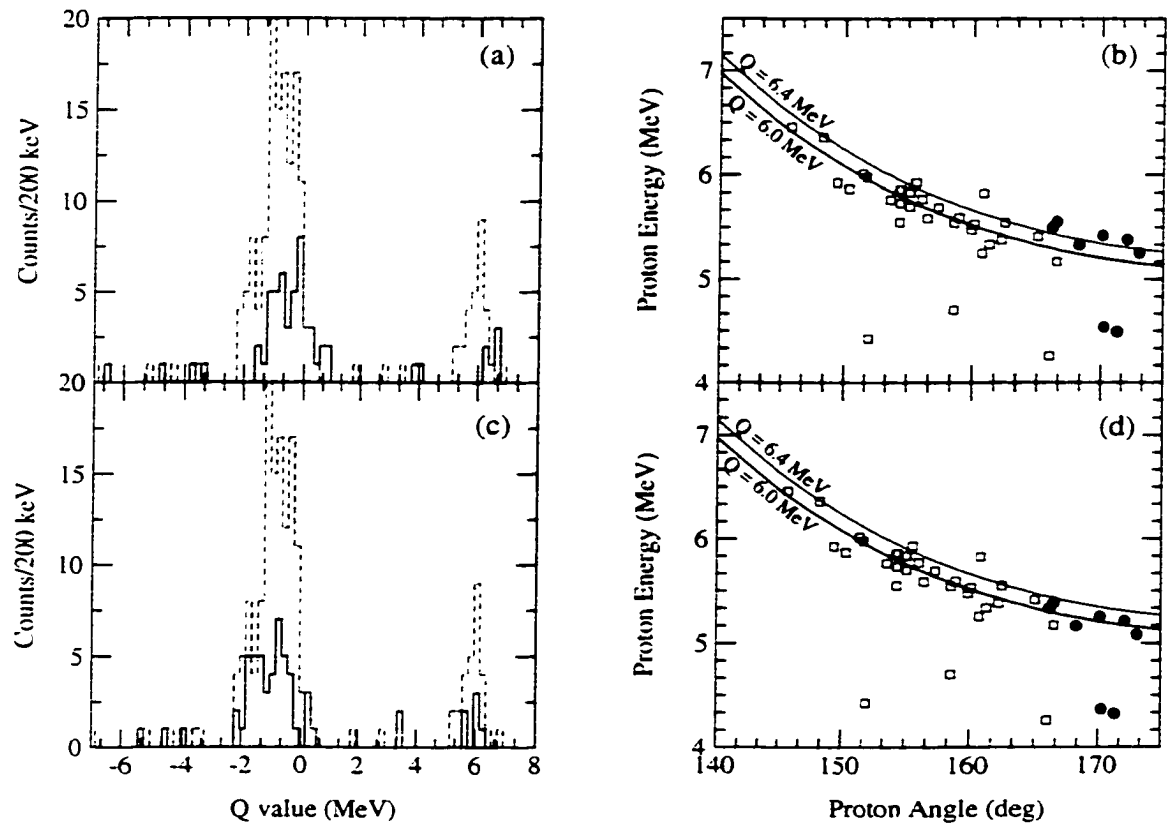


Figure 4.27. (a) Comparison of the measured Q-value spectra in CD1 (solid histogram) with the measured Q-value spectra in CD2 (dashed histogram). (b) Plot of the measured proton energy vs angle for CD1 (circle) and CD2 (square). The solid curves represent constant Q-value. (c) Corrected Q-value spectra for the energy-shifted CD1 (solid histogram) compared with the measured Q-value spectra in CD2 (dashed histogram). (d) Measured proton energy vs angle for energy shifted CD1 (circle) and CD2 (square).

4.3 Analysis of ${}^9\text{Li}(d,p){}^{10}\text{Li}$ Data

Data were taken on the ${}^9\text{Li}(d,p){}^{10}\text{Li}$ reaction for approximately 121 hours of beam time on target. During that time, 1880 total events were measured in all of the silicon detectors while 10^6 events were collected in the focal plane of the spectrograph. Figure 4.28(a) shows the $\Delta E - E$ plot for all of the focal plane events measured during the experiment. Two different ${}^9\text{Li}$ groups are apparent, as well as two different ${}^9\text{Be}^{3+}$ groups. Although the $B\rho$ setting of the S800 spectrograph during the experiment was too low to allow the direct ${}^9\text{Li}$ beam up onto the focal plane, it was still possible for particles from the direct beam to reach the focal plane due to scattering within the walls of the spectrograph itself. This was confirmed by performing a run with the target lowered out of the beam and the $B\rho$ of the spectrograph set to focus the reaction ${}^9\text{Li}$ particles up to the focal plane. This no-target run was performed for 2 hours with an average incident beam rate of 5600 particles/second based on the measurements from the BLT. During this run, 6700 ${}^9\text{Li}$ events were detected in the focal plane, along with a small amount of ${}^9\text{Be}^{3+}$. While ${}^9\text{Li}$ was detected in the focal plane during the no target run, no events were detected in the silicon detectors. Because of the presence of ${}^9\text{Li}$ in the focal plane with no target in place, it was necessary to use the coincidence requirement between the silicon detectors and the focal plane to positively identify the events of interest. This coincidence requirement cleaned up the $\Delta E - E$ spectrum from the real data considerably, with only one ${}^9\text{Li}$ group now present in the focal plane as shown in Fig. 4.28(b). With the coincidence gate in place, the number of events seen in the focal plane was reduced from 10^6 events down to 1021 events, with 93% of these events identified as ${}^9\text{Li}$.

Additional evidence for the production of ${}^{10}\text{Li}$ in the reaction was observed in the kinematics of the protons. Figure 4.29 shows the energy measured in the silicon

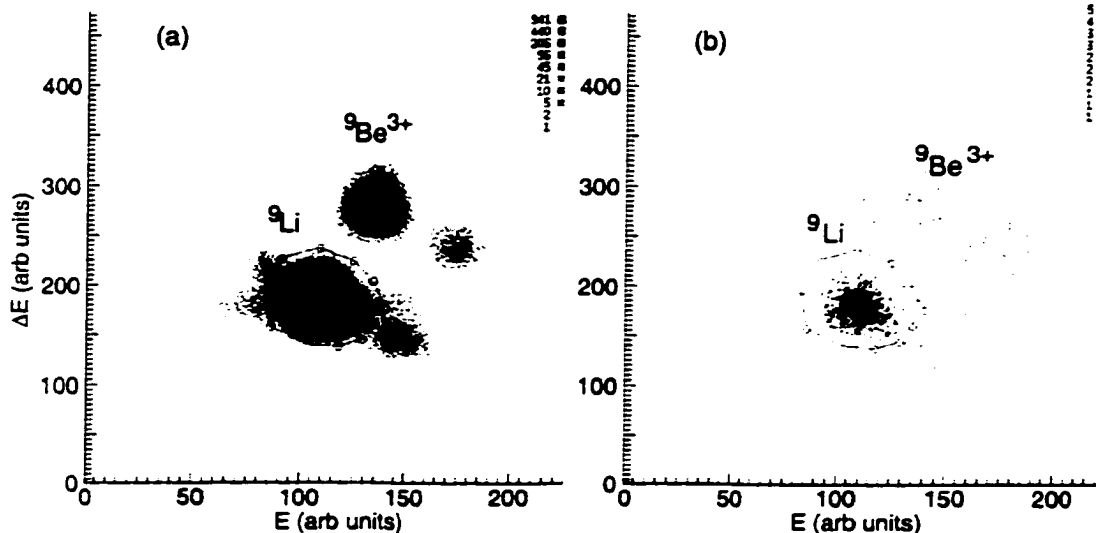


Figure 4.28. (a) Plot of the ΔE vs E spectra of the reaction products from the ${}^9\text{Li}(d,p){}^{10}\text{Li}$ reaction. (b) Plot of the ΔE vs E spectra for reaction events in coincidence with a silicon detector.

detectors as a function of the detector angle for all of the detected silicon events (Fig. 4.29(a)) and those events that were in coincidence with ${}^9\text{Li}$ in the focal plane (Fig. 4.29(b)). In both of these spectra, the line which appears at 5.4 MeV is due to the presence of the ${}^{241}\text{Am}$ alpha source on the target ladder below the optical axis. With the placement of a coincident gate between the silicon detectors and a detected ${}^9\text{Li}$ particle in the focal plane, a kinematic edge in the distribution becomes evident in Fig. 4.29(b) at energies lower than the ${}^{241}\text{Am}$ alpha line. This kinematic edge is relatively consistent with the calculated kinematics for protons produced in the ${}^9\text{Li}(d,p)$ reaction shown as the solid curve in Fig. 4.29(b). The kinematic calculations were performed using the code PKIN assuming a mass excess for ${}^{10}\text{Li}$ of $33.050 \pm 0.015 \text{ MeV}/c^2$ [42] where the mass excess is defined as the difference between the mass of the nucleus and the mass of the sum of the constituent nucleons

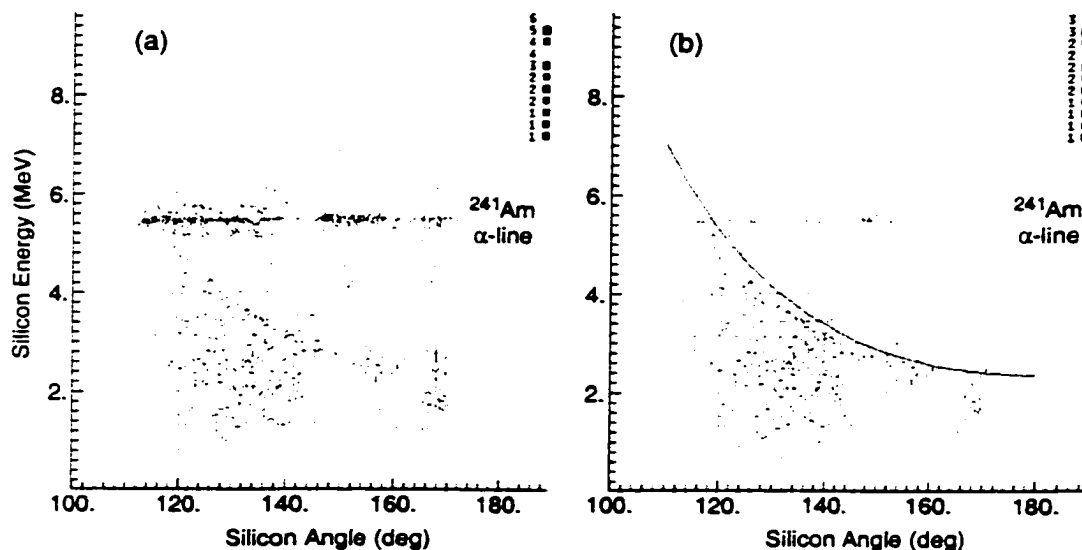


Figure 4.29. (a) Plot of the silicon energy as a function of angle for all of the events detected by the silicon detectors. (b) Plot of the silicon energy as a function of angle for events in coincidence with ${}^9\text{Li}$ in the focal plane. The solid line indicates the calculated kinematic edge for the ${}^9\text{Li}(d,p){}^{10}\text{Li}$ reaction.

within the nucleus [16]:

$$\Delta = (m - A) * 931.4940 \text{ MeV}/c^2 \quad (4.14)$$

Here m is the mass of the nucleus in atomic mass units and A is the number of nucleons within the nucleus. The kinematic calculations in Fig. 4.29(b) also assumed that the reaction took place at the center of the target. The spread of proton events which occur below this kinematic edge is consistent with the production of ${}^{10}\text{Li}$ in the reaction since such a spread in the kinematics would correspond to the population of continuum states in ${}^{10}\text{Li}$, all of which will appear below the solid line.

The fact that the alpha line appears constant in energy in Fig. 4.29 implies that all of the silicon detectors were functioning properly during the experiment. However, problems were discovered with some of the strip detectors after the experiment was completed. At the end of Run #24, a problem occurred somewhere

within the beam line causing the vacuum in the target chamber to become quite poor. This problem with the vacuum system was the apparent cause of problems with some of the strip detectors. In the case of Strip Detector #3, for instance, the resolution of the detector became dramatically worse after Run #25 as is evident in Figure 4.30(b) which shows the raw energy signal from the strip detector as a function of the number of buffers that had been written to tape since the beginning of the ${}^9\text{Li}(d,p)$ experiment. In Fig. 4.30, the ${}^{241}\text{Am}$ alpha line appears as a line in both Strip #2 (a) and Strip #3 (b) near channel 250 before Run #25. After this run, the line has clearly become much broader in Strip #3 while no such effect is seen in Strip #2 for that same time period, indicating a problem in Strip #3. Because of the poor resolution in Strip #3, data from this detector after the vacuum accident were rejected in the analysis. In addition to the problems observed in Strip #3, the vacuum problems also appear to have affected Strip #6 causing it to discharge shortly after the start of Run #25 (Fig. 4.30(c)), at which point it stopped working until bias voltage was re-applied in Run # 44. Unfortunately, the low count rate in the silicon detectors during the running of the experiment caused these problems to go undetected for a long period of time. The loss of these two strip detectors over this period of time reduced the ability of the experimental setup to detect the events of interest, causing a reduction in the statistics that were available for analysis.

Although the alpha source was useful in diagnosing the problems with the two strip detectors, as well as to monitor the gains in the other silicon detectors, its presence on the target ladder adds a certain amount of uncertainty to the proper identification of the (d,p) events. The fact that the alpha line is evident in Fig.4.29(b) indicates that the coincidence requirement between the focal plane and the silicon detectors does not fully eliminate the possibility of random coincidences occurring between the silicon detectors and the focal plane. Hence, the presence of the alpha

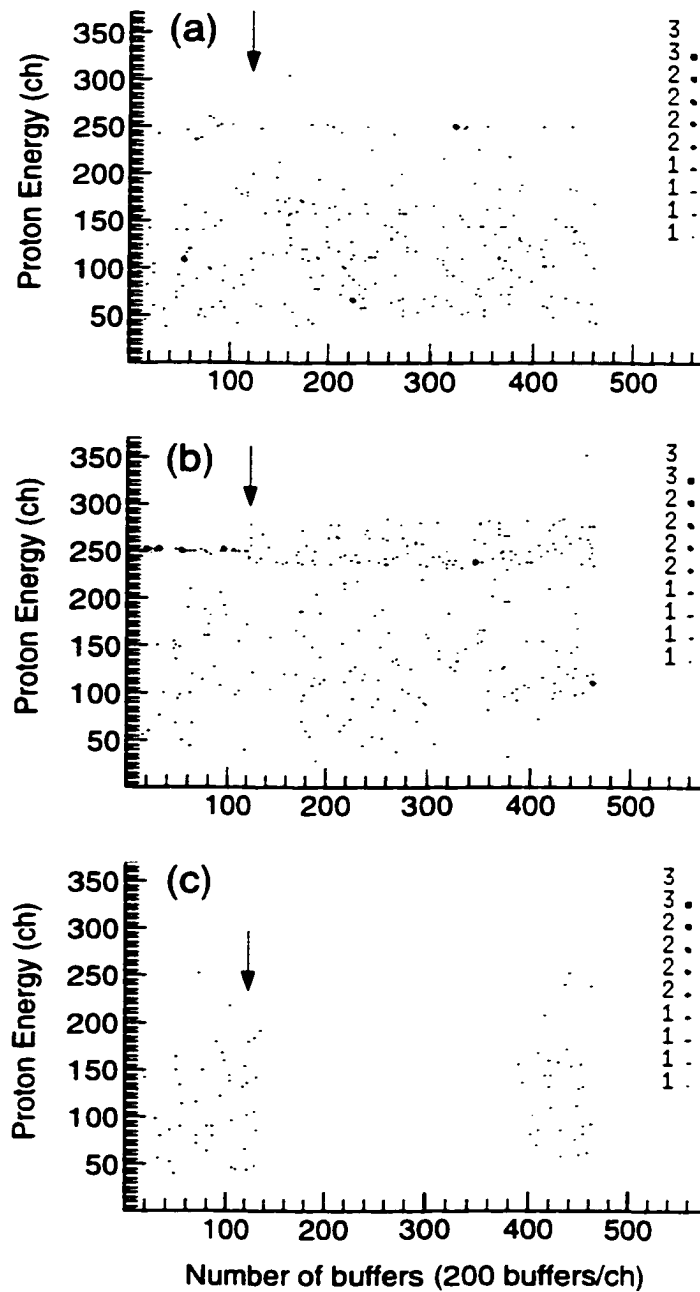


Figure 4.30. (a) Plot of the proton energy as a function of buffer number for (a) Strip #2 (b) Strip #3 and (c) Strip #6 for the ${}^9\text{Li}(d,p){}^{10}\text{Li}$ reaction runs. The arrow indicates the start of Run # 25.

source near the silicon detectors acts as a source for random background events in the coincidence spectrum. For scattering angles greater than 120° , the alpha peak is clearly distinguishable from the region of interest and hence was easily gated out of the data. For scattering angles less than 120° , however, the alpha-particle events overlapped the region of interest and were indistinguishable from the real data. In addition, the energy spectrum of the ^{241}Am source produced a continuous spectrum of alpha particles at energies lower than the alpha peak as shown in Figure 4.31. Here, the measured energy spectrum of the alpha source is presented for three strip detectors operating with the event trigger produced directly from the silicon detectors themselves (singles mode). The uniform spread of events from the alpha source at energies lower than the 5.4 MeV alpha peak constituted a source of background which needed to be accounted for in the analysis of the experiment.

The background produced by the alpha source in the coincidence spectrum at energies less than 5 MeV can be estimated based on the ratio of counts measured in singles mode in the alpha peak to the number of counts measured at energies below the alpha peak for each detector. Using this ratio and assuming that the coincidence gate does not affect the shape of the energy spectra from the alpha source, the number of counts that are present in the region below the alpha peak was deduced based on the number of coincidence events observed in the alpha peak. In Table 4.3, the calculated background from the alpha source in the coincidence spectra is presented for each strip detector. The background listed in the table is for the entire energy range below the lower edge of the alpha peak at approximately 4.8 MeV indicated by the solid line in Fig. 4.31. Since the shape of the background from the alpha source was essentially flat for energies below 4.8 MeV, the total number of background counts that was determined for each detector is evenly distributed throughout this energy range. Even in the case of Strip #4, which was the closest

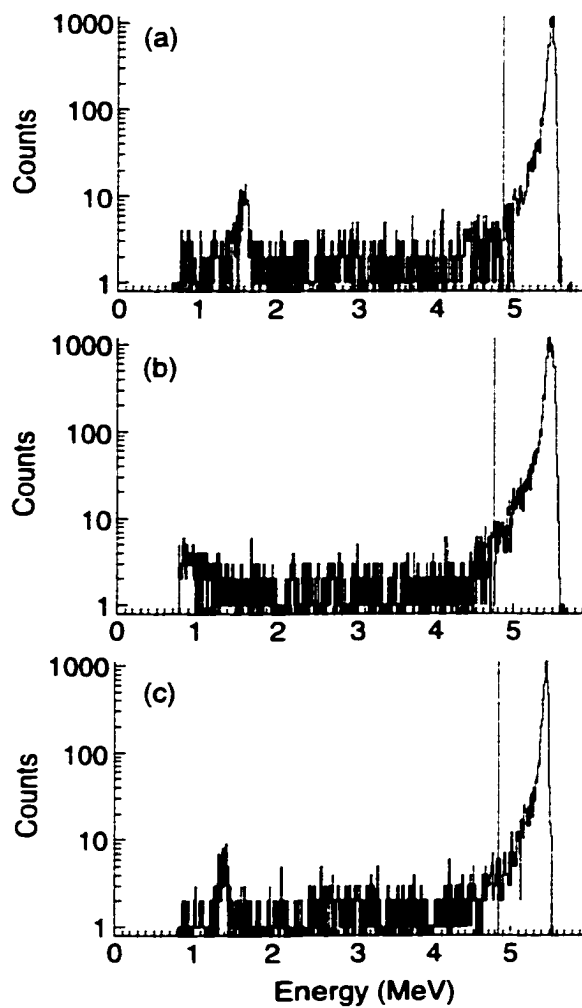


Figure 4.31. Energy spectrum of the ^{241}Am source as measured by (a) Strip #2, (b) Strip #4, and (c) Strip #6 in singles mode. The solid line indicates the lower edge of the alpha peak used to separate the alpha peak from the flat background.

Table 4.3. Estimated background in the coincidence spectra for the strip detectors due to the ^{241}Am source.

Strip Det	Ratio $\frac{\text{background}}{\text{peak}}$ (singles)	Alpha peak area (coinc)	Background area
1	0.055	0	-
2	0.081	9	0.726
3	0.089	25 ^a	2.2
4	0.055	48	2.64
6	0.085	3	0.25

^a Total for runs before Run 25.

to the alpha source and thus measured the highest number of events in the alpha peak, the number of background counts that would be measured at energies below 4.8 MeV is negligible. Hence, for energies less than 4.8 MeV, the background due to the alpha source can be neglected.

In addition to the coincidence requirement between ^9Li particles in the focal plane and the silicon detectors, which also included the presence of the two focal plane CRDCs (S801 and S802) in the event, the CRDCs in the analysis line (S803 and S804) must also be present in order to be able to determine the energy and angle of the incident beam. While the two focal plane CRDCs detected ^9Li particles with nearly 100% efficiency, the efficiency for S803 and S804 in detecting the incident ^9Li particles was determined to be 68% based on the direct beam runs that were performed during the experiment. This poor efficiency of S803 and S804 in detecting the incident ^9Li particles was mostly likely due to the fact that ^9Li does not produce a strong ionization signal in the gas along with the fact that the volume of gas that was present within the two detectors is quite small. While the information from S803 and S804 is not necessary in order to identify the events of interest, the ability of the experiment to measure the events from the (d,p) reaction is reduced

without S803 and S804 due to the fact that the incident beam had a $\pm 1\%$ spread in energy. This large spread in the incident energy increases the uncertainty in determining the Q-value of the reaction as is illustrated in Figure 4.32 which shows the calculated uncertainty in the Q-value as a function of the proton scattering angle. In Fig. 4.32, the solid curve represents the uncertainty in the Q-value assuming an uncertainty in the measured incident energy of $\pm 0.17\%$ (σ) due to the uncertainties in measuring the incident energy using S803 and S804 while the dashed curve is the uncertainty in the Q-value assuming the $\pm 1.0\%$ energy spread in the incident beam as the uncertainty. In both calculations, the uncertainty in the measured proton energy was assumed to be $\pm 1.5\%$ (σ) for all of the scattering angles considered in the calculation and any error in determining the energy losses for the incident ${}^9\text{Li}$ and proton in the target was neglected. Although the effect of not measuring the incident energy in the resolution of the Q-value measurement appears to be small, it still hampers the ability of the experiment to accurately resolve any low lying states which may appear in the structure of ${}^{10}\text{Li}$.

4.3.1 Mass measurement

Since the mass of ${}^{10}\text{Li}$ is not well known, an attempt was made to measure the mass based on the location of the kinematic edge of the proton events from the ${}^9\text{Li}(d,p)$ reaction. The proton events used to determine the mass of ${}^{10}\text{Li}$ were selected if their energy was the largest observed relative to the other proton events detected within a similar angular range. Those proton events which were near the energy of the ${}^{241}\text{Am}$ line were excluded from this selection process in order to ensure that the events being considered were from the (d,p) reaction. Also excluded were those events in Strip #3 which were recorded after Run #25. In addition, only those events which were in coincidence with S803 and S804 were considered in order to

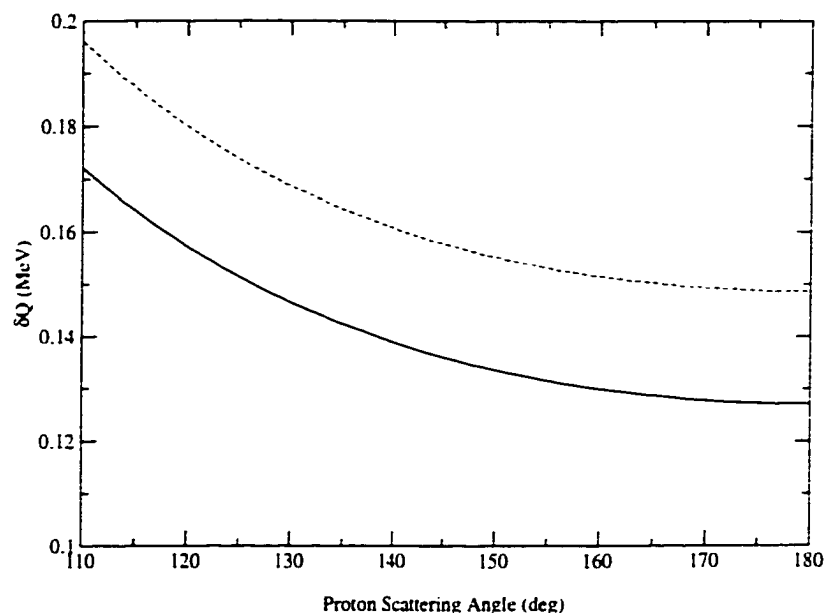


Figure 4.32. Plot of calculated uncertainty in the Q-value as a function of the proton scattering angle with the measurement of the incident included (solid curve) and without a measured incident energy (dashed curve). Both calculations were performed for a Q-value of -2.25 MeV assuming an uncertainty in the measured proton energy of $\pm 1.5\%$ (σ) for all of the scattering angles.

optimize the accuracy of the determination by accounting for the energy and angle of the incident beam. Once these edge events were selected, the mass of ^{10}Li was determined by fitting the energy of the protons on the edge of the distribution based on the angle at which they were scattered at as well as the measured incident energy of the beam. In the fitting procedure, the energies of the incident beam and the proton were corrected for energy losses in the target assuming the event took place at the center of the target. The scattering angle of the protons was determined by performing a dot product between the incident beam vector and the vector determined from the location of the detected proton in the silicon array. Errors were considered in the fit for both the angles and energies of the proton as well as the incident beam. The resulting fit to the proton events is shown in Figure 4.33 with

Figure 4.33 with the gold points indicating the events that were considered in fitting the kinematic edge of the distribution.

The mass excess for ^{10}Li that resulted from the fit of the kinematic edge of the protons from the (d,p) reaction was 33.10 ± 0.08 MeV ($\pm\sigma$). The error in the mass excess is based on the point where the reduced χ^2 deviates from the global minimum by one unit. In the inset of Fig. 4.33, the reduced χ^2 for the fit is shown as a function of the mass excess for ^{10}Li that was considered in fitting the data. It should be noted that this mass measurement for ^{10}Li should only be considered as a lower limit due to the fact that most of the observed events lie below the fit which correspond to a more massive ^{10}Li nucleus. Although this mass measurement is only a lower limit to the mass of ^{10}Li , it still appears consistent with the current value of 33.050 ± 0.015 MeV [42] listed in the NUBASE mass evaluations.

4.3.2 Q-value measurement

In addition to determining the mass of ^{10}Li directly from the kinematic edge of the proton distribution, the Q-value for the $^9\text{Li}(d,p)$ reaction was also determined based on the measured proton energies and angles. Figures 4.34(a) and (b) show the Q-value spectra for the CD detectors and the strip detectors, respectively, for all of the coincident events measured in the experiment without requiring an additional coincidence with S803 and S804. A peak is evident in both spectra at approximately -2.9 MeV. Including the information from S803 and S804 to account for the incident beam appears to improve the resolution of the Q-value spectra slightly as is illustrated in Figs. 4.34(c) and (d), although the peak in the spectrum for the strips now seems to have shifted to lower Q-values. In the case of the CD spectrum, a possible second peak becomes apparent at a Q-value which corresponds to the measured ground state mass for ^{10}Li . This peak, if real, would seem to correspond

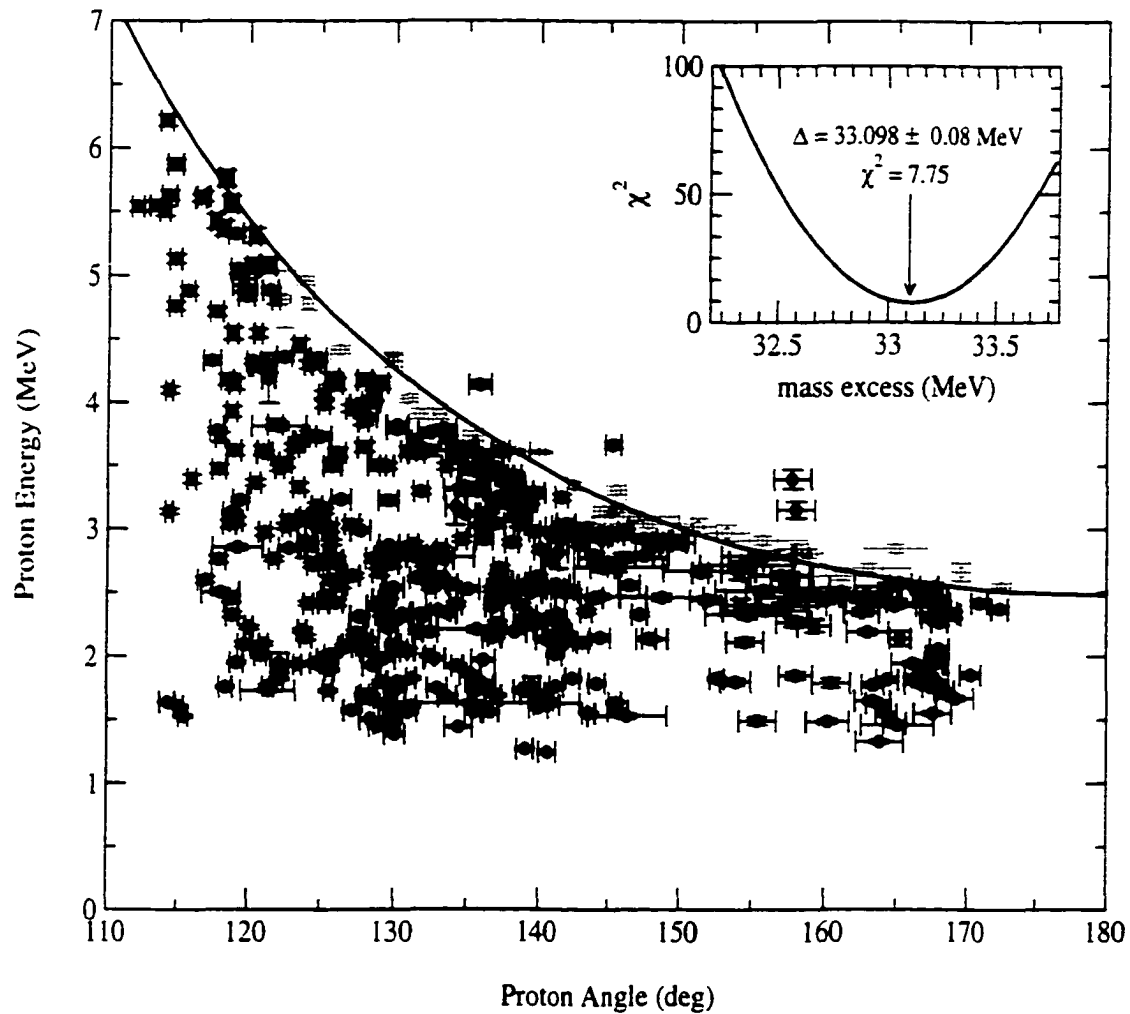


Figure 4.33. Plot of proton energy vs proton angle for data in coincidence with ${}^9\text{Li}$ in focal plane, S803, and S804. The solid curve is the best kinematic fit to the data varying only the mass of ${}^{10}\text{Li}$ while the gold points indicate the events which were considered in fitting the kinematic edge. In the inset, the reduced χ^2 for the kinematic fit as a function of the mass excess of ${}^{10}\text{Li}$.

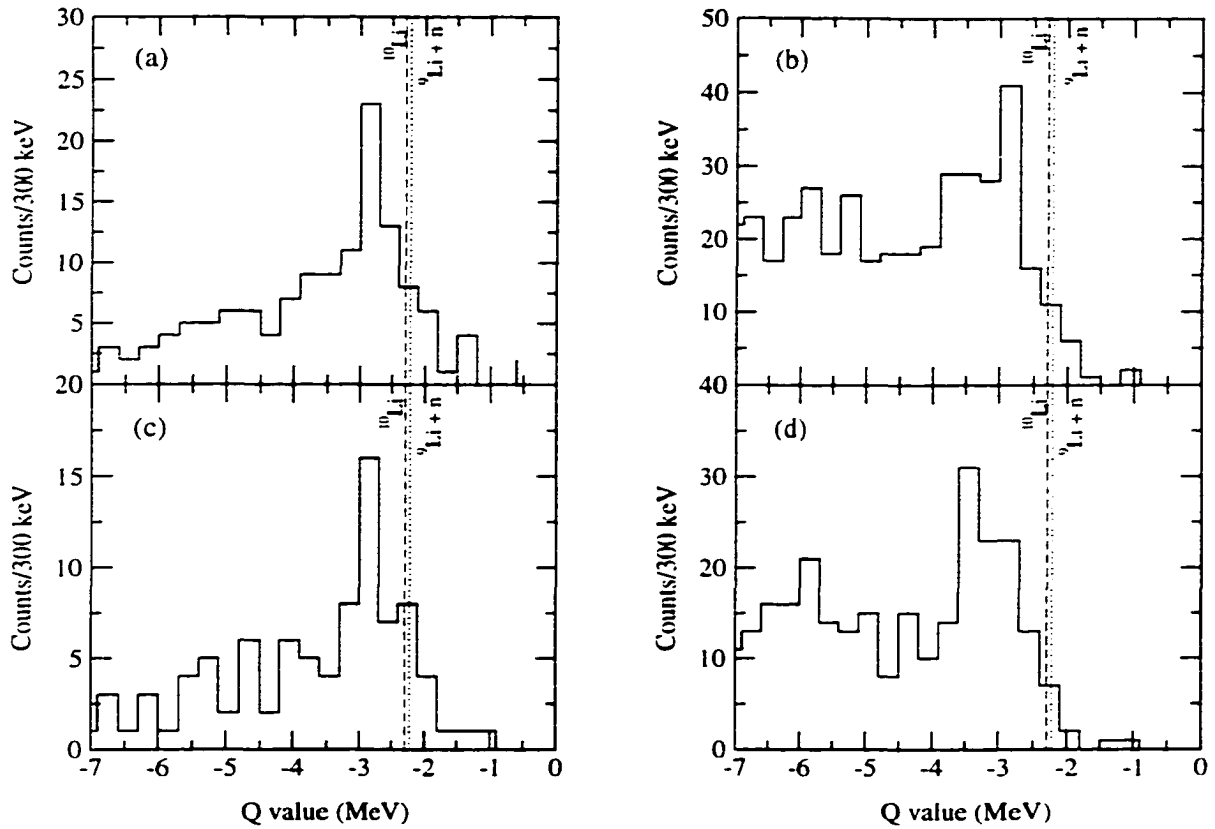


Figure 4.34. (a)-(b) Q-value spectra for the CD detectors and Strip detectors, respectively, for all coincident proton events. (c)-(d) Q value spectra for CD detectors and Strip detectors, respectively, for proton data in coincidence with S803 and S804 as well as the focal plane. In all of the figures, the dotted line is Q-value corresponding to the ${}^9\text{Li}+n$ threshold while the dashed line is the Q-value corresponding to the measured mass of ${}^{10}\text{Li}$.

to the ground state of ${}^{10}\text{Li}$ confirming the presence of a low-lying state that has been observed in previous experiments [5, 6, 7, 9].

While the presence of peaks in the Q-value spectrum for both the CD detectors and the Strip detectors indicate the presence of structure in the reaction, the fact that the peak extends up to -1.0 MeV in Q-value is a potential problem. Since ${}^{10}\text{Li}$ is known to be unbound to neutron decay, a threshold can be determined for the Q-value spectra corresponding to a lower limit in the mass of ${}^{10}\text{Li}$. This lower limit

in can be determined based on the masses of ${}^9\text{Li}$ and neutron:

$$m_{10} \geq m_9 + m_n \quad (4.15)$$

Using the known masses of ${}^9\text{Li}$ and neutron from previous studies [42], the mass excess for this threshold is $33.025 \text{ MeV}/c^2$, which places an upper limit on the Q-value for the (d,p) reaction of -2.23 MeV . The fact that the peaks seen in Figs. 4.34(c) and (d) extend beyond this upper limit in the Q-value is possibly indicative of poor resolution in measuring the Q-value of the reaction. Another potential problem that is evident in these Q-value spectra is the fact that the measured Q-values extend below -6.3 MeV at which point it becomes energetically possible for ${}^{10}\text{Li}$ to decay via the 2n channel. This is due to the fact that for Q-values below -6.3 MeV , enough excitation energy has been imparted into the ${}^9\text{Li} + n$ system so as to separate a neutron from the ${}^9\text{Li}$ core ($S_n = 4.063 \text{ MeV}$ for ${}^9\text{Li}$ [32]). The resulting ${}^8\text{Li}$ from a two neutron decay of ${}^{10}\text{Li}$ would not be detected in the focal plane of the spectrograph since it would not have the proper magnetic rigidity to pass through the spectrograph. Since it is not possible to detect ${}^8\text{Li}$ in the spectrograph from the breakup of ${}^{10}\text{Li}$, the probability in detecting real events from the (d,p) reaction with Q-values much smaller than -6.3 MeV is reduced due to the availability of the 2n decay channel. Unlike the ${}^{13}\text{C}(\text{d,p})$ experiment in which the experimental threshold for measuring the Q-value of the reaction was determined by the S_n of ${}^{14}\text{C}$, no such threshold exists in the ${}^9\text{Li}(\text{d,p})$ experiment due to the fact that the excitation energy that is imparted into the ${}^{10}\text{Li}$ nucleus, or more appropriately the ${}^9\text{Li} + n$ system, does not necessarily cause the ${}^9\text{Li}$ nucleus to become excited. Hence, while it is possible that the events observed with Q-values less than -6.3 MeV are true ${}^9\text{Li}(\text{d,p})$ events, the substantial number of events seen in this Q-value range may indicate the presence of background processes in the experiment that have not been accounted for.

If one assumes that the peaks in the Q-value spectra are due to the presence of structure in ^{10}Li , then the relative angular distribution of the events may provide some insight into the nature of that structure. Figure 4.35(a) shows the relative angular distribution of events with Q-value ≥ -4.0 MeV measured in both CD detectors as well as Strips #1, #2 and #4, as a function of the laboratory proton scattering angle. Due to a lack of statistics, each CD detector was treated as a single angular bin, with the events in the given detector summed and placed at the central angle of the detector. Because of the physical offset in the silicon strip array, the events measured in the strip detectors were placed into two angular bins, each of which covered 22° . The solid angle for each angular bin was determined separately for each strip detector and then summed together to determine the total solid angle for the angular bin. Although the angular distribution only consists of four points with rather large error bars, there are possible signs of structure as is illustrated in Fig. 4.35(b) where the angular distribution is given as a function of the subsequent ^{10}Li center of mass angle. This distribution was determined by transforming the solid angle as measured in the lab into the solid angle covered in the center of mass reference frame using the Jacobian that was determined using PKIN. Although there are indications of structure in the angular distribution, it should be noted that the angular distributions shown in Figs. 4.35(a) and (b) have not been corrected for the efficiency of the experimental setup in detecting coincident events as a function of the proton lab angle. These corrections to the angular distribution will be determined using Monte Carlo techniques and will be presented in the next chapter.

While many questions surround these Q-value spectra, it may be possible to confirm that the peaks observed in the Q-value spectra are due to the structure of ^{10}Li by performing a full reconstruction on the data using the measured energies and

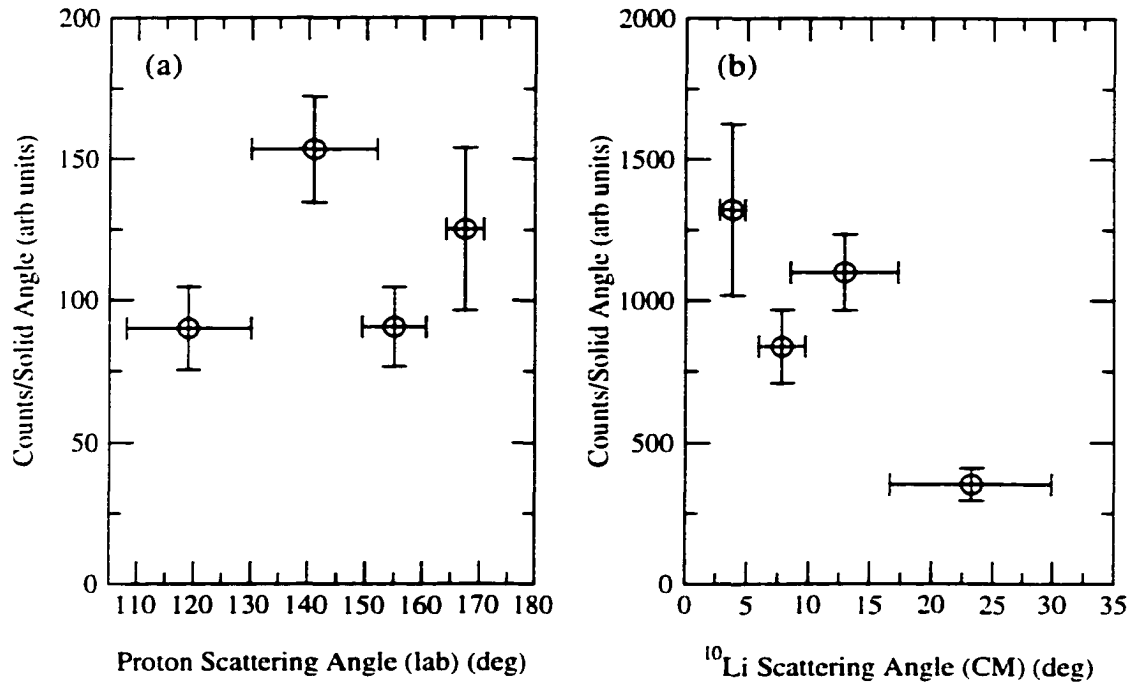


Figure 4.35. Relative angular distribution of the (d,p) events with $Q \geq -4.0$ MeV as a function of (a) the proton laboratory scattering angle and (b) the ^{10}Li center of mass angle.

angles of the outgoing ^9Li in addition to the information from the silicon detectors, as well as the two tracking detectors in the analysis line S803 and S804. In order to properly understand the results of such a reconstruction, as well as to address the issues surrounding the Q-value spectra, Monte Carlo simulations of the experimental setup and breakup process were performed. From these, we hoped to determine the response of the experimental setup in detecting the events from the $^9\text{Li}(d,p)$ reaction, in terms of the Q-value resolution as well as the efficiency of the setup in detecting coincident events between the focal plane and the silicon detectors. The results of the full reconstruction of the data, as well as the interpretation of the data using Monte Carlo techniques, are presented in the next chapter.

CHAPTER 5

INTERPRETATION AND CONCLUSIONS

5.1 Full Reconstruction

In determining the Q-value of the ${}^9\text{Li}(\text{d},\text{p})$ reaction using the information from the silicon detectors and the incident beam tracking detectors, the spectrograph was only used to identify the events of interest. This usage of the spectrograph completely neglects its abilities to precisely measure the energy and angle of the outgoing ${}^9\text{Li}$ particle. Performing a full reconstruction of the breakup of ${}^{10}\text{Li}$ using the measured information from all of the various detector systems could improve the ability of the experimental setup to resolve the structure of ${}^{10}\text{Li}$ as well as provide a way to remove any background that is present in the data.

The first step in performing this reconstruction was to determine the total energy of the outgoing ${}^{10}\text{Li}$ from the (d,p) reaction based on the measured energies of the proton and incident ${}^9\text{Li}$ particle. This was done by using conservation of energy:

$$E_{10} = T_9 + m_9 + m_d - T_p - m_p \quad (5.1)$$

where T_9 and T_p are the kinetic energies of the ${}^9\text{Li}$ nucleus and the proton, respectively, corrected for an assumed energy loss in the target consistent with the reaction occurring at the physical center of the target (where the speed of light c has been set equal to 1, here and elsewhere in this Chapter). With the total energy of ${}^{10}\text{Li}$

determined, the magnitude of its momentum is then:

$$|p_{10}| = \sqrt{E_{10}^2 - m_{10}^2} \quad (5.2)$$

where m_{10} is the mass of ^{10}Li that was measured in this experiment. The scattering angle of ^{10}Li , θ_{10} , is related to the proton scattering angle measured relative to the incident ^9Li vector by [34]:

$$\tan(\theta_{10}) = \frac{p_p \sin \theta_p}{p_9 - p_p \cos \theta_p} \quad (5.3)$$

Due to the angular divergence that was present in the incident beam, the reference frame used to describe the motion of ^{10}Li in Equation 5.3 is rotated relative to the optical axis by an amount equal to the incident angle of the incoming particle. Because the angles of the outgoing ^9Li at the target were reconstructed from the information in the focal plane of the spectrograph, the motion of the outgoing ^9Li was reconstructed at the target relative to the optical axis of the spectrograph. In order to properly relate the motion of the outgoing ^9Li with the motion of ^{10}Li prior to its breakup, \vec{p}_{10} must be measured with respect to the optical axis as well. To transform the measured \vec{p}_{10} into the reference frame defined by the optical axis of the spectrograph, the coordinate system was rotated by an amount equal to the measured angles of the incident ^9Li particle, namely a_{inc} and b_{inc} . With \vec{p}_{10} described in Cartesian coordinates, and defining $\vec{p}_{10,lab}$ as the momentum of ^{10}Li that is measured with respect to the optical axis, the relationship between \vec{p}_{10} and $\vec{p}_{10,lab}$ is given by:

$$\vec{p}_{10,lab} = R_x(b_{inc})R_y(a_{inc})\vec{p}_{10} \quad (5.4)$$

where R_x is the rotation about the x-axis and R_y is the rotation about the y-axis given by:

$$R_x(b_{inc}) = \begin{pmatrix} 1 & 0 & 0 \\ 0 & \cos(b_{inc}) & -\sin(b_{inc}) \\ 0 & \sin(b_{inc}) & \cos(b_{inc}) \end{pmatrix} \quad (5.5)$$

$$R_y(a_{inc}) = \begin{pmatrix} \cos(a_{inc}) & 0 & -\sin(a_{inc}) \\ 0 & 1 & 0 \\ \sin(a_{inc}) & 0 & \cos(a_{inc}) \end{pmatrix} \quad (5.6)$$

Once the momentum and total energy of ^{10}Li had been determined with respect to the optical axis, the velocity of ^{10}Li was then calculated using Equation 3.8 in order to transform the outgoing ^9Li energy and momentum measured in the lab into the breakup center of mass reference frame. In order to calculate the velocity of ^{10}Li in the lab, it was necessary to assume that the the mass of ^{10}Li was constant, which neglects any increase in the the mass energy of ^{10}Li due to additional excitation energy produced in the initial (d,p) reaction. Thus, the velocity of ^{10}Li that was calculated in this manner was only a first order approximation and has a certain amount of systematic error associated with it, illustrated in Figure 5.1. Here, the velocity of ^{10}Li , β , is presented as a function of the mass of ^{10}Li near the ground state mass for ^{10}Li that was measured in this work (9348.038 MeV/c²). In the figure, β was calculated assuming an incident ^9Li energy of 177.08 MeV and a detected proton energy of 2.8 MeV, which are typical for this experiment. As can be seen, variation of the mass of ^{10}Li by a rather large amount corresponds to a very small change in β . Hence, the approximate β that is calculated in the reconstruction process is within a few percent of the actual value. While varying the mass of ^{10}Li has a small affect on the accuracy of the reconstructed β , the uncertainty in the incident energy has a pronounced effect. In Fig. 5.1, the dashed curves represent a two σ uncertainty in

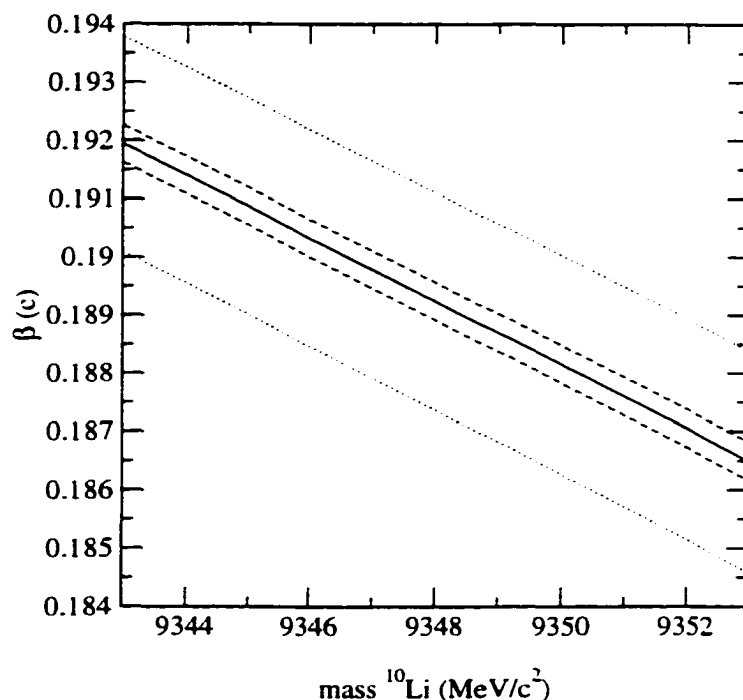


Figure 5.1. Plot of β as a function of the mass of ^{10}Li . The β value was calculated assuming an incident ^9Li energy of 177.09 MeV and a detected proton energy of 2.4 MeV. The dashed curve represents a 2σ error in the determined ^{10}Li total energy assuming that the energy of the incident ^9Li was detected. The dotted curve is the error without an incident energy measurement.

β based on the uncertainties in measuring the incident beam energy using S803 and S804, while the dotted curves are the uncertainties in β when no measurement of the incident beam energy was made. In both of these error calculations, the uncertainty in the proton energy was taken to be $\pm 1.5\%$. Because of the large difference in the error associated with β , the full reconstruction was only accurate when using the events in which S803 and S804 were also in coincidence with a silicon detector and the spectrograph.

With the direction and magnitude of the velocity of ^{10}Li now determined, the momentum vector of the outgoing ^9Li was rotated into the reference frame defined by the motion of the ^{10}Li nucleus so as to determine the components of the outgoing

${}^9\text{Li}$ momentum that were parallel and perpendicular to the motion of ${}^{10}\text{Li}$. This rotation was performed using the matrices $R_x(b_{10})$ and $R_y(a_{10})$, with the angles a_{10} and b_{10} determined with respect to the optical axis of the spectrograph. Once the momentum of the outgoing ${}^9\text{Li}$ was determined in the ${}^{10}\text{Li}$ reference frame, it was then Lorentz transformed into the rest frame of ${}^{10}\text{Li}$ using Equation 3.9. The energy released in the subsequent breakup of ${}^{10}\text{Li}$, Q_{break} , was then determined using Equation 3.15. The results of the full reconstruction are shown in Figures 5.2(a) and (b) where the summed breakup Q-value spectra are presented for the CD detectors and strip detectors, respectively. The spectra shown in Fig. 5.2 are only for those events which include the information from S803 and S804, and exclude the events from Strip #3 for runs which occurred after Run #25. In both spectra, a peak is evident in both sets of silicon detectors at approximately $Q_{break} = 0.6$ MeV with the tail of the peaks appearing to extend beyond 2.0 MeV. While the location of the peak observed in the spectra is relatively consistent with the peak that was observed in the (d,p) Q-value spectra (Fig. 4.34), questions concerning the amount of background present in the spectra still remain. Because Q_{break} is by definition a positive number, the events that were measured with a Q-value for the (d,p) reaction greater than the known upper limit will possibly lie underneath the observed peak in the Q_{break} spectra. These are indicated as the dashed histogram in Fig. 5.2 for both spectra.

To illustrate that the two methods for measuring the structure of ${}^{10}\text{Li}$ were consistent with one another, the values of Q_{break} from the full reconstruction are plotted as a function of the measured Q-value for the (d,p) reaction as shown in Figures 5.3(a) and (b) for the CD and strip detectors, respectively. While the lack of statistics makes it difficult to determine if the two measurements are correlated in the CD detectors, a correlation between the two parameters is observed in the

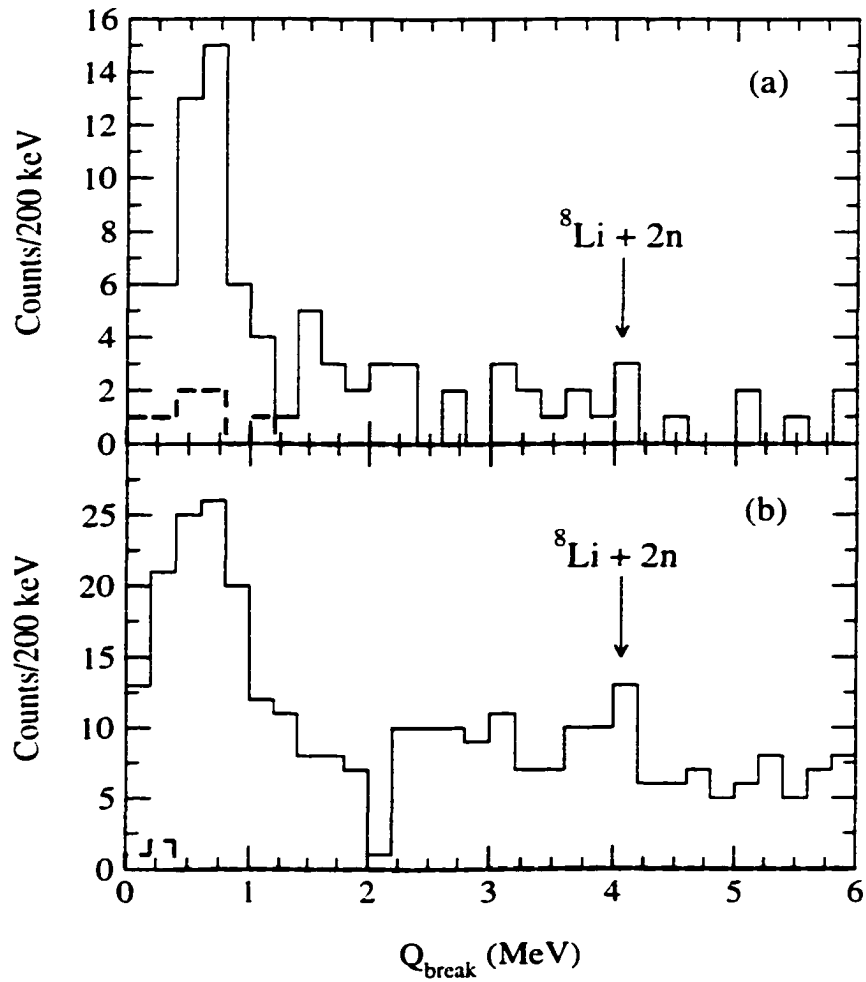


Figure 5.2. Summed reconstructed breakup Q -value spectra for the (a) CD detectors and the (b) Strip detectors. In both (a) and (b), the dashed histogram is the distribution of events in which the Q -value for the (d,p) reaction was measured larger than -2.20 MeV.

strip detectors. Although this correlation is broad, the fact that it exists indicates that the two methods are consistent with one another for the strip detector data. While the majority of events in Fig. 5.3(b) appear within the correlated band, two distinct groups are apparent above and below this band. The group which lies below the correlated band are events in which less energy was measured from the breakup of ^{10}Li than was initially imparted into ^{10}Li from the (d,p) reaction. The presence of this group indicates that either Q_{break} was improperly reconstructed, or that not all of the energy that was released in the breakup of ^{10}Li can be determined from the outgoing ^9Li momentum. Assuming that Q_{break} was in fact reconstructed appropriately, one possible explanation for the missing energy from the breakup of ^{10}Li would be if ^{10}Li was produced in the (d,p) reaction with ^9Li in its excited state at $E_x = 2.691$ MeV [32], which subsequently decays to the ground state via gamma decay prior to entering the spectrograph. This becomes energetically possible when the Q-value of the (d,p) reaction is less than -4.9 MeV. If the ^9Li core were to be excited in the production of ^{10}Li , the emission of the gamma ray from the excited ^9Li nucleus would reduce the Q_{break} that is determined in the full reconstruction relative to the Q-value that was measured in the (d,p) reaction. The fact that this group appears at Q-values which are approximately 2.5 MeV smaller than the determined ground state Q-value for the (d,p) reaction provides some credence to this possibility, which will be discussed in more detail by comparing the data with Monte Carlo simulations in the next section.

Unlike the events which lie at lower Q_{break} values than the correlated band in Fig. 5.3(b), the events that are at larger Q_{break} values are unlikely to be true coincidence events due to the fact that the amount of energy that was reconstructed in the breakup center of mass frame is larger than that produced in the (d,p) reaction based on the measured Q-value of the reaction. An indication of this can

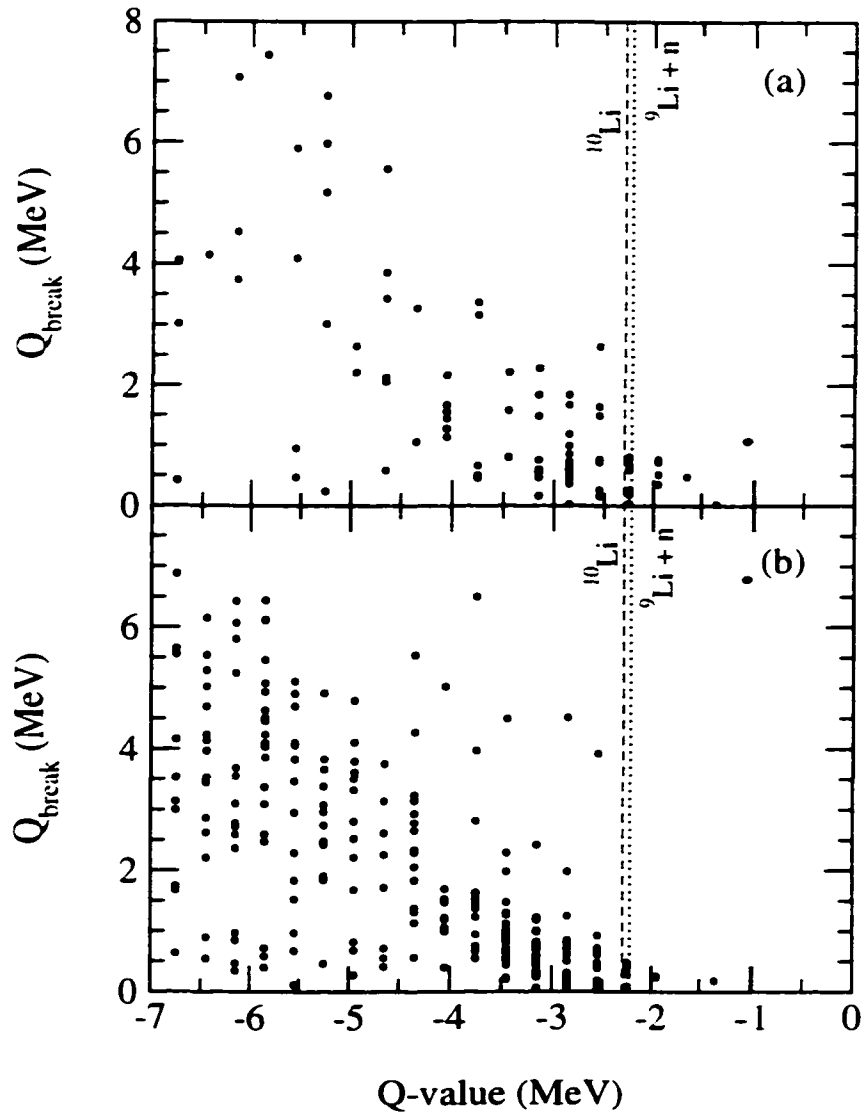


Figure 5.3. Reconstructed Q-value spectra for the breakup of ^{10}Li as a function of the Q-value for the (d,p) reaction as measured by (a) the CD detectors and the (b) strip detectors. In both figures, the dashed line indicates the reaction Q-value corresponding to the measured ^{10}Li mass while the dotted line indicates the reaction Q-value corresponding to the $^9\text{Li} + n$ threshold.

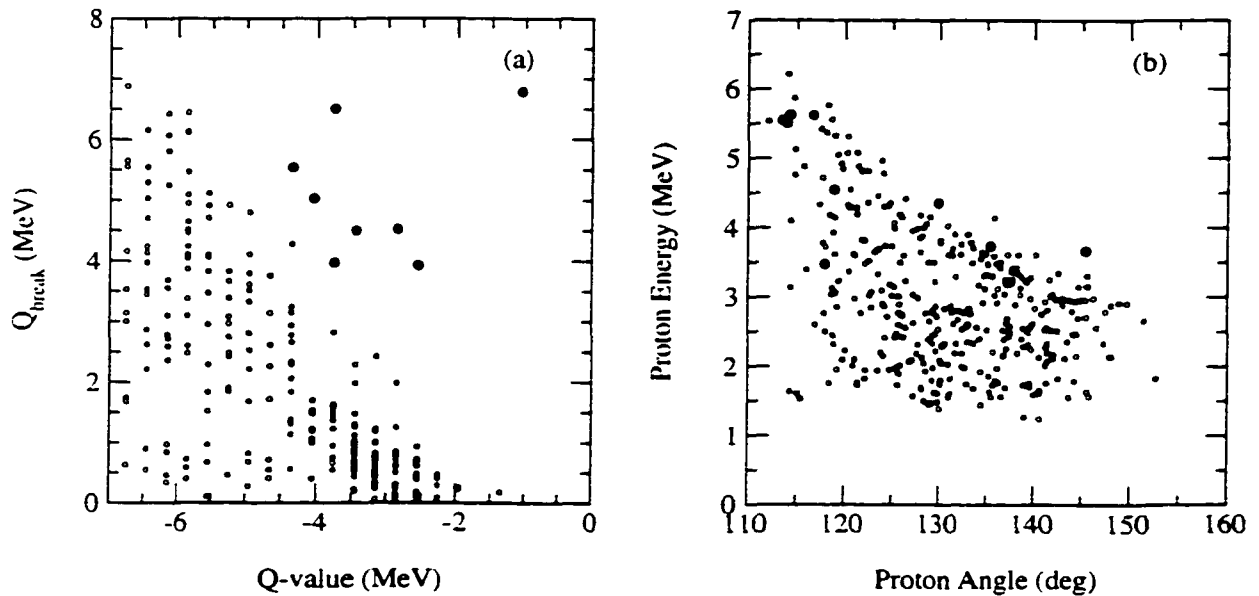


Figure 5.4. (a) Q_{break} vs Q -value for the Strip detector data from Fig. 5.3(b). (b) Proton Energy vs Proton Angle for the Strip data. In both cases, the solid dots indicate the events which do not have the proper correlation between Q_{break} and the reaction Q -value.

be deduced from the position of these events in the proton kinematic plot for the strip detectors. This is shown in Figure 5.4(b) as the solid circles, which can be compared with the location of the remaining events that are shown as the open circles. The fact that almost half of the uncorrelated events lie in a band near 5.5 MeV, corresponding to the energy of the alpha line from the ^{241}Am source, indicates that these uncorrelated events were very likely due to random coincidence events and not true (d,p) events. This would also explain why no such events are visible in the CD data since the number of random coincidences that were calculated for these detectors was essentially zero. Since these uncorrelated events are relatively well separated from the correlated data, they can be subsequently removed from the data.

While the correlation is relatively strong between the reaction Q-value and Q_{break} at small Q_{break} values, the fact that the correlation between the two gets broader at higher excitation energies raises questions as to whether the events observed at the higher excitation energies were measured properly, or if there is any indication of other background processes that are present in the data. To ascertain the nature of the events at large excitation energies, an attempt was made to determine what relationship, if any, could be made between the measured Q-value spectra of the (d,p) reaction and the measured angles of the outgoing ${}^9\text{Li}$ particle from the spectrograph. In Figure 5.5, the profile of the reconstructed ${}^9\text{Li}$ angles at the target, a_{target} and b_{target} , in coincidence with (a) Strip #1, (b) Strip #2 and (c) Strip #4 are presented. In each plot, the black solid circles represent events with reaction Q-values > -4.05 MeV, the red solid circles represent events with Q-values ranging from -4.05 MeV to -6.35 MeV, and the open black circles representing events with Q-values < -6.35 MeV. As is evident by comparing the data from the three different strip detectors, the location of the large Q-value events with respect to the two reconstructed ${}^9\text{Li}$ angles vary depending on which strip detector measured the proton. For instance, in the case of Strip #1 (Fig. 5.5(a)) which detects protons moving primarily in the + x direction and is centered about the y-axis, the events with high Q-values are centered at approximately -30 mr in a_{target} , indicating that all of these events entered into the spectrograph moving in the -x direction. A similar correlation is seen in Strip #2 (Fig. 5.5(b)) which is located slightly above the optical axis in the x-direction and is offset from the optical axis in the -y direction. In this case, ${}^9\text{Li}$ particles which are associated with high Q-value events enter the spectrograph moving in the + y direction and are nearly centered in the x direction. The fact that the direction of the detected ${}^9\text{Li}$ in the spectrograph is correlated with the Strip detector that detected the outgoing proton in coincidence indicates that the two detector systems are not

measuring random coincident events but are measuring particles from the same reaction. Furthermore, at small breakup energies, the motion of ${}^9\text{Li}$ is essentially the same as the motion of ${}^{10}\text{Li}$ prior to its breakup. Hence the correlation between the detected ${}^9\text{Li}$ motion and the proton motion is strongest when the excitation energy of the ${}^{10}\text{Li}$ nucleus is small corresponding to a larger Q-value for the (d,p) reaction. Due to the inverse kinematics of the reaction, the large spread in proton angles that is detected by an individual strip detector (approximately 30°) corresponds to a very small spread in the angle for the ${}^{10}\text{Li}$ nucleus (approximately 1.5° or 26 mr). Hence, the distribution of events at larger Q-values in Fig. 5.5 is centered about a central point which corresponds to the direction of the ${}^{10}\text{Li}$ motion prior to its breakup.

As the excitation energy of ${}^{10}\text{Li}$ becomes larger, the range of angles at which ${}^9\text{Li}$ is emitted in the lab relative to the original motion of ${}^{10}\text{Li}$, referred to as the breakup angle θ_{br} , also increases. As a result, those events in Fig. 5.5 which correspond to larger excitation energies in ${}^{10}\text{Li}$ cover a larger range of planar angles about the same point as the events corresponding to smaller excitation energies. This correlation between the excitation energy of ${}^{10}\text{Li}$ and the breakup angle is also evident in Figures 5.6(a) and (b), in which the (d,p) Q-value is presented as a function of the measured breakup angle, θ_{br} for the CD and Strip detectors, respectively. In both cases, a relatively sharp upper edge is apparent in both distributions which is indicative of a limit in θ_{br} due to the kinematics of the breakup. The uncorrelated events that were gated in Fig. 5.3 for the strip detectors appear above the upper edge of the distribution as indicated by the solid dots in Fig. 5.6(b). While the upper edge to the distribution is quite pronounced, a lower edge is much more diffuse. The upper edge to the distributions shown in Fig. 5.6 is primarily due to the kinematics of the breakup of ${}^{10}\text{Li}$ in the lab, but the diffuse lower edge of the distribution indicates a possible limitation in the experimental technique in detecting

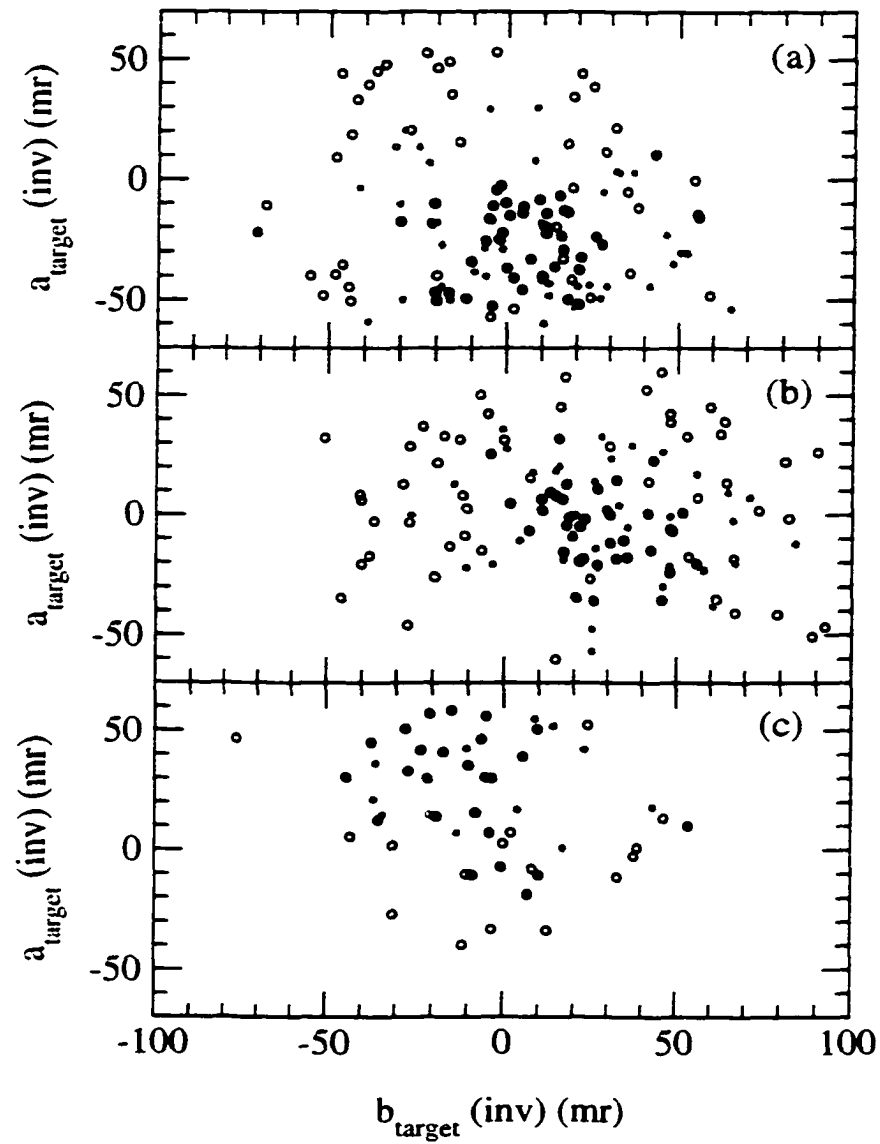


Figure 5.5. a_{target} vs b_{target} as reconstructed from the spectrograph information for the outgoing ${}^9\text{Li}$ measured in coincidence with the proton detected in (a) Strip #1, (b) Strip #2, and (c) Strip #4. In each figure, the black filled circles are events with the (d,p) Q-value > -4.1 MeV, the gold filled circles are events with Q-values ranging from -4.1 MeV down to -6.3 MeV, and the open black circles are events with $Q < -6.3$ MeV.

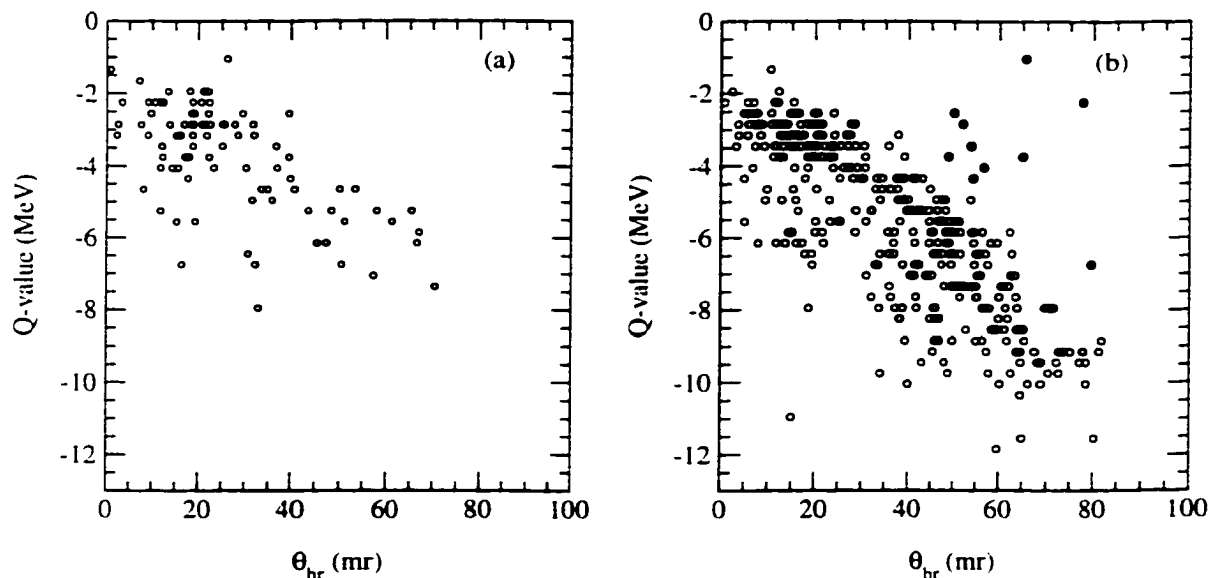


Figure 5.6. Q-value of the (d,p) reaction as a function of ^{10}Li laboratory breakup angle θ_{br} for (a) the CD and (b) the Strip detectors. The solid dots in (b) are the uncorrelated events which were selected in Fig. 5.4

small breakup angles at larger excitation energies for ^{10}Li . Such a limitation would imply that the efficiency of the experimental setup in detecting the events of interest was dependent on the excitation energy of the ^{10}Li nucleus that was produced in the reaction. This energy dependent detection efficiency would distort the measured reaction Q-value and Q_{break} spectra and thus would have to be corrected for in the analysis of the data. While an estimate could be made for this efficiency function based on the range of breakup angles that were not measured at a given reaction Q-value relative to the observed upper edge of the distribution, the best method for determining this efficiency function is through the use of Monte Carlo calculations which will be discussed in the next section.

5.2 Monte Carlo Simulation

5.2.1 Overview

In order to relate the results of this experiment with the physical processes that occurred in the production and breakup of ^{10}Li , the response of the experimental setup in detecting the events of interest must be fully understood and accounted for in the analysis of the data. Because of the complex nature of the $^9\text{Li}(d,p)$ reaction, a series of Monte Carlo calculations were performed to determine the effects that the experimental setup had on the measured results. In a Monte Carlo calculation, the details of the experimental setup are folded in with the physical processes of the reaction through the random sampling of the the pertinent probability density distributions. Sampling the distributions in this manner allows for the generation of simulated sets of data which are comparable with the experimental data and thus allow for a direct comparison between the theoretical physics involved in the reaction and the measured data. [53]. The specific experimental details that are often incorporated into Monte Carlo calculations include such quantities as the resolution and geometry of the various detector systems, the size and divergence of the incident beam, and the effects of the target on the particles that are detected in the experiment. The essential benefit in performing Monte Carlo calculations is the fact that it utilizes numerical integration techniques to calculate the quantities of interest. For instance, the intrinsic detection efficiency for an experimental setup can be calculated using a Monte Carlo simulation by determining the number of simulated events that were detected in the experimental setup for a given number of reaction events which were generated in the simulation. The calculated efficiency for the experiment is then simply the ratio of the number of detected events to the number of generated events with an uncertainty equal to the statistical errors in the two numbers added in quadrature. Hence, a calculation which analytically involves

the integration of a multi-dimensional function over several variables reduces to the calculation of a simple ratio of two numbers.

In this particular experiment, Monte Carlo calculations were needed to determine several different quantities which were not directly attainable from the data nor through the use of other techniques. One important quantity that needed to be determined was the intrinsic detector efficiency of the experimental setup for coincidence events. Based on Fig. 5.6, this efficiency function is dependent on the ^{10}Li excitation energy. The reason for this is that the finite angular and momentum acceptance of the spectrograph limits the range of ^9Li momentum which can be detected in coincidence with the silicon detectors. If the detection efficiency were also dependent on the proton scattering angle, then the measured angular distribution of the proton events would also have to be corrected in order to determine the proper Jacobian for transforming the angular distribution as measured in the lab into the center of mass reference frame where it could be compared with theoretical predictions.

Another important quantity that was needed from the Monte Carlo calculation was the energy resolution of the experimental setup in measuring the Q-value of the (d,p) reaction as well as the subsequent breakup of ^{10}Li . Although an estimate of the resolution could be made based on the measured resolution of the ground state Q-value for the $^{13}\text{C}(\text{d,p})$ reaction, enough differences existed between the conditions of the two experiments that it was necessary to determine the resolution of the experiment using a Monte Carlo simulation.

5.2.2 Event Generation

The $^9\text{Li}(\text{d,p})$ events were generated in the Monte Carlo simulation using the incident beam parameters that were measured at the target by S803 and S804. These

measured incident beam parameters were reproduced in the simulation using one of two possible techniques. If the shape of the distribution for a particular parameter was Gaussian in nature, the subroutine GASDEV [55] was used to transform a uniform distribution of random numbers that was generated by the random number generator RAN2 [55] into a Gaussian distribution. If the distribution of a particular incident parameter was not Gaussian, then the incident beam parameter was selected using the rejection method, in which two random numbers chosen from uniform distributions are used to indicate the location of the event in a two dimensional plot that encompasses the probability function of interest [53]. If the location of the event lies outside the region that is defined by this function, as illustrated in Figure 5.7(a) [where the set of random numbers (x_1, y_1) lie outside the measured distribution for incident beam parameter a_{inc}] then the event is rejected in the Monte Carlo simulation and a new set of random numbers are generated until a set of numbers which lie inside the region defined by the function is selected. This is the case for the second set of random numbers (x_2, y_2) in Fig. 5.7(a). Once this occurs, the value of the random number x_2 is taken to be the value of the beam parameter of interest for the simulated event. The results of using the rejection method to generate the a_{inc} distribution is presented in Fig. 5.7(b), where the black histogram is the simulated a_{inc} distribution while the red circles are the measured a_{inc} distribution.

Along with ensuring that the simulated distribution for each incident parameter was consistent with the distribution that was measured in the experiment, the correlations between the various incident beam parameters were also reproduced in the Monte Carlo distribution. An example of a correlation that was observed between the incident beam parameters is shown in Figure 5.8(a), in which the measured angle at the target b_{inc} is shown as a function of the measured target position, y_{inc} for the

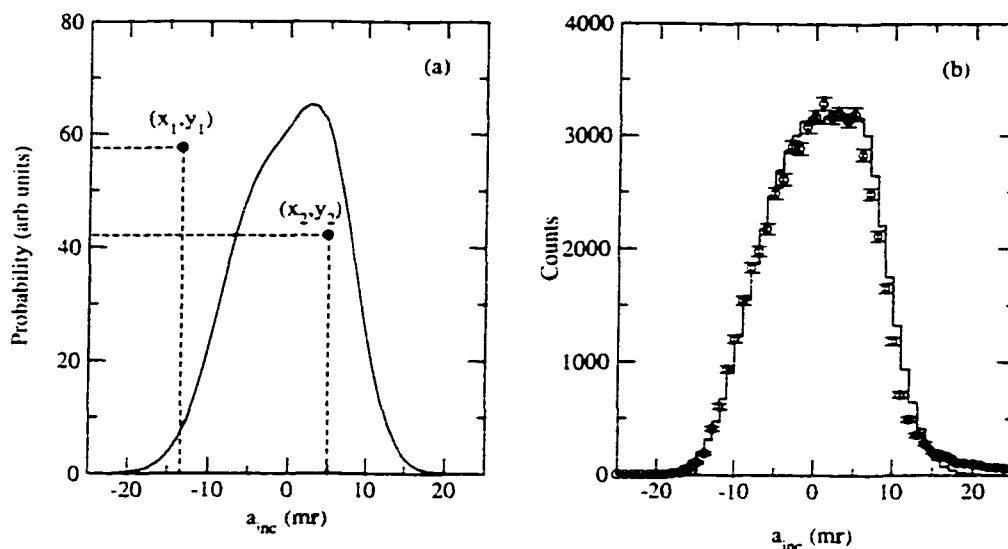


Figure 5.7. (a) Illustration of the rejection method in producing the a_{inc} distribution. (b) Resultant a_{inc} distribution from the Monte Carlo calculation (solid line) compared with the measured a_{inc} distribution from a direct beam run (red circles).

direct beam Run# 62. To simulate the correlation between these two incident beam parameters, the distribution was projected onto axes that were parallel and perpendicular to the central axis of the distribution shown by the red line in Fig. 5.8(a). This was done by first rotating the distribution counter-clockwise in the b - y plane about its center by an amount equal to the angle between the central axis of the distribution and the original b_{inc} axis, in order to remove the correlation between the two parameters. After rotating the distribution this way, projections were made onto the two rotated axes y_{rot} and b_{rot} . The result of this projection is shown in Fig 5.8(b) where no correlation is evident between the two rotated axes b_{rot} and y_{rot} in the measured distribution. The parameters b_{rot} and y_{rot} were then selected at random in the Monte Carlo calculation based on these measured distributions and transformed into b_{inc} and y_{inc} by applying a clockwise rotation on the two parameters with the appropriate angle. With the application of this clockwise rotation on the initially selected parameters in the simulation, the correlation between b_{inc} and

y_{inc} is properly simulated as is evident in Fig. 5.8(c) which shows the simulated b_{inc} as a function of y_{inc} for 2500 simulated events. The grey line in Fig. 5.8(c) is the same as shown in Fig. 5.8(a).

Once the parameters for the incident ${}^9\text{Li}$ particle had been determined for a given simulated event, the location of the (d,p) reaction within the target was chosen at random to account for the possible variations in the distance traveled by the incident ${}^9\text{Li}$ particles prior to the occurrence of the (d,p) reaction. In addition to varying the location of the reaction with the target, energy straggling effects due to the random interactions between the individual particle and the target atoms were calculated for both the incident and exiting ${}^9\text{Li}$ particles as well as the exiting proton. The energy straggling within the target was assumed to have a Gaussian distribution with a mean of zero and a width that was determined on an event by event basis using calculations performed with the code STOPX [52], which accounted for the energy of the particle as well as the amount of material the particle traveled through in the target. Multiple scattering effects within the target due to small angle Coulomb scattering between the particle and the atoms within the target were also considered in the simulation. The effects of multiple scattering within the target were considered for both the angle at which the particle moved through the target, as well as in the final position of the particle. The width of the angular straggling distribution that resulted from the multiple scattering, θ_{stra} , was determined based on STOPX calculations for the given energy of the particle and the effective target thicknesses that the particle passed through in the reaction. Once the width of the angular straggling was calculated, the change in the position of the particle was determined from [56]:

$$\Delta y = \frac{z_1 L \theta_o}{\sqrt{12}} + \frac{z_2 L \theta_o}{2} \quad (5.7)$$

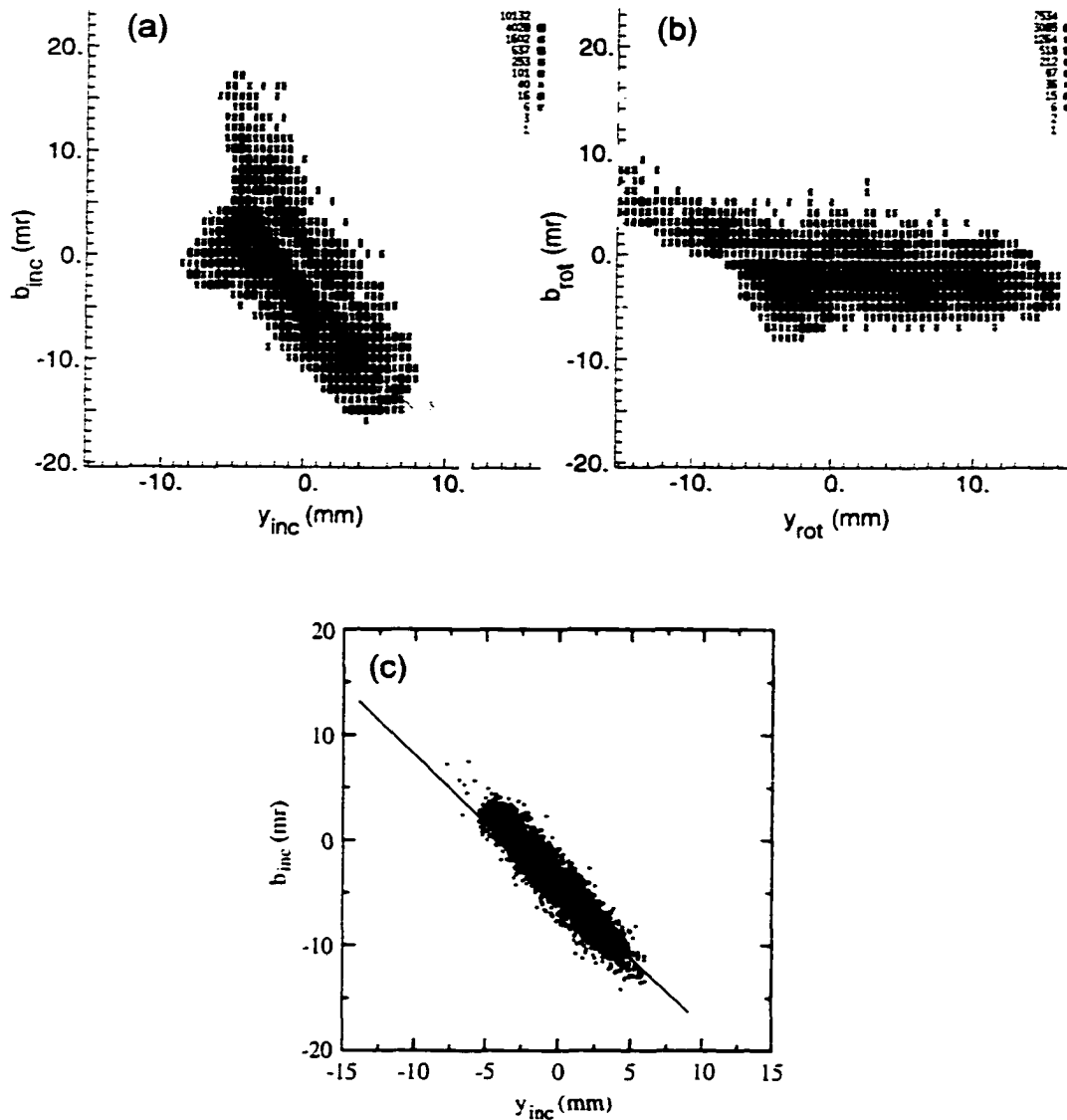


Figure 5.8. (a) Measured b_{inc} as a function of y_{inc} for the direct beam Run #62. (b) Rotated b_{inc} as a function of the rotated y_{inc} used to determine the projections of the two variables onto the rotated axes. (c) b_{inc} vs y_{inc} for 2500 events generated in the Monte Carlo simulation. The line in Figures (a) and (c) represents the slope used to determine the angle for rotating the spectrum.

where Δy is the change in the position of the particle in the y-direction. z_1 and z_2 are random numbers chosen from a Gaussian distribution with a mean of zero and standard deviation of one, L is the physical distance traveled through the target material, and θ_o is related to the width of the angular straggling distribution θ_{stra} that was determined from STOPX by:

$$\theta_o = \frac{\theta_{stra}}{\sqrt{2}} \quad (5.8)$$

The change in the position of the particle due to the angular straggling with the target was treated equally in both directions, with a separate set of random variables z_1 and z_2 selected for each direction. The change in the planar angles of the particle, a and b , was calculated from [56]:

$$\Delta a = z_2 \Theta_o \quad (5.9)$$

where Δa is the change in the planar angle, a , of the particle.

With the location of the reaction determined within the target, the scattering and azimuthal angles for ^{10}Li , θ_{Li} and ϕ_{Li} respectively, were randomly chosen in the center of mass frame for the (d,p) reaction along with the excitation energy E_x for ^{10}Li in order to generate the energy and momentum of the outgoing proton from the $^9\text{Li}(d,p)$ reaction. To simplify the Monte Carlo calculation, the possibility of polarization of the reaction products was neglected, allowing for ϕ_{Li} to be chosen from a uniform distribution for all of the Monte Carlo calculations that were performed. In the initial calculations, the ^{10}Li nucleus that was produced in the simulation was assumed to consist of a neutron and ^9Li core which was in its ground state configuration. Two different distributions for θ_{Li} were considered depending on the quantities that were being calculated in the Monte Carlo simulation. An isotropic distribution was used for θ_{Li} when calculating the efficiency of the experimental setup in detecting the (d,p) events as a function of the proton scattering

angle. The angular distributions that were calculated with the coupled channels code FRESKO [31] were used when directly comparing the measured angular data with theory.

In addition to selecting different angular distributions for the ^{10}Li center of mass scattering angle, different distributions were considered in selecting the excitation energy for ^{10}Li . To determine if the efficiency of the experimental setup was dependent on the breakup energy of ^{10}Li , a uniform excitation energy distribution was used in order to probe the entire phase space that was measured in the experiment. In calculating the resolution of the experiment in measuring either Q-value of the (d,p) reaction or the Q-value of the breakup of ^{10}Li , a delta function was used when selecting E_x so that the resulting shape and width of the spectra was only due to the effects of the experimental setup on the spectra.

Assuming the (d,p) reaction is two body in nature, the random selection of these reaction parameters immediately defines the motion for both the ^{10}Li nucleus and the proton in the center of mass frame and subsequently in the laboratory frame, where the motion of the incident particle is by definition along the z-axis. In order to determine if the proton was detected by a silicon detector, however, it is necessary to describe the motion of the proton in the reference frame where the z-axis is defined as the optical axis of the spectrograph. Hence, Eqn. 5.4 was used to transform the coordinates of the proton and outgoing ^{10}Li from the reference frame defined by the incident particle to the reference frame defined by the optical axis.

In order to assume that the (d,p) reaction was two body in nature, the breakup of ^{10}Li must occur at some time after the proton had been emitted from the reaction so that the emission of the neutron from ^{10}Li has no effect on the motion of the proton. This implies that the location of the breakup of ^{10}Li within the target is slightly different than the location of the initial (d,p) reaction. However, because

the relatively short lifetime of ^{10}Li (approximately 10^{-23} s), the distance the ^{10}Li would travel before breaking up would be extremely small. Thus, the simulation assumed that the breakup of ^{10}Li occurred at essentially the same location within the target as the initial (d,p) reaction.

The breakup of ^{10}Li was assumed to be isotropic in the ^{10}Li rest frame and independent of the (d,p) reaction. The magnitude of the velocity of ^9Li in the breakup center of mass frame is given by [54]:

$$\beta_{Li,cm} = \sqrt{\frac{2m_n(Q_{break})}{m_9(m_9 + m_n)}} \quad (5.10)$$

where Q_{break} is related to the excitation energy of ^{10}Li that was produced in the (d,p) reaction by:

$$Q_{break} = Q_o + E_x \quad (5.11)$$

Here, Q_o is the difference between the ground state mass of ^{10}Li and the masses of ^9Li and a neutron:

$$Q_o = m_{10} - m_9 - m_n \quad (5.12)$$

In the simulation, $Q_o = 0.073$ MeV based on the mass excess of ^{10}Li that was measured in this experiment of 33.098 MeV/ c^2 . The momentum of ^9Li in the center of mass frame is given by:

$$p_{Li,cm} = \frac{m_9\beta_{Li,cm}}{\sqrt{1 - \beta_{Li,cm}^2}} \quad (5.13)$$

With the momentum of ^9Li now defined in the breakup center of mass frame, the motion of ^9Li can then be determined in the laboratory frame by performing a Lorentz transformation on the reference frame based on the motion of ^{10}Li that was determined from the (d,p) reaction. Once the ^9Li motion had been properly

transformed into the laboratory frame, it was then be tracked through the S800 spectrograph so as to determine whether or not the simulated event was detected in the focal plane of the spectrograph.

5.2.3 Detection of simulated events

Once an event had been generated, the next step in the Monte Carlo simulation was determining if the outgoing proton and ${}^9\text{Li}$ were detected in coincidence in the experimental setup. To simulate the acceptance of the S800 spectrograph, a series of 8 COSY transfer maps were used, which transformed the positions, angles, and momentum of the outgoing ${}^9\text{Li}$ particles at the target into a measurement of the position at each of the physical apertures that were present within the spectrograph. These transfer maps were generated based on the measured $B\rho$ settings of the spectrograph for the reaction runs and were applied sequentially in the simulation, in the order in which the particle encounters the various apertures in the spectrograph. If the position of the particle at a given aperture was larger than the physical dimensions of the aperture, then the event was assumed to have not passed through the aperture and hence was not detected in the focal plane of the spectrograph. In Table 5.1, the physical limits of the apertures for each beam line element are presented with respect to the central axis of the spectrograph [48]. If the ${}^9\text{Li}$ particle successfully passed through all eight of these apertures, then the position and angle of the particle was determined at S801 based on the forward spectrograph transfer map in order to ascertain if the particle hit the active area of the detector. As a final check to make certain that the particle was properly detected in the focal plane, a final transfer map was applied, transforming the generated position and angle of ${}^9\text{Li}$ at the target up to the E1 scintillator at the end of the focal plane. Only those events which passed through the active area of S801 and hit the active area of the

Table 5.1. Size of limiting apertures within S800 spectrograph.

Spectrograph Element	X Limit (mm)	Y Limit (mm)
Q1	$\pm 120.$	$\pm 120.$
Q2	$\pm 210.$	$\pm 210.$
D1	$\pm 340.$	± 76.2
D2	$\pm 340.$	± 76.2

E1 scintillator were counted as events which were detected by the spectrograph in the simulation.

To test this method of tracking the events up to the focal plane of the spectrograph, a Monte Carlo simulation was performed which sent the direct ${}^9\text{Li}$ beam up to the focal plane using COSY generated transfer maps that were created with the $B\rho$ of the spectrograph set to measure the direct beam. Figure 5.9 shows the resulting focal plane distributions that were produced in the simulation as compared with the measurements that were made during the actual experiment. While the results from the simulation are not in perfect agreement with the measured focal plane data, the fact that all of the simulated distributions have the same central location as well as the same size as the measured distributions indicated that this method of tracking events up to the focal plane was accurate in the simulation. A second Monte Carlo simulation was performed in which the simulated direct beam was sent into the spectrograph using transfer maps that were generated with the reaction $B\rho$ setting. The results of these simulations confirmed that it was not possible for direct beam events to reach the focal plane of the spectrograph when the magnetic fields were set to measure the reaction products.

The response of the silicon detectors in measuring the energies and angles of the outgoing protons from the (d,p) reaction was simulated by first determining if a proton would pass through a region that was occupied by the active area of the

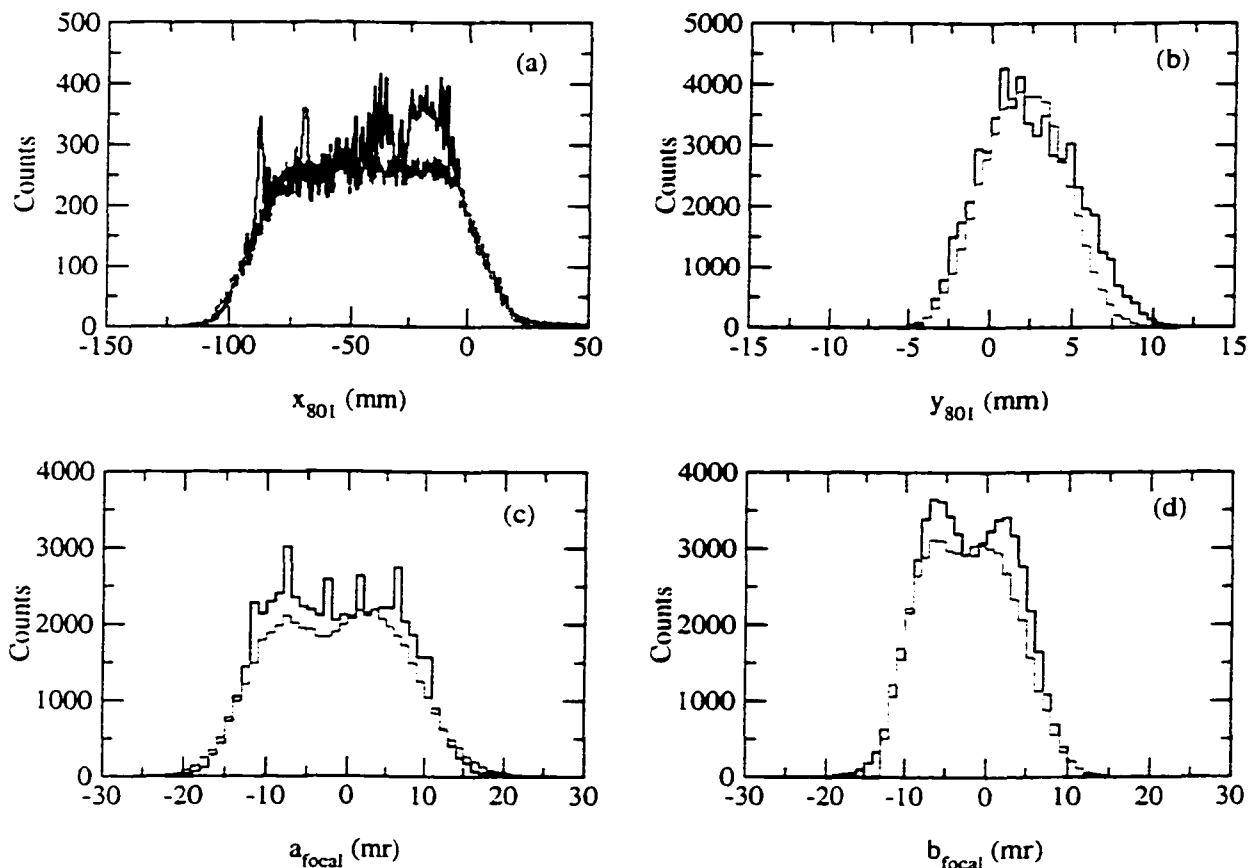


Figure 5.9. Comparison between data (black curve) and the Monte Carlo results (gold curve) for (a) x_{801} (b) y_{801} (c) a_{focal} and (d) b_{focal} for a run with no target in place and the spectrograph set to measure the direct ${}^9\text{Li}$ beam. In all of the figures, the data have been scaled down by a factor of 15 to match the Monte Carlo results.

detector assuming that the detector was positioned with the measured offsets that were determined in the $^{13}\text{C}(\text{d,p})$ experiment with respect to the optical axis. Once a proton was tracked onto the active area of a silicon detector, its exact location was then determined so as to find the specific sector and ring which was triggered in the case of a CD detector, or the specific strip in the case of the Strip detector. The energy that was measured in that silicon channel was then simulated by adding a random number to the proton energy that was selected from a Gaussian distribution with a mean of 0 and a width determined by the relative energy resolution for that channel that was determined using the mixed alpha source. (See Tables A.1 and A.2 for energy resolutions for the various silicon channels) If the measured energy of the proton was greater than the energy threshold that was used in the analysis (to cut out the noise in the channel), then the proton was considered to have been detected in the event. The measured angle of the proton was then determined based on the specific ring and sector which were triggered in the event in the case of the CD detectors, or based on the measured position of the event along the strip. As was done with determining the measured energy of the proton, the position along an individual strip was folded with a Gaussian distribution having a width based on the alpha calibrations in order to simulate the position along the strip that was measured by the strip detector.

Along with including the resolutions of the silicon detectors in measuring the energy and angle of the proton in the simulation, resolutions were also considered for the target positions and angles of the incident beam and the reconstructed outgoing ^9Li based on the resolutions of the forward and inverse target parameters that were measured for the direct beam runs. These simulated parameters were then processed through the same routines that were used in the analysis of the real data for those simulated events in which the proton and ^9Li were both detected

in the event, in order to reproduce the effects of the experimental setup on the measurements. These simulated results could then be directly compared with the data, and used to apply the appropriate efficiency corrections.

5.2.4 Monte Carlo results

To confirm that the Monte Carlo calculation was accurate in simulating the measured results from the ${}^9\text{Li}(d,p)$ reaction, the resulting focal plane distributions from the calculation were compared with the measured data. Figure 5.10 shows the focal plane parameters for all of the ${}^9\text{Li}$ particles that were detected by the spectrograph with the CD_2 target in place (labeled as raw data in the figure), along with what was measured in coincidence with the silicon detectors (blue histogram) and the Monte Carlo results for the outgoing ${}^9\text{Li}$ particles assuming a uniform range of excitation energies for ${}^{10}\text{Li}$ from 0 to 10 MeV (gold histogram). With the exception of b_{focal} , a good agreement can be seen between the simulated distributions and the measured coincidence distributions. The difference that is observed between the simulated and measured distributions for b_{focal} is primarily due to errors that were associated with the forward map used in tracing the particles from the target to the focal plane and are not necessarily due to problems in the simulation. This discrepancy between the simulation and the data for b_{focal} affects the inverse reconstructed y_{target} position and has only a slight effect on the inverse reconstructed b_{target} due to the fact that b_{focal} is strongly dependent on y_{target} and only weakly dependent on b_{target} . Since the inverse reconstructed y_{target} is only used in the analysis to ensure that the event came from the target material and not the aluminum frame of the target, discrepancies in the inverse reconstructed y_{target} distribution between the simulation and the data will have little consequence on the interpretation of the data.

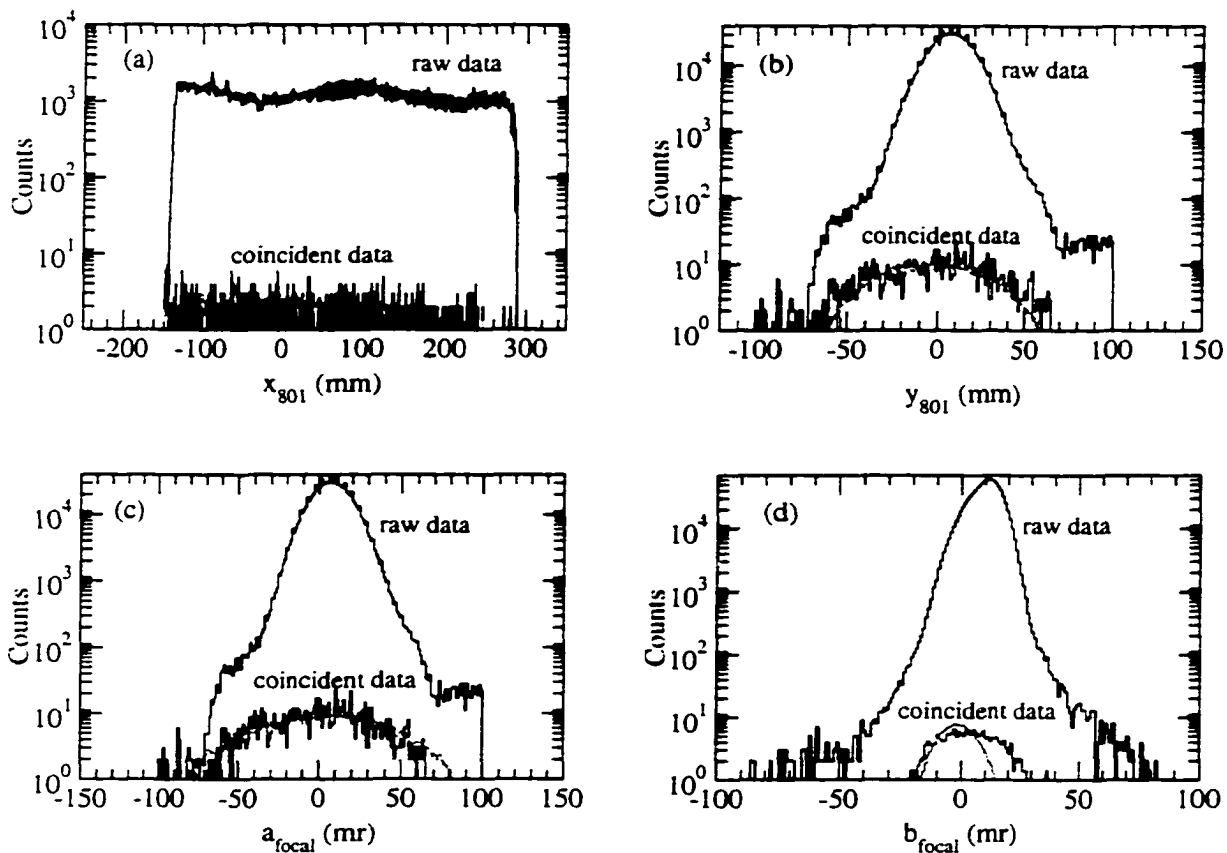


Figure 5.10. Comparison between data (blue histogram) and Monte Carlo results (gold histogram) for (a) x_{801} (b) y_{801} (c) a_{focal} and (d) b_{focal} with the CD_2 target in place. In all of the figures, the simulated results have been scaled to match the measured data.

Another issue concerning the simulated focal plane parameters is that the range of values that were measured for x_{801} during the experiment were smaller than the known active area of the detector. Specifically, the lower edge of the measured distribution occurs at $x_{801} = -150$ mm whereas the active area of S801 is known to extend to $x_{801} = -203$ mm based on the pulser calibration runs that were performed at the end of the experiment. It turned out that this cutoff in the measured x_{801} position was due to the presence of a beam block in the focal plane which had been installed prior to this experiment in order to allow for the possible blocking of the direct beam in cases where the $B\rho$ of the spectrograph was lower than the $B\rho$ of the direct beam. To block the higher momentum particles from the direct beam, the beam block was positioned near the top of the focal plane which corresponds to the $-x_{801}$ direction. Because of its recent installation, the mechanism for moving the beam block in and out of the focal plane was not working at the time of this experiment and thus the position of the beam block remained fixed throughout the experiment. The presence of this beam block in the focal plane caused a reduction in the momentum acceptance of the spectrograph by effectively reducing the active area of x_{801} . In order to properly simulate the response of the focal plane, this focal plane beam block was included in the Monte Carlo simulation resulting in the simulated x_{801} distribution that is presented in Fig. 5.10(a).

Because of the reduction in the momentum acceptance of the spectrograph, this focal plane beam block also reduced the efficiency of the experimental setup for detecting coincidence events. This is illustrated in Figures 5.11(a) and (b) where the excitation energy for ^{10}Li , E_x , is presented as a function of the simulated kinetic energy of the outgoing ^9Li that resulted from the breakup of ^{10}Li for those events in which the protons were detectable by the CD and Strip detectors, respectively. In both Figs 5.11(a) and (b), the solid gold circles are events which were detected

at the focal plane, the open black circles are events which did not reach the active area of S801, and the open green squares are events which hit the focal plane beam block. As is evident by comparing the range of kinetic energies that are detectable by the spectrograph relative to the energy range that is possible from the breakup of ^{10}Li , the effect of the focal plane beam block on the efficiency of the setup is more pronounced at excitation energies less than 1 MeV which is where the structure of interest is located. Hence, a reduction in this energy region hampers the ability of the experiment to determine the nature of the low-lying structure in ^{10}Li .

In addition to reducing the efficiency of the experiment setup, the focal plane beam block also slightly reduces the range of θ_{br} that are detectable for a given range of E_x , or equivalently, a given range of reaction Q-values. At any given reaction Q-value, the minimum and maximum kinetic energies of ^9Li that are produced in the reaction corresponds to events which were emitted at 0° and 180° in the breakup center of mass reference frame, respectively. These center of mass angles correspond to the outgoing ^9Li particles moving parallel to the motion of ^{10}Li in the lab. Because the spectrograph only accepts a specific range of kinetic energies for ^9Li , the minimum detectable θ_{br} varies as a function E_x . As the range of the ^9Li energies in the lab grows larger with increasing excitation energy of ^{10}Li , the minimum θ_{br} that is detectable by the spectrograph grows larger as well. While the minimum θ_{br} that is observed in the experiment for a given reaction Q-value is dependent on the properties of the spectrograph, the maximum detectable θ_{br} is only dependent on the kinematics of the ^{10}Li breakup due to the fact that the $B\rho$ of the spectrograph was set to detect the central energy region of the outgoing ^9Li nuclei which corresponded to the emission of ^9Li at 90° in the center of mass frame.

These restrictions in the observable range of θ_{br} result in a strong correlation in the Monte Carlo simulation between the Q-value of the (d,p) reaction and θ_{br}

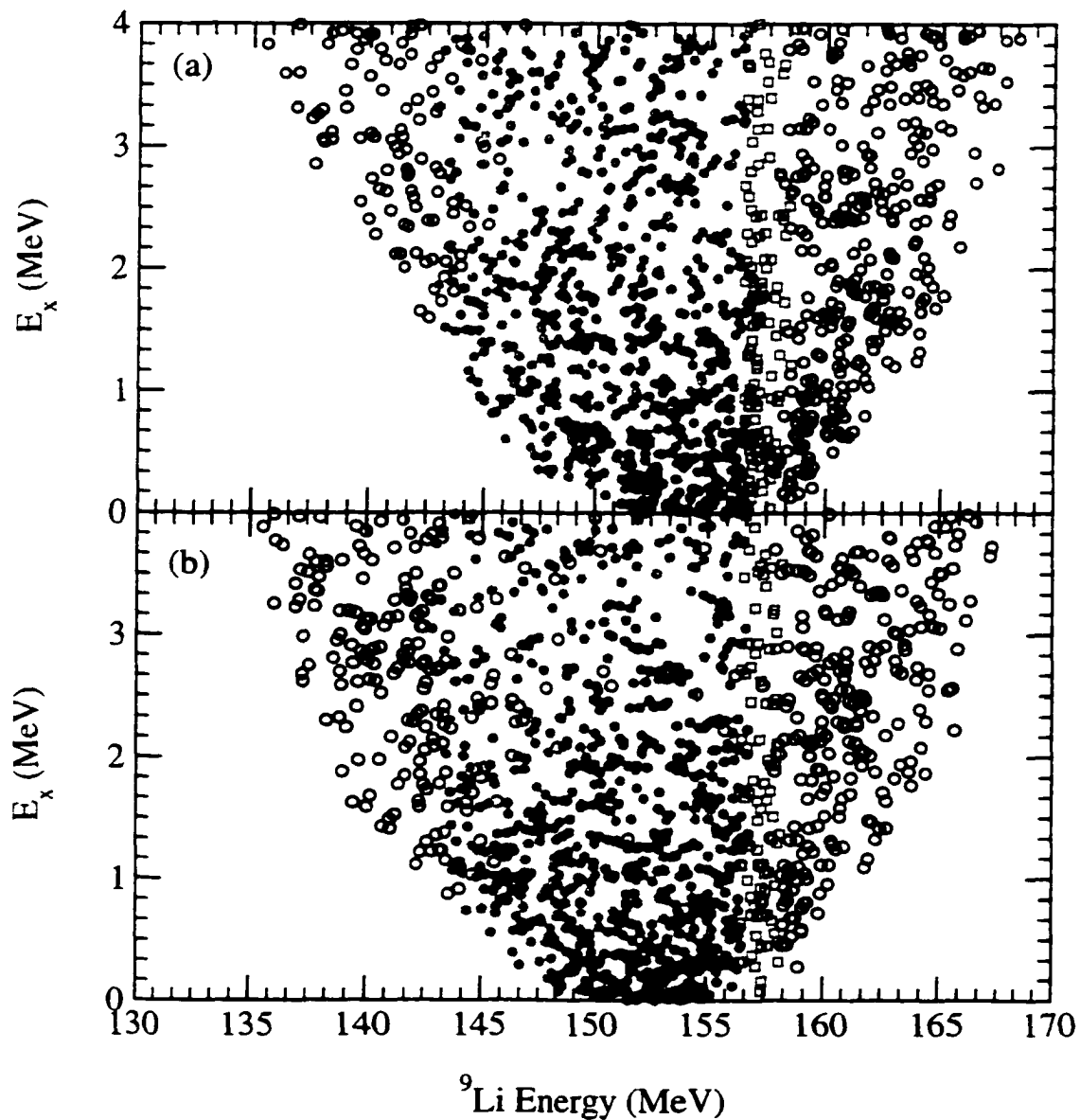


Figure 5.11. Simulated excitation energy of ^{10}Li E_x as a function of the kinetic energy of the outgoing ^9Li for events in which the corresponding proton was detected by (a) the CD detectors and (b) Strip detectors. The solid gold circles indicate events which were detected by S801 and S802, the open black circles indicate events which were not detected in the focal plane, and the open green squares are the events which hit the beam block in front of S801.

which defines a narrow region of acceptable events as is evident in Figures 5.12(a) and (b) where the simulated results (light blue circles) for 2000 coincidence events are shown along with the measured data from the CD and Strip detectors, respectively. For the CD and Strip data, the red circles indicate those events which lie within the simulated region while the open blue circles indicate the data which were considered outside this region. Note that virtually all of the events in the Strip data (Fig. 5.12(b)) that lie at larger Q -values than the simulated results have been previously identified as alpha particles from the ^{241}Am source. (See Fig. 5.4(b)) It is apparent that while a good agreement exists between the data and the Monte Carlo simulation for the upper edge of the distribution for both the CD and Strip data, a number of events in the Strip data extend out beyond the lower edge that is defined by the Monte Carlo simulation. It is also apparent from Figs. 5.12(c) and (d) that the data which lie within the simulated Q -value vs θ_{br} region correspond to the correlated region of the Q_{break} vs reaction Q -value space in agreement with the region that is predicted by the Monte Carlo simulation.

Along with predicting the appropriate correlations that are observed in the data, the Monte Carlo simulation also produces Q_{break} and reaction Q -value distributions which are comparable with the distributions from the gated data as shown in Figure 5.13. In the figure, the simulated distributions (red curves) have been normalized to the data based on the number of coincidence events that were observed for reaction Q -values less than -4.0 MeV in (a) and (b) and for Q_{break} values greater than 1.7 MeV in (c) and (d). This method for normalizing the simulated results with the measured data was used as a first attempt to match that part of the distributions that was believed to correspond to little or no structure in ^{10}Li . Because the Monte Carlo calculation essentially probes the entire phase space that is available in this reaction, the simulated coincidence distributions for the reaction Q -value and Q_{break}

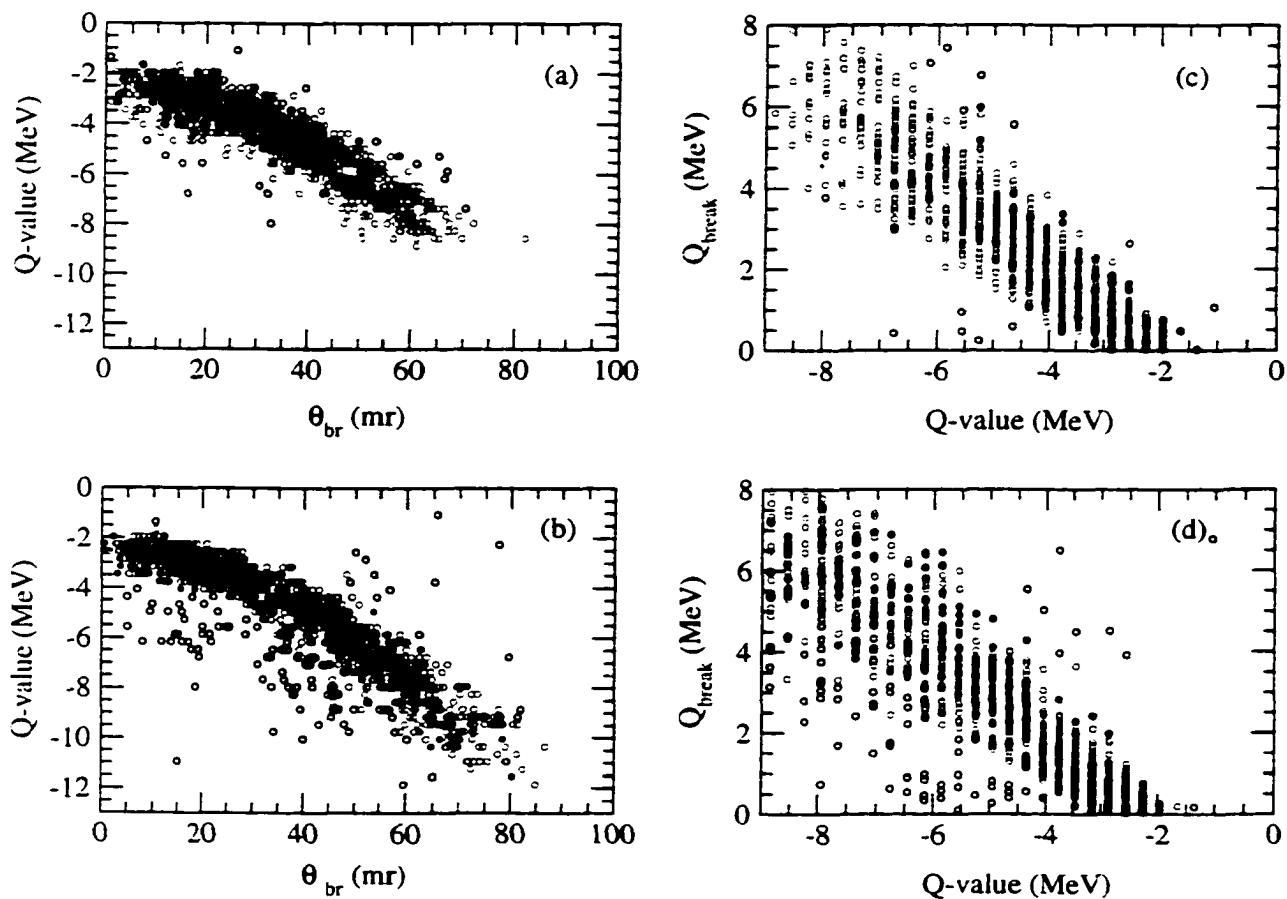


Figure 5.12. (a)-(b) Reaction Q -value as a function of θ_{br} for the CD and Strip detectors, respectively. In the figures, the red circles are the data gated based on the results of the Monte Carlo simulation which assumed the ^9Li core in its ground state (light blue circles), while the blue open circles indicate the data that were not included in the gate. (c)-(d) Q_{break} as a function of the reaction Q -value for the CD and Strip detectors, respectively.

only correspond to the response of the experimental setup in detecting coincidence events. Thus, any deviations in the measured spectra from these simulated distributions are evidence for the presence of structure in ^{10}Li . The fact that the data from the Strip detectors show no significant deviation from the simulated response curve indicate that these detectors had no sensitivity in measuring the structure of ^{10}Li . While the Strip detectors were unable to measure any structure in ^{10}Li , the peak that is present in the CD Q-value and Q_{break} spectra above the simulated response of the detector indicate the detection of one or more states in ^{10}Li . The interpretation of this peak in terms of the structure of ^{10}Li will be discussed in the next section.

While the Monte Carlo simulation appropriately describes the data in the correlated Q_{break} vs Q-value band for both the CD and Strip detectors, it is unable to describe the events in the Strip data which appear at lower Q-values relative to the Monte Carlo predictions in Figs. 5.12(b) and (d). One plausible way to account for these events in the Monte Carlo simulation is to consider the availability of other possible channels for the production or decay of ^{10}Li . The fact that the events which lie below the simulated region are centered at Q-values near -5 MeV for breakup angles less than 10 mr indicate the possible presence of ^{10}Li with a ^9Li core in its bound excited state at $E_x = 2.691$ MeV [32]. To determine if this reaction would explain the events observed in Fig. 5.12, a second set of Monte Carlo simulations were performed in which the ^{10}Li nucleus consisted of a $^9\text{Li}^*$ core and a neutron. In the simulation, the threshold reaction Q-value, Q_o , was adjusted to account for the additional mass energy of $^9\text{Li}^*$ relative to its ground state mass. In detecting the outgoing $^9\text{Li}^*$ nucleus, the simulation assumed that the outgoing $^9\text{Li}^*$ would completely decay to its ground state via gamma emission before being detected in the focal plane of the spectrograph. To properly account for the additional energy

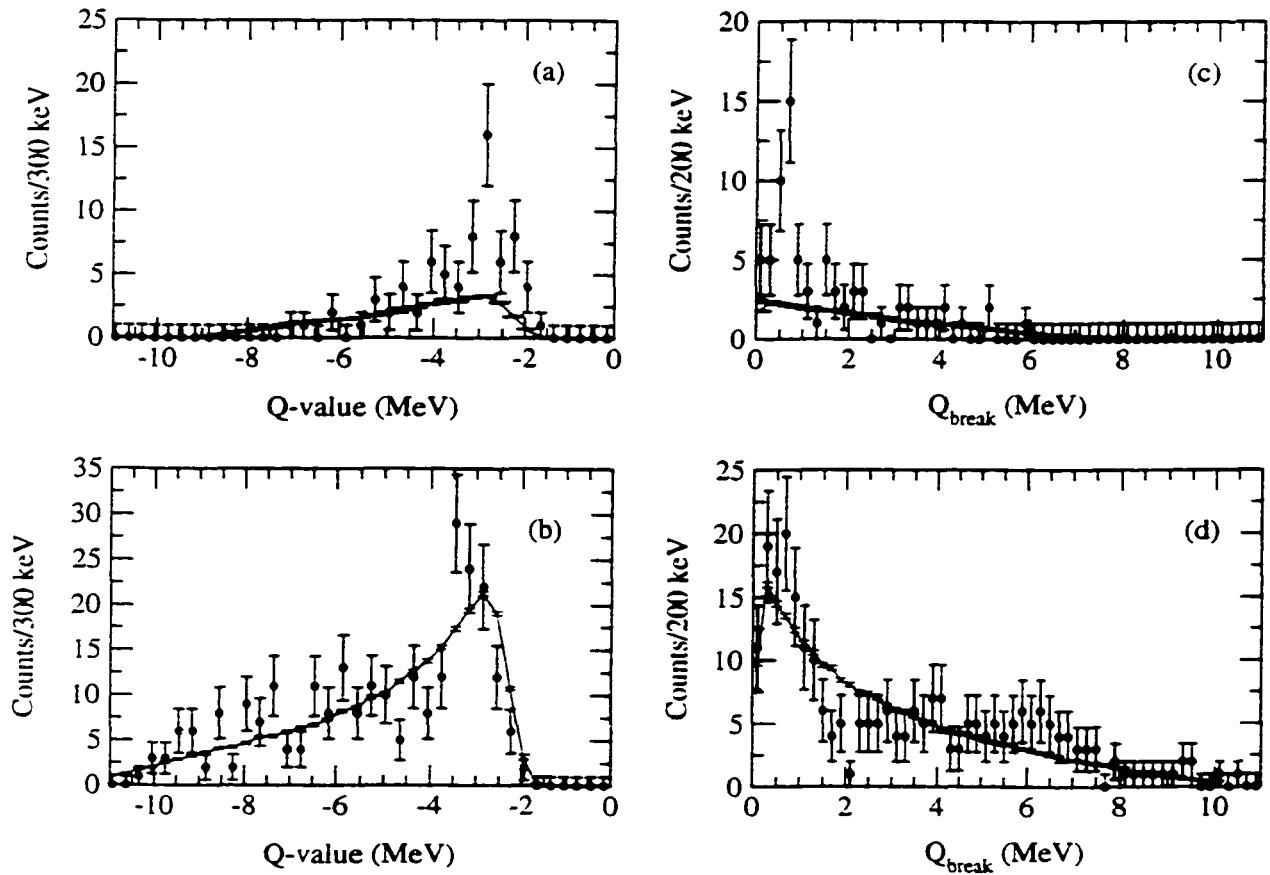


Figure 5.13. (a)-(b) Gated reaction Q -value distributions for the CD and Strip detectors, respectively, (black circles) along with the normalized results of the Monte Carlo simulation. (c)-(d) Gated Q_{break} distributions for the CD and Strip detectors, respectively, with the corresponding normalized Monte Carlo results.

and momentum loss of the ${}^9\text{Li}$ nucleus due to the emission of the gamma ray, two additional angles were chosen at random to describe the direction of the gamma ray relative to the motion of the outgoing ${}^9\text{Li}$ nucleus. Since the emitted gamma ray corresponds to a $1/2^-$ to a $3/2^-$ transition in ${}^9\text{Li}$, an isotropic distribution was chosen for the two angles in the simulation due to the fact that it is equally probable to populate the various sublevels within the final state. As had been done in the previous calculation, E_γ was selected from a uniform distribution in order to probe the available phase space for this particular reaction channel.

The results of this second Monte Carlo simulation are shown as the brown circles in Figure 5.14 along with the results of the original simulation now shown as the yellow circles. As is evident from the figure, the ${}^9\text{Li}^*$ simulation is in good agreement with the events in the Strip data that are at lower Q-values relative to the initial Monte Carlo prediction. Furthermore, the second Monte Carlo simulation also predicts the lower edge of the measured reaction Q-value vs θ_{br} distribution in Fig. 5.14(b). This agreement between the excited-state Monte Carlo simulation and the data in terms of the correlations between the reaction Q-value and θ_{br} , as well as the reaction Q-value and Q_{break} shown in Figs. 5.14(c) and (d), gives credence to the usage of a two-step model in describing the ${}^9\text{Li}(d,p){}^{10}\text{Li}$ reaction as well as the presence of both a ground state and an excited state ${}^9\text{Li}$ core in the ${}^{10}\text{Li}$ coincidence data.

The fact that the two reaction channels occupy relatively distinct regions in Figs. 5.14(a) and (b) makes it possible to separate one reaction channel from the other in the measured coincidence data. The coincidence data located in the simulated ${}^9\text{Li}^*$ region in Fig. 5.12 were gated in the reaction Q-value vs θ_{br} phase space based and are indicated by the black solid circles in Fig. 5.14. For those few coincidence events which were located in the overlap region between the two simulated

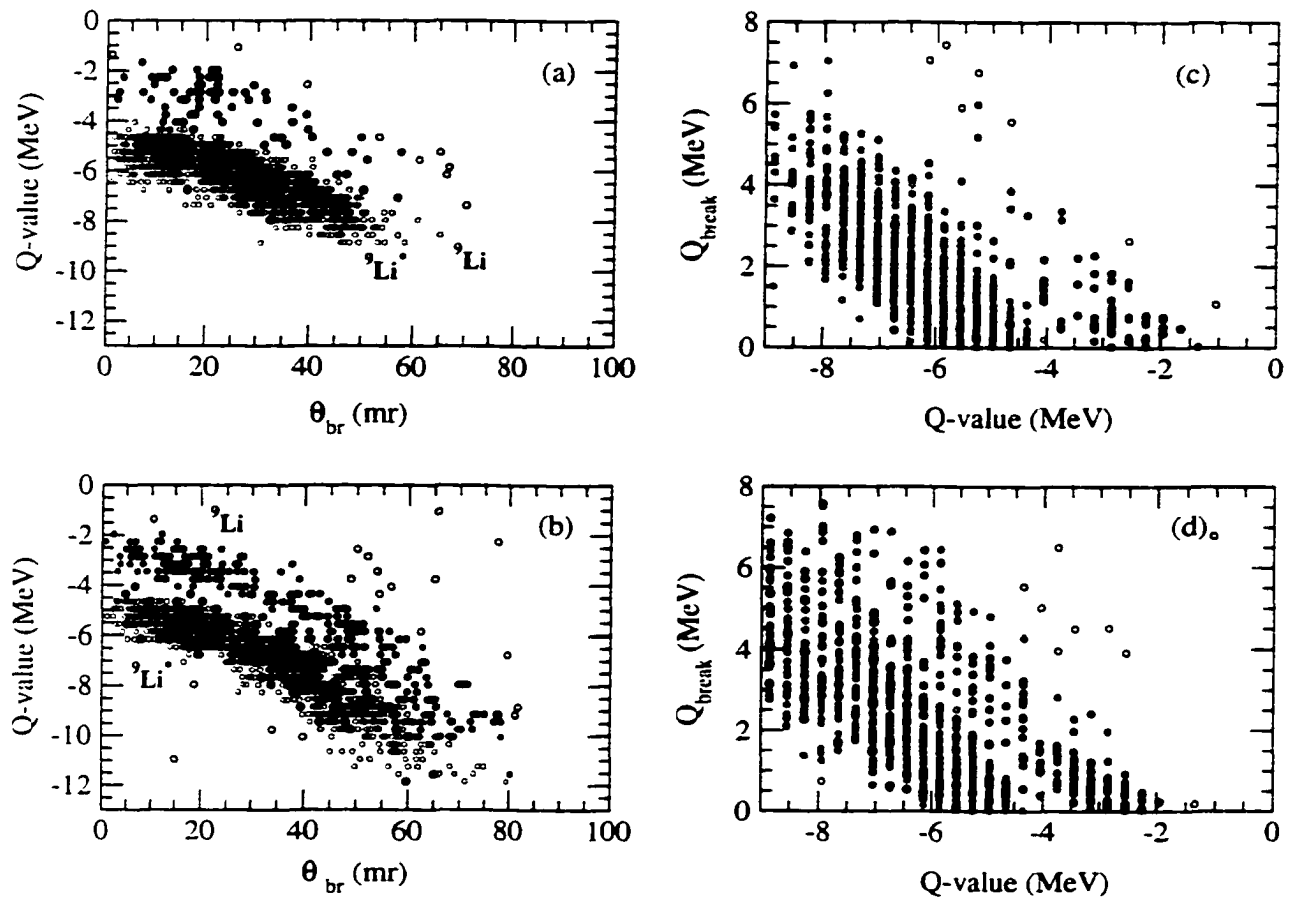


Figure 5.14. (a)-(b) Reaction Q-value as a function of θ_{br} for the CD and Strip detectors, respectively. The brown circles are the result of the simulation where a ${}^9\text{Li}^*$ was produced in the breakup, while the yellow circles indicate the simulated results producing ${}^9\text{Li}$ in its ground state shown in Fig. 5.12. (c)-(d) Q_{break} as a function of the reaction Q-value for the CD and Strip detectors, respectively.

regions. the data were assumed to originate from the ${}^9\text{Li}$ ground state core events. While no events were observed in the overlap region for the CD data, 9 events were located in the overlap region for the Strip data out of a total of 364 coincidence events. By taking the ratio of the number of ${}^9\text{Li}^*$ events relative to the total number of events observed, neglecting events which were identified as random coincidence events, an estimate can be made as to the relative population of ${}^{10}\text{Li}$ existing with a ${}^9\text{Li}^*$ core. The observed ratios of ${}^9\text{Li}^*$ core events to the total number of ${}^{10}\text{Li}$ events which were detected is 0.098 ± 0.04 for the CD detectors (covering 2.7° to 9.5° in the center of mass), and 0.244 ± 0.03 for the Strip detectors (covering 11° to 26° in the center of mass). The error bars listed for the two ratios are due to statistical error only. In the case of the Strip detector ratio, the given ratio assumes that all of the events which lie in the overlap region are identified as having a ${}^9\text{Li}$ core. If one assumes that these events in the overlap region are due to ${}^{10}\text{Li}$ having a ${}^9\text{Li}^*$ core, then the upper limit to the ratio becomes 0.27 ± 0.03 .

The Q-value and Q_{break} spectra for the ${}^9\text{Li}^*$ data are shown in Figure 5.15 for the CD and Strip data, respectively, along with the simulated distributions that have been normalized based on the total number of events observed in the spectra. The agreement that is seen between the simulated results and the distributions from the excited-state gated data indicate that there is little to no evidence of any discernible structure in the measured distributions as was the case with the ${}^9\text{Li}$ ground state Strip data. Note that the Q_{break} spectrum for the events with ${}^9\text{Li}^*$ core have the same range of values as was observed for the ${}^9\text{Li}$ core events. Because the gamma ray that is emitted from the ${}^9\text{Li}^*$ goes undetected in the experiment, the measured Q_{break} for these events are shifted down in energy causing an overlap to occur with the ${}^9\text{Li}$ core distribution. Thus, in the analysis of the ${}^9\text{Li}$ ground state spectra, the

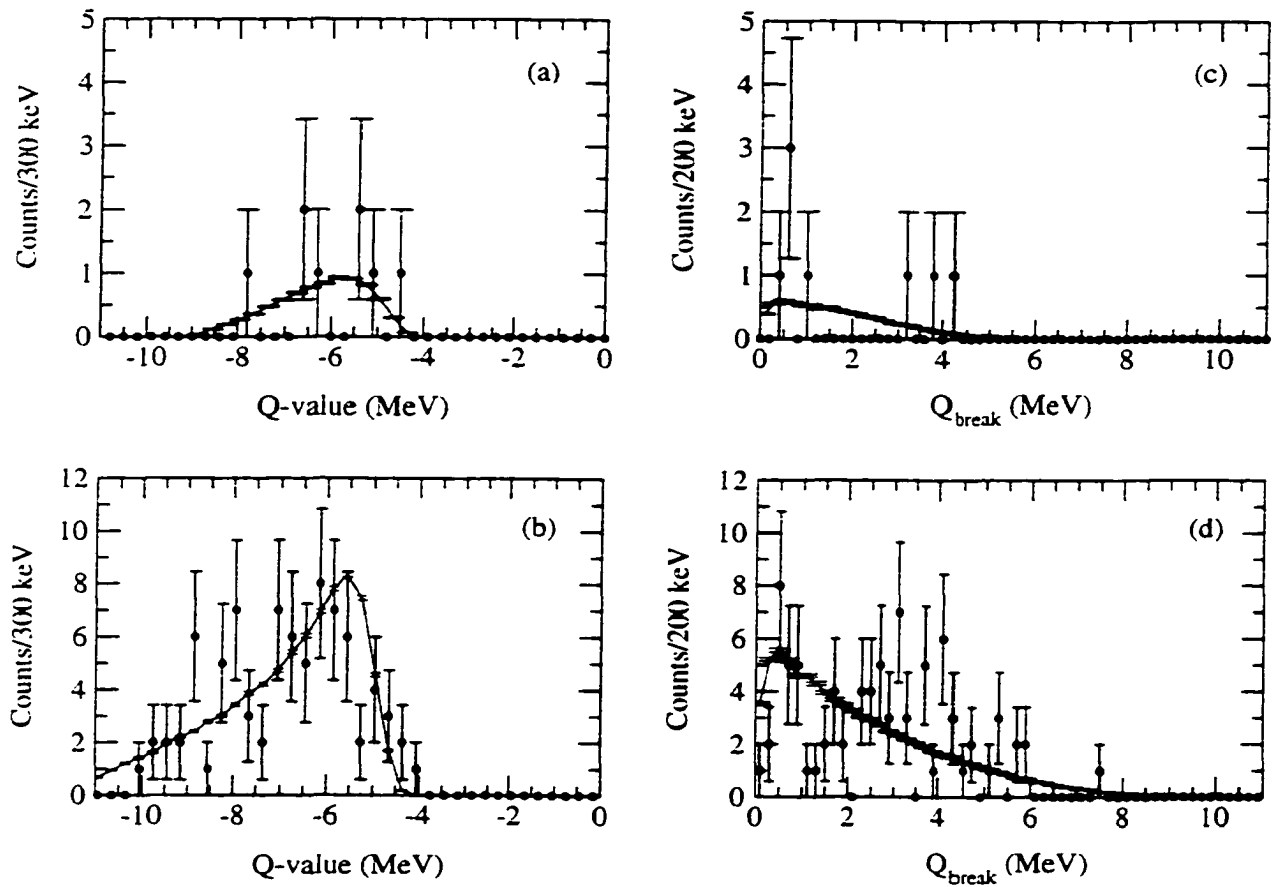


Figure 5.15. (a)-(b) ${}^9\text{Li}^*$ gated reaction Q -value distributions for the CD and Strip detectors, respectively, (black circles) along with the normalized results of the Monte Carlo simulation. (c)-(d) ${}^9\text{Li}^*$ gated Q_{break} distributions for the CD and Strip detectors, respectively, with the corresponding normalized Monte Carlo results.

events corresponding to the ${}^9\text{Li}^*$ core were gated out of the ${}^9\text{Li}$ core spectra in order to remove a source of background from the ${}^9\text{Li}$ core Q_{break} distribution.

5.2.5 Fitting procedure

Because of the low statistics that were collected in the various coincidence spectra, the maximum likelihood technique was used in fitting the data. Unlike the standard least-squares fitting technique which assumes a Gaussian distribution for the measured number of events in a given histogram channel, the maximum likeli-

hood technique makes no assumptions concerning how the data is distributed but rather maximizes the probability that a given model function describes the data set by varying the parameters of the model function [53]. Since the measured number of counting events has a Poisson distribution by nature, the use of the standard least squares fitting technique is only valid in cases when the number of events is large, at which point the Poisson distribution approaches a Gaussian distribution.

The probability of observing a number of events, y_i , at a given value, x_i , having a Poisson distribution about a average number, μ , is given by:

$$P(y_i, \mu) = \frac{\mu^{y_i}}{y_i!} e^{-\mu} \quad (5.14)$$

The likelihood of a model function, $f(x_i, a_j)$, in describing a set of measured data, (x_i, y_i) , is given by the product of the individual probability distributions for every value of x_i [7]:

$$L(a_j) = \prod_i \frac{[f(x_i, a_j)]^{y_i}}{y_i!} e^{-f(x_i, a_j)} \quad (5.15)$$

where a_j are the parameters of the model function. The values of a_j which maximize the likelihood function $L(a_j)$ for the measured set of data are understood to correspond with the best fit of the data. It is often preferable to work with the figure of merit of the fit rather than the likelihood function itself. In this particular case, the figure of merit for the maximum likelihood technique is defined as:

$$M = -\ln(L) = \sum_i (f(x_i, a_j) + \ln(y_i!) - y_i[\ln(f(x_i, a_j))]) \quad (5.16)$$

where a minimum in the figure of merit will correspond to a maximum in the likelihood function. In the routine that was used in the analysis to fit the data, the minimum to the figure of merit function was determined using the function minimization routine AMOEBA [55].

The line shapes for the possible states in ^{10}Li were estimated using a Breit-Wigner of the form [27]:

$$\sigma(E) = A \frac{\Gamma}{(E - E_R)^2 + (\frac{\Gamma}{2})^2} \quad (5.17)$$

where E_R is the energy of the resonance measured with respect to the threshold of the reaction channel, Γ is the energy-dependent width of the state, and A was assumed to be an energy-independent amplitude. For both the s-wave and p-wave states, the width $\Gamma(E)$ was calculated using Equation 2.29 based on the penetrability factors for s-wave and p-wave neutrons (Eq. 2.33). Although the usage of the Breit-Wigner shape for the possible s-wave virtual state is not ideal, it is used in this case to determine if any evidence for the presence of such a state can be inferred from this data set based on the resulting fits to the data.

The line shape for the states was then convoluted with the response function of the experimental setup as determined from the Monte Carlo calculations. In these calculations, the excitation energy distribution for ^{10}Li was treated as a delta function in order to determine both the shape and the magnitude of the response function. Figure 5.16 show the results of an 8000 iteration simulation for the Q-value and Q_{break} spectra using a $E_x = 0.5$ MeV delta function for ^{10}Li . The simulated spectra were fitted with Gaussian distributions with widths in the Q-value spectra of 0.380 MeV (σ) for the CD detectors and 0.300 MeV (σ) for the Strip detectors, respectively. This simulated resolution is much worse than was measured for the Q-value of the $^{13}\text{C}(d,p)^{14}\text{C}$ reaction of 0.276 MeV (σ) for the CD2 detector.

To ensure that the Monte Carlo simulation was predicting the appropriate response function for the $^9\text{Li}(d,p)$ reaction, a separate Monte Carlo calculation was performed to simulate the $^{13}\text{C}(d,p)$ reaction in order to compare the predicted Q-value resolution for populating the ground state of ^{14}C with what was measured in the experiment. The simulation took into consideration the beam spot size and

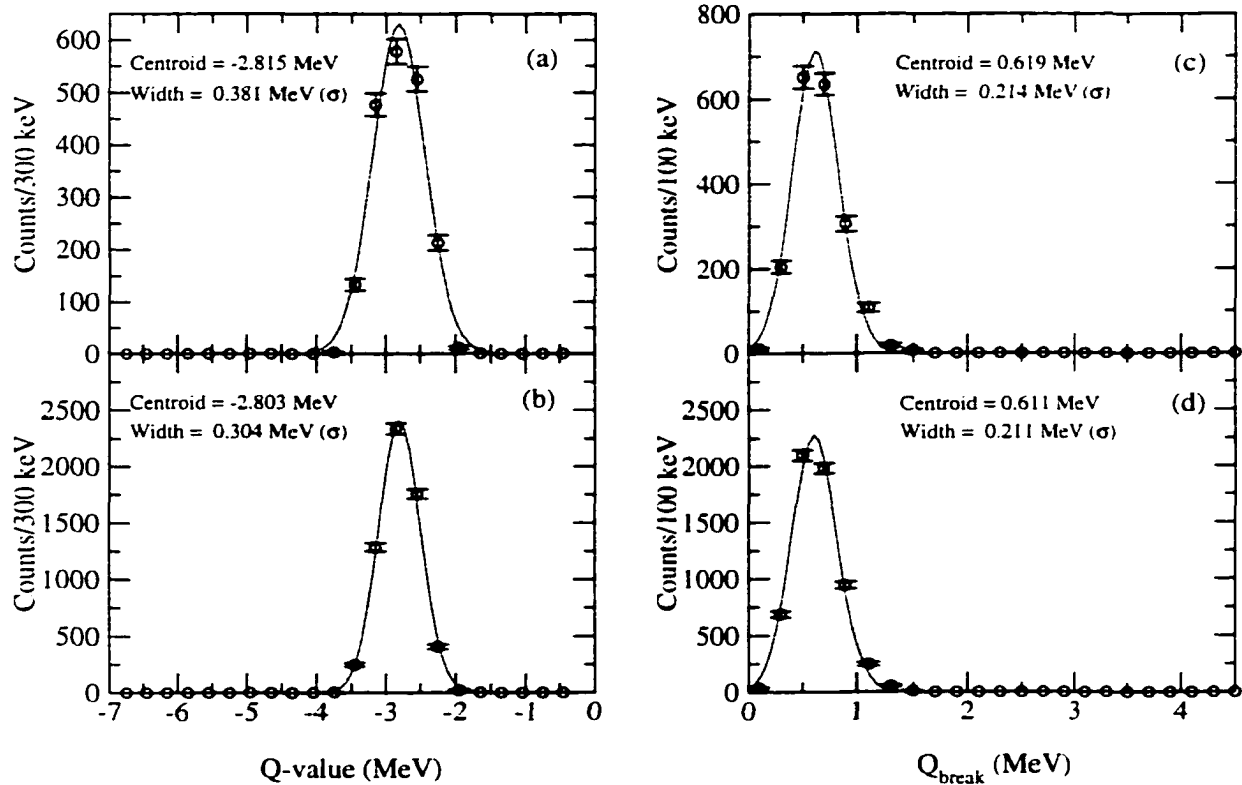


Figure 5.16. (a)-(b) Simulated Q-value spectra for the CD and Strip detectors, respectively. (c)-(d) Simulated Q_{break} spectra for the CD and Strip detectors, respectively. In both cases, a delta function was assumed for the excitation of ^{10}Li centered at $E_x = 0.5$ MeV. The solid lines in the figures are the results of fits to the simulation using Gaussian distributions.

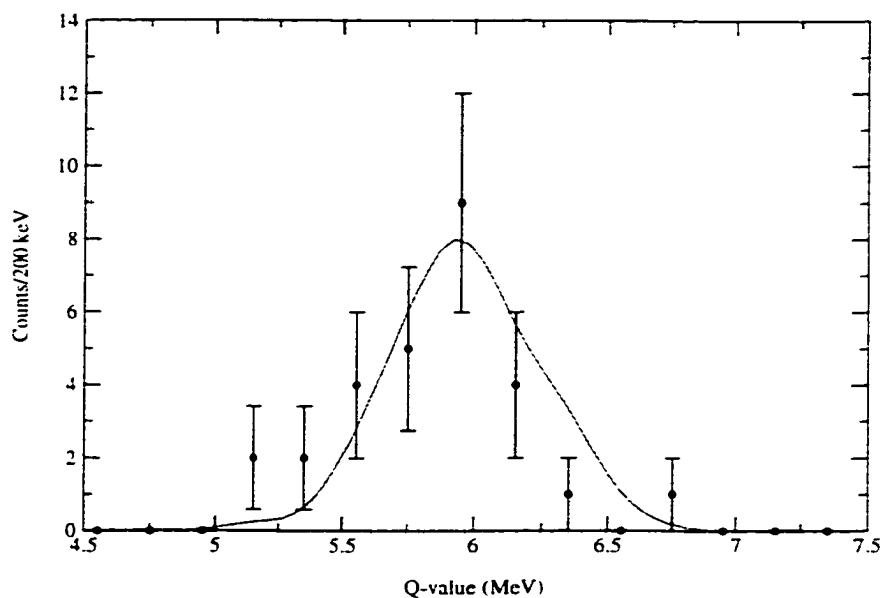


Figure 5.17. Ground state Q-value spectrum of the $^{13}\text{C}(\text{d},\text{p})^{14}\text{C}$ as measured by the CD2 detector compared with the results from the Monte Carlo simulation normalized by the number of events in each spectrum.

divergence, as well as the energy spread of the incident ^{13}C beam. The results of the simulation are shown as the solid line in Figure 5.17 in comparison with the measured ground state Q-value data from CD2. Note that the Monte Carlo results have been normalized to match the data based on the number of events that were observed in the ground state peak. Fig. 5.17 shows a relatively good agreement between the data and the simulation, with the simulation predicting a width for the ground state peak of 0.288 MeV (σ) in comparison with the 0.276 MeV width that was measured in the data. Hence, this good agreement between the simulation and measurement indicates that the Monte Carlo simulation is accurate in predicting the Q-value resolution for the $^9\text{Li}(\text{d},\text{p})$ reaction.

Even though the uncertainties in the incident beam parameters were much smaller for the ^9Li beam than the ^{13}C beam due to the use of the tracking detectors in the analysis line, the discrepancies in Q-value resolution between the

${}^9\text{Li}(d,p)$ reaction and the ${}^{13}\text{C}(d,p)$ reaction is due to the fact that the protons were produced at a lower energy in the ${}^9\text{Li}(d,p)$ reaction relative to the protons that were produced in the ${}^{13}\text{C}(d,p)$ reaction. Since the Q-value measurements rely strongly on the measured energy of the proton, larger uncertainties in the amount of energy loss in the target directly translate into larger uncertainties in the measured reaction Q-value. Because the protons from the ${}^9\text{Li}(d,p)$ reaction lose more energy in the target and have a larger energy spread exiting the target, the effect of energy loss in the target on the measured reaction Q-value will be larger for the ${}^9\text{Li}(d,p)$ reaction than the ${}^{13}\text{C}(d,p)$ reaction. Since there is no way to precisely determine the amount of energy lost in the target by the protons on an event by event basis, no corrections can be made to the data to improve the reaction Q-value resolution. This poor Q-value resolution further hampers the chance of determining the nature of the low-lying structure of ${}^{10}\text{Li}$.

While the Q-value resolution is quite poor, the Q_{break} resolution appears to be a bit better in Fig. 5.16 with widths of 0.214 MeV and 0.211 MeV (σ) for the CD and Strip detectors, respectively, for a peak located at $E_x = 0.5$ MeV. However, while the shape of the resolution curve in the Q-value spectra remained essentially constant for different values of E_x as shown in Figure 5.18, the location and width of the resolution curve in the Q_{break} spectra does not remain constant. Varying E_x in the Monte Carlo simulation from 0.2 MeV to 1.2 MeV causes the widths of the resulting Q_{break} spectrum to vary from 0.15 MeV to 0.33 MeV (σ) as is shown Figs. 5.18(a) and (b) for the CD and Strip detectors, respectively. This variation in the width of the response function creates problems in attempting to determine the exact nature of the structure of ${}^{10}\text{Li}$. Another problem that is apparent from the simulations is the fact that two peaks are separated by 1.1 MeV in the Q_{break} spectra for simulated states in ${}^{10}\text{Li}$ which were separated by 1 MeV in excitation energy. This indicates

that the Q_{break} parameter does not quite scale appropriately with the ^{10}Li excitation energy. While the Q-value spectra were essentially calibrated by determining the ground state Q-value of the $^{13}\text{C}(d,p)^{14}\text{C}$ reaction, it is not possible to check the Q_{break} spectra to ensure that it is accurately measuring the amount of energy produced in the breakup of ^{10}Li . Because of these systematic uncertainties with Q_{break} , it is difficult to determine the accuracy with which the observed structure in the Q_{break} spectra can be used to measure the states in ^{10}Li . Although useful in identifying the two different ^{10}Li decay channels, it is unclear how the parameters attained from fitting the Q_{break} spectra would relate to the structure of ^{10}Li . Hence, fits were only performed on the reaction Q-value spectra.

The CD Q-value spectrum was first fit with a single p-wave resonance with the background that was determined using the Monte Carlo simulation assuming a flat excitation energy distribution. Due to the large statistical uncertainties in the normalizing the simulated background to the data, a scaling factor was multiplied onto the background curve and used as an adjustable parameter in the fit. The best overall one resonance fit to the CD Q-value spectrum, shown as the black curve in Figure 5.19, yielded a resonance located at $Q = -2.58(11)$ MeV which corresponds to a neutron separation energy (Eq. 2.2) $S_n = -0.35(11)$ MeV. The error that is associated with the peak location was ascertained by determining how much the peak location would have to be varied in order to increase the figure of merit M by $1/2$ [53]. In determining this error of the peak location, all other parameters in the fit were allowed to vary in order to fully explore the parameter space associated with the fit. Because of the poor resolution of the Q-value spectrum, an upper limit of $\Gamma_0 < 0.32$ MeV could only be established for the resonance based on the variance in the fits to the Q-value spectrum.

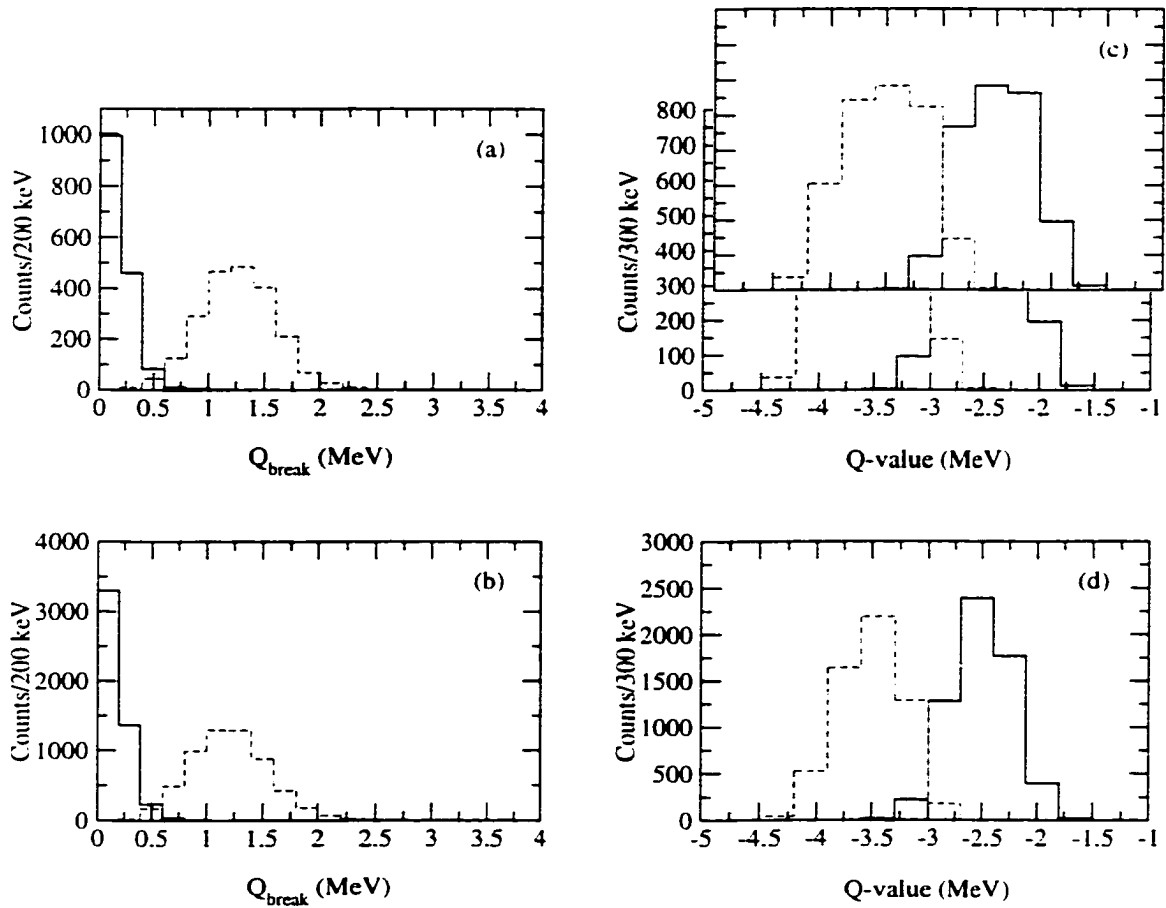


Figure 5.18. (a)-(b) Simulated Q_{break} spectra for the CD and Strip detectors, respectively, assuming a delta function excitation curve located at $E_x = 0.2$ MeV (solid histogram) and $E_x = 1.2$ MeV (dashed histogram). (c)-(d) Simulated Q-value spectra for the CD and Strip detectors, respectively, for $E_x = 0.2$ MeV (solid histogram) and $E_x = 1.2$ MeV (dashed histogram).

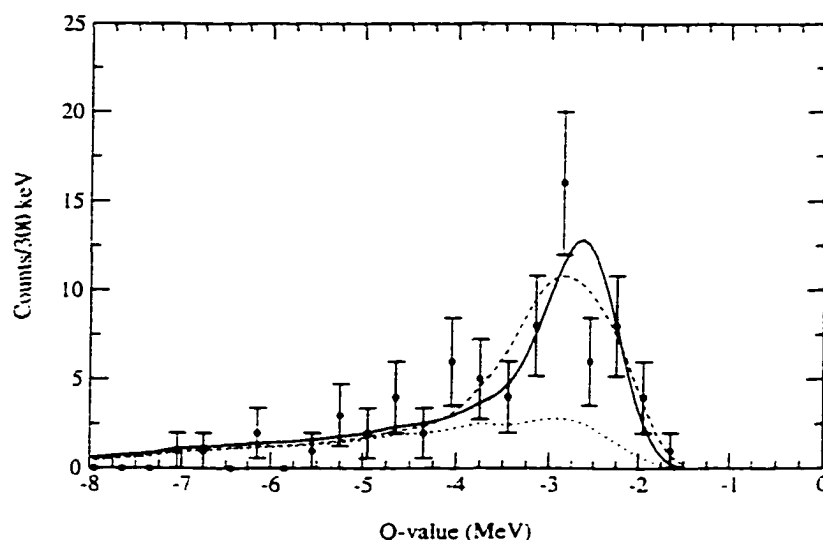


Figure 5.19. Fits to the CD Q-value spectrum assuming a single resonance (solid curve) and 2 resonances (dashed curve) along with an uncorrelated background (dotted curve). The parameter for the fits are presented in Table 5.2.

Since most of the previous measurements of ^{10}Li have only quoted a neutron separation energy in describing the location of the various states that were observed in ^{10}Li , it is necessary to use this quantity in order to compare the results of this work with previous measurements. The location of the peak that is measured in this work is slightly higher in separation energy than the peak that has been previously observed by Caggiano, et al. [14] ($S_n = -0.50(6)$ MeV $\Gamma = 0.4(6)$ MeV) and Young, et al. [7] ($S_n = -0.54(6)$ MeV $\Gamma = 0.36(2)$ MeV) and appears more consistent with the p-wave state that was observed by Bohlen, et al. [13] at $S_n = -0.24(6)$ MeV. The observed upper limit for the width of this state is also relatively consistent with previous measurements [7, 14].

An attempt was also made to fit the CD Q-value spectrum using two separate resonances. The best fit that was achieved with two resonances is shown as the dashed curve in Fig. 5.19 with the parameters used in the fit listed in Table 5.2.

Table 5.2. Fitting parameters for the CD Q-value spectra.

Fit type	Peak location (MeV)	Γ_0 (MeV)	S_n (MeV)
One peak	-2.58(11)	< 0.32	-0.35(11)
Two peak	-3.00(24) > -2.43	< 0.62	-0.77(24) > -0.2

Because of the limitations in the data, only an upper limit can be ascertained for the location of a peak near threshold of $Q > -2.43$ MeV ($S_n > -0.2$ MeV) based on the results of the fit. Furthermore, no distinction could be seen in the fit between a p-wave resonance and an s-wave resonance for such a low lying state. Although this two resonance fit produced a slightly smaller figure of merit ($M = 36.51$) than in the case of the one resonance fit ($M = 37.81$), the shape of the fit does not appear to correspond as well to the data as the one resonance fit did. The reason for the slight improvement in the figure of merit for the fit may be due to the additional degrees of freedom that are present in the two resonance fit.

Attempts were also made to fit the Q-value spectrum from the Strip detectors to determine if any structure could be ascertained from the data. However, because of the good agreement between the simulated response function for the detector and the shape of the coincidence data itself, no statistically significant fits were achieved to the data using either a one or two resonance model function.

5.3 Angular Distribution

In order to account for the response of the experimental setup on the angular distribution of the protons from the ${}^9\text{Li}(d,p)$ reaction, corrections must be made to the geometric solid angle that is covered by the various silicon detectors for the efficiency of detecting protons in coincidence with the outgoing ${}^9\text{Li}$. The angular efficiencies for the various silicon detectors was determined using the Monte Carlo

simulations assuming an isotropic angular distribution for the protons as well as assuming a flat excitation energy distribution for ^{10}Li .

Although there is no discernible evidence of structure in the Strip detector Q-value spectra due to the shape of the response function for that detector, the structure that is evident in the CD spectra gives some credence to the assumption that was made when producing the initial relative angular distribution in Fig. 4.35 of structure being present in ^{10}Li for reaction Q-values ≥ -4.0 MeV. Making that same assumption for the Strip detectors, a new relative angular distribution was produced using the efficiency corrected solid angles for the silicon detectors that were calculated using the Monte Carlo simulation and is presented in Figure 5.20. It should be noted that events which had been identified as alpha particles from the ^{241}Am source as well as events which corresponded to ^{10}Li consisting of a $^9\text{Li}^*$ core were not considered in the angular distribution.

In Fig 5.20(b), the black and red curves are the results of the FRESCO calculations for the s-wave and p-wave states, respectively, that have been scaled to match the data based on the value of the data at the first angular bin. It appears upon first glance when comparing the data with the two calculations that the data seems to follow the p-wave distribution a bit better than the s-wave distribution. However, considering the fact that the points which correspond to the two CD detectors are at small center of mass angles where the shapes of both calculations agree relatively well with the data, a comparison between the calculations and the data is inconclusive at best. If the Strip data had shown any structure, then more credence could have been given to the data at larger center of mass angles.

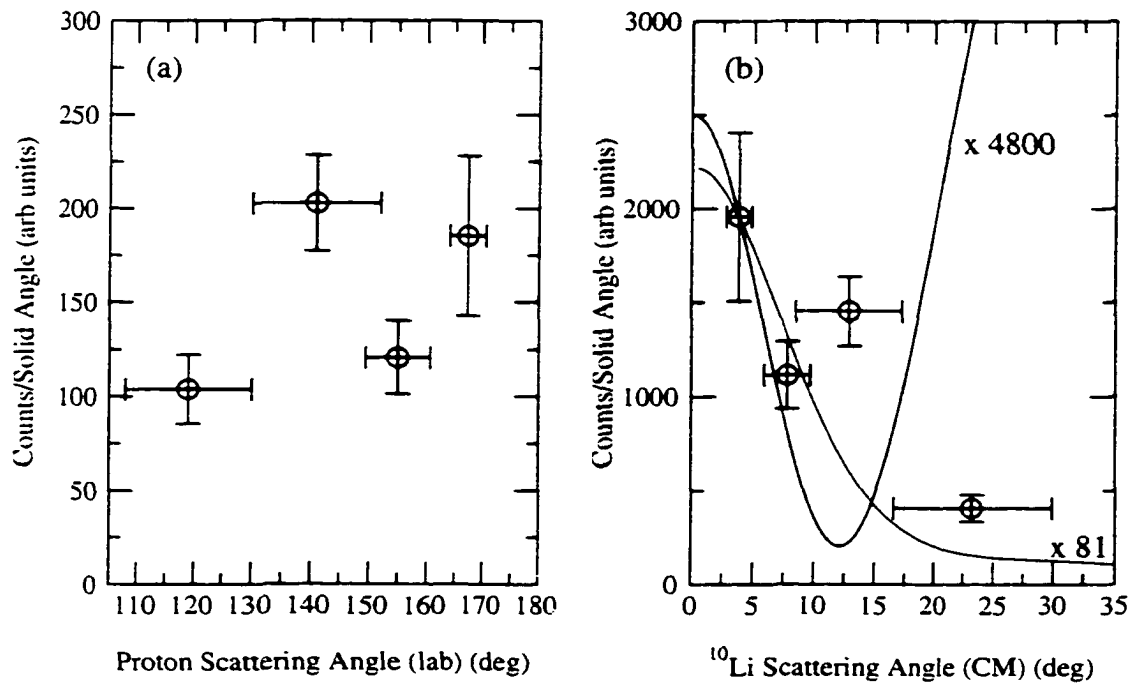


Figure 5.20. Efficiency corrected relative angular distribution of the (d,p) events with $Q \geq -4.0$ MeV as a function of (a) the proton laboratory scattering angle and (b) the ^{10}Li center of mass angle. The black and red curves in (b) are the FRESCO calculations for the s-wave and p-wave, respectively. The calculations have been normalized to match the data based on the first data point.

5.4 Conclusions

The analysis of the ${}^9\text{Li}(d,p){}^{10}\text{Li}$ reaction that is presented in this work has yielded a measurement for the ground state mass of ${}^{10}\text{Li}$, based on the kinematics of the proton from the (d,p) reaction, as well as identified the breakup of ${}^{10}\text{Li}$ into the ${}^9\text{Li}^* + n$ channel which had not been observed before in the previous studies of ${}^{10}\text{Li}$. The identification of this decay channel was made possible by performing a full reconstruction of the breakup of ${}^{10}\text{Li}$ on an event by event basis. Although the strength of this reaction channel is small relative to the ${}^9\text{Li} + n$ channel at forward center of mass angles, it was shown to produce a significant background in the Q_{break} spectra which measures the excess energy produced in the breakup of ${}^{10}\text{Li}$. The generation of this background from the ${}^9\text{Li}^* + \text{neutron}$ decay channel could also have an effect on the results of previous studies which were reliant on measuring the relative motion between the outgoing ${}^9\text{Li}$ and neutron from the breakup of ${}^{10}\text{Li}$ and assumed that the detected ${}^9\text{Li}$ was initially produced in its ground state [5, 6, 9].

In terms of the structure of ${}^{10}\text{Li}$, the results of this work were inconclusive as to the possible presence of a low-lying virtual state in ${}^{10}\text{Li}$ due to the small number of ${}^{10}\text{Li}$ events that were detected as well the poor Q-value resolution that was achieved in this experiment. The data was best fit with a single resonance located at $S_n = -0.35(11)$ MeV which may correspond to the previously observed p-wave state in ${}^{10}\text{Li}$. A two resonance fit to the data yielded an upper limit to the position of a state near threshold of $S_n < -0.2$ MeV but did not reproduce the shape of the Q-value spectrum as well as the one resonance fit did.

Although the relative angular distribution of the proton events at low excitation energies appeared somewhat similar in shape to the calculated angular distribution of a p-state in ${}^{10}\text{Li}$, the relevance of such a distribution is in question due to the fact that no states were positively identified at large center of mass angles, but only

assumed to exist based on the measurements at small angles. In addition, because of the possible presence of more than one state at low excitation energies, the angular distribution as presented in this work will have the net effects of all states that are present at low excitation energies. More work needs to be done in studying the ${}^9\text{Li}(d,p)$ reaction in order to determine a proper angular distribution for the emitted proton.

While this work has shown that it is possible to produce and study an unbound nucleus using the (d,p) reaction, as well as demonstrated the benefits of performing a kinematically complete experiment with an unbound nucleus, it fell short in its attempt to clarify the exact nature of the low-lying structure of ${}^{10}\text{Li}$. The main reason for this failure was due to the lack of statistics. While the usage of a relatively thick CD_2 target had a tremendous impact on the Q-value resolution of the experiment, the use of a thinner CD_2 target in this case would have made the identification of structure in ${}^{10}\text{Li}$ extremely difficult due to the reduction in statistics that is associated with using a thinner target. In order to significantly improve upon the results of this work, the incident beam rate on target would have to be increased by at least a factor of 10 in order for a thinner CD_2 target to be used while still increasing the number of coincidence events that is observed in the experiment by a factor of 5. Another way to increase the number of coincidence events observed in the experiment would be to improve the efficiency of the tracking detectors from the 68% value that was observed in this experiment. Measuring the parameters of the incident beam on an event by event basis helped to improve the Q-value resolution as well as clearly identify the second reaction channel in the breakup of ${}^{10}\text{Li}$. Without the incident beam information, it would have been difficult to cleanly separate the two decay channels. Hence, it is necessary to tracking the incident beam on an event by event basis in order to optimize the Q-value resolution as well as

identify the events of interest. It is evident from the results of this experiment that using the (d.p) reaction to populate ^{10}Li has the potential to provide a good deal of information on the structure of ^{10}Li and clarify some of the ambiguities that are associated with it.

APPENDIX A

SILICON DETECTOR INFORMATION

Table A.1. Energy resolution for individual sectors of CD1 and CD2 as determined by measuring the width of the 3.18 MeV α -line in ^{148}Gd .

Sector	CD1 (keV) (FWHM)	CD2 (keV) (FWHM)
1	84.8	-
2	61.3	95.3
3	58.3	95.9
4	73.1	103.3
5	74.5	106.3
6	67.8	110.8
7	68.3	89.9
8	196.7	89.0
9	78.8	161.4
10	68.7	172.9
11	78.4	84.4
12	87.5	102.8
13	97.2	120.8
14	80.5	119.4
15	80.0	95.7
16	95.0	-

Table A.2. Energy resolution for the individual strip detectors based on the measured width of the 3.18 MeV α -line in ^{148}Gd .

Strip Detector	Resolution (keV) (FWHM)
1	58.0
2	83.0
3	85.0
4	54.0
6	38.0

Table A.3. Average position resolution of the different strips on the strip detectors based on the measured width of the slits on the calibration mask. All resolutions given are FWHM in mm.

Strip #	Strip Det. 1 ^a	Strip Det. 2 ^b	Strip Det. 3 ^c	Strip Det. 4 ^b	Strip Det. 6 ^b
1	1.51	2.1	1.45	2.8	2.4
2	1.54	2.1	0.5	0.67 ^a	2.2
3	1.29	1.87	0.5	-	1.9
4	1.34	1.42	0.91	2.72	2.21
5	0.98	0.86 ^c	0.71	1.96	2.0
6	1.32	0.51	0.69	1.88	2.25
7	1.16	0.88 ^c	0.79	1.67	2.35
8	1.54	0.70 ^c	1.55	1.71	2.13
9	1.21	0.79	1.63 ^b	-	2.03
10	1.29	2.09 ^a	1.65	-	2.03
11	1.24	1.36	0.52	2.14	2.0
12	1.25	1.74	0.89	2.05	2.28
13	1.17	0.75	1.32	2.40	2.09
14	1.18	0.76	0.83	2.28	1.21
15	1.09	0.78	0.73	2.17	1.14
16	1.6	-	1.21	1.92	2.4

^aPosition determined by In/Back

^bPosition determined by Out/Back

^cPosition determined by In/(In + Out)

BIBLIOGRAPHY

- [1] E. Rutherford, *Philosophy Magazine* **21**, 669 (1911).
- [2] I. Tanihata, H. Hamagaki, O. Hashimoto, Y. Shida, N. Yoshikawa, K. Sugimoto, O. Yamakawa, T. Kobayashi, and N. Takahashi. *Physical Review Letters* **55**, 2676 (1985).
- [3] I. Tanihata, *J. Phys. (London)* **G22**, 157 (1996).
- [4] M.V. Zhukov, B.V. Danilin, D.V. Federov, J.M. Bang, I.J. Thompson, and J.S. Vaagen. *Physics Reports* **231**, 151 (1993).
- [5] R.A. Kryger, A. Azhari, A. Galonsky, J.H. Kelley, R. Pfaff, E. Ramakrishnan, D. Sackett, B.M. Sherrill, M. Thoennesen, J. A. Winger, and S. Yokoyama, *Physical Review* **C47**, R2439 (1993).
- [6] M. Thoennesen, S. Yokoyama, A. Azhari, T. Baumann, J.A. Brown, A. Galonsky, P.G. Hansen, J.H. Kelley, R.A. Kryger, E. Ramakrishnan, and P. Thirolf, *Physical Review* **C59**, 111 (1999).
- [7] B.M. Young, W. Benenson, J.H. Kelley, N.A. Orr, R. Pfaff, B.M. Sherrill, M. Steiner, M. Thoennesen, J.S. Winfield, J.A. Winger, S. J. Yennello, and A. Zeller, *Physical Review* **C49**, 279 (1994).
- [8] M. Zinser, F. Humbert, T. Nilsson, W. Schwab, Th. Blaich, M.J.G. Borge, L.V. Chulkov, H. Eickhoff, Th.W. Elze, H. Emling, B. Franzke, H. Freiesleben, H. Geissel, K. Grimm, D. Guillemaud-Mueller, P.G. Hansen, R. Holzmann, H. Irnich, B. Jonson, J.G. Keller, O. Klepper, H. Klingler, J.V. Kratz, R. Kulessa, D. Lambrecht, Y. Leifels, A. Magel, M. Mohar, A.C. Mueller, G. Müzenberg, F. Nickel, G. Nyman, A. Richter, K. Riisager, C. Scheidenberger, G. Schrieder, B.M. Sherrill, H. Simon, K. Stelzer, J. Stroth, O. Tengbald, W. Trautmann, E. Wajda, and E. Zude, *Physical Review Letters* **75**, 1719 (1995).
- [9] M. Zinser, F. Humbert, T. Nilsson, W. Schwab, H. Simon, T. Aumann, M.J.G. Borge, L.V. Chulkov, J. Cub, Th.W. Elze, H. Emling, H. Geissel, D. Guillemaud-Mueller, P.G. Hansen, R. Holzmann, H. Irnich, B. Jonson, J.V. Kratz, R. Kulessa, Y. Leifels, H. Lenske, A. Magel, A.C. Mueller, G. Müzenberg, F. Nickel, G. Nyman, A. Richter, K. Riisager, C. Scheidenberger, G. Schrieder, K. Stelzer, J. Stroth, A. Surowiec, O. Tengbald, E. Wajda, and E. Zude, *Nuclear Physics* **A619**, 151 (1997).
- [10] I.J. Thompson and M.V. Zhukov, *Physical Review* **C49**, 1904 (1994).

- [11] K.H. Wilcox, R.B. Weisenmiller, G.J. Wozniak, N.A. Jelley, D. Ashery, and J. Cerny, *Physics Letters* **B 59**, 142 (1975).
- [12] A.I. Amelin, M.G. Gornov, Yu.B. Gurov, A.L. Il'in, P.V. Morokhov, V.A. Pechkurov, V.I. Savel'ev, F.M. Sergeev, S.A. Smirnov, B.A. Chernyshev, R.R. Shafigullin, and A.V. Shishkov, *Soviet Journal of Nuclear Physics* **52**, 782 (1990).
- [13] H.G. Bohlen, W. von Oertzen, Th. Stolla, R. Kalpakchieva, B. Gebaur, M. Wilpert, Th. Wilpert, A.N. Ostrowski, S.M. Grimes, and T.N. Massey, *Nuclear Physics* **A616**, 254c (1997).
- [14] J.A. Caggiano, D. Bazin, W. Benenson, B. Davids, B.M. Sherrill, M. Steiner, J. Yurkon, A.F. Zeller, and B. Blank, *Physical Review* **C60**, 064322 (1999).
- [15] Kenneth S. Krane, *Introductory Nuclear Physics* (John Wiley and Sons, Inc., New York, 1988), Vol. I.
- [16] Samuel S. M. Wong, *Introductory Nuclear Physics*, 1st ed. (Prentice Hall Inc., Englewoods Cliff, New Jersey, 1990).
- [17] G.W. Hoffmann, L. Ray, M. Barlett, J. McGill, G.S. Adams, G.J. Igo, F. Irom, A.T.M. Wang, C.A. Witten, Jr., R.L. Boudrie, J.F. Amann, C. Glashausser, N.M. Hintz, G.S. Kyle, and G.S. Blanpied, *Physical Review* **C21**, 1488 (1980).
- [18] I. Tanihata, T. Kobayashi, O. Yamakawa, S. Shimoura, K. Ekuni, K. Sugimoto, N. Takahashi, T. Shimoda, and H. Sato, *Physics Letters* **B 206**, 592 (1988).
- [19] H.F. Esbensen, G.F. Bertsch, and K. Hencken, *Physical Review* **C56**, 3054 (1997).
- [20] D.H. Wilkinson and D.E. Alburger, *Physical Review* **113**, 563 (1959).
- [21] H. Sagawa, B.A. Brown, and H. Esbensen, *Physics Letters* **B 309**, 1 (1993).
- [22] P.G. Hansen, *Nuclear Physics* **A630**, 285c (1998).
- [23] Leonard I. Schiff, *Quantum Mechanics*, 3rd ed. (McGraw-Hill Book Company, New York, 1968).
- [24] Leslie E. Ballentine, *Quantum Mechanics*, 1st ed. (Prentice Hall Inc., Englewoods Cliff, New Jersey, 1990).
- [25] G.R. Satchler, *Introduction to Nuclear Reactions*, 2nd ed. (Oxford University Press, New York, 1990).
- [26] K.W. McVoy, *Nuclear Physics* **A115**, 481 (1968).
- [27] K.W. McVoy and P. Van Isacker, *Nuclear Physics* **A576**, 157 (1994).
- [28] A.M. Lane and R.G. Thomas, *Review of Modern Physics* **30**, 257 (1958).
- [29] Attila Csótó and G.M. Hale, *Physical Review* **C59**, 1207 (1999).

- [30] I.J. Thompson, Lecture Notes: Nuclear Theory, 1995, (unpublished).
- [31] I. J. Thompson, *Computer Physics Communications* **7**, 167 (1988).
- [32] Richard B. Firestone, in *Table of Isotopes*, eighth ed., edited by Virginia S. Shirley (John Wiley and Sons, Inc., New York, 1996), Vol. I.
- [33] D.E. Alburger and D.H. Wilkinson, *Physical Review* **C13**, 835 (1976).
- [34] J.B. Marion and F.C. Young, *Nuclear Reaction Analysis* (John Wiley and Sons, Inc., New York, 1968).
- [35] N.R. Fletcher, *Nuclear Instruments and Methods in Physics Research* **A316**, 143 (1992).
- [36] David Griffiths, *Introductory to Elementary Particles* (John Wiley and Sons, Inc., New York, 1987).
- [37] B.M. Sherrill, D.J. Morrissey, J.A. Nolen Jr., and J.A. Winger, *Nuclear Instruments and Methods in Physics Research* **B56/57**, 1106 (1991).
- [38] H. Geissel, Th. Schwab, P. Armbruster, J. P. Dufour, E. Hanelt, K.-H. Schmidt, B. Sherrill, and G. Münzenberg, *Nuclear Instruments and Methods in Physics Research* **A282**, 247 (1989).
- [39] G. Hempel, F. Hopkins, and G. Schatz, *Nuclear Instruments and Methods in Physics Research* **131**, 445 (1975).
- [40] J. Yurkon, D. Bazin, W. Benenson, D.J. Morrissey, B.M. Sherrill, D. Swan, and R. Swanson, *Nuclear Instruments and Methods in Physics Research* **A422**, 291 (1999).
- [41] William R. Leo, *Techniques for Nuclear and Particle Physics Experiments* (Springer-Verlag, New York, 1994).
- [42] G. Audi, O. Bersillon, J. Blachot, and A.H. Wapstra, *Nuclear Physics* **A624**, 1 (1997).
- [43] M. Berz, *Nuclear Instruments and Methods in Physics Research* **A298**, 473 (1990).
- [44] C. M. Perey and F. G. Perey, *Atomic Data and Nuclear Data Tables* **17**, 1 (1976).
- [45] R.J. Prestwood, D.B. Curtis, and J.H. Capps, *Physical Review* **C24**, 1346 (1981).
- [46] M. Berz, K. Joh, J.A. Nolen, B.M. Sherrill, and A.F. Zeller, *Physical Review* **C47**, 537 (1993).
- [47] B.M. Sherrill, Lecture Notes: The Basics of Magnetic Spectrographs, Introduction to Beam Theory, 1997, (unpublished).
- [48] Daniel Bazin, 1999, private communication.

- [49] Martin Berz, *COSY Infinity Version 8 User's Guide and Reference Manual*, National Superconducting Cyclotron Laboratory, 1997.
- [50] D.C. Carey, K.L. Brown, and F. Rothacker, Technical Report No. R-95-462, SLAC (unpublished).
- [51] F. Ajzenberg-Solve, *Nuclear Physics* **A523**, 1 (1991).
- [52] J. F. Ziegler, *The Stopping and Ranges of Ions in Matter* (Pergamon Press, New York, 1980), Vol. I.
- [53] Phillip R. Bevington and D. Keith Robinson, *Data Reduction and Error Analysis for the Physical Sciences*, 2nd ed. (McGraw-Hill Inc., New York, 1992).
- [54] I.M. Szöghy, Q. Haider, and R. Oullet, *Nuclear Instruments and Methods in Physics Research* **A242**, 277 (1986).
- [55] William H. Press, Saul A. Teukolsky, William T. Vetterling and Brian P. Flannery, *Numerical Recipes in Fortran*, 2nd ed. (Cambridge University Press, Cambridge, 1992).
- [56] *A Physicist's Desk Reference: The Second Edition of Physics Vade Mecum.*, 2nd ed., edited by Herbert L. Anderson (Springer-Verlag Inc., New York, 1989).